From Subduction to Collision:
Sedimentary Basin Constraints on Timescales and Geodynamic Drivers

Megan A. Mueller

A dissertation

submitted in partial fulfillment of the

requirements for the degree of

Doctor of Philosophy

University of Washington

2021

Reading Committee:

Alexis Licht, Chair

Katharine Huntington

Darrel Cowan

Program Authorized to Offer Degree:

Department of Earth and Space Sciences

University of Washington

Abstract

From Subduction to Collision:

Sedimentary Basin Constraints on Timescales and Geodynamic Drivers

Megan A. Mueller

Chair of the Supervisory Committee:

Dr. Alexis Licht

Department of Earth and Space Sciences

The Tethyan orogenic belt extends from the western Mediterranean to southeast Asia and the exposed rocks and landscapes present today are records of multiple orogenic events. The most recent, the Alpine-Himalayan orogeny, evolved during the Mesozoic-Cenozoic closure of the Neotethys Ocean during the convergence of Gondwana with Laurasia. Over the last few decades, significant advances in geochemical and geochronological methods and their widespread application have created a high-resolution temporal framework that reveals that various proxy records of intercontinental collisions across the Alpine-Himalayan belt differ by tens of millions of years. Consequently, new questions have arisen, including how to unite these seemingly disparate records of subduction and collision into a temporally and spatially credible reconstruction.

The work set forth in this dissertation situates the Anatolian segment of the Alpine-Himalayan orogenic belt in the broader discussion on the timescales and drivers of intercontinental collisions and their effect on biogeography. The various suture zones in Anatolia that delineate former branches of the Neotethys Ocean have complex and unresolved geodynamic reconstructions, including single and double subduction systems, pre-collisional subduction of lower plate terranes, forearc and backarc extension, ophiolite obduction, and protracted collisional deformation. Resolving these competing geodynamic scenarios is essential for paleogeographic reconstructions for refining the mechanistic links between subduction, accretion, and collision processes. Furthermore, the role of collisions in the early Cenozoic Anatolian archipelago in facilitating mammalian faunal exchange, including anthropoid primates, between Europe, Asia and Africa relies on accurate paleogeographic and topographic reconstructions.

Near-continuous deposition in western Anatolian sedimentary basins preserves an unbroken record of subduction through collision that is unparalleled across the Tethyan realm. This dissertation utilizes this sedimentary record by providing new stratigraphic, sedimentologic, petro- and geochronologic, and sedimentary provenance constraints on the chronology of collision along the İzmir-Ankara-Erzincan suture zone and the Intra-Pontide suture zone in western Anatolia. The sedimentary basin reconstructions presented in this dissertation, synthesized with existing datasets, provide a model for multi-stage continental collision that is applicable across the Tethyan realm.

Detrital zircon U-Pb geochronology and sandstone petrography data from the forearc-foreland Central Sakarya Basin in western Anatolia indicate that collision along the İzmir-Ankara-Erzincan suture zone began at 76 Ma, recorded as a major shift in provenance and the

onset of exhumation, sediment recycling, and suture zone uplift. Furthermore, new stratigraphy, sedimentology and sedimentary provenance studies from the foreland Sarıcakaya Basin in western Anatolia reveal that significant upper plate deformation was delayed by 20 Myr. By 54 Ma, the Central Sakarya Basin was partitioned by a basement-involved thrust fault, and flexural loading from the thrust created the Sarıcakaya Basin. This 20 Myr protracted collision along the İzmir-Ankara-Erzincan suture zone can be explained by three Tethyan models for multi-stage collision: slab breakoff, relict basin closure, or subduction of thinned passive margin lithosphere.

The validity of relict basin closure is evaluated using detrital zircon U-Pb geochronology, detrital rutile U-Pb and trace element geochemistry, and sandstone petrography from sedimentary units across the Intra-Pontide suture. A major shift in provenance in the Paleocene-early Eocene caused by accretionary prism exhumation demonstrates that collisional stress from incipient İzmir-Ankara-Erzincan suturing could have been taken up by the Intra-Pontide suture. Furthermore, the sedimentary evolution of both suture zones reveals that the uplift and exhumation of the accretionary prism is an important signal of collisional geodynamics. Even though continental collisions assembled a larger landmass that favored trans-Tethyan mammalian dispersals, for 30 Myr after initial collision, collisional deformation did not form significant topography; marine barriers and endemism persisted until the late Eocene. Accretionary orogenies, like those in Anatolia, likely have an important control on biogeography. The findings presented in this dissertation bear on fundamental questions regarding the interconnectedness of Earth systems, including the effects of plate tectonics, the causes of topographic change, and the geologic drivers of biodiversity.

TABLE OF CONTENTS

LIST OF FIGURES

LIST OF TABLES

ACKNOWLEDGEMENTS

The work presented in this dissertation would not have been possible without the expertise, enthusiasm, and encouragement of many colleagues, friends, and family. First, I would like to acknowledge the enormous support, guidance and passion of my advisor, Alexis Licht. Alexis' energy in the field, delight in new discoveries, and creative storytelling inspired the same in me. He always guided me to exciting research questions, new field and lab opportunities, cross-disciplinary collaborations, and to ultimately pursue my own research interests. Thank you to my co-advisor, Kate Huntington, for helping me navigate the academic world, for always providing expert organizational and managerial advice, and for pushing me to think big picture and then think even bigger. I am especially grateful for the ways in which Kate taught me to believe in my expertise and skill by treating me as a peer and colleague starting early in my graduate career.

Thank you to the members of my committee: Cailey Condit, Darrel Cowan, Emma Elliott-Groves, and Harold Tobin. Thanks to Cailey Condit for inviting me into the metamorphic petrology world and for always remaining positive and constructive in the face of setbacks. Thank you to Darrel Cowan for always being open to chat about geology and for leading incredible field trips across the western U.S. I would like to thank Emma Elliott-Groves for welcoming me into her world of educational research and providing thoughtful and gracious feedback on how to incorporate Indigenous voices and pedagogies into geoscience. Thanks to Harold Tobin for bringing wisdom and direction to committee meetings and for providing perspectives from modern forearcs.

It has been an incredible joy to work in Turkey: I have learned so much from the extraordinary culture and geology, and especially from the remarkable people I have met. Thank

you to Faruk Ocakoğlu for welcoming us to Turkey and providing logistical support. I am especially grateful for Faruk's depth of knowledge in sedimentary geology, expertise the field, and his support and encouragement in my career. Thank you to the Anadolu team: Chris Beard, Clay Campbell, Pauline Coster, Grégoire Métais, and Mike Taylor. Thanks to Matt Jones, Mustafa Kaya, Begüm Kurtoğlu, Spencer Mattingly, Andreas Möller, Çelik Ocakoğlu, Jan Westerweel, and Melissa Wood. Working with such talented scientists and fun people in beautiful field locations has been a highlight of my graduate career.

I received incredible support and mentorship from numerous faculty members in the Department of Earth and Space Sciences, including Knut Christianson, Ken Creager, Juliet Crider, Alison Duvall, Bruce Nelson, and Eric Steig. Thank you to Mike McGroder for being a fantastic field geology instructor and mentor. This dissertation would not have been possible without the incredible staff of ESS, including Michelle Barr, Noéll Bernard-Kingsley, Nathan Briley, Scott Dakins, Scott Kuehner, Ed Mulligan, Andrew Schauer, and Eunice Yang. I would also like to thank Tamas Ugrai, the manager of TraceLab, and Scott Braswell in the Molecular Analysis Facility for teaching me about lab instrumentation, supporting my experimentations, always squeezing me into the schedule, and patiently running lab equipment over Zoom. A special thank you to former ESS undergraduates Gui Akşit, Chris Baird, Lauren Burch, Kyle Lowery, Derek Pierce, and Sam Shekut.

The graduate students at UW made this experience more memorable and fun than I could have imagined. Thank you for pushing me to work hard, take breaks, and enjoy the Ave. Thanks to my fellow Supergroupers: Cassandra Brigham, Landon Burgener, Elizabeth Davis, Sarah Harbert, Emma Heitmann, Julia Kelson, Sean LaHusen, Virginia Littell, Susannah Morey, Sarah Schanz, Philip Schoettle-Greene, and Mike Turzewski. Thanks to my peers, cohort, and office

mates, especially Andrew Hoffman, Nick Cuozzo, Peter Lindquist, Zack McIntire, Jana Meixnerová, Carolyn Nuyen, and Paige Wilson.

Thank you to my non-geoscience community for believing that I am the coolest outdoor adventure buddy, supporting all my personal endeavors, and inspiring me to be myself; thank you to Stephanie Berliant, Karen Brigham, Kristen Choi, Peter Condit, Leslie Hampson, Elam Lantz, Ben Mishkin, Stacey Prince, Julian Robinson, Phil Ross, and Darcy Wyatt. Thank you to my family, especially my parents, Cathy Curry and Phil Mueller, and my brother, Sean Mueller, for teaching me to always pursue my interests and for celebrating all of my accomplishments.

Chapter 1. Introduction

1.1 Motivation

The Tethyan orogenic belt stretches from the western Mediterranean to southeast Asia and is one of the largest collision belts on Earth. The landscapes and rocks present today preserve a history of multiple cycles of oceanic basin opening and closing. The most recent event, the Alpine-Himalayan orogeny, marks the Mesozoic-Cenozoic closure of the Neotethys Ocean during the convergence of Afro-Arabia with Eurasia. The Alpine-Himalayan belt is one of the most well-studied ancient orogenic systems, defining our current conceptual models of subduction initiation and ophiolite formation and emplacement (van Hinsbergen et al., 2015; Plunder et al., 2015; Pourteau et al., 2019), forearc and backarc extension and basin formation (Görür, 1988; Royden, 1993; Maffione et al., 2015), subduction zone thermal regime and metamorphism (Whitney and Davis, 2006; Agard et al., 2018; Kotowski and Behr, 2019; Holt and Condit, 2021), topographic development and plateau formation (Clark and Royden, 2000; Schildgen et al., 2012; Göğüş et al., 2017; Meijers et al., 2018), and the structural, metamorphic, sedimentary and geodynamic evolution of accretionary and collisional events (Royden and Burchfiel, 1989; von Blanckenburg and Davies, 1995; Beaumont et al., 1996; Sinclair, 1997; Kaymakci et al., 2009; Soret et al., 2021). Furthermore, extensive reconstructions of the Neotethyan realm elucidate how convergent margin tectonics and paleogeography exert first-order controls on species migration and evolution (Sen, 2013; Beard, 2016; Métais et al., 2017, 2018; Whittaker et al., 2017) and atmospheric circulation, hydrology and global climate change (Raymo and Ruddiman, 1992; Kerrick and Caldeira, 1998; Clift et al., 2008; Goddéris et al., 2014; Licht et al., 2014; Zhang et al., 2014; Caves et al., 2014; Jagoutz et al., 2016). Consequently, it is a scientific priority to continue to discover the mechanistic

links between convergent margin tectonics, geodynamics, biology and climate in order to reconstruct Earth's past and predict Earth's future (Huntington and Klepeis et al., 2018; NASEM, 2020).

Even with decades of research on Tethyan collisions, there is significant disagreement on their timing and dynamics. A variety of proxies are used to determine the onset of collision, as defined by the disappearance of intervening oceanic lithosphere: the slowing of convergence velocity, paleo-position of continents, appearance of upper plate material on the lower plate, cessation of subduction-related arc magmatism, ophiolite obduction, high-pressure metamorphism, "significant" contractional deformation, and faunal exchange (Ding et al., 2005; Najman et al., 2010; Hu et al., 2016, p. 201; Kapp and DeCelles, 2019). Yet, these proxies result in significant discrepancies of collision age, for example, ~40 Myr for India-Asia (65-25 Ma) (Hu et al., 2016; Kapp and DeCelles, 2019) and ~20 Myr for Arabia-Eurasia (40-20 Ma) (McQuarrie et al., 2003; Okay et al., 2010; Ballato et al., 2011, 2018; Cowgill et al., 2016; Darin et al., 2018). It is important to resolve whether these discrepancies are an artifact of inter-proxy comparison (i.e., magmatism, sedimentation, deformation, exhumation, metamorphism), comparisons across geographical area (e.g., diachronous collision, non-linear margins), or a genuine signal of collisional processes. In order to explain the discrepancy in collision ages, a variety of geodynamic mechanisms have been proposed to explain the driving forces behind protracted intercontinental collisions. Multi-phased collisions have been proposed numerous times in the Tethyan domain and contain a variety of driving mechanisms: subduction of a large oceanic basin (van Hinsbergen et al., 2011, 2012), arc-continent collision (Jagoutz et al., 2016; Martin et al., 2020), relict basin closure (Cowgill et al., 2016), increased lower plate lithospheric thickness (Ballato et al., 2011; Soret et al., 2021), and slab breakoff (Sinclair, 1997; DeCelles et al., 2011). Resolving the driving

forces of protracted collision requires a refined along-strike chronology of collision and a self-consistent geodynamic model that integrates all proxies.

This dissertation focuses on (1) resolving the collision chronology in the western Anatolian segment of the Alpine-Himalayan orogeny, and (2) documenting the tectonic processes at play in all continental collisions. The Anatolian part of the orogen comprises a series of Gondwanan- and Laurasian-derived oceanic and continental units that accreted and collided in the late Mesozoic through Cenozoic (Şengör and Yilmaz, 1981). Despite the large volume of work on the numerous Neotethyan suturing events in Anatolia, basic tectonic and geodynamic questions remain enigmatic, including the number and polarity of subduction zones, number of terranes and their collision chronology, style of collisional deformation, and development of topography and thrust belts (Şengör and Yilmaz, 1981; Moix et al., 2008; Meijers et al., 2010; Lefebvre et al., 2013; Pourteau et al., 2016; Akbayram et al., 2016; Göğüş et al., 2017; Gürer and van Hinsbergen, 2018; van Hinsbergen et al., 2020). Western Anatolia includes, from north to south, the Pontides, İzmir-Ankara-Erzincan suture (İAES)—the main Neotethyan suture zone, Anatolides, and Taurides (Şengör and Yilmaz, 1981; Moix et al., 2008). The closure of Neotethyan oceans at the İAES was facilitated by one or two synchronous or asynchronous subduction zones (Göncüoğlu et al., 2000, 2014; Okay and Whitney, 2010; Speciale et al., 2012; Shin et al., 2013; Pourteau et al., 2016; Akbayram et al., 2016; Gürer and van Hinsbergen, 2018; Marroni et al., 2020). The pre-collisional subduction and metamorphism of lower plate Anatolide terranes (i.e., Tavşanlı Zone, Afyon Zone, Kırşehir Block), low convergence rates, small changes in paleolatitude, and multiple subduction zones make it difficult to date collision along the İAES by shortening, metamorphism, ophiolite obduction, or paleolatitude (Gürer and van Hinsbergen, 2018). Collision estimates along the İAES span more than 20 Myr, from the Late Cretaceous to early Eocene, based on ophiolite obduction

and Barrovian metamorphism (Göncüoğlu et al., 2000; Seaton et al., 2009; Whitney et al., 2011), structural deformation (Meijers et al., 2010; Lefebvre et al., 2013; Şahin et al., 2019), magmatism (Harris et al., 1994; Dilek and Altunkaynak, 2009; Kasapoğlu et al., 2016; Ersoy et al., 2017a; Schleiffarth et al., 2018), and sedimentary basin analysis (Okay et al., 2001; Kaymakci et al., 2009; Licht et al., 2017; Ocakoğlu et al., 2018; Mueller et al., 2019). To explain this range, various collision scenarios for the İAES are proposed (Pourteau et al., 2016 and references therein), including a pre-collisional non-linear Pontide or Anatolide-Tauride margin (Floyd et al., 2000; Yaliniz et al., 2000; Kaymakci et al., 2003; Meijers et al., 2010), subdividing the Anatolide-Tauride into multiple terranes that accreted diachronously (Moix et al., 2008; van Hinsbergen et al., 2016; Gürer and van Hinsbergen, 2018), and an initial "soft" collision followed by a final "hard" collision (Görür et al., 1984, 1998; Kaymakci et al., 2009; Robertson et al., 2009; Pourteau et al., 2010; Menant et al., 2016; Licht et al., 2017).

Geodynamic reconstructions are only further complicated by the synchronous evolution of the Intra-Pontide suture zone (IPS). The Intra-Pontide Ocean was also closed by one, two or three subduction zones of debated polarity that initiated in the Late Jurassic to Early Cretaceous (Akbayram et al., 2013; Göncüoğlu et al., 2014; Çimen et al., 2017, p. 201; Marroni et al., 2020), followed by Intra-Pontide suturing sometime from the Early Cretaceous through Eocene (Okay et al., 1994; Akbayram et al., 2013, 2016; Catanzariti et al., 2013; Göncüoğlu et al., 2014; Frassi et al., 2017; Di Rosa et al., 2019; Marroni et al., 2020; Akdoğan et al., 2020).

Resolving the chronology of collision is critical for paleogeographic and biogeographic reconstructions. The Anatolian archipelago could have played a key role in Paleogene trans-Tethyan biotic interchanges due to its location at the intersection of Afro-Arabia, Asia and Europe (Sen, 2013). For example, Anatolia is along one of the potential dispersal routes for anthropoid

primates that originated in Asia then colonized the then-island continents of Africa and South America in the middle Paleogene (Jaeger et al., 2010; Chaimanee et al., 2012; de Queiroz, 2014; Beard, 2016; Beard et al., 2020). Yet, the migration of species via island-hopping or rafting across wide marine barriers (i.e., sweepstakes dispersal) are subject to intense debate (e.g., de Queiroz, 2014; Beard, 2016). The tectonic convergence of formerly isolated terranes, in concert with global climate and sea-level change, is directly linked to the opening of dispersal corridors and large-scale biotic interchanges (Whittaker et al., 2017). However, the geodynamic, tectonic, topographic and climatic context for trans-Tethyan dispersals is missing in Anatolia.

The Pontides were isolated from Eurasia in the middle Cretaceous during backarc rifting and Black Sea spreading (Görür, 1988; Okay et al., 1994; Hippolyte et al., 2010; Akdoğan et al., 2019), likely setting the stage for faunal endemism. In Cretaceous-Paleogene times, Anatolia resembled an island archipelago separated from Afro-Arabia, Europe and Asia by remnants of the Paleotethys (e.g., Turgai strait) and Neotethys oceans (Barrier and Vrielynck, 2008; van Hinsbergen et al., 2020). Gradual Late Cretaceous to early Eocene collision and deformation from İAES suturing assembled a larger, emergent terrestrial landmass (e.g., MTA, 2002). Laurasian and Gondwanan mammalian clades (e.g., omomyid primates, embrithopods, marsupials, ungulates) colonized the Pontides in the Paleocene-Eocene via sweepstakes dispersal (Kappelman et al., 1996; Sen, 2013; Métais et al., 2017, 2018; Jones et al., 2018; Beard et al., 2020), perhaps aided by the Eocene expansion of mid-latitude monsoon ecosystems across the Tethyan margin (Licht et al., 2014, 2017). Some vertebrate mammal fauna (e.g., ungulates) persisted millions of years longer on the Pontides than in Europe, and their endemic radiations indicate that there was *in situ* diversification (Maas et al., 2001; Métais et al., 2018). This extreme provincialism persisted until at least the Lutetian (44-43 Ma; Licht et al., 2017) when many Anatolian sedimentary basins record

a marine incursion (Racey, 2001; MTA, 2002; Ocakoğlu et al., 2012; Lygina et al., 2016; Licht et al., 2017; Özcan et al., 2019). Endemism signifies that the Pontides were isolated from the Paleocene through Lutetian, though the Pontides could have been a dispersal corridor between Europe and Asia in the Priabonian-Bartonian (Sen, 2013; Métais et al., 2017, 2018; Licht et al., 2017; Jones et al., 2018; Beard et al., 2020). It is unknown whether tectonics or climate forcing were responsible for emerging land bridges that reconnected Anatolia with Europe and Asia (Sen, 2013). The influence of tectonics on Anatolian biogeography and trans-Tethyan dispersals cannot be properly evaluated without improved reconstructions of Mediterranean paleogeography and topographic development.

Anatolia is therefore the ideal location to parse the links between geodynamics, tectonics, and biogeography. Compared with other collisions in the Alpine-Himalayan orogeny, Anatolia had low convergence rates (i.e., 50-60 mm/yr on average and up to 140 mm/yr for India-Asia versus 20 mm/yr or less for Anatolia; Jagoutz et al., 2015; van Hinsbergen et al., 2020) and it is extremely rare for collision zones to preserve a continuous record of sedimentation. Therefore, the near-continuous Jurassic through Eocene deposition in forearc-to-foreland sedimentary basins on the western Pontides (i.e., Kocaeli, Central Sakarya, Sarıcakaya basins) provides an invaluable, uninterrupted archive of subduction through collision. This dissertation reconstructs the Late Cretaceous through Eocene tectonostratigraphic evolution of western Anatolian sedimentary basins using sedimentology, stratigraphy, geochronology, and sedimentary provenance proxies. The sedimentary basins record uplift, exhumation and sediment recycling near the suture zone during initial collision, followed by basement-involved deformation and basin partitioning ca. 20 Myr later. The work presented here integrates sedimentary basin analysis with existing structural,

metamorphic and magmatic records to propose a protracted collisional model applicable across the Tethyan realm.

1.2 Dissertation Organization

This dissertation is subdivided into the following subsequent chapters:

Chapter 2 presents the first tectonostratigraphic analysis of the Sarıcakaya Basin, a small sedimentary basin in western Anatolia containing Eocene terrestrial sedimentary deposits and volcanic units and bounded by the İAES and basement-involved Söğüt thrust fault. The results from measured stratigraphic sections, geochronologic age constraints, interpreted depositional environments, and provenance proxies indicate that the Sarıcakaya Basin is a flexural basin formed by loading from the Söğüt Thrust which partitioned the Central Sakarya foreland basin by the early Eocene. The evolution of the Sarıcakaya Basin demonstrates that collision between the Pontides and Taurides occurred before the early Eocene in western Anatolia and was therefore synchronous in western and central Anatolia, with implications for the paleogeography of Tauride terranes. Furthermore, the new evidence for early Eocene contractional deformation calls into question previous interpretations of Eocene slab breakoff.

Eocene thick-skinned deformation and basin formation in western Anatolia provides an upper limit to Pontide-Tauride collision in western Anatolia (Chapter 2; Mueller et al., 2019), yet collision proxies such as ophiolite obduction and Barrovian metamorphism (Göncüoğlu et al., 2000; Seaton et al., 2009; Whitney et al., 2011), sedimentary basin changes (Okay et al., 2001; Açıkalın et al., 2016; Ocakoğlu et al., 2018), magmatism (Harris et al., 1994; Dilek and Altunkaynak, 2009; Kasapoğlu et al., 2016; Ersoy et al., 2017), and structural deformation (Şahin et al., 2019) indicate that collision was sometime from the Late Cretaceous through Eocene.

Chapter 3 reconstructs the sedimentary provenance evolution of the Central Sakarya basin from the Late Cretaceous through Eocene. The results indicate that there was sediment recycling and uplift and exhumation of the suture zone starting at 76 Ma which, in tandem with other records, is interpreted as the early signal of intercontinental collision. This reveals a ~20 Myr long multi-stage collision, during which significant thrust belt development was delayed due to changes in plate coupling from thinned passive margin subduction, relict basin closure, and/or slab breakoff. Emergent landmasses and terrestrial environments only appeared on the Pontides and Taurides in the later stages of collision, highlighting a geodynamic effect on Paleocene-Eocene biogeography.

In collisions between large continental domains, such as Afro-Arabia with Eurasia, the early stages of collisional deformation can be modulated by the closure or relict upper plate backarc basins (e.g., Cowgill et al., 2016). Accordingly, Chapter 3 hypothesizes that relict basin closure at the Intra-Pontide suture is one possible mechanism to control the protracted collisional evolution in western Anatolia. However, it is unknown whether this mechanism is applicable among smaller terrane collisions, such as between the Pontides and Taurides, especially because of the wide range in estimates for the closure of the Intra-Pontide suture (i.e., Early Cretaceous through Eocene; Akbayram et al., 2013, 2016; Robertson and Ustaömer, 2004). **Chapter 4** uses detrital zircon U-Pb geochronology, detrital rutile U-Pb and trace element geochemistry, and sandstone petrography to compare the evolution of sedimentary provenance across the Intra-Pontide suture. A significant provenance shift in the Paleocene-early Eocene associated with accretionary prism uplift and exhumation indicates that the closure of the Intra-Pontide oceanic basin could have delayed collisional deformation from İAES suturing.

The final chapter, **Chapter 5**, contains concluding remarks about the state of tectonics, geodynamics, and biogeography in Anatolia and across the Tethyan realm. Supplementary materials for each chapter are included in the appendices. Large data tables are included separately.

1.3 Positionality in the Geosciences

I grew up in Michigan as a settler on Peoria and Anishinaabe land. As a kid, my family spent summers "up north" in northern Michigan doing all things water: swimming in the lake, fishing, canoeing, water skiing, boating, and floating. My family shaped my love of water, especially in their dedication to and joy in water skiing. My grandparents and parents taught me to water ski in the same way they were taught. The waters have been one of the highlights to completing my PhD in Seattle. I frequently watched the salmon, seal, and cormorants, always hoping to spot orcas and river otters. I have been a temporary settler here on the ancestral lands of the Duwamish and Coast Salish tribes. I grew up experientially learning that the land has inherent value and is worth protecting in its own right, but in Seattle, I have learned to ask, who makes decisions on behalf of the land, and how do we know if the land consents? I have started to join the movements to return land, including the power of decision making, to Indigenous people.

Benefitting from the wisdom, expertise and support of the faculty and peers in the UW College of Education, part of my graduate studies has been dedicated to developing my own pedagogical framework in the geosciences. Dr. Emma Elliott-Groves expanded my vision for geoscience through her class's framework of land as pedagogy and introduced me to incredible scholars and teachers. The work of Coulthard (2014), Simpson (2014) and Kimmerer (2020) outlined my foundational ethical commitments to human-land interactions. Wildcat (2001) and Bang (2020) taught me to consider the connection between land and human health, and the role of

land in cultivating intellectual health. Mentors and peers helped me see that the intersection of geoscience and Indigenous sovereignty is rooted in both land and place. From this, Whyte (2018) sparked a vision for how to incorporate land, place-based pedagogy, and Indigenous sovereignty with local Pacific Northwest geology in classroom settings. My endeavors to create geoscience curriculum that includes land as pedagogy is part of my journey to integrate my moral and ethical commitments to land, passion for geoscience, and the Indigenous sovereignty, resurgence, and decolonization movements. My goal is that every student who enrolls in a geoscience course develops both technical skills and their moral and ethical frameworks to be accountable for co-creating a sustainable and equitable future. The seminal piece, *Decolonization is not a metaphor*, Tuck and Yang (2012) reframed my understanding of decolonization and pushed my intellectual interests out of the classroom into the rest of my life. In interviews, the authors of *Education in movement spaces: Standing Rock to Chicago Freedom Square* (Shield et al., 2020) gifted me their vision for collective freedom that continues to sustain and inspire me.

Chapter 2. Collision Chronology Along the İzmir-Ankara-Erzincan Suture Zone: Insights from the Sarıcakaya Basin, Western Anatolia

Megan A. Mueller, Alexis Licht, Clay Campbell, Faruk Ocakoğlu, Michael H. Taylor, Lauren Burch, Tamas Ugrai, Mustafa Kaya, Begum Kurtoğlu, Pauline M. C. Coster, Grégoire Métais, K. Christopher Beard. 2019. Collision Chronology Along the İzmir-Ankara-Erzincan Suture Zone: Insights from the Sarıcakaya Basin, Western Anatolia. Tectonics 38: 3652–3674. DOI: 10.1029/2019TC005683

Abstract

Debate persists concerning the timing and geodynamics of intercontinental collision, style of syn-collisional deformation, and development of topography and fold-and-thrust belts along the >1,700-km-long İzmir-Ankara-Erzincan suture zone (İAES) in Turkey. Resolving this debate is a necessary precursor to evaluating the integrity of convergent margin models and kinematic, topographic, and biogeographic reconstructions of the Mediterranean domain. Geodynamic models argue either for a synchronous or diachronous collision during either the Late Cretaceous and/or Eocene, followed by Eocene slab breakoff and post-collisional magmatism.

We investigate the collision chronology in western Anatolia as recorded in the sedimentary archives of the 90-km-long Sarıcakaya Basin perched at shallow structural levels along the İAES. Based on new zircon U-Pb geochronology and depositional environment and sedimentary provenance results, we demonstrate that the Sarıcakaya Basin is an Eocene sedimentary basin with

sediment sourced from both the İAES and Söğüt Thrust fault to the south and north, respectively, and formed primarily by flexural loading from north-south shortening along the syn-collisional Söğüt Thrust. Our results refine the timing of collision between the Anatolides and Pontide terranes in western Anatolia to Maastrichtian-Middle Paleocene and Early Eocene crustal shortening and basin formation. Furthermore, we demonstrate contemporaneous collision, deformation, and magmatism across the İAES, supporting synchronous collision models. We show that regional post-collisional magmatism can be explained by renewed underthrusting instead of slab breakoff. This new İAES chronology provides additional constraints for kinematic, geodynamic, and biogeographic reconstructions of the Mediterranean domain.

2.1 Introduction

Anatolia is a complex mosaic of Gondwanan and Laurasian microcontinents that collided from the Late Cretaceous through the Paleogene (Şengör and Yilmaz, 1981). Today, the >1,700-km-long İzmir-Ankara- Erzincan suture zone (İAES) demarcates the Pontides in the north from the Anatolide-Tauride Block (ATB) to the south (Figure 2.1). It is debated whether Pontide-ATB collision was synchronous or diachronous along strike (Kaymakci et al., 2003, 2009; van Hinsbergen et al., 2016). These different models resulted in competitive paleogeographic scenarios requiring unique geodynamic (e.g., Pourteau et al., 2016) and biogeographic (Sen, 2013; Métais et al., 2017; Jones et al., 2018) reconstructions of the Mediterranean domain and the broader Alpine-Zagros-Himalayan-Tibetan orogen. Synchronous collision models suggest contemporaneous collision in central and western Anatolia whereas diachronous collision models suggest westward younging of collision and suturing across Anatolia (cf. Section 2.2). In western Anatolia, the timing of Pontide-ATB collision is poorly resolved, sometime in the Late Cretaceous,

Paleocene, or Early Eocene (e.g., Pourteau et al., 2016). Eocene slab breakoff is inferred from geochemical data (Harris et al., 1994; e.g., Altunkaynak, 2007; Dilek and Altunkaynak, 2009; Yildiz et al., 2015; Kasapoğlu et al., 2016; Ersoy et al., 2017b, 2017a) but is either not supported or unresolved in mantle tomography (e.g., van Hinsbergen et al., 2010; Portner et al., 2018) or topographic expression (e.g., Okay et al., 2001; Ustaömer et al., 2009). Models consistent with collision or slab breakoff can be tested by examining the stratigraphic record against the expected crustal response. Slab breakoff predicts surface uplift, erosion, and local extension (Davies and von Blanckenburg, 1995; e.g., von Blanckenburg and Davies, 1995), whereas continued underthrusting predicts shortening, basin development, and syntectonic sedimentation.

This study presents the first tectonostratigraphic analysis of the Sarıcakaya Basin in western Anatolia. We refine depositional ages through volcanic zircon U-Pb geochronology, interpret depositional environments from measured sections, and evaluate provenance through detrital zircon U-Pb geochronology and sandstone petrography. We use the Sarıcakaya Basin to appraise models of intercontinental collision and slab breakoff in northwest Turkey and to discuss the implications of our results for geodynamic models of the İAES.

2.2 Geological Context

2.2.1 Western Anatolian Tectonic Provinces

Northwestern Anatolia encompasses four major tectonic domains, including, from south to north, the Tavşanlı Zone, İAES, Sakarya Zone, and Istanbul Zone (Figure 2.1 and Figure 2.2). The ATB zones display distinct and varied metamorphic gradients (van Hinsbergen et al., 2016). The northernmost zone is the Tavşanlı Zone, a mélange of HP/LT blueschist- and eclogite-facies rocks (Okay, 2002). Today, the Tavşanlı Zone comprises, from highest to lowest structural levels,

Eocene and Neogene siliciclastic and volcanic rocks of the peripheral Eskişehir foreland basin, obducted Cretaceous ophiolites of the İAES, metamorphosed Paleozoic basement, and Late Cretaceous and Eocene-early Oligocene granitoids intruded into the ophiolites and basement (Harris et al., 1994; Okay et al., 1998; Sherlock et al., 1999; Okay and Whitney, 2010; Şengüler and Izladi, 2013). The HT/LP Kırşehir Block in central Anatolia (also known as the Kırşehir Massif or Central Anatolian Crystalline Complex) is arguably either a distinct terrane (e.g., Görür et al., 1984) or the lateral continuation of the Tavşanlı Zone (Yaliniz et al., 2000; van Hinsbergen et al., 2016; Plunder et al., 2018).

North of the Tavşanlı Zone is a highly deformed accretionary prism of metamorphosed oceanic crust and former continental margin units termed the İAES. The İAES marks the former location of Tethyan oceans that opened and closed in the Mesozoic-Paleogene (Şengör, 1979, and references therein) and consists mainly of ophiolitic mélange, serpentinite, blueschist, and amphibolite rocks (Okay et al., 2002; Okay and Whitney, 2010; Plunder et al., 2013a; Sarıfakıoğlu et al., 2017).

The Sakarya Zone of the Pontides is directly north of the İAES. The two basement units in the Sakarya Zone are (1) Central Sakarya Basement, composed of Precambrian to Paleozoic crystalline basement, metamorphosed continental units called the Söğüt Metamorphics, and Carboniferous Söğüt granodiorites (also termed Söğüt magmatics, Central Sakarya granite, and Sarıcakaya granitoid) (Okay, 2000; Okay and Göncüoglu, 2004; Kibici et al., 2010; Ustaömer et al., 2016) and (2) the Permian-Triassic subduction-accretion Karakaya Complex composed of metamorphic rocks, ophiolitic mélange, deformed flysch, and limestone (Okay, 2000; Okay and Göncüoglu, 2004; Ustaömer et al., 2016). Basement rock units are exposed in south directed thrust sheets and overlain by a thick sequence of unmetamorphosed Jurassic-Miocene sedimentary and

volcanic rocks, which are well exposed in the Sarıcakaya and Central Sakarya Basins (Yildiz et al., 2015; Kasapoğlu et al., 2016; Ocakoğlu et al., 2018). North of the İAES and Karakaya Complex is the Sarıcakaya Basin (SB), a triangular sedimentary basin (~90 × 0 × 10 km) delimited to the north by the Söğüt Thrust (also termed Nallıhan Thrust), a south directed, basement-involved thrust fault. The thrust fault juxtaposes SB sedimentary units in the footwall under Central Sakarya Basement and Mesozoic-Cenozoic sedimentary units belonging to the forearc-to-foreland Central Sakarya Basin (CSB; also termed the Mudurnu-Göynük Basin) in the hanging wall (Altiner et al., 1991; Okay et al., 2001; Açıkalın et al., 2015, 2016; Ocakoğlu et al., 2018).

The controversial Intra-Pontide Suture Zone, now occupied by the North Anatolian Fault, demarcates the northern extent of the Sakarya Zone from the Istanbul Zone (Robertson and Ustaömer, 2004; Akbayram et al., 2016).

2.2.2 Evolution of the İzmir-Ankara-Erzincan Suture Zone

Collision in central Anatolia involved three terranes: the Pontides, the Kırşehir Block (KB) and ATB (Figure 2.1). Based on the wealth of data from central Anatolia, three different collision scenarios are envisaged. (1) In the diachronous promontory collision model, the KB was a promontory of the ATB. Initial collision of the apex of the KB in the latest Cretaceous preceded collision in western and eastern Anatolia (Figure 2.3a; Floyd et al., 2000; Yaliniz et al., 2000; Kaymakci et al., 2003; Meijers et al., 2010). Ophiolitic belts at the southern KB were from foreland-propagating thrust nappes from the İAES not an Intra-Tauride Suture Zone. (2) In a second diachronous model, the soft-hard collision model, the KB was an isolated terrane bounded to the north and south by subduction zones of debated polarity (Görür et al., 1984, 1998; Robertson et al., 2009; Menant et al., 2016). Incipient Pontides-KB “soft” collision in the Maastrichtian-

Paleocene was followed by the ATB colliding with southern KB at the Intra-Tauride Suture Zone in a final, “hard” Eocene collision (Figure 2.3b; Kaymakci et al., 2009; Pourteau et al., 2010; Licht et al., 2017). The presence of the Intra-Tauride Suture Zone is highly debated (Lefebvre et al., 2013; Advokaat et al., 2014; Menant et al., 2016). In both diachronous models, Pontide-KB collision predated Pontide-ATB collision. (3) The synchronous collision model suggests that the KB was the lateral continuation of the Tavşanlı Zone (Figure 2.3c). Contemporaneous Paleocene collision of Tavşanlı-KB with the Pontides was followed by a Miocene collision of the eastern ATB with the Pontides (van Hinsbergen et al., 2016; Gürer et al., 2016; Gürer and van Hinsbergen, 2018). Key to this model is the interpretation that contrasting metamorphic grades between the KB and Tavşanlı Zone resulted from NE verging oblique subduction of the KB into an east dipping subduction zone (Lefebvre et al., 2013; Plunder et al., 2018). The synchronous model does not advocate for or against an Intra-Tauride suture but allows for an oceanic basin separating the Tavşanlı-KB from the rest of the ATB.

Several models have been proposed for the evolution of subduction and collision in western Anatolia (Pourteau et al., 2016, and references therein). Regardless of which model is correct, most invoke two Late Cretaceous subduction zones. In the north, the Sakarya Zone was an Andean-type margin (Pourteau et al., 2016; Ocakoğlu et al., 2018), with a volcanic arc occupying E-W trending Campanian extensional structures (Ocakoğlu et al., 2018). In the south, an intra-oceanic subduction zone was also active and eventually obducted onto the Tavşanlı Zone, which was itself subducted to blueschist and eclogite facies between 95 and 85 Ma (Okay et al., 1998; Pourteau et al., 2010; Plunder et al., 2013a).

The absence of the KB in western Anatolia provides the perfect location to appraise competing Pontide-ATB collisional scenarios. All models agree upon a latest Cretaceous-earliest

Paleocene Pontide-KB collision. Therefore, in western Anatolia, a latest Cretaceous-early Paleocene collision would support the synchronous collision model, whereas finding a post-Paleocene collision would support a diachronous suturing model.

2.2.3 Syn-collisional Evolution

The timing of Tavşanlı-Sakarya collision remains imprecise in the literature, with most citing a Late Cretaceous-Eocene collision due to the CSB transition from flysch to molasse (Okay et al., 1998, 2001; Göncüoğlu et al., 2000; Pourteau et al., 2016). Açıkalın et al. (2016) proposed an early collision at 71 Ma due to the sudden influx of mafic material into the CSB. Yet changes in subduction dynamics or Tavşanlı Zone slab breakoff between 85 and 75 Ma (Okay and Whitney, 2010) could explain pre-collisional accretionary prism uplift. On the other hand, collision was dated at ~61 Ma based on coeval uplift and an angular unconformity at the southern CSB and prograding deltaic sequences deeper into the basin (Ocakoğlu et al., 2018).

Collision is loosely constrained by structural relationships. Along the suture zone, Paleogene units are the oldest to unconformably overlie both Karakaya Complex and accretionary mélange, indicating that thrust faults juxtaposed the Karakaya Complex and mélange (Figure 2.2) sometime between deposition of the Upper Cretaceous and lower Paleogene strata (Göncüoğlu et al., 2000) and likely date the age of collision. The east-west trending folds and thin-skinned thrust faults in the CSB and SB comprise the syn-collisional Eocene to Mio-Pliocene fold-and-thrust belt (e.g., Okay et al., 2001; Şahin et al., 2019). The most significant thrust is a basement-involved structure, the Söğüt Thrust, which has an along-strike length of ~150-km parallel to the suture zone. At its western end, the Söğüt Thrust juxtaposes Central Sakarya Basement over the Karakaya Complex and Mesozoic-Paleogene sedimentary units. Whereas in the east, Cenozoic sedimentary

and volcanic units are in the hanging wall and footwall. Based on a simple linear scaling relationship between fault trace length and amount of displacement, it is reasonable to estimate 15 km of displacement along the ~150-km-long Söğüt Thrust (Walsh and Watterson, 1988; Marrett and Allmendinger, 1991; Cowie and Scholz, 1992). The Söğüt Thrust likely reactivated the paleo-suture zone between the accreted Karakaya Complex and the Pontide crystalline basement (Central Sakarya Basement) as there is no Karakaya Complex exposed along the thrust or further north and no Central Sakarya Basement exposed south of the thrust. It would be unlikely for convergent-margin deformation in the accretionary prism to be accommodated along a lithospheric-scale structure like the Söğüt Thrust (e.g., Noda, 2016). Şahin et al. (2019) argue that this fault was syn-collisional and active by at least the Eocene but refined dating of the Söğüt Thrust would fine-tune the collision age.

In most places in the SB, the thick Paleogene sedimentary sequence unconformably overlies the Karakaya Complex (Figure 2.2; Gedik and Aksay, 2002). The basal Paleogene unit is dated from Early Paleocene to Middle Eocene and given various names: the Mihalgazi Formation, including the Çamaklı Member (Yildiz et al., 2015), Kabalar Formation, and Kızılçay Member/Group (Gedik and Aksay, 2002; Kasapoğlu et al., 2016). Uğuz (2013) briefly describes and interprets this unit as debris flow, alluvial fan, flood plain, and lacustrine limestone facies. Based on the rapid Paleocene-Eocene lateral facies changes and coeval magmatism, Göncüoğlu et al. (2000) interpreted the SB as a transtensional basin. Conversely, mapping and structural analysis by Şahin et al. (2019) determined that Paleogene-Miocene units were deposited in a contractional regime.

Volcanism migrated southward from the Late Cretaceous to Eocene (Ocakoğlu et al., 2018). Eocene Nallıhan volcanic rocks are presently between 6- and 10-km north of the İAES,

implying slab rollback or steepening between the Late Cretaceous and Eocene, perhaps due to syn-collisional slowing of the convergence velocity. Here we remain consistent with the published body of literature by using the term “post-collisional” for Eocene magmatism but include it within the “syn-collisional” evolution because underthrusting and deformation was active from at least the Cenomanian through Miocene (e.g., Şahin et al., 2019).

The tectonic setting and geodynamic implications of post-collisional magmatism is debated. There are three belts of post-collisional magmatism in western Anatolia: (1) 54- to 48-Ma granodiorite plutons and associated HP/LT metamorphism in the Tavşanlı Zone (Figure 2.2; Harris et al., 1994; Okay and Satir, 2006; Altunkaynak, 2007; Dilek and Altunkaynak, 2009; Özdamar et al., 2018); (2) 53- to 47-Ma basaltic to rhyolitic Nallıhan volcanic rocks in the SB and eastern CSB (Figure 2.2; Harris et al., 1994; Yildiz et al., 2015; Kasapoğlu et al., 2016); and (3) the Kizderbent belt of 53- to 38-Ma volcano-plutonic rocks ~80-km north of the İAES (Altunkaynak, 2007; Ersoy et al., 2017b, 2017a). Because the Kizderbent volcanic rocks exhibit different geochemical properties (Ersoy et al., 2017b) and could belong to a different subduction system (Okay and Satir, 2006), we only consider the Nallıhan and Tavşanlı igneous rocks. Whole rock major and trace elements and Sr–Nd–Pb isotopic compositions of the Nallıhan rocks indicate some fractional crystallization and crustal contamination, and mixture modeling supports increased asthenospheric (Ersoy et al., 2017b) or metasomatized mantle lithospheric sources (Altunkaynak, 2007). The geochemistry, in addition to the linear geometry of the volcano-plutonic belt, the late Paleocene-early Eocene transition from marine to terrestrial deposition (e.g., Okay et al., 2001), and a possible relict slab interpreted from seismic tomography (van Hinsbergen et al., 2010; Portner et al., 2018) have led many authors to conclude that slab breakoff or delamination processes generated the volcanism (Altunkaynak, 2007; Altunkaynak et al., 2012; Yildiz et al.,

2015; Kasapoğlu et al., 2016; Ersoy et al., 2017a). However, (Ustaömer et al., 2009) outlined the inconsistencies in the slab breakoff hypothesis, most notably that magmatism from slab breakoff or delamination is emplaced into thickened and elevated crust, yet there was Early-Middle Eocene marine deposition in the three foreland basins. Furthermore, new papers argue that slab breakoff is amagmatic (Niu, 2017; Garzanti et al., 2018). Alternative hypotheses are that the Tavşanlı plutons and Nallıhan volcanic rocks were derived from the mantle wedge or anatexis of the lower continental crust (Harris et al., 1994; Okay et al., 1998), or that magmatism could be explained by migration of the volcanic front toward the suture zone where the crust is thinner (Chapman et al., 2017).

All these different approaches yield contrasting results regarding the timing of Sakarya-Tavşanlı collision and syn-collisional deformation and geodynamics. In this part of western Anatolia, the interpretation of slab breakoff has not been tested outside of geochemical analyses. Provenance, deformation, and magmatism have yet to be integrated into a broader model describing collisional evolution. Our work in the Sarıcakaya Basin presents a new holistic model of suturing in this region of western Anatolia.

2.3 Methods

2.3.1 Sedimentology

To determine the Paleogene evolution of the Sarıcakaya Basin, we measured 13 stratigraphic sections at decimeter- to-meter resolution at four localities—Mayıslar, İğdir, Kapıkaya, and Ozanköy—in a ~130-km-wide area between Sarıcakaya and Ozanköy (Figure 2.2), starting at the oldest exposure at the base of the Paleogene series. We subdivide the basin fill into six units and designate informal member names. From the measured sections, we construct a

composite stratigraphic section. We describe the sedimentary facies, group them into five main lithofacies, and interpret depositional environments. In our study area, the SB is less than 10-km wide and the Söğüt Thrust has around 15 km of displacement, assuming simple displacement-length scaling relationships (Cowie and Scholz, 1992). Therefore, our stratigraphic sections totaling 1.5 km likely do not reflect significant change in north-south position; in other words, we interpret stratigraphic changes as temporal not spatial evolution because they do not represent any consequential upsection migration toward the thrust front.

2.3.2 Zircon U-Pb Geochronology

Zircon U-Pb geochronology is used to determine the age of SB sedimentary strata, provenance of the basin sedimentary units, and signatures of potential sediment sources. We collected 12 samples along our stratigraphic sections. Additionally, we analyzed two samples from the İAES and one from the Söğüt Thrust hanging wall to characterize the age distributions in these two potential source areas.

The zircon separation, mounting, LA-ICP-MS analysis, and data reduction follow the University of Washington protocol (Licht et al., 2018). Zircons were separated by standard heavy mineral separation methods. A minimum of 140 grains per sample were randomly selected, mounted with standards (Black et al., 2004; Sláma et al., 2008; Eddy et al., 2016), and analyzed using a laser ablation-inductively coupled plasma-mass spectrometer (LA-ICP-MS) at the University of Washington. The data were reduced with *Iolite* using their Geochron Data Reduction Scheme to calculate U-Pb ages uncorrected for common lead (Paton et al., 2011). Individual zircons with >20% discordance, >5% reverse discordance, or abnormal patterns in raw signal intensity were excluded from analyses and interpretations (after Gehrels, 2012, 2014).

Crystallization ages of the volcaniclastic zircon samples were determined using *TuffZirc* (Ludwig, 2012). Kernel density estimates were calculated using the plug-in adaptive bandwidth selection method (Botev et al., 2010). Supporting information includes data and detailed analytical protocols.

2.3.3 Sandstone Petrography

In addition to U-Pb geochronology, we evaluated the provenance of the SB strata from modal sandstone compositions determined through petrographic analysis. Thin sections from 25 fine- to coarse-grained sandstone samples were prepared by National Petrographic Service, Inc. and at the University of Washington. Poorly indurated samples were sieved, and the 63- to 250-μm fractions were mounted in epoxy cups then made into thin sections. At least 340 points per slide were counted using the Gazzi-Dickinson point-counting method (Dickinson, 1985). Ternary diagrams were plotted using *Triplot* (Graham and Midgley, 2000a) and interpreted using typical provenance source fields (Dickinson and Suczek, 1979; Dickinson et al., 1983; Dickinson, 1985). Quartz grains include monocrystalline quartz (Qm) and polycrystalline quartz (Qp); feldspar grains (F) include plagioclase and orthoclase; lithic fragments include metamorphic (Lm), sedimentary (Ls; chert, mudstone, siltstone, and sandstone), and volcanic (Lv). The supplemental data files include the modal data.

2.4 Results

2.4.1 Sedimentology of the Eocene Deposits in the Sarıcakaya Basin

We combined individual measured sections into a composite stratigraphic section (Figure 2.4). There are many small reverse faults throughout the basin, so all measured thicknesses are

minimum thicknesses measured from continuous sections. In our study area, contacts between the Karakaya Complex, Jurassic limestone, Cretaceous marine deposits, and Paleogene deposits were reactivated as thrust fault contacts. Growth strata and paleocurrent indicators were not observed, primarily due to faulting, limited exposure, and advanced weathering; weathering also made sedimentary structures difficult to observe. The clastic units are given informal member names and are described from oldest to youngest in the following section: Basal Conglomerate, Lower Lacustrine, Andesitic, Red, Lower Purple, Brown Conglomerate, and Upper Lacustrine Members. We observed depositional contacts between all units (Figure B.1, Figure B.2, Figure B.3, and Figure B.4); thrust faults in Figure 2.4 represent small faults observed in some measured section locations. The main lithofacies are synthesized in Table 2.1.

The Basal Conglomerate Member unconformably overlies Karakaya Complex, Jurassic limestone, or thin remnants of Late Cretaceous marine clastics (Gedik and Aksay, 2002; Timur and Aksay, 2002). The Basal Conglomerate Member is mainly 1- to 3-m-thick massive sets of matrix- and clast-supported conglomerates with very angular serpentinite, chert and greenschist clasts (LF1 in Table 2.1; Figure 2.5a). Weakly to strongly calcareous brown mudstones, siltstones, and sandstones are interbedded with the conglomerates.

The base of the Lower Lacustrine Member is made of cross-bedded conglomerate beds interbedded with strongly developed paleosols with root traces and carbonate nodules (LF2), sometimes forming 10- to 50-cm-thick caliches (LF3). The strata then grade into green and gray mudstones and siltstones (LF3), interbedded with 50- to 100-cm-thick white, tabular, and continuous limestone beds (LF4), thick coarse sandstones and isolated conglomerate lenses containing serpentinite, andesitic, and sparse greenschist clasts (LF5).

The Lower Lacustrine Member is capped by the Andesitic Member, which is andesite-bearing volcanic conglomerate beds and massive andesite (Figure 2.5b). This member is overlain by the Red Member (Figure 2.5c and Figure 2.5d), comprising thick red-brown mudstones with gray-green and brown mottling, carbonate nodules, sparse root traces, and isolated greenschist and carbonate clasts (LF2). Typically, the mudstones are capped by either a 50- to 200-cm-thick caliche with isolated clastic matrix (LF3) or 50- to 800-cm-thick tabular and lenticular (5- to 10-m wide) conglomerate beds with clasts of serpentinite, andesite, carbonate, and chert (LF5) (Figure 2.5d).

The Lower Purple Member is characterized by heavily mottled, carbonaceous purple mudstone (Figure 2.5e) and siltstone with root traces and isolated clasts (LF2). These mudstones and siltstones are interbedded with <50-cm-thick organic-rich mudstone and lignite and tabular to lenticular conglomerate and gravel with well-rounded greenschist, quartz, chert, gneiss, schist, and carbonate clasts (LF5; Figure 2.5f).

The contact between the Lower Purple and Brown Conglomerate Member is an angular unconformity (Figure 2.5g). The Brown Conglomerate Member is characterized by 1- to 12-m-thick packages of pebble to boulder clast-supported, fining-upward, trough cross-bedded conglomerate with well-rounded clasts of greenschist, carbonate, gneiss, schist, and quartz (LF5; Figure 2.5h and Figure 2.5i). Conglomerate troughs are interbedded with mudstones, siltstone, and sandstone with root traces, mottling, pedogenic carbonate nodules, and 50- to 150-cm-thick caliche horizons (LF2; Figure 2.5j).

The Brown Conglomerate Member vertically transitions into the Upper Lacustrine Member (Figure 2.5k). Brown-gray mudstone and siltstones with root traces, mottling, pedogenic carbonate nodules (LF2), and 50- to 300-cm caliche (LF3) characterize the basal Upper Lacustrine Member. Additionally, trough crossbedded conglomerates with quartz, gneiss, greenschist, and

carbonate clasts are present (LF5). The top of the Upper Lacustrine Member is red-brown planar laminated very fine, mature (quartz, mica) sand interbedded with mudstone with small, wavy ripples, trough cross lamination, load casts, mudcracks, and trace fossils (Figure 2.5l and Figure 2.5m), as well as 5- to 20-cm thick, continuous tabular limestone beds (LF4).

2.4.2 Volcaniclastic Zircon U-Pb Ages

We present the ages of SB volcaniclastic samples in Table 2.2 and their stratigraphic location in Figure 2.4. We also include one volcaniclastic sample from Campbell (2017). Volcaniclastic layers are massive, gray-green mudstones predominantly composed of feldspar, which we interpret as weathered pyroclastics (LF3). Zircon grains are angular to rounded, predominantly euhedral, tabular to prismatic, and some grains are broken. The age spectra reveal a single age population (Figure B.5; after Vermeesch, 2018) interpreted to reflect a single provenance tied to an eruption event rather than a mixed provenance reflecting recycling from multiple age source areas.

Together, the results constrain deposition of the Basal Conglomerate through Red Members to 52.4 through 48.0 Ma (Figure 2.4). Results refine the age of these strata as lower Eocene (Ypresian), previously described as upper Paleocene to lower Eocene (Gedik and Aksay, 2002; Yildiz et al., 2015). Deposition was coeval with 53- to 47-Ma Nallıhan volcanism (Kasapoğlu et al., 2016). Maximum depositional ages from sandstones (cf. Section 2.4.3) were also calculated and are compatible with volcaniclastic ages without bringing any additional constraint so are not provided. The age of the Lower Purple through Upper Lacustrine Members is poorly constrained due to the absence of volcanic layers and young zircons. However, laterally correlative deposits in the eastern SB are interbedded with 51.7- to 44.7-Ma lavas and tuffs

(Kasapoğlu et al., 2016; Şahin et al., 2019). Therefore, we suspect that our SB sections extend into the middle Eocene.

2.4.3 Detrital Zircon U-Pb Ages

Detrital zircon grains from eight SB samples (n = 759) yielded ages with acceptable concordance and precision for geochronologic interpretation. Within each sample, zircon grains vary from angular to rounded and euhedral to anhedral, and some contain inclusions. The results, plus two detrital samples (n = 242) from Campbell (2017), are presented in their stratigraphic position in Figure 4. Sample 16SKY04 has a prominent Ypresian peak and minor Jurassic, Triassic, and Carboniferous age peaks. Sample 16SKY23 has a prominent Ypresian age peak. Sample 16SKY26 has prominent Jurassic, Triassic, and Carboniferous age peaks and a minor Devonian age peak. Sample 15YP08 has broad Permian-Devonian and Silurian-Ordovician age peaks. Sample 16SKY37 has a broad Phanerozoic age peak centered around the Triassic-Carboniferous. Sample 15YP09 has Ypresian, Carboniferous, and Devonian age peaks. Sample 16SKY42 has broad Jurassic and Devonian age peaks. Sample 17OZK05 displays a broad peak centering around the late Neoproterozoic. Sample 17OZK12 only has one broad peak centering around the Devonian and no zircons younger than the earliest Cretaceous. All samples except 16SKY04, 16SKY23, and 17OZK12 have late Neoproterozoic (~600 Ma) and late Mesoproterozoic (~1,000 Ma) age zircons. All samples except the two oldest (16SKY04 and 16SKY23) have various minor Paleoproterozoic-late Archean age peaks.

The apparent temporal trends in SB samples are the appearance of Precambrian age peaks starting at the top of the Red Member (16SKY26; after 48.0 Ma), the appearance of Late Cretaceous age zircons starting at the top of the Lower Purple Member, and the disappearance of

<120- and >2,000-Ma zircons at the top of the Upper Lacustrine Member (17OZK12). These trends are not associated with any trend in depositional environments. A multidimensional scaling map, a visual assessment of misfit between age distributions, is provided in Appendix B (Figure B.6; Vermeesch, 2013).

We present new (n = 223) and include previously published zircon U-Pb data (n = 769) to characterize provenance source regions (Table 2.3 and Figure 2.6). Sample 15YP12, a Karakaya Complex schist, has one prominent Carboniferous age peak (Campbell, 2017). Sample KK.10 is a sandstone sample from the Upper Karakaya Complex in our study region and has prominent late Carboniferous-early Permian and Triassic age peaks (Ustaömer et al., 2016). New modern river samples drain the accretionary prism mélange: 17RIVER01 contains minor Carboniferous, Permian, Triassic, and Eocene age peaks, and 16ESK01 has a prominent Carboniferous age peak. Together these samples characterize the İAES age distribution. Samples north of the basin characterize the zircon signature of sediment derived from the Söğüt Thrust hanging wall. The sample included from (Ustaömer et al., 2012; named here SgtMeta), a sillimanite-garnet schist from Central Sakarya Basement, contains only zircons older than 500 Ma, with two prominent Neoproterozoic age peaks. Sample 17BASE01 is a new gneiss sample from the Söğüt Metamorphics and has one prominent Ordovician peak. Together, SgtMeta and 17BASE01 characterize the Central Sakarya Basement signature. Central Sakarya Basin detrital sandstone samples from Ocakoğlu et al. (2018) and Campbell (2017) are included to characterize the sedimentary strata of the Söğüt Thrust hanging wall that could be reworked and deposited in the SB. Jurassic 15YP04 has one Carboniferous age peak, Upper Cretaceous sample 15YP13 contains one prominent Campanian peak, and Upper Cretaceous 15GO02 and Paleocene-Eocene(?) 15YP14 have a prominent Campanian age peaks and a minor Carboniferous peak.

Next, we grouped all samples by location—north (Söğüt Thrust hanging wall) and south (İAES) of the SB— to evaluate the similarity and relative contribution of each source area to the SB strata (Figure 2.7). Therefore, we plot both all Söğüt Thrust hanging wall samples and only Central Sakarya Basement samples (no Mesozoic-Cenozoic sedimentary samples), and all İAES samples and only Karakaya Complex samples. The Central Sakarya Basement has characteristic age peaks >450 Ma. The signal from the Late Cretaceous arc is unique to the Upper Cretaceous and Paleo-Eocene(?) sedimentary samples in the Söğüt Thrust compilation. The Triassic age peak is characteristic of the Karakaya Complex.

2.4.4 Sandstone Petrography

The modal framework grain composition of 25 SB samples is shown in four ternary diagrams (Figure 8). The majority of samples classify as lithic, quartzo-lithic, and litho-quartzose sandstones with <10% feldspar and varying proportions of quartz and lithic grains (after Garzanti, 2018); three lower lacustrine member samples contain larger proportions of feldspar. Most samples plot within the recycled orogen and magmatic arc province fields. The Red through Upper Lacustrine Members display a trend of increasing proportions of monocrystalline and polycrystalline quartz. On average, accessory minerals, including epidote, white mica, biotite, zircon, serpentine, amphibole, calcite, and opaque minerals, comprise 10%–30% of total framework grains. and magmatic arc province fields.

2.5 Interpretation

2.5.1 Depositional Environments

The Sarıcakaya Basin sedimentary facies reflect three main depositional environments: alluvial fan, fluvial (channels and floodplain), and lacustrine. There is no evidence for marine deposition.

Laterally extensive, clast-supported, massive conglomerate beds with very angular clasts and an erosive base, interbedded with medium-to-coarse sandstone and mudstone, are interpreted as debris flow deposits on alluvial fans (LF1; Table 2.1; Prothero and Schwab, 1996; Nichols, 2009). Massive, matrix-supported conglomerates are interpreted as proximal fluvial and sheetflood deposits within alluvial fans (LF1; Nichols, 2009). Structureless, red-brown mudstones are massive and laterally extensive; they commonly coarse upward and are capped by caliche. Due to the abundant root traces, carbonate nodules, mottling, we interpret these facies as pedogenized overbank deposits (LF2; Retallack, 1988). Continuous, tabular, unfossiliferous, and laminated limestones can be easily distinguished from massive, nodular caliches (LF3) and are interpreted as lacustrine limestones (LF4; Prothero and Schwab, 1996). Conglomerate and sandstone bodies display the characteristic wing shape and fining upward sequence with erosive, coarse basal lags found in fluvial channel bodies (LF5; Nichols, 2009).

Overall, the depositional environments reflect long-term, repetitive changes along an alluvial fan-floodplain-lake system. The juxtaposition of well-developed soil horizons on top of alluvial fans and fluvial channels suggests frequent alluvial fan lobe and fluvial channel avulsions. Lacustrine limestone formation suggests periods of low sedimentary input.

2.5.2 Sedimentary Provenance

The provenance results from detrital zircon, modal sandstone, and field observations establish that the SB sediments contain detritus sourced from the İzmir-Ankara-Erzincan suture zone and Söğüt Thrust fault hanging wall.

2.5.2.1 Detrital Zircon U-Pb Geochronology

Here we interpret the source of zircons found in SB samples, from oldest to youngest, based on the comparison with potential sediment sources (Figure 2.7). Early Paleozoic and Precambrian zircons present in SB samples younger than 48.0 Ma are derived from exposed Central Sakarya Basement. Minor Proterozoic peaks present in the SB are not present in the two source compilations, such as the 1,500-Ma peak (0.5%). This could indicate that there were other sedimentary sources, or it could be an artifact of sample size. The Devonian age peak (~400 Ma) is not useful for provenance because it is present in both sources. Similarly, our dataset does not determine whether Carboniferous zircons in the SB are from Central Sakarya Basement exposed by the Söğüt Thrust, Karakaya Complex, or reworked Söğüt Thrust sedimentary strata. Triassic zircons are abundant in the SB and İAES (especially KK.10) and minorly present in the post-Jurassic Söğüt Thrust samples (2.7%). We suggest that Triassic zircons in the SB reflect sediment input from the Karakaya Complex in the suture zone. Jurassic zircons in the SB do not appear to be derived from either potential source. The Late Cretaceous zircons are present in the post-Jurassic Söğüt Thrust sedimentary samples and in most SB samples younger than 48.0 Ma. These zircons could come directly from the Cretaceous volcanic arc in the CSB or Beypazarı plutons or reworked Söğüt Thrust hanging wall. Eocene volcanism is well documented within the SB;

therefore, Eocene zircons likely reflect sediment or ash derived directly from the arc. The Eocene age peak in the İAES samples could be from Nallıhan volcanic rocks or Tavşanlı plutons.

We summarize and interpret the provenance data as follows. The oldest SB detrital zircon sample (Basal Conglomerate Member) contains Triassic zircons, which are characteristic of Karakaya Complex, and almost no pre-Carboniferous zircons, suggesting a predominant input of material from the İAES and locally from the Nallıhan volcanics around 52.4 Ma. The dominance of the Eocene peak in 16SKY23 suggests continued sediment sourcing from the Nallıhan arc through 48.0 Ma. There is a change in provenance around 48.0 Ma. Samples from the Red through Upper Lacustrine Members contain age peaks uniquely associated with the Central Sakarya Basement (>450 Ma). This signal demonstrates that Central Sakarya Basement was exposed along the Söğüt Thrust by 48.0 Ma, and the continued presence of Triassic age zircons demonstrates sustained input from the İAES.

2.5.2.2 Sandstone Petrography and Clast Composition

Modal sandstone compositions affirm the same provenance trends as the detrital zircon data (Figure 2.8). The Basal Conglomerate through Red Members samples plot in the oceanic affinity region of the recycled orogenic province or volcanic arc province. Lower Purple through Upper Lacustrine Members demonstrate an upsection increase in quartz and plot in the mixed or continental affinity region of the recycled orogenic province, especially the Brown Conglomerate and Upper Lacustrine Members. The İAES lithologies are low in quartz and feldspar unlike the exposed Central Sakarya Basement and overlying sedimentary units. Therefore, we interpret the upsection trend as an increase in sediment supply from the Söğüt Thrust hanging wall. The dominance of sedimentary lithics suggests that material was reworked from the İAES, Söğüt Thrust, and/or within the SB.

Field observations suggest similar changes in conglomerate clast compositions upsection, from predominantly greenschist, serpentine, red radiolarian chert, and andesitic clasts in the lower half of the section to mostly quartz, gneiss, and schist in the upper half. Field observations suggest that carbonate clasts are derived from two sources: eroded and reworked caliche and lacustrine limestone and from Jurassic limestone. Reworked carbonate clasts indicate progressive deformation of sedimentary strata in the SB, supporting syntectonic deposition.

2.5.3 History and Origin of the Sarıcakaya Basin

In this section, we synthesize geochronologic, provenance, and sedimentologic data to describe the origin and evolution of the Sarıcakaya Basin. We conclude that the SB was a broken foreland basin formed by flexural loading from the Söğüt Thrust.

We used volcaniclastic U-Pb ages to determine that the oldest exposed Paleogene deposits are ~52.4 Ma. Therefore, the SB was set up by at least 52 Ma and deposition continued through at least 48 Ma. Deposition was coeval with post-collisional magmatism. Because there were no tuffs to constrain the upper age of our section, the duration of deposition is uncertain. Correlative deposits in the eastern SB are interbedded with 51.7- to 44.7-Ma lavas and tuffs, and our section is entirely terrestrial, so it is possible that our section captures at least the early Lutetian prior to the late Lutetian-Bartonian/Priabonian(?) marine incursion (Ocakoğlu et al., 2018; Şahin et al., 2019).

All provenance data are consistent with the SB system being fed by the hanging wall of the Söğüt Thrust and İAES. Detrital zircon and sandstone petrography results display a similar trend of increasing relative proportions of Central Sakarya Basement material, starting at the top of the Red Member around 48.0 Ma.

The presence of Central Sakarya Basement material demonstrates that the Söğüt Thrust was active and accommodating syn-collisional convergence by at least 48 Ma. The presence of a sedimentary basin requires a mechanism of formation and accommodation space creation. Models for sedimentation in foreland basins correlate periods of fold-and-thrust belt buildup (flexural loading) to depositional environments. It is debated whether coarse-grained deposition in foreland basins reflects periods of tectonic activity in the fold-and-thrust belt or isostatic adjustment and progradation during fold-and-thrust belt quiescence. Either (1) tectonically driven uplift and erosion increases subsidence rate, sediment flux, and grain size (Burbank et al., 1988; Heller and Paola, 1992; Paola et al., 1992) or (2) periods of rapid tectonic loading from fold-and-thrust belt activity flex the crust and increase both accommodation space and subsidence rates to drive fine-grained deposition (deeper facies) in the basin (Flemings and Jordan, 1990; Heller and Paola, 1992; Paola et al., 1992). Neither model is universally applicable (Burbank et al., 1988), but both confirm that the repetitive change between coarse- and fine-grained deposition is characteristic of thrust-loading flexural basins.

The provenance data support an active thrust and repetitive changes from coarse-grained alluvial fan and fluvial channel facies to fined-grained overbank and lake facies (Figure 2.4) by 48.0 Ma. Therefore, we classify the SB as a Laramide-style broken foreland basin by 48.0 Ma (Dickinson et al., 1988). We argue that the SB was likely formed as a broken foreland basin as early as 52.4 Ma because the same repetitive change in depositional environments are present by 52.4 Ma. The delay in Central Sakarya Basement material in the zircon results and in quartz-rich compositions until around 48.0 Ma can be explained in two ways. First, we measured section along the southern limb of the basin; it would have taken some to overfill the basin such that material from the northern limb reached the southern limb. Second, based on measured sections (Ocakoğlu

et al., 2018), field observations and local geologic maps (Duru and Aksay, 2002; Gedik and Aksay, 2002; Timur and Aksay, 2002), there was at least 2 km of Jurassic-Cretaceous sedimentary cover at the southern margin of the CSB. Therefore, there must have been at least 2 km of throw and correlative erosion on the Söğüt Thrust by about 48.0 Ma to shed basement-derived zircons into the SB.

2.6 Discussion

2.6.1 Western İzmir-Ankara-Erzincan Suturing and Geodynamics

2.6.1.1 Sakarya-Tavşanlı Collision

We refine the age of Sakarya-Tavşanlı collision via two pieces of evidence. First, we constrain the minimum age for the onset of syn-collisional deformation to 52.4 Ma. Yet, collision was likely much earlier because the Söğüt Thrust must have been active before the onset of deposition in the SB. Second, the timing of collision is further constrained by our geochronologic dataset of magmatic flare-ups and lulls in western Anatolia near the İAES: 73- to 115-Ma magmatism, 59- to 72-Ma lull, and 44- to 58-Ma magmatism. This magmatic cyclicity suggests that the Late Cretaceous arc was active until 72 Ma and collision occurred sometime in the Maastrichtian-Middle Paleocene. This 72- to 59-Ma lull is compatible with both ages previously proposed in western Anatolia, 71 and 61 Ma (Açıkalın et al., 2016; Ocakoğlu et al., 2018), and with the age of collision in central Anatolia (Kaymakci et al., 2009).

2.6.1.2 Slab Dynamics in Western Anatolia

Without conclusive mantle tomography, slab breakoff must be identified by its surface expression: uplift, local extension, and extensional exhumation. No Paleogene extensional features

have been described. There are three periods of uplift and erosion that could be correlated to slab breakoff. (1) The SB and CSB Paleogene deposits are in angular unconformity with underlying units (Ocakoğlu et al., 2018; Şahin et al., 2019). Therefore, there was uplift and erosion sometime between the Late Cretaceous and 52 Ma, during a magmatic lull. If slab breakoff is amagmatic (Niu, 2017; Garzanti et al., 2018), then this period could encompass initial Tavşanlı-Sakarya collision, slab rollback, and/or steepening and slab breakoff. This is the best candidate for slab breakoff, and this scenario does not change the interpretation of the Eocene SB. (2) Our data demonstrate there was uplift and erosion at the southern and northern SB coeval with post-collisional magmatism. Yet, the Söğüt Thrust was accommodating shortening in the Paleogene (Şahin et al., 2019) and the Central Sakarya Basement was exposed by the Ypresian. The SB could not have formed during an extensional regime: the Söğüt Thrust is the boundary between Karakaya Complex and Central Sakarya Basement, so any extension along this structure would not expose Central Sakarya Basement. (3) The angular unconformity at the base of the Brown Conglomerate Member likely reflects a period of uplift and erosion. The unconformity is poorly constrained to younger than 48.0 Ma. There is no clear change in depositional style or provenance before and after the unconformity. There is no evidence to suggest the unconformity represents a long period of major uplift, exhumation, and erosion.

Based on the contractional regime in the Early Eocene, we prefer the interpretation that the Nallıhan and Tavşanlı igneous rocks are consistent with continued underthrusting, southward mantle wedge migration, and magmatism, as opposed to slab breakoff, lithospheric delamination, or arc root foundering (Figure 2.9). Syn-collisional convergence is facilitated by continued slab pull from the Tavşanlı slab and/or a southward jump in subduction to the Afyon-Tavşanlı Zone interface or the northern margin of the African plate (Figure 2.1; e.g., Pourteau et al., 2016). There

was ~250 km of convergence between Africa and Europe from 50 to 35 Ma (van Hinsbergen et al., 2010). If the Söğüt Thrust only accommodated 15 km of convergence, faults in the accretionary prism and/or the Intra-Pontide suture, in addition to southern active subduction zones, might have accommodated a significant amount of shortening.

The geochemical signature of the Nallıhan and Tavşanlı igneous rocks is interpreted as from an asthenospheric (Ersoy et al., 2017b) or metasomatized lithospheric mantle source (Altunkaynak, 2007). Alternatively, the magmatic rocks could be the result of several factors other than slab breakoff. First, the Sakarya Zone, a rifted terrane (Ustaömer et al., 2012), could have been thin in the Eocene, as the Tavşanlı Zone crust was only 30-km thick at that time (Okay et al., 1998). Second, if the Söğüt Thrust marks the boundary between Central Sakarya Basement and Karakaya Complex, then the crust beneath the SB was thin and oceanic, explaining why there was little crustal contamination (Altunkaynak, 2007). Lastly, the Eocene volcanic front, located within 5 km of the accretionary mélange, could have been derived from the mantle wedge (Harris et al., 1994; Okay et al., 1998).

2.6.2 Geodynamic Model

In this section, we synthesize the Sarıcakaya Basin interpretation into a holistic model for the evolution of this part of western Anatolia (Figure 2.9).

1) Prior to Sakarya-Tavşanlı collision, the CSB was one large forearc-backarc basin complex bisected by the Late Cretaceous volcanic arc (Açıkalın et al., 2016; Ocakoğlu et al., 2018).
2) Initial collision in the Maastrichtian-Middle Paleocene was marked by a magmatic lull (72–59 Ma; Figure 2.7). Collision was marked in the CSB stratigraphic record

as uplift, northward deltaic progradation, shallowing, increased sedimentation rates, and an angular unconformity (Ocakoğlu et al., 2018). Shortening and underthrusting were accommodated by the Söğüt Thrust, the paleosuture between Karakaya Complex and Central Sakarya Basement. There was syn-collisional slab rollback.

3) By 52 Ma, the SB formed by flexural loading from Söğüt Thrust and was partitioned from the CSB. Sediment was initially sourced from the volcanic arc and suture zone and likely the sedimentary cover in the Söğüt Thrust hanging wall. Around 48.0 Ma, Central Sakarya Basement was exposed along the thrust and feeding the SB. Post-collisional Nallıhan and Tavşanlı magmatism occurred over a 14-Myr span, from 58 to 44 Ma. The slab was steeply dipping, evidenced by the short distance from the suture zone to volcanic front.

2.6.3 Central-Western Anatolian Geodynamics

The three collision models for central Anatolia estimate Pontides-Kırşehir Block collision was in the Maastrichtian-early Paleocene based on stratigraphic, metamorphic, magmatic, and structural analyses (Görür et al., 1984, 1998; Kaymakci et al., 2009; Robertson et al., 2009; Meijers et al., 2010; Lefebvre et al., 2013; van Hinsbergen et al., 2016; Licht et al., 2017). Here we affirm a Maastrichtian-Middle Paleocene collision in western Anatolia, supporting the synchronous collision model (e.g., Gürer and van Hinsbergen, 2018).

Furthermore, there is coeval deformation and basin formation along the İAES. We demonstrate fold-and-thrust belt development and basin formation by 52 Ma. Large Cretaceous-Eocene peripheral and retro-arc foreland basins and fold-and-thrust belts developed in central

Anatolia (Janbu et al., 2007; Leren et al., 2007; Hippolyte et al., 2016) and generally recorded a switch from Late Cretaceous extension to syn-collisional contraction in the Paleocene-Early Eocene (Kaymakci et al., 2009; Nairn et al., 2013). There are a few differences, such as, after collision in central Anatolia, deformation fronts of thin-skinned thrust belts and depocenters migrated perpendicularly away from the suture zone (Kaymakci et al., 2009; Advokaat et al., 2014) as opposed to deposition in the SB near the suture zone. Also, thick-skinned deformation in the west preceded Middle-Late Eocene thick-skinned deformation in central Anatolia (e.g., Kaymakci et al., 2009; Nairn et al., 2013). This along-strike change in deformation remains unexplained in collision models but could be a result of changes in lithology, basement thickness, preexisting structures, or effects of oblique subduction on orogen dynamics (Plunder et al., 2018).

In addition, magmatic flare-ups and lulls were synchronous along the İAES. From a large, compiled dataset (n = 702) of <100-Ma magmatism in central and eastern Anatolia, (Schleiffarth et al., 2018) find a high-flux magmatic event from 73 to 100 Ma, magmatic lull from 60 to 72 Ma, and flare-up from 40 to 58 Ma. This is almost exactly the results of our dataset (n = 2,245): 73- to 115-Ma magmatism, 59- to 72-Ma lull, and 44- to 58-Ma magmatism.

Contemporaneous collision, deformation, and magmatism across the western and central İAES all suggest that the synchronous collision model is the most suitable. Our data and interpretations of the SB are more aligned with a coeval collision of the KB and Tavşanlı Zone with the Pontides, suggesting that the KB is the lateral equivalent of the Tavşanlı Zone and not a promontory or separate terrane.

2.7 Conclusions

We constrain Pontide-Tavşanlı Zone collision to Maastrichtian-Middle Paleocene. We demonstrate that the Sarıcakaya Basin was a syn-collisional, Eocene broken foreland basin that formed by flexural loading from the Söğüt Thrust by 52 Ma. Sediment was sourced from both the İzmir-Ankara-Erzincan suture zone and basement-involved Söğüt Thrust. The SB cautions against the overuse of slab breakoff to explain post-collisional magmatism (Niu, 2017; Garzanti et al., 2018). Our reconstruction of the SB elucidates complete opposite crustal response than what is predicted by slab breakoff. The SB formed in contractional regime, with significant basin subsidence coeval with post-collisional magmatism. We provide a new model of syn-collisional evolution in western Anatolia in which convergence, underthrusting, and accommodation space creation dominate during the early Eocene. Compared to the record of collisional evolution in central Anatolia, we demonstrate a synchronous magmatic history and onset of deformation along the İzmir-Ankara-Erzincan suture zone. Contemporaneous collision supports synchronous collision models which imply the Kırşehir Block was the lateral continuation of the Tavşanlı Zone not an independent terrane or promontory.

Acknowledgements

This research was funded by the U.S. National Science Foundation (EAR- 1543684). Raw data and additional files supporting our analyses and conclusions are in the Supporting Information and a Mendeley Data repository (https://data.mendeley.com/datasets/vs292g83c4). Thoughtful reviews by N. Lom and M. Darin improved this manuscript. We thank K.W. Huntington, M.D. Turzewski, M. Wood, P. Ballato, Ç. Ocakoğlu, M.Z. McIntire, D.S. Cowan, J.G. Crider, S.

Kuehner, P. Schoettle-Greene, C.D. Rowe, and D. McDougall for their prolific discussions and assistance in the field and in the lab.

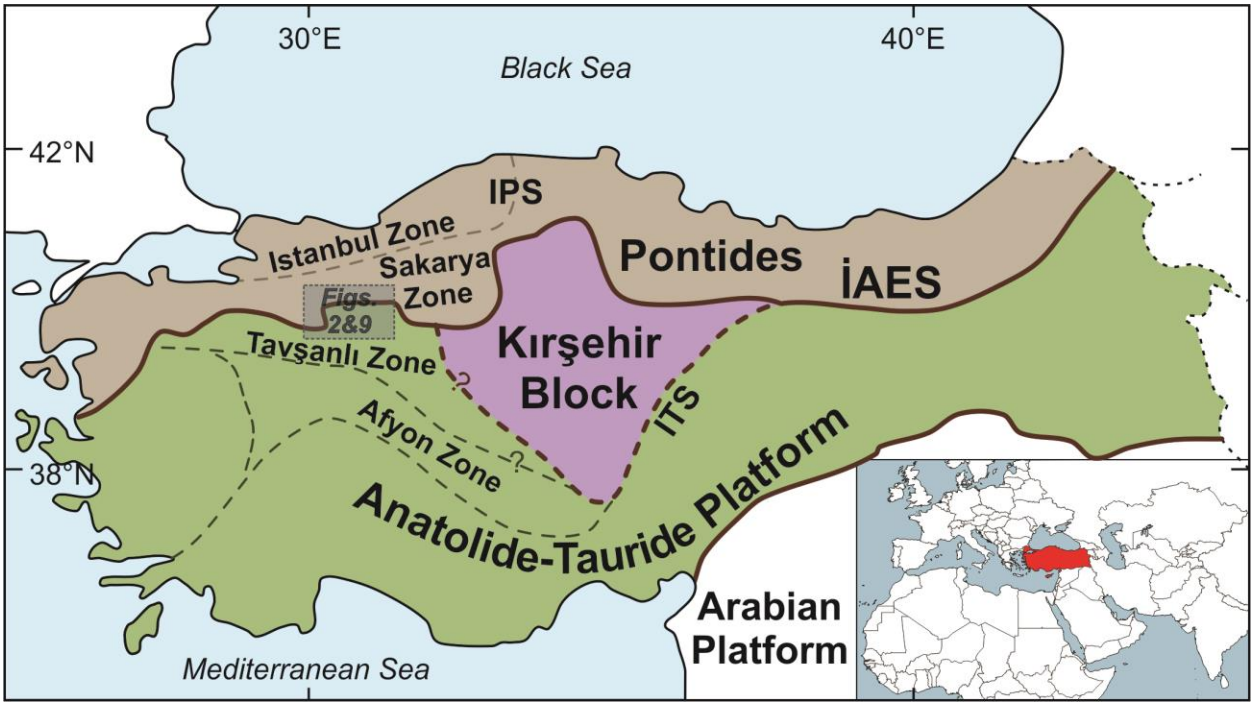

Figure 2.1. Generalized and simplified tectonic map of Anatolia (modified from Licht et al., 2017; Pourteau et al., 2013; van Hinsbergen et al., 2016, and references therein). İAES = İzmir-Ankara-Erzincan suture; IPS = Intra-Pontide suture; ITS = Intra-Tauride suture.

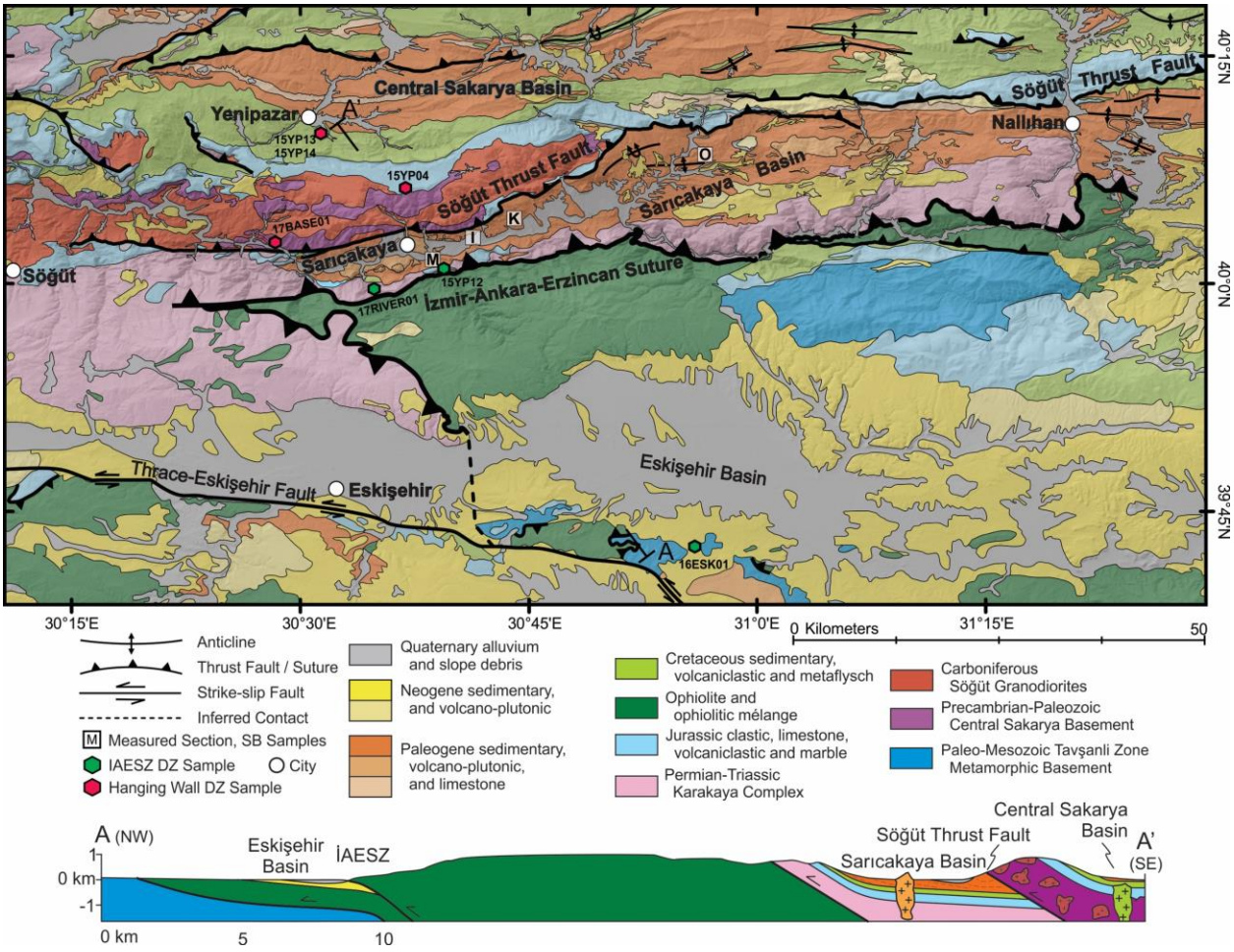

Figure 2.2. Regional geologic map and schematic cross section of the southern Central Sakarya Basin, Sarıcakaya Basin, İzmir-Ankara-Erzincan suture zone, and Eskişehir Basin (modified from Aksay et al., 2002; Duru and Aksay, 2002; Gedik and Aksay, 2002; Timur and Aksay, 2002; Turhan, 2002; Ustaömer et al., 2012; Şengüler and Izladi, 2013; Kasapoğlu et al., 2016). İAES and Söğüt Thrust detrital zircon sample locations are labeled (including those from Campbell, 2017); measured sections locations include SB detrital zircon and sandstone petrography samples (M = Mayıslar sections, I = Iğdir sections, K = Kapıkaya sections, and O= Ozanköy sections). The Paleogene volcano-plutonic unit includes the Nallıhan volcanic rocks and Tavşanlı Zone plutons. See Figure 2.1 for location.

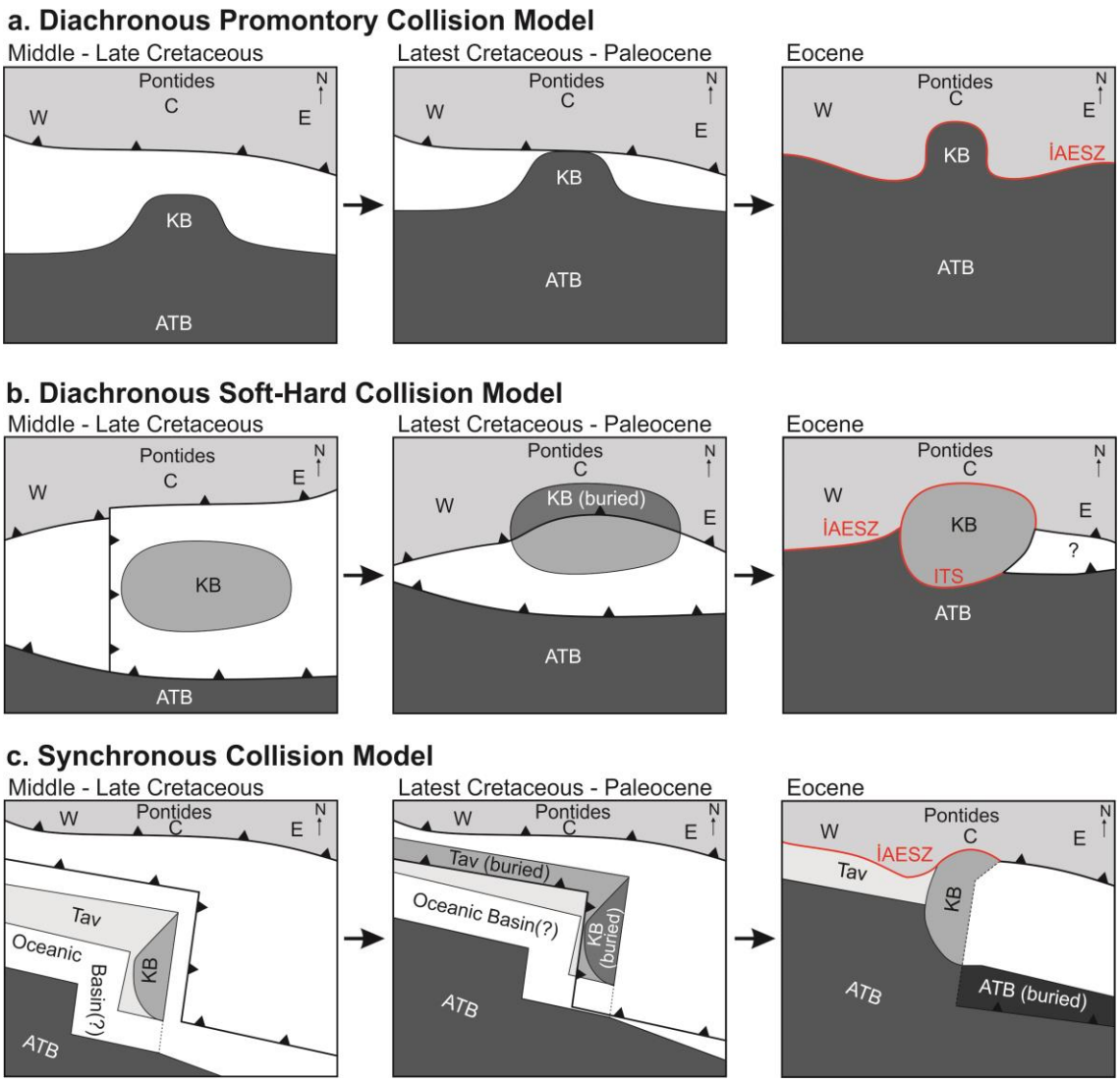

Figure 2.3. Simplified schematics of various İAES evolution models; see text for discussion. (a) Diachronous promontory collision model with the Kırşehir Block as a promontory of the Anatolide-Tauride Block. (b) Diachronous soft-hard collision model with the Kırşehir Block as a distinct terrane bound to the north and south by oceanic basins and subduction zones. (c) Synchronous collision model: the Kırşehir Block and Tavşanlı Zone are connected to the entire ATB and subjected to differing metamorphic conditions during subduction and ophiolite obduction. ATB = Anatolide-Tauride Block; İAESZ = İzmir-Ankara-Erzincan suture zone; ITS = Intra-Tauride suture; KB = Kırşehir Block; Tav = Tavşanlı Zone (part of ATB in a and b).

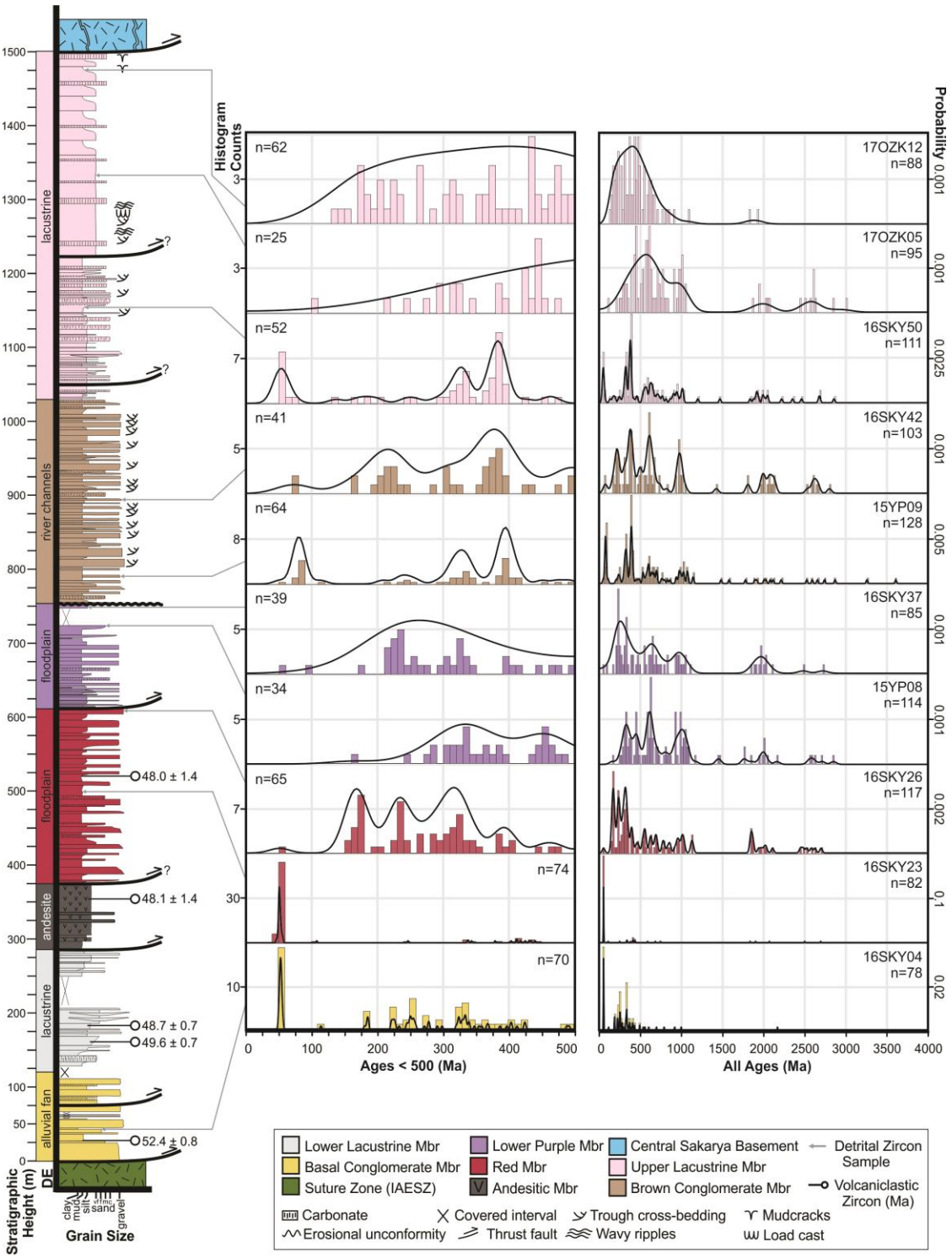

Figure 2.4. Composite stratigraphic section of the Sarıcakaya Basin with volcaniclastic zircon U-Pb ages. Fill colors correspond with informal members; sedimentary structures symbols and the one fill pattern (carbonate) are defined in the legend. Here observed thrust faults are depicted; see

Figure B.1, Figure B.2, Figure B.3 and Figure B.4 for depositional contacts. The main depositional environment (DE) is given to the left. To the right of the stratigraphic column, histograms, and kernel density estimates (Botev et al., 2010) display detrital zircon age distributions from this study and (Campbell, 2017). Histograms display all ages in 20-Myr bins in the right column and only ages <500 Ma in 10-Myr bins on the left. Gray arrows connect detrital zircon data to their respective stratigraphic location.

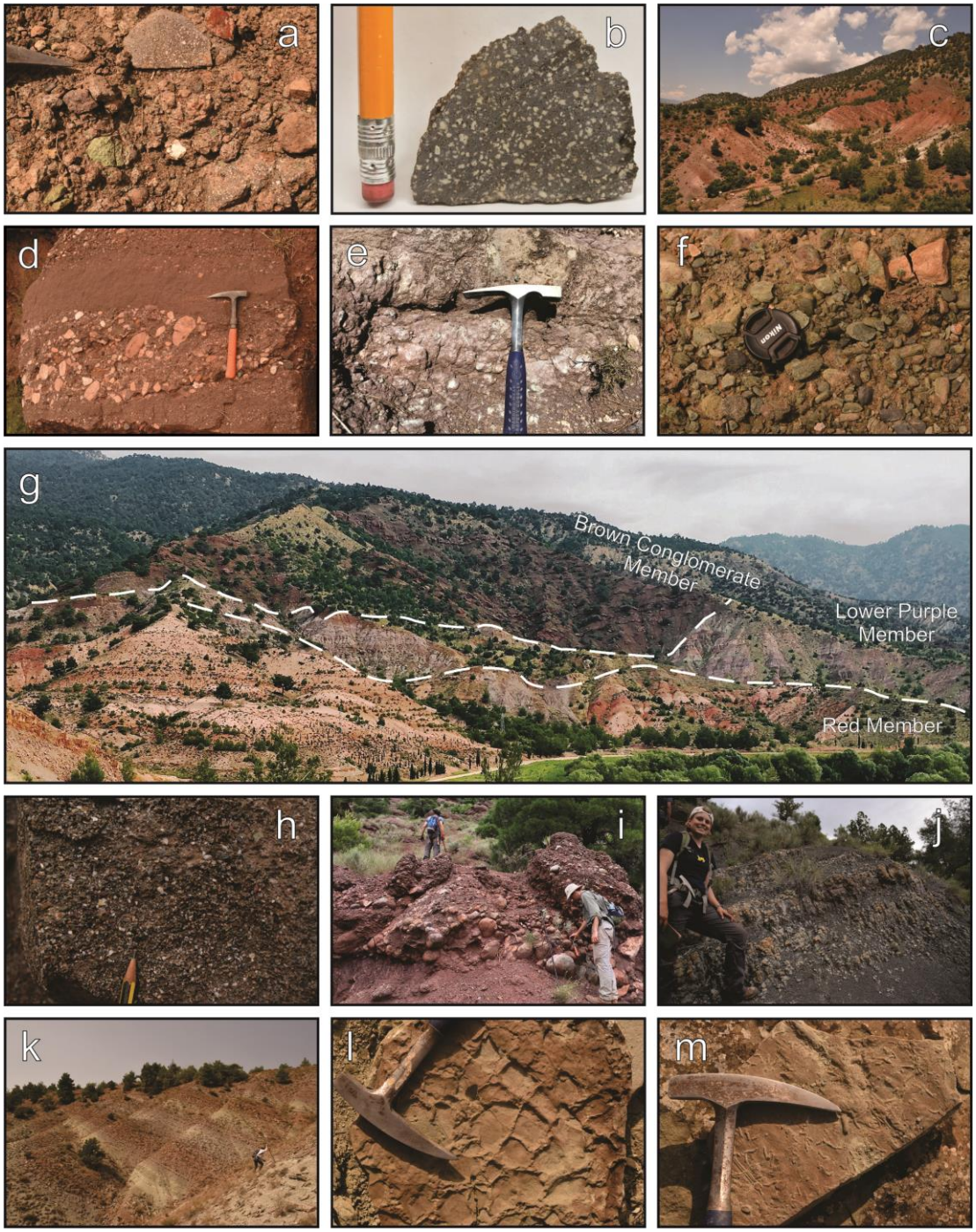

Figure 2.5. Field photographs. (a) Basal conglomerate member with poorly sorted, angular to rounded andesitic and weathered greenschist clasts (LF1). (b) Andesitic Member (sample 16SKY18). (c) View of the Red Member looking toward the west (predominantly LF2) and (d) photograph of lenticular coarse sand to cobble conglomerate with clasts of ophiolitic material,

andesite, carbonate, and chert in the Red Member (LF5). (e) Mottled, carbonaceous purple mudstone (LF2/3), and (f) well-rounded to subrounded greenschist, chert, and serpentinite clasts in the Lower Purple Member. (g) View looking toward the north of the Red, Lower Purple, and Brown Conglomerate Members in the Kapıkaya Section. (h) Coarse sand-sized clasts of greenschist, carbonate, gneiss, chert, and quartz in the Brown Conglomerate Member, (i) a trough cross-bedded channel body with rounded boulders (LF5) eroded into a pedogenized brown mudstone (LF2), and (j) a stacked caliche horizon (LF3). (k) View looking toward the west of the Upper Lacustrine Member with laterally continuous, tabular lacustrine limestones (LF5), including (l) mudcracks and (m) trace fossils.

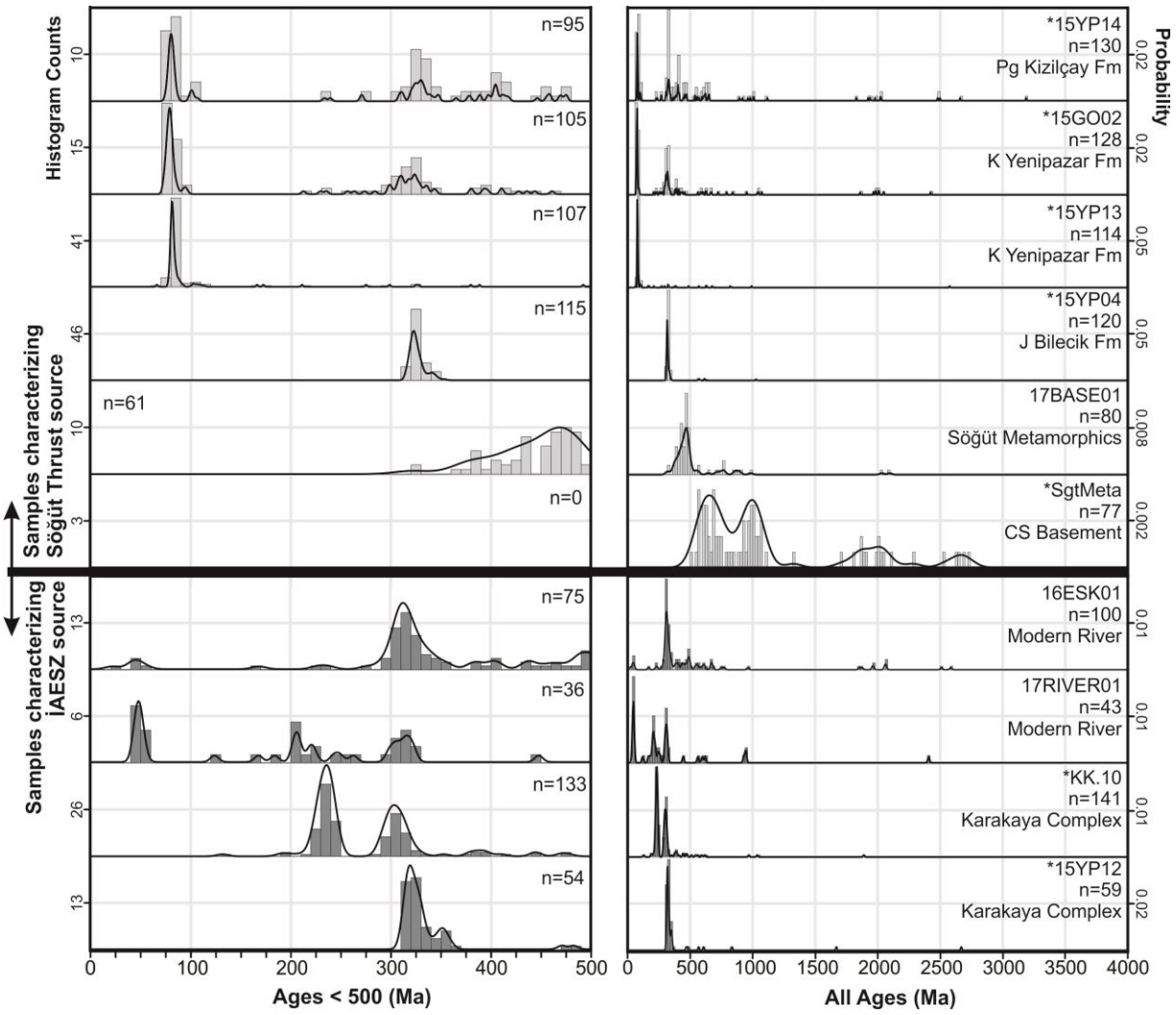

Figure 2.6. Detrital zircon spectra of potential Saricakaya Basin sediment sources. Histograms and kernel density estimate diagrams for detrital zircon age distributions of samples characterizing potential Sarıcakaya Basin sedimentary sources. Samples are grouped by potential source regions and stacked in stratigraphic order: Sedimentary units and Central Sakarya Basement of Söğüt Thrust hanging wall (light gray, top) characterize sediment derived from the north; Karakaya Complex and modern rivers draining the İAES characterize the south (dark gray, bottom). All ages are displayed in the right column in 20-Myr bins and only ages <500 Ma in 10-Myr bins on the left. CS = Central Sakarya; J = Jurassic; K = Cretaceous; Pg = Paleogene; * previously published data (Table 2.3).

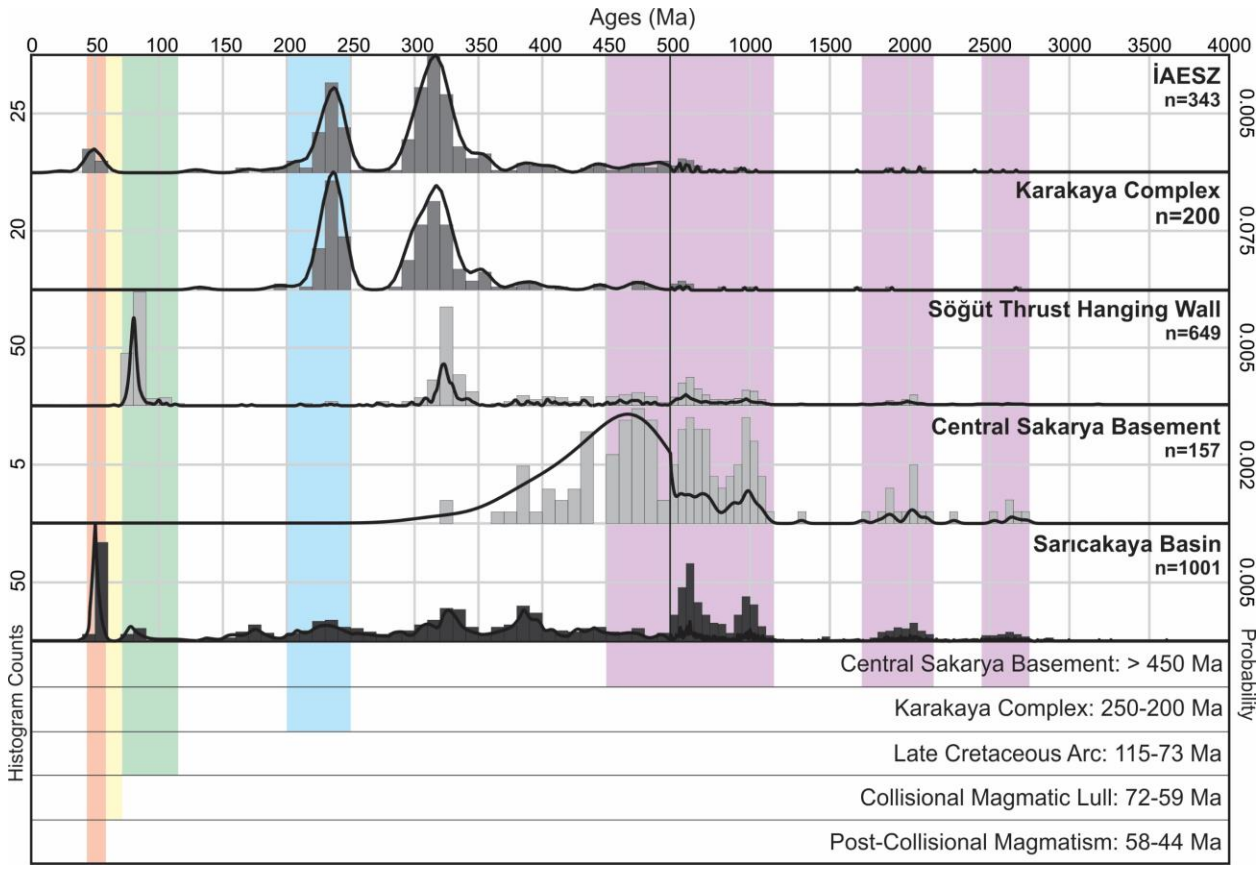

Figure 2.7. Histograms and kernel density estimate diagrams of sample groups: Sarıcakaya Basin (dark gray), Söğüt Thrust hanging wall and only Central Sakarya Basement samples (light gray), and İAES and only Karakaya Complex samples (medium gray). Colored bars highlight both Cretaceous-Paleogene magmatic cyclicity, and age peaks diagnostic of SB provenance. Histograms are in 10-Myr bins for ages <500 Ma, and 50-Myr bins for ages >500 Ma.

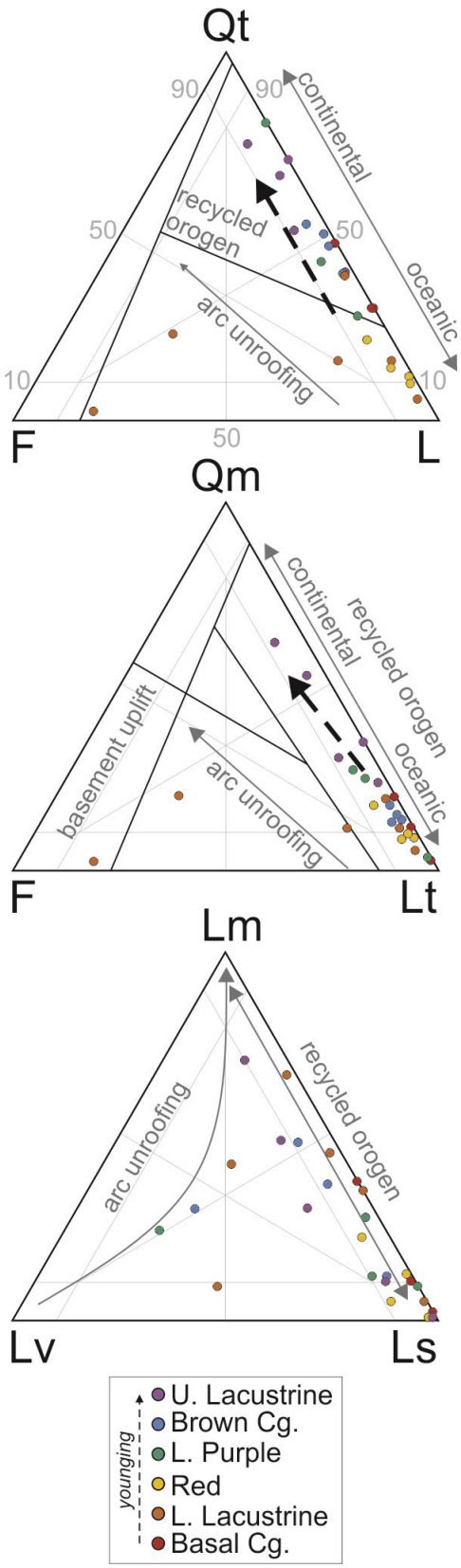

Figure 2.8. Ternary diagrams of sandstone modal framework-grain composition from the Sarıcakaya Basin showing petrographic ranges of typical source provinces following (Dickinson and Suczek, 1979; Dickinson, 1985; Garzanti, 2018). Points are colored by informal sedimentary members. Black dashed arrows indicate general upsection trends where present. Province fields and trends are labeled with dark gray text and arrows. Light gray lines and numbers label the axes. Ternary diagram poles—Qt = total quartz (Qm = monocrystalline quartz and Qp = polycrystalline quartz), F = total feldspar, L = lithic fragments (Lm = metamorphic, Ls = sedimentary, Lv = volcanic, Lt = total lithic fragments including polycrystalline quartz).

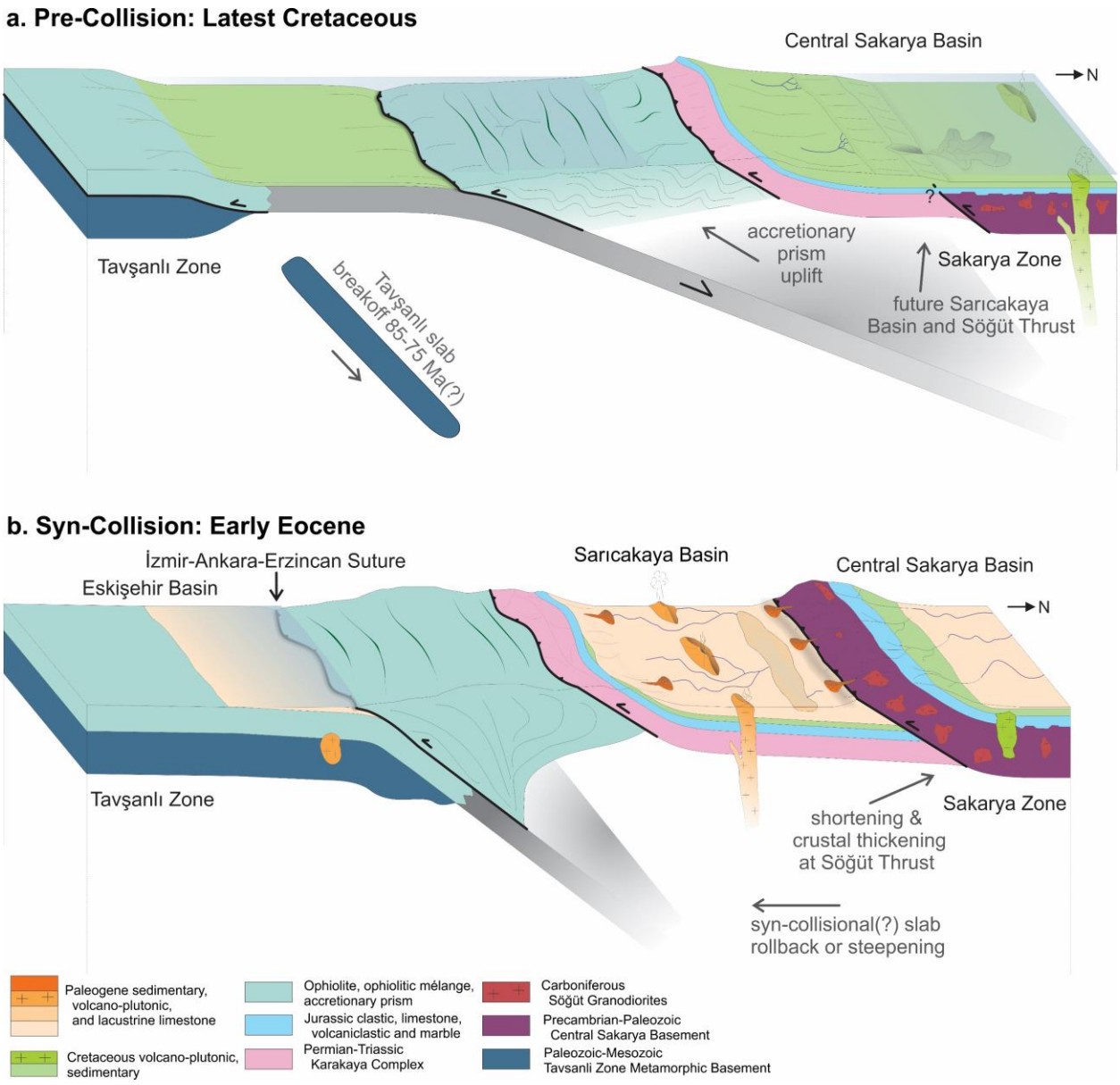

Figure 2.9. Conceptual model of the Sarıcakaya, Eskişehir, and Central Sakarya Basins and İzmir-Ankara-Erzincan suture zone. See text for detailed discussion and Figure 2.1 for location. (a) Reconstruction of the İzmir-Ankara subduction zone in the latest Cretaceous prior to collision of the Sakarya Zone with the Tavşanlı Zone at 66 Ma. (b) Reconstruction of the Sarıcakaya Basin in the Early Eocene (~52–47 Ma) based on interpreted depositional environments and provenance.

Table 2.1. Main lithofacies identified in the Sarıcakaya Basin. Note: Lithofacies numbers correspond to this in the text.

Lithofacies		**Description**	**Members Present**	**Depositional Environment Interpretation**
LF1	Clast-supported conglomerate	Clast-supported, massive conglomerate unit of 1-3-m plurimetric sets with very angular, 15- to100-cm clasts; erosive base; laterally extensive; occasionally matrix-supported	Basal Conglomerate	Alluvial fan
LF2	Red-brown mudstone	Red-brown mudstone; structureless, massive and laterally extensive; root traces, carbonate nodules, isolated clasts and gray-green to brown mottling; ~1- to 8-m thick; commonly coarsen upward to silt or fine sand and capped by caliche	Lower Lacustrine, Red, Lower Purple, Upper Lacustrine	Pedogenized overbank deposits
LF3	Caliche	10- to 200-cm thick, nodular, massive carbonate horizon, often with isolated clastic matrix	Lower Lacustrine, Red, Lower Purple, Brown Conglomerate, Upper Lacustrine	Paleosol Bk to K horizon
LF4	Tabular limestone	White, tabular, laminated to massive, laterally continuous limestone; 5- to 100-cm thick; afossiliferous	Lower Lacustrine, Upper Lacustrine	Lacustrine limestone
LF5	Trough cross-bedded conglomerate	Pebble- to boulder-sized, clast-supported, well-rounded, trough cross-bedded conglomerate; 1- to 12-m thick lenticular troughs with erosive base and coarse basal lag that commonly fines upward to coarse sand to cobble conglomerate	Lower Lacustrine, Lower Purple, Brown Conglomerate, Upper Lacustrine	River channels

Table 2.2. Volcaniclastic zircon U-Pb ages from the Sarıcakaya Basin. Note: Mean square weighted deviation (MSWD) reflects the degree to which the calculated age and uncertainty are representative of a single population. We provide the 2s error with and without the 1.3% modelling error (see Appendix A for discussion). 15YP11 is from Campbell (2017); N_0 is the total number of grains; N is the number of grains used in weighted mean age calculation.

Sample Name	**Source**	**Age (Ma)**	**±2σ abs**	**±2σ abs incl. modeling error**	**MSWD**	**Member**	**N_0**	**N**
15YP11	Campbell (2017)	52.4	0.6	0.8	0.99	Basal Conglomerate Mbr	98	56
16SKY11	this study	49.6	0.1	0.7	1.30	Lower Lacustrine Mbr	108	20
16SKY18	this study	48.7	0.2	0.7	0.51	Lower Lacustrine Mbr	24	24
16SKY17	this study	48.1	1.3	1.4	0.09	Andesitic Mbr	27	14
16SKY24	this study	48.0	1.2	1.4	0.28	Red Mbr	8	8

Table 2.3. Detrital zircon U-Pb samples from this study and from previously published sources categorized by provenance source regions.

Sample Name	**Source**	**Provenance Category**	**Stratigraphic Unit and Lithology**
15YP12	Campbell (2017)	İAESZ	Upper Karakaya Complex greenschist
KK.10	Ustaömer et al. (2016)	İAESZ	Upper Triassic Kendirli Fm (Karakaya Complex) sandstone
17RIVER01	this study	İAESZ	Modern river sand draining the accretionary prism into Sarıcakaya Basin
16ESK01	this study	İAESZ	Modern river sample draining accretionary prism and Karakaya Complex
16SKY04	this study	Sarıcakaya Basin	Basal Conglomerate Mbr sandstone
16SKY23	this study	Sarıcakaya Basin	Red Mbr sandstone
16SKY26	this study	Sarıcakaya Basin	Red Mbr sandstone
15YP08	Campbell (2017)	Sarıcakaya Basin	Lower Purple Mbr sandstone
16SKY37	this study	Sarıcakaya Basin	Lower Purple Mbr sandstone
15YP09	Campbell (2017)	Sarıcakaya Basin	Brown Conglomerate Mbr sandstone
16SKY42	this study	Sarıcakaya Basin	Brown Conglomerate Mbr sandstone
16SKY50	this study	Sarıcakaya Basin	Upper Lacustrine Mbr sandstone
17OZK05	this study	Sarıcakaya Basin	Upper Lacustrine Mbr sandstone
17OZK12	this study	Sarıcakaya Basin	Upper Lacustrine Mbr sandstone
SgtMeta	Ustaömer et al. (2012)	Söğüt Thrust Hanging Wall	Central Sakarya Basement sillimanite-garnet schist
17BASE01	this study	Söğüt Thrust Hanging Wall	Gneiss from the Söğüt Metamorphics
15YP04	Campbell (2017)	Söğüt Thrust Hanging Wall	Jurassic Bilecik Fm sandstone
15YP13	Campbell (2017)	Söğüt Thrust Hanging Wall	Upper Cretaceous Yenipazar Fm sandstone
15GO02	Campbell (2017); Ocakoğlu et al. (2018)	Söğüt Thrust Hanging Wall	Upper Cretaceous Yenipazar Fm conglomerate
15YP14	Campbell (2017)	Söğüt Thrust Hanging Wall	Paleogene Kizilçay Fm sandstone

Chapter 3. Closing the Neotethys in Western Anatolia: Protracted Intercontinental Collision from Evolving Plate Coupling

The content of this chapter is part of companion manuscripts submitted for publication in *Geochemistry, Geophysics, Geosystems:*

Megan A. Mueller, Alexis Licht, Clay F. Campbell, Faruk Ocakoğlu, Gui Aksit, Grégoire Métais, Pauline M. C. Coster, K. Christopher Beard, Michael H. Taylor. Closing the Neotethys in Western Anatolia, Part 2: Protracted Intercontinental Collision from Evolving Plate Coupling.

Clay F. Campbell, Megan A. Mueller, Michael H. Taylor, Faruk Ocakoğlu, Andreas Möller, Grégoire Métais, Pauline M. C. Coster, K. Christopher Beard, Alexis Licht. Closing the Neotethys in Western Anatolia, Part 1: Evidence for Protracted Extension as Continental Lithosphere Subducted in Late Cretaceous Times.

Abstract

The closure of the northern branch of the Neotethys Ocean along the İzmir-Ankara-Erzincan suture in Anatolia has been variously estimated from the Late Cretaceous to Eocene. It remains unclear whether this age range results from a protracted, multi-phase collision or disparities between proxies and geographic location. Here, we leverage the Cretaceous-Eocene evolution of the forearc-to-foreland Central Sakarya Basin system in western Anatolia to determine when and how collision progressed. By integrating sedimentary provenance with other geologic proxies, we show the onset of intercontinental collision at 76 Ma, marked by sediment recycling and uplift of the suture. This first contractional phase is followed by thick-skinned

deformation and basin partitioning starting at ca. 54 Ma, coeval to regional syn-collisional magmatism. Three non-exclusive mechanisms potentially explain a change in plate coupling during this protracted regime: relict basin closure north and south of the İAES, gradual underthrusting of thicker lithosphere, and Paleocene slab breakoff. Protracted collision along the İAES highlights links between geodynamics, topography and biogeography in small continental collisions.

3.1 Introduction

Continental collisions across the Tethyan realm are striking by their protracted and polygenetic history, often resulting in significant discrepancies among proxies of collision age: ~40 Myr for India-Asia (65-25 Ma; Ding et al., 2005; Hu et al., 2016; Kapp & DeCelles, 2019; Najman et al., 2010) and ~20 Myr for Arabia-Eurasia (Ballato et al., 2011; Cowgill et al., 2016; Darin et al., 2018; McQuarrie et al., 2003; Okay et al., 2010). Their unusual duration and complexity have even put into question the nature of the forces driving intercontinental convergence (Alvarez, 2010), leading to multi-phase scenarios either involving either varying plate coupling at the subduction interface (Beaumont et al., 1996; Ballato et al., 2011; Tye et al., 2020) or the role of forearc, backarc, and other remnant basins as early buffers of deformation (Cowgill et al., 2016).

Collision age discrepancies are also found in western Anatolia where continental collision between the Pontides and the Anatolide-affinity Tavşanlı Zone (TVZ) along the İzmir-Ankara-Erzincan suture (İAES) closed the Neotethys Ocean (Figure 3.1; Şengör & Yilmaz, 1981). Collision estimates along the İAES span 20 Myr from the Late Cretaceous to early Eocene based on ophiolite obduction and Barrovian metamorphism (Göncüoğlu et al., 2000; Seaton et al., 2009;

Whitney et al., 2011), structural deformation (Meijers et al., 2010; Lefebvre et al., 2013; Şahin et al., 2019), magmatism (Dilek and Altunkaynak, 2009; Kasapoğlu et al., 2016; Ersoy et al., 2017a), and sedimentary basin analysis (Kaymakci et al., 2009; Okay, 2011; Ocakoğlu et al., 2018). However, a model that encompasses the insights from all proxies is still missing. To address this, we leverage the power of a ~50 Myr continuous depositional record from the Central Sakarya Basin system, a forearc-to-foreland basin directly north of the İAES. Integrating new sedimentary provenance data with previously published stratigraphic and provenance data reveals a multi-phase collisional evolution. The TVZ was subducted to ca. 80 km depth sometime 95 to 85 Ma in an intra-oceanic subduction zone (Plunder et al., 2015; Pourteau et al., 2019) during which the Central Sakarya Basin was a forearc basin. The underthrusting of TVZ continental lithosphere beneath the Pontides initiated at 76 Ma, resulting in sediment recycling and uplift of the accretionary complex, followed ~20 Myr later with thick-skinned deformation and basin partitioning at 54 Ma. We evaluate the timing of this protracted deformation in light of previously proposed multi-phase collision models for the Tethyan realm, including passive margin subduction, relict basin closure, and slab breakoff.

3.2 Background

The tectonic units in northwest Anatolia include, from north to south, the İstanbul Zone and Sakarya Zone (SKZ) of the Eurasian-affinity Pontides, the İzmir-Ankara-Erzincan suture zone (İAES), and the Tavşanlı Zone (TVZ) of the Gondwanan-affinity Anatolides (Figure 3.1). The Pontides rifted from the Eurasian margin between 94 and 75 Ma by backarc spreading of the Black Sea (Okay et al., 2013), and formed an isolated microcontinent where faunal endemism prevailed until the late Paleogene (Métais et al., 2018). The SKZ, bound to the north by the Intra-Pontide

suture zone, presently occupied by the North Anatolian Fault, comprises Sakarya Zone basement units and the forearc-to-foreland Central Sakarya Basin system (Figure 3.2). The Sakarya Zone continental basement is subdivided into two units: (1) the Central Sakarya Basement (also called Söğüt metamorphics) comprising Paleozoic paragneiss, schist and amphibolite rocks intruded by Carboniferous granitoids called the Söğüt magmatics, Central Sakarya granite, or Sarıcakaya granitoid (Göncüoğlu et al., 2000; Ustaömer et al., 2012), and (2) the Permian-Triassic Karakaya Complex, partly metamorphosed clastic and volcanic rocks from either a rift or subduction-accretion complex setting (see Okay & Göncüoglu, 2004). The Central Sakarya Basin system is divided into the Jurassic-Eocene forearc-to-foreland Central Sakarya Basin (CSB; also called the Mudurnu-Göynük Basin) to the north and the Eocene broken foreland Sarıcakaya Basin (SB) to the south (e.g., Ocakoğlu et al., 2007; Okay et al., 2001). The basement-involved Tuzaklı-Gümele Thrust (also termed the Söğüt Thrust and Nallıhan Thrust) structurally partitioned the CSB by the early Eocene and flexural loading formed the SB. Sakarya Zone basement units are exposed in the hanging wall (Duru and Aksay, 2002; Gedik and Aksay, 2002). The SB contains Eocene terrestrial deposits and hosts one of the Eocene volcanic belts (Yildiz et al., 2015; Kasapoğlu et al., 2016). The fold-thrust belt is located within the basin system; W-E and SW-NE striking oblique thrust faults and folds deform Jurassic through Eocene units. Thin-skinned thrust faults in the CSB are likely reversed extensional faults from a phase of Santonian-Campanian extension (Ocakoğlu et al., 2018). The SKZ and İstanbul Zone are intruded by Eocene (58-41 Ma) syn-collisional plutons disputedly attributed to TVZ slab breakoff, lithospheric delamination, or anatexis of the lower crust (Harris et al., 1994; van Hinsbergen et al., 2010; Kasapoğlu et al., 2016; Mueller et al., 2019; Ustaömer et al., 2009).

The SKZ is bound to the south by the İAES, a highly deformed accretionary complex containing obducted ophiolite, ophiolitic mélange and metamorphic rocks (MTA, 2002). To the south, the TVZ is generally considered the passive margin of the northernmost Gondwana-derived Anatolide-Tauride Block (e.g., Okay, 2011; Okay et al., 1996). Platform carbonates and passive margin clastics were subducted and metamorphosed to blueschist facies between 92 and 83 Ma (e.g., Okay et al., 1998; Plunder et al., 2015; Sherlock et al., 1999; Whitney et al., 2011), exhumed sometime 85-60 Ma (Seaton et al., 2009; Sherlock et al., 1999; Whitney & Davis, 2006), then underwent Barrovian-type metamorphism from 63 to 57 Ma (Seaton et al., 2009; Whitney et al., 2011). The blueschist unit is tectonically overlain by metamorphosed accretionary complexes (Plunder et al., 2013b) and obducted ophiolites and mélange (Yaliniz et al., 2000; Göncüoğlu, 2010). The western Anatolian ophiolites, considered similar or larger in size than the Semail ophiolite in Oman, have metamorphic sole ages between 101 and 88 Ma (Harris et al., 1994; Dilek et al., 1999; Pourteau et al., 2019) and are cut by 92 to 90 Ma mafic dikes (Dilek et al., 1999), and, therefore, were obducted sometime after ~90 Ma during pre-collisional TVS subduction (Okay & Whitney, 2010; Robertson et al., 2009). The blueschists and ophiolites are intruded by Eocene granodiorites (Harris et al., 1994) and unconformably overlain by lower Eocene shallow marine limestones and siliciclastic rocks (Baş, 1986; Özgen-Erdem et al., 2007) and lower-to-middle(?) Eocene continental deposits (Turhan, 2002).

3.3 Central Sakarya Basin Stratigraphy

Jurassic through Eocene sedimentation is preserved in the Central Sakarya Basin (e.g., Aksay et al., 2002). Figure 3.3 displays stratigraphic columns with biostratigraphic ages for the

Upper Cretaceous through Eocene units along two transects across the CSB (after Ocakoğlu et al., 2018).

Unconformably overlying Sakarya Zone basement units are the Jurassic through Lower Cretaceous series of shallow water platform carbonates (Bilecik Fm.), pelagic micrites and calciturbidites (Soğukçam Fm.), and interbedded volcanics (Mudurnu Fm.) (Altiner et al., 1991; Genç and Tüysüz, 2010). The CSB formed as a rift basin, as indicated by overall basin deepening facies and bimodal Jurassic volcanism (Altiner et al., 1991; Göncüoğlu et al., 2000; Genç and Tüysüz, 2010), bounded by two branches of the Neotethys Ocean: the Intra-Pontide ocean to the north and the İzmir-Ankara Ocean to the south. There is uninterrupted Jurassic through Paleocene sedimentation in the eastern CSB (e.g., Nallıhan transect in Figure 3.3), whereas much of the Albian through Lower Campanian section is missing in the western CSB (e.g., Okay et al., 2001). The Albian-Lower Campanian sequence exhibits complex basin architecture, for which Ocakoğlu et al. (2018) provided updated biostratigraphic ages and tectonostratigraphic interpretations. This interval includes siliciclastic turbidites and pelagic mudstones (Yenipazar and Seben Fms.) interfingered with the Albian-Turonian Üzümlü Mbr. volcaniclastics and submarine lava flows, the Santonian-Lower Campanian Değirmenözü Fm./Mbr. pelagic carbonates, and lower to middle Campanian Eymür Mbr. submarine fan deposits. The shallow marine to deltaic Paleocene Taraklı Fm. conformably overlies the Yenipazar Fm. The shelf was likely located near the Nallıhan section, where deltaic progradation began sometime early Paleocene, then deltaic sands and muds reached the northern Taraklı section in the late Paleocene where sedimentation rates were up to 420 m/Myr (Ocakoğlu et al., 2018).

In the Yenipazar section in the west, the Kızılçay Fm. unconformably overlies the Yenipazar Fm, whereas in the Nallıhan section in the east, the Kızılçay Fm. conformably overlies

the Taraklı Fm. The shoaling sequence is overlain by coal beds, cross bedded sandstones and caliches of the Kızılçay Fm. (Ocakoğlu et al., 2018). Ostracod fauna indicate a Ypresian age (Ocakoğlu et al., 2018). In the proximal Nallıhan and Yenipazar sections, fluvial conglomerates contain reworked Upper Cretaceous clasts and marine microfauna, and cross beds and clast imbrications indicate paleocurrent directions to the NW and NE. The Kızılçay Fm. grades northward into the Yenipazar Fm. where prograding delta-front sandstones are present in the Akdoğan section (Ocakoğlu et al., 2018). The Kızılçay Fm. is likely correlative with the Ypresian to Lutetian(?) continental clastics and volcanics of the Mihalgazi Fm. in the Sarıcakaya Basin (Gedik and Aksay, 2002; Yildiz et al., 2015; Kasapoğlu et al., 2016; Mueller et al., 2019; Şahin et al., 2019). The coarse marine clastics, alternating sands and muds, and turbidite deposits of the Kabalar Mbr. of the Kızılçay Fm. and the conformably overlying Güvenç Fm., Çataltepe Fm., and Halidiye Fm. record a Ypresian through early Bartonian marine transgression (Ocakoğlu et al., 2012, 2018). The Lutetian maximum flooding surface is recorded in sedimentary basins across the Black Sea region, including Anatolia, Crimea and the Caucasus (Racey, 2001; MTA, 2002; Lygina et al., 2016; e.g., Licht et al., 2017; Özcan et al., 2019). The Gemiciköy Fm. comprises mudstone and cross-bedded sandstones that coarsen upward to fluvial conglomerates with clasts of reworked Cretaceous-Paleocene units (Ocakoğlu et al., 2007); it only crops out north of Yenipazar where it conformably overlies the Güvenç Fm. (Gedik and Aksay, 2002; Ocakoğlu et al., 2018).

3.4 Methods

We collected 37 new sandstone samples from Cretaceous through Eocene strata in the CSB and 2 new gneiss samples from the Central Sakarya Basement (Figure 3.3, Table 3.1). The sandstone samples were collected along five published measured sections from two proximal

(south) to distal (north) transects through the CSB (Figure 3.2; Ocakoğlu et al., 2018). The provenance of 19 sandstone samples was evaluated using detrital zircon (DZ) U-Pb geochronology and sandstone petrography.

For new CSB samples, heavy mineral separation, analysis, and data reduction followed the University of Washington TraceLab protocol (Licht et al., 2018; Shekut & Licht, 2020). Zircons were separated following standard heavy mineral separation procedures. A minimum of 140 grains per sample were randomly selected, mounted with reference materials, imaged in a backscattered electron detector with a scanning electron microscope, and analyzed using a quadrupole laser ablation-inductively coupled plasma-mass spectrometer (LA-ICP-MS). The data were reduced in Iolite using the Geochron Data Reduction Scheme (Paton et al., 2011) in order to calculate U-Pb ages uncorrected for common lead (Shekut and Licht, 2020). Individual zircons with abnormal patterns in raw signal intensity, >20% discordance, or >5% reverse discordance are reported in the supporting information but are excluded from analyses and interpretations (following Gehrels, 2012, 2014). All zircon U-Pb data are presented as histograms, probability density functions and kernel density estimates with an optimized fixed bandwidth, all plotted using detritalPy (Sharman et al., 2018).

The ages of the sedimentary samples were constrained by published biostratigraphic and volcanic zircon U-Pb ages along the measured sections (Campbell, 2017; Ocakoğlu et al., 2018). Maximum depositional ages, calculated using the youngest cluster of 2 or more ages with overlapping 2s uncertainties (Sharman et al., 2018), are included in Table 4.2 but do not provide any new age constraint on the samples.

We characterize the zircon age signature of potential sediment sources from new Central Sakarya Basement bedrock samples alongside published Central Sakarya Basement, Karakaya

Complex, and İAES bedrock and modern river samples (Campbell, 2017; Mueller et al., 2019; P. Ustaömer et al., 2012; T. Ustaömer et al., 2016). We also include the crystallization ages of Cretaceous-Eocene plutons in Central and Western Anatolia compiled in Scheliffarth et al. (2018). The two new basement samples and one CSB sample (15YP15) were analyzed at the University of Kansas Isotope Geochemistry Laboratory following the analytical protocol outlined in Campbell (2017). Zircons were separated following standard methods, mounted with international standards, and analyzed in a high resolution sector-field LA-ICP-MS. Data were reduced in Iolite (Paton et al., 2011) and ET_Redux (McLean et al., 2016) and are presented uncorrected for common lead.

We further characterize sedimentary provenance using petrographic analysis of sandstone samples (N=31). Thin sections were made by National Petrographic Service, Inc., then at least 400 framework grains per sample were point counted according to the Gazzi-Dickinson method (Dickinson, 1985). The new CSB sandstone modal composition data are presented as ternary diagrams (Triplot; Graham and Midgley, 2000b) and interpreted following standard source fields (Dickinson and Suczek, 1979; Dickinson, 1985).

3.5 Provenance Results and Interpretation

3.5.1 Provenance Results

New DZ data are presented with published DZ data (N=13; Campbell, 2017; Mueller et al., 2019; Ocakoğlu et al., 2018). Additionally, Campbell et al. (in review) present εHf isotopic data from the detrital zircons extracted from CSB samples. The εHf isotopic data are synthesized in the figures and discussion; see (Campbell et al., in review) for a detailed discussion.

Detrital zircon distributions of potential sources and basin samples are given in Figure 3.4 and Figure 3.5, respectively. To facilitate comparison, distributions are colored according to the ages of known late Neoproterozoic and Eocene volcanic and plutonic outcrops across the Black Sea region (Figure 3.6). Sandstone petrography results of new CSB samples are displayed in Figure 3.7.

New (n=169) and published (n=769) bedrock and modern river zircon U-Pb ages characterize the zircon signature of basement units (Figure 3.4). The Central and Western Anatolian volcanic arc is characterized by 30-56 Ma and 67-99 Ma peaks. The Karakaya Complex samples are characterized by 200-250 and 325 Ma populations, and, additionally, the modern river sample (17RIVER01) draining the İAES contains minor Eocene, Late Cretaceous, Triassic, and Paleozoic populations. The Central Sakarya Basement bedrock samples exhibit a prominent ~325 Ma peak, and the oldest samples include 375-500 Ma age populations; the metasedimentary sample ('SgtMeta' from Ustaömer et al., 2012) contains a range of Proterozoic-Archean zircons with peaks centered around 600 Ma, 1000 Ma, 2000 Ma, and 2650 Ma. The absence of Devonian-Precambrian age zircons in some bedrock samples is due to the lithology of the samples (i.e., zircons from gneiss versus metasedimentary units).

New (n=3199) and published (n=1457) CSB and SB detrital zircon results (Figure 3.5) and new sandstone petrography results (Figure 3.7) characterize the provenance of sediment. The oldest CSB samples are Cenomanian to lower Campanian in age and are characterized by a major 76-110 Ma peak; few zircons are older than 110 Ma (n=22/660). These samples plot in the volcanic arc and recycled orogen fields. Samples younger than the lower Campanian have prominent Late Cretaceous (67-110 Ma) and Carboniferous (~325 Ma) peaks. The youngest CSB samples also contain a prominent Eocene peak (~41-58 Ma). About half of these samples have major or minor

Triassic (~250 Ma), Devonian (375-400 Ma), and Proterozoic peaks around 600 Ma, 1000 Ma and 2000 Ma. The Sarıcakaya Basin samples have a similar distribution of DZ ages, yet for many SB samples, the pre-Cretaceous populations are more prevalent.

3.5.2 Three Phases of the Central Sakarya Basin System

We subdivide the samples into three age groups based on changes in major changes in DZ age distributions and sedimentary basin evolution (Figure 3.5, Figure 3.7, and Figure 3.8). The sample ages, and therefore sample groups, are constrained in the CSB using published biostratigraphy, primarily planktonic foraminifera, and one tuff and one maximum depositional zircon U-Pb age (Ocakoğlu et al., 2018). The age of the SB samples is constrained by volcaniclastic U-Pb ages (Mueller et al., 2019). Paleogene continental deposits are not well dated and the maximum depositional ages do not offer much insight (Table 4.2).

Phase 1 includes Turonian through lower Campanian (94-76 Ma) DZ samples from the eastern CSB. This phase is characterized by a major 76-110 Ma peak; few zircons are older than 110 Ma (n=22/660) (Figure 3.5 and Figure 3.8). The Late Cretaceous volcanic arc was located along the present-day Black Sea coast north of the CSB (Figure 3.6; Keskin & Tüysüz, 2018). However, there is an outcrop of 95-70 Ma granitoids on the Pontides to the southeast of the CSB (i.e., Beypazarı granitoid; Speciale et al., 2012). Ocakoğlu et al. (2018) find Upper Cretaceous pyroclastic flows in Yenipazar section and tuffs in the Göynük and Okçular sections, and postulate there was Late Cretaceous submarine centers within the southern margin of the CSB. Given the proximity to the submarine volcanism, the volcanic arc sediment compositions and the prevalence of Late Cretaceous zircon ages, Phase 1 strata are presumably first-cycle detritus derived from the southern Late Cretaceous volcanic center.

Phase 2 is defined by a major change in DZ spectra (Figure 3.5), increased sedimentation rates (Ocakoğlu et al., 2018) and the onset of a lowstand systems tract (Ocakoğlu et al., 2007) around 76 Ma. In the Nallıhan section, the oldest samples in this phase fall between 77.61 Ma and 76.82 Ma based on planktonic foraminifera, and in the Göynük section the oldest Phase 2 sample has a published maximum depositional age of 76.4 ± 1.7 Ma based on the youngest 19 zircons (Ocakoğlu et al., 2018). The middle Campanian through lower Eocene (76-54 Ma) sandstone compositions plot in the recycled orogen and volcanic arc fields. A trend of increasing quartz and sedimentary and metamorphic lithic compositions (Figure 3.7) coincides with the appearance of Paleozoic-Precambrian zircons. DZ samples are generally characterized by 67-90 Ma, 300-450 Ma and 550-700 Ma peaks. The presence of Carboniferous zircons alone or in tandem with Devonian and older zircons are either first-cycle zircons from Central Sakarya Basement or poly-cyclic zircons. The Central Sakarya Basement, containing Devonian and older zircon ages, was intruded by Variscan Carboniferous granitoids that are together exposed in the hanging wall of the Tuzaklı-Gümele Thrust (Figure 3.2 and Figure 3.4). The exposures of Devonian through upper Neoproterozic plutons and crystalline basement rocks to the west and north of the CSB are an unlikely sediment source due to the NE to NW paleocurrent directions (Ocakoğlu et al., 2018). The absence of Precambrian-aged zircons in most Central Sakarya Basement samples is likely due to sampling bias as most of the samples are gneiss and granitoids, with only one metasedimentary sample (‘SgtMeta’ from Ustaömer et al., 2012). The fact that there was not deposition in the flexural SB until 52 Ma indicates that the Tuzaklı-Gümele Thrust likely did not expose basement rocks in Phase 2. Therefore, during Phase 2, the basement-age zircons in the CSB appear from sediment recycling during uplift and deformation of the southern margin of the Pontides. It is

uncertain exactly where sediment recycling occurred or which structures were active, but it could be from the unroofing older sedimentary strata on the hanging wall of the Tuzaklı-Gümele Thrust.

Partitioning of the CSB by the basement-involved Tuzaklı-Gümele Thrust formed the broken-foreland SB. The Phase 2 to Phase 3 transition is defined by the onset of deposition in the SB, which is determined at 52.4 ± 0.6 Ma by volcaniclastic bed at the base of the Paleogene series in the SB (Campbell, 2017; Mueller et al., 2019). CSB sandstone compositions plot in the recycled orogen and volcanic arc fields, and lithics are predominantly sedimentary (Figure 3.7). Middle to upper Eocene (38-48 Ma) CSB samples are similar to those in Phase 2, with the addition of a 41-58 Ma peak. Eocene SB DZ samples are generally characterized by a 46-58 Ma peak along with 200-250 Ma, 325 Ma, 375-400 Ma, 600 Ma, 1000 Ma, 2000 Ma and 2600 Ma peaks. The increase in sedimentary lithics along with negligible changes in CSB DZ age spectra—except for the appearance of Eocene zircons—are consistent with continued sediment recycling and no major change in provenance.

The SB is interpreted as a flexural basin formed during partitioning of the CSB by the Tuzaklı-Gümele Thrust (Mueller et al., 2019). The SB received sediment from the Eocene volcanic arc, Karakaya Complex, and Central Sakarya Basement (Figure 3.5 and Figure 3.8; Mueller et al., 2019). The SB is in the footwall of the Tuzaklı-Gümele Thrust; depositional environments, detrital zircon ages, and pebbles and boulders of quartz, mica and gneiss indicate that the Central Sakarya Basement was exposed in the hanging wall of the thrust by 52 Ma (Mueller et al., 2019). Therefore, the CSB received sediment from the hanging wall of the thrust, including recycled Phase 1 and Phase 2 deposits. The Eocene CSB samples contain Eocene zircons likely derived directly from Eocene volcanic and plutonic rocks located at the northern margin of the CSB or within the SB (Figure 3.2 and Figure 3.6). The Triassic and Carboniferous age doublet is distinctively Karakaya

Complex in origin (Figure 3.4) and, given the absence of Triassic igneous rocks across Anatolia (Figure 3.6), the presence of this doublet indicates poly-cyclic zircons recycled from the Karakaya Complex. Only a few CSB samples received sediment from the Karakaya Complex (i.e., 18TBTG and 18TK01 from the Taraklı section in Phase 2), yet the Karakaya Complex is a prominent source to the Eocene SB samples. Therefore, sediment was likely sourced from exposed Karakaya Complex units near the suture zone into the nearby SB, and the absence of the Triassic-Carboniferous doublet in middle to upper Eocene CSB samples could point to disconnected CSB and SB depocenters. In addition, the scarcity of Silurian and older zircons in the middle to upper Eocene CSB samples and the difference in εHf values between the CSB and SB (Figure C.1; Campbell et al., in review) also support disconnected drainage networks.

3.6 Evolution of the Central Sakarya Basin in Context

All CSB and SB DZ ages from 150 to 30 Ma are combined and plotted alongside simplified composite stratigraphic columns (Figure 3.9). We interpret the combined DZ ages from 150 to 30 Ma as the magmatic arc tempo (Paterson and Ducea, 2015). The apparent magmatic lulls at 67-58 Ma and starting at 41 Ma agree with the 72-58 Ma and 40-20 Ma magmatic lulls in central and eastern Anatolia based on a compilation of 100-0 Ma bedrock crystallization and cooling ages (Schleiffarth et al., 2018).

We discuss the three major provenance phases in terms of basin evolution. During Phase 1 (110-76 Ma), the Late Cretaceous volcanic arc, located within the CSB (Gedik and Aksay, 2002; Ocakoğlu et al., 2018) and along the southern Black Sea coast (Keskin and Tüysüz, 2018), was the dominant source of sediment to the forearc CSB (Figure 3.5; Yilmaz et al., 2010). This 34 Myr-long phase is not associated with any change in depositional style, accumulation rate (Ocakoğlu et

al., 2018) or provenance (Figure 3.5 and Figure 3.7). This period corresponds to a standard Andean-type active margin setting (Okay et al., 1994) with a phase of Santonian-Campanian extension (Ocakoğlu et al., 2018). The brief magmatic lull and switch from juvenile to evolved εHf values at 88 Ma (Figure 3.9 and Figure C.1) could be the signal of pre-collisional TVZ subduction (Campbell et al., in review).

During Phase 2 (76-54 Ma), CSB strata are characterized by DZ ages typical of Pontide basement units (Figure 3.4; Ustaömer et al., 2012) and evolve toward quartz- and sedimentary lithic-rich compositions suggesting an unroofing sequence in which poly-cyclic basement-aged zircons appeared in the basin. Input of ophiolitic material into the CSB starting at ca. 73 Ma, as shown by increased mafic/felsic element ratios (Ni/Zr, Ni/Y, Cr/Zr) in the distal İsmailler section (Açıkalın et al., 2016), pinpoint the area of exhumation to the İAES where ophiolitic units and the Karakaya Complex are exposed today. Flute casts and asymmetrical ripples record paleocurrent directions ranging from the NE to NW (Ocakoğlu et al., 2018). Together this indicates that the southern margin of the SKZ, including the İAES accretionary complex, began uplifting, exhuming, and creating south-to-north flowing, transverse drainage systems in the southern CSB at 76 Ma. Arc shutdown and initial underthrusting is contemporaneous with the slowing of convergence rates: convergence rates slowed from 28 mm/yr from 110-76 Ma to 5 mm/yr from 76 Ma onwards (rates calculated from plate reconstructions based on paleomagnetic and kinematic data in van Hinsbergen et al., 2020). Evolved εHf values in Late Cretaceous zircons indicate either crustal thickening, lower plate continental underthrusting, or arc migration into evolved continental crust; we favor lower plate underthrusting due to the coeval decrease in magmatic tempo (Campbell et al., in review; Figure 3.9 and Figure C.1). Exhumation and underthrusting continued, recorded as the onset of northward prograding deltas at 61 Ma, development of a major unconformity in the

proximal (southern) CSB, transition from flysch to molasse, and an order of magnitude increase in CSB accumulation rates (Açıkalın et al., 2016; Ocakoğlu et al., 2018). These CSB changes coincide with a 67-58 Ma magmatic lull (Figure 3.5), and 63-57 Ma TVZ Barrovian metamorphism to greenschist and amphibolite facies (e.g., Whitney et al., 2011) and subsequent 60 Ma exhumation as indicated by white mica 40Ar/39Ar cooling ages (Seaton et al., 2009).

The Phase 2 to Phase 3 transition (~54 Ma) is marked by the onset of deposition in the SB by 52.4 Ma (Mueller et al., 2019) and partitioning of the CSB by the basement-involved Tuzaklı-Gümele Thrust. Basin partitioning is coeval with the resumption of deposition in the southern CSB and the transition to continental facies and prograding clastic wedges in the CSB sometime around 58-54 Ma (Ocakoğlu et al., 2018). There was continued sediment recycling and no significant provenance change in the CSB (Figure 3.4 and Figure 3.7). Deformation and exhumation propagated north of the İAES; basement-involved shortening (Şahin et al., 2019) structurally partitioned the SB and CSB foreland along the lithospheric-scale Karakaya Complex–Central Sakarya Basement boundary (Tuzaklı-Gümele Thrust in Figure 3.2; Mueller et al., 2019). The difference in Precambrian zircon abundance between the CSB and SB likely indicates fully disconnected basin depocenters (Figure 3.5). This phase is coeval with linear belts of Eocene magmatism (58-41 Ma) along the İAES and Intra-Pontide suture zones (Altunkaynak, 2007; Altunkaynak et al., 2012; Dilek & Altunkaynak, 2009; Ersoy, Akal, et al., 2017; Ersoy, Palmer, et al., 2017; Harris et al., 1994; Kasapoğlu et al., 2016; Okay & Satir, 2006; Yildiz et al., 2015). Lutetian-Priabonian marine deposition in the distal (northern) CSB (e.g., Ocakoğlu et al., 2018) suggests a >15 Myr delay between TVZ underthrusting and regional uplift.

3.7 Implications for Multi-Phase Collision Scenarios

3.7.1 Geodynamic Controls on Biogeography

This section explores the possible geodynamic mechanisms that could explain a ~20 Myr long, multi-phase collision along the İAES. Even though it is difficult to pinpoint a specific mechanism for protracted collision, our results highlight a direct—and unexpected—geodynamic and paleogeographic control on the regional fauna. Backarc rifting in the middle Cretaceous isolated the Pontides from Eurasia (Akdoğan et al., 2019; Okay & Nikishin, 2015), setting the stage for Paleogene endemism. In Cretaceous-Paleogene times, Anatolia was an island archipelago separated from large continental domains (i.e., Afro-Arabia, Europe and Asia) by strands of the Paleotethys and Neotethys oceans (Barrier and Vrielynck, 2008; van Hinsbergen et al., 2020). Gradual Late Cretaceous to early Eocene İAES closure favored colonization of the Pontides by Gondwanan and Laurasian mammalian clades via "island hopping" across the Neotethyan archipelago (Beard et al., 2020; Jones et al., 2018; Kappelman et al., 1996; Licht et al., 2017; Métais et al., 2017; Sen, 2013). The TVZ-SKZ collision assembled a larger terrestrial landmass that further promoted *in situ* diversification of endemic taxa (Maas et al., 2001; Métais et al., 2018). Endemism persisted until at least the Lutetian (44-43 Ma; Licht et al., 2017), a time when much of Anatolia was near sea level—many sedimentary basins record a Lutetian marine incursion (Racey, 2001; MTA, 2002; Ocakoğlu et al., 2012; Lygina et al., 2016; e.g., Licht et al., 2017; Özcan et al., 2019). Finally, the late Paleogene demise of endemism evidences the reconnection of Anatolia to Eurasia (Métais et al., 2018), after which Anatolia could have been a dispersal corridor between Europe and Asia in the Priabonian-Bartonian (Sen, 2013; Licht et al., 2017; Jones et al., 2018; Métais et al., 2018; Beard et al., 2020). The protracted nature of İAES collision is relevant

to the evolution of emergent landmasses and exemplifies a direct influence of geodynamics and tectonics on biogeography.

3.7.2 Geodynamic Mechanisms for Protracted Collision

Multi-phased, "soft-hard" collisions have been proposed numerous times in the Tethyan domain and world-wide (Beaumont et al., 1996; Kaymakci et al., 2009; Pourteau et al., 2016; Jagoutz et al., 2016; Darin et al., 2018; e.g., Ballato et al., 2018; Tye et al., 2020). These scenarios are based on a variety of mechanisms: subduction of a large oceanic basin (van Hinsbergen et al., 2011, 2012), arc-continent collision (Jagoutz et al., 2016; Martin et al., 2020), upper plate pre-exiting structures and sediment thickness (Jones et al., 1998, 2011; Parker and Pearson, 2021), relict basin closure (Cowgill et al., 2016), increased lower plate lithospheric thickness (Ballato et al., 2011; Soret et al., 2021), and slab breakoff (Sinclair, 1997; DeCelles et al., 2011). One or a combination of these scenarios could explain the protracted nature of intercontinental collision in western Anatolia, including thick-skinned deformation and basin partitioning at 54 Ma.

Several mechanisms for protracted Tethyan collisions are not applicable in western Anatolia. In order to account for shortening and convergence deficits (Hu et al., 2016; Kapp and DeCelles, 2019 and references therein), the large oceanic basin model proposes a significantly wider pre-collisional lower plate (i.e., Greater India Basin; van Hinsbergen et al., 2011, 2012). However, there is no known shortening deficit in Anatolia, so no need to invoke a wide oceanic basin. The arc-continent hypothesis splits the lower plate (here the TVZ) into several individual fragments separated by oceanic arcs (Jagoutz et al., 2015, 2016; Martin et al., 2020), but the absence of volcanic arc units in the western İAES does not support an accreted oceanic arc between the TVZ and SKZ. Upper plate conditions, such as those proposed for the North American

Cordillera (i.e., sediment thickness, pre-existing structures, cratonic keel; e.g., Jones et al., 1998, 2011; Parker & Pearson, 2021), could control the activation of the thick-skinned Tuzaklı-Gümele Thrust, which could be the reactivation of the boundary between the accreted Karakaya Complex and the SKZ crystalline basement, but there is no evidence for insufficient sediment thickness in the CSB that would cause thick-skinned deformation. In the remaining part of the discussion, we focus on the three mechanisms that we think are the most viable for the İAES closure.

3.7.2.1 Slab Dynamics

Slab breakoff is a mechanism commonly employed to explain coeval surface uplift, extension and magmatism (Davies and von Blanckenburg, 1995; von Blanckenburg and Davies, 1995), although its prevalence in the geologic past and connection to magmatism is questioned (Niu, 2017; Garzanti et al., 2018). In western Anatolia, slab breakoff can explain the timing and geochemical signature of ~58-40 Ma magmatism (Harris et al., 1994; Dilek and Altunkaynak, 2009; Altunkaynak et al., 2012; Kasapoğlu et al., 2016; Ersoy et al., 2017b, 2017a; Campbell et al., in review). However this interpretation is questioned (Ustaömer et al., 2009; see also Mueller et al., 2019; Okay & Whitney, 2010; Okay & Satir, 2006; van Hinsbergen et al., 2010) for four main reasons: (1) the TVZ slab was subducted to mantle depths in the Late Cretaceous and the exhumation of blueschists in the Campanian-Maastrichtian suggests slab breakoff was in the Late Cretaceous not Eocene (e.g., Okay & Satir, 2006); (2) during early Eocene magmatism, there was not significant uplift as marine deposition is recorded in the CSB and south of the suture near Eskisehir (Figure 3.2); (3) there was early Eocene contractional deformation in the SB and no evidence for extension (Mueller et al., 2019; Şahin et al., 2019); (4) magmatism was contemporaneous across three parallel volcano-plutonic belts at the northern margin of the CSB, bisecting the SB, and in the TVZ (Figure 3.6; e.g., Ersoy, Akal, et al., 2017; Ersoy, Palmer, et al.,

2017; Harris et al., 1994; Kasapoğlu et al., 2016). Slab breakoff should be recorded in extensional sedimentary basins as alternating clastic and lacustrine deposits, an overall fining-upward sedimentary succession, high sedimentation rates, and an absence of contractional growth structures (DeCelles et al., 2011; Leary et al., 2016). Although the SB contains alternating floodplain clastic and lacustrine limestone deposits and no contractional growth strata, clasts of quartz, mica and gneiss in coarse-grained fluvial deposits along with the presence of basement-aged zircons indicates that the basement-involved Tuzaklı-Gümele Thrust was active in the early Eocene (Mueller et al., 2019). Geodynamic explanations for Eocene magmatism remain inconclusive; alternative arguments include lithospheric delamination (van Hinsbergen et al., 2010; Pourteau et al., 2013), arc volcanism from a different subduction zone system (Okay & Satir, 2006), and mid-to-late Eocene orogenic collapse and extension (Ustaömer et al., 2009). Yet, if slab breakoff was amagmatic (Niu, 2017; Garzanti et al., 2018), it could have occurred ~10 Myr after initial collision during the 67-58 Ma magmatic lull. Although this model fails to explain many observations of Paleogene deformation, it remains a popular mechanism. Therefore, this scenario is possible if amagmatic slab breakoff occurred in the Paleocene, shortly followed by Eocene continental underthrusting, contractional deformation, and juvenile magmatism (Figure 3.10c).

3.7.2.2 Relict Basin Closure

Although slightly different in nature, in both the Arabia-Eurasia and India-Asia collisions, the initial collision of upper plate island arcs or continental terranes with the lower plate continental lithosphere results in upper plate backarc basin closure (Jagoutz et al., 2015; e.g., Cowgill et al., 2016; Kapp and DeCelles, 2019). Initial Arabian collision is inferred from the coeval ca. 36 Ma magmatic lull and switch in kinematic regime from extensional to contractional in the Alborz Mountains of Iran (Ballato et al., 2011), and increased exhumation rates in the eastern Taurides

(Darin et al., 2018) and in the central Pontides (Ballato et al., 2018), for example. Yet initial foreland basin sedimentation (Ballato et al., 2011), slowed convergence rates (McQuarrie et al., 2003), increased exhumation near the Bitlis suture zone (Okay et al., 2010) was delayed until at 20-17 Ma. Cowgill et al. (2016) suggest that significant upper plate deformation from the Arabia-Eurasia collision was delayed by ~15-20 Myr by northward jumping deformation. In this scenario, collisional stress was transferred through the lithosphere and closed several upper plate basins (Cowgill et al., 2016). Eocene-Oligocene Arabian collision along the Bitlis-Zagros suture (McQuarrie et al., 2003; McQuarrie and van Hinsbergen, 2013; e.g., Koshnaw et al., 2019) initiated backarc basin subduction between the Lesser and Greater Caucasus (e.g., Avdeev and Niemi, 2011); then, basin closure around 5 Ma produced a 10-fold increase in Greater Caucasus exhumation rates (Avdeev and Niemi, 2011) coincident with foreland basin erosion and non-deposition, mixing of sediment from the upper and lower plates, and provenance signatures of progressive crustal exhuming (e.g., Tye et al., 2020).

In line with this relict basin closure scenario, major collisional deformation from initial TVZ-SKZ underthrusting could be delayed by >20 Myr due to the closure of relict basins to the north or south of the İAES (Figure 3.10a). The closure of the Intra-Pontide suture zone is a strong candidate to explain this delay because the timing of suturing remains unclear, with proposed ages spanning from the Early Cretaceous (Akbayram et al., 2013), Late Cretaceous-Paleocene (Göncüoğlu et al., 2000; Robertson and Ustaömer, 2004; Özcan et al., 2012; Di Rosa et al., 2019) to the Paleocene-Eocene (Akbayram et al., 2016; Göncüoğlu et al., 2014; Okay et al., 1994). Major contractional deformation could also be delayed by the hypothesized southward-jumping subduction zones synchronously or sequentially facilitating the closure of Neotethyan oceanic basins between Anatolide and Tauride terranes south of the İAES (Pourteau et al., 2013, 2016).

Resumed or increased continental underthrusting at 54 Ma along the İAES could partly explain the renewal of magmatism without explaining its regional distribution. The lack of clear constraints on the IPS suturing age makes it difficult to estimate the accuracy of this mechanism.

3.7.2.3 Increasing Lithospheric Thickness of the Lower Plate

An alternate two-stage collision scenario, also invoked for Tethyan collisions, involves the gradual increase in thickness of underthrusting lower plate lithosphere (e.g., Ballato et al., 2011; Darin et al., 2018; Soret et al., 2021). In the Himalayan sector, the initial collision of India with Asia is generally accepted to be 60-55 Ma, when the final vestiges of Neotehyan oceanic crust were subducted (Hu et al., 2016 and references therein). In northern Pakistan, Barrovian metamorphism from 47 to 38 Ma is coincident with the formation and exhumation of eclogites (Soret et al., 2021) along with a >50% decrease in convergence rates at 50-45 Ma (van Hinsbergen et al., 2011) and increased exhumation in the Himalaya starting around 35 Ma (Ding et al., 2016). Soret et al. (2012) suggest that initial collision, as defined by oceanic basin closure, was followed by a phase of "continental subduction" when there was Barrovian metamorphism and convergence was accommodated by underplating and tectonic stacking during the slow underthrusting of thinned passive margin lithosphere beneath Asia. Then, "collisional initiation" began ca. 38 Ma when increased mechanical coupling between India and Asia significantly increased thrust faulting (i.e., Main Mantle thrust, Karakorum fault), exhumation, uplift and erosion rates (Soret et al., 2021).

Therefore, multi-phase collision in western Anatolia could be attributed to the arrival of progressively thicker, buoyant TVZ continental lithosphere beneath the SKZ (Figure 3.10b). At 76 Ma, the initial "soft" collision, or "continental subduction," involving thin passive margin lithosphere locked the subduction zone megathrust and triggered upper plate shortening

(Beaumont et al., 1996; Tye et al., 2020). The appearance of basement-aged zircons in the CSB at 76 Ma is closely followed by a regional unconformity (Ocakoğlu et al., 2007), magmatic lull (67-58 Ma), TVZ Barrovian metamorphism (63-57 Ma; e.g., Whitney et al., 2011), and TVZ exhumation (60 Ma; Seaton et al., 2009). Then, thick-skinned deformation and basin partitioning by 54 Ma (Mueller et al., 2019; Şahin et al., 2019) would represent the final "hard" collision, or "collisional initiation," defined by the arrival of full-thickness continental lithosphere along the subduction zone and a more substantial plate coupling manifested as widespread regional contractional deformation. A convergence rate of ~5 mm/yr from 76 to 54 Ma (van Hinsbergen et al., 2020) predicts 110 km of TVZ underthrusting, which is on the order of narrower passive margins on Earth today and significantly smaller than estimates for the amount of underthrust thinned, passive margin Arabian lithosphere (~400-480 km; Ballato et al., 2011; Darin et al., 2018). This could point to the unknown effect of pre-collisional subduction and ophiolite emplacement of the TVZ on its syn-collisional passive margin width and lithospheric thickness.

3.8 Conclusion

Our results confirm the protracted nature of the closure of the Neotethys and TVZ-SKZ collision in western Anatolia. The first step of Neotethyan closure (i.e., the obduction of Neotethyan ophiolitic material on the TVZ at ca. 95 Ma) left barely any mark on the CSB forearc basin. This first phase was associated with backarc spreading (i.e., Black Sea basin) that separated the Pontides from the Eurasian margin, thus highlighting that extension rather than shortening dominated upper plate dynamics (Okay et al., 2013; Okay and Nikishin, 2015; Ocakoğlu et al., 2018; Campbell et al., in review). During that time, the CSB forearc basin received detritus from the Pontide volcanic arc and was unaffected by TVZ subduction and subsequent exhumation. This

confirms that this first phase occurred far offshore the SKZ margin, at ca. 750 km based on calculations from the plate reconstructions in van Hinsbergen et al. (2020). It remains unclear if this first phase corresponds to the obduction of an intra-oceanic arc, or the distal part of a wide oceanic forearc basin, as proposed for the India-Asia collision zone (van Hinsbergen et al., 2011, 2012). Phase 2 started at 76 Ma with the appearance of basement-derived zircons in CSB strata followed by the onset of northward prograding deltas and increased in mafic input (Açıkalın et al., 2016; Ocakoğlu et al., 2018; this study). These results all highlight an onset of İAES uplift and exhumation, and indicate a switch in deformation regime at the southern margin of the basin. These events are coeval to a regional arc shutdown, and are thus attributed to the onset of TVZ-SKZ continental collision and the beginning of TVZ underthrusting below SKZ. Phase 3 began at 54 Ma and is associated with basin partitioning, shift from thin- to thick-skinned thrusting, and regional syn-collisional magmatism. These events indicate a second shift of deformation regime and highlight the protracted nature of the collision.

The structural complexity of the Anatolian lithosphere with numerous tectonic units and sutures calls for a polygenetic evolution. İAES closure and suturing may be explained best by aspects of three multi-phase collision models: slab breakoff, relict basin closure, and subduction of progressively thicker lithosphere. Given the debated chronology of Intra-Pontide suturing and Eocene magmatism, the subduction of progressively thicker lithosphere remains the best and simplest explanation for protracted collision in western Anatolia. The uninterrupted sedimentary record of the forearc-foreland Central Sakarya Basin records a complete history of progressive intercontinental collision that can serve as an example for Tethyan collisions. This sedimentary basin highlights how the 15-40 Myr discrepancies of collision age across the Alpine-Himalaya belt

can be reconciled and synthesized into a holistic model for protracted collisions with changing plate coupling.

Acknowledgments

We thank Cassandra Brigham, Alison Duvall, Katharine Huntington, Begüm Kurtoğlu, Spencer Mattingly, Çelik Ocakoğlu, Ben Paulson, Aurora Rosenberger, Theresa Schwartz, Tamas Ugrai, and Melissa Wood for prolific discussions and for field and lab assistance. We thank Editor Peter van der Beek and two anonymous reviewers for improving the manuscript. This work was supported by NSF EAR-1543684. Datasets for this research are included in the supplemental data files.

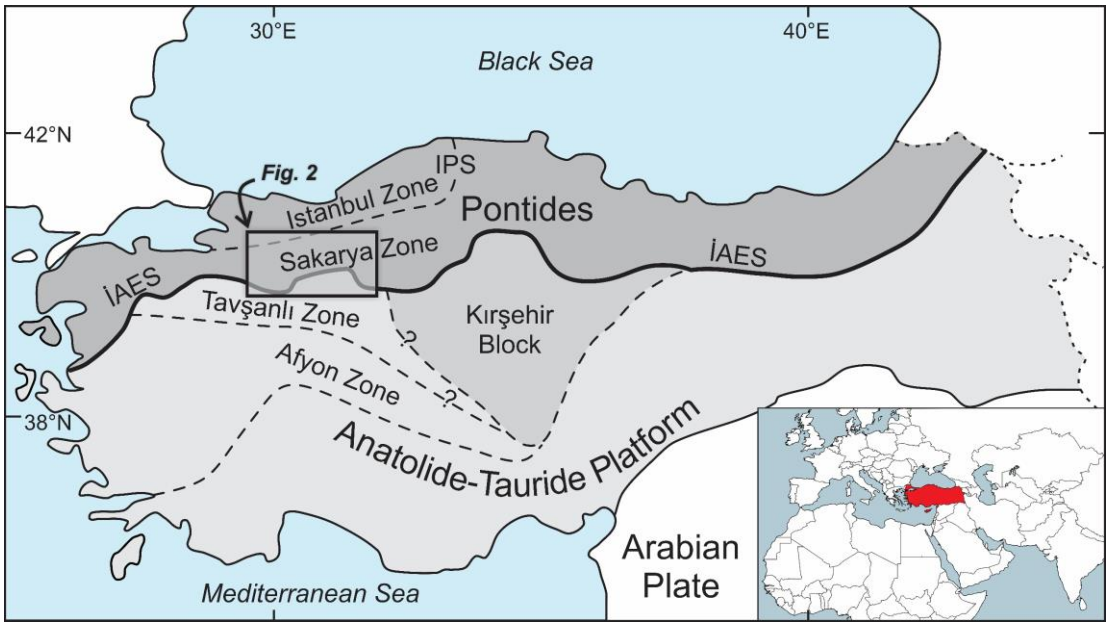

Figure 3.1. Simplified terrane map of Anatolia including hypothesized suture zones (dashed lines) modified from Licht et al. (2017). İAES: İzmir-Ankara-Erzincan suture zone; IPS: Intra-Pontide suture zone.

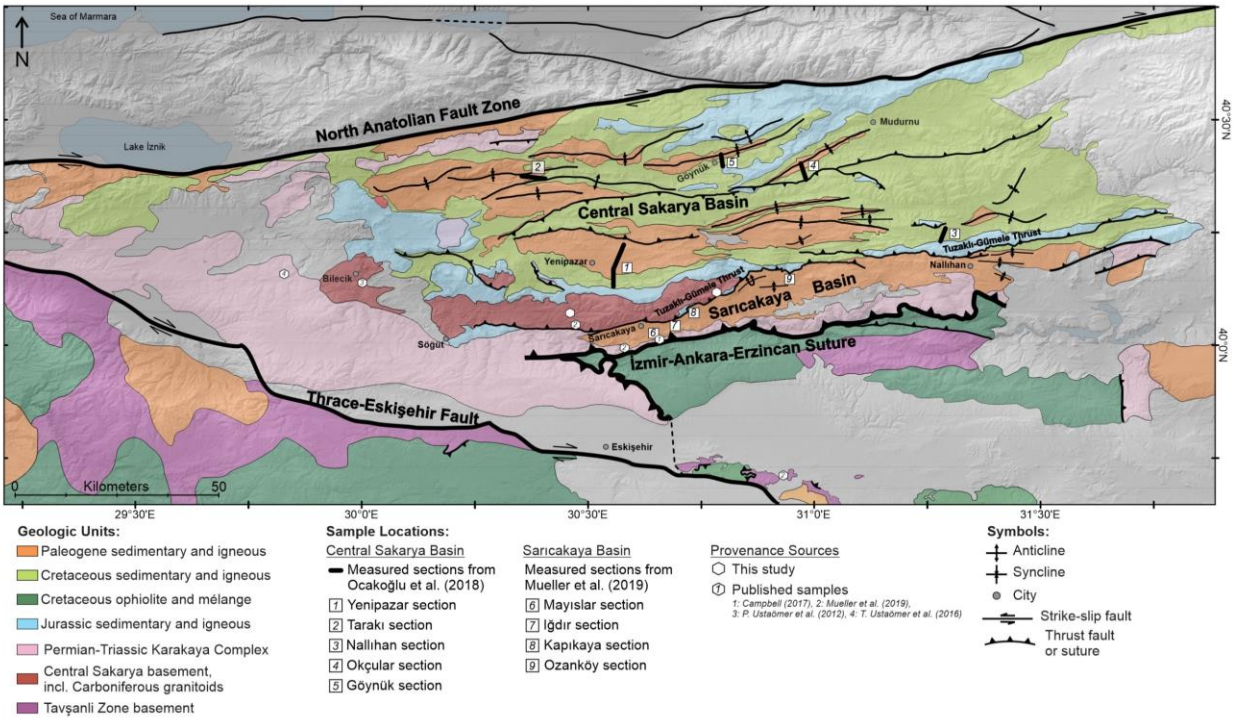

Figure 3.2. Simplified geologic map of northwestern Anatolia (after Aksay et al., 2002; Duru and Aksay, 2002; Gedik and Aksay, 2002; Timur and Aksay, 2002; Turhan, 2002; Şahin et al., 2019). See Figure 3.1 for location.

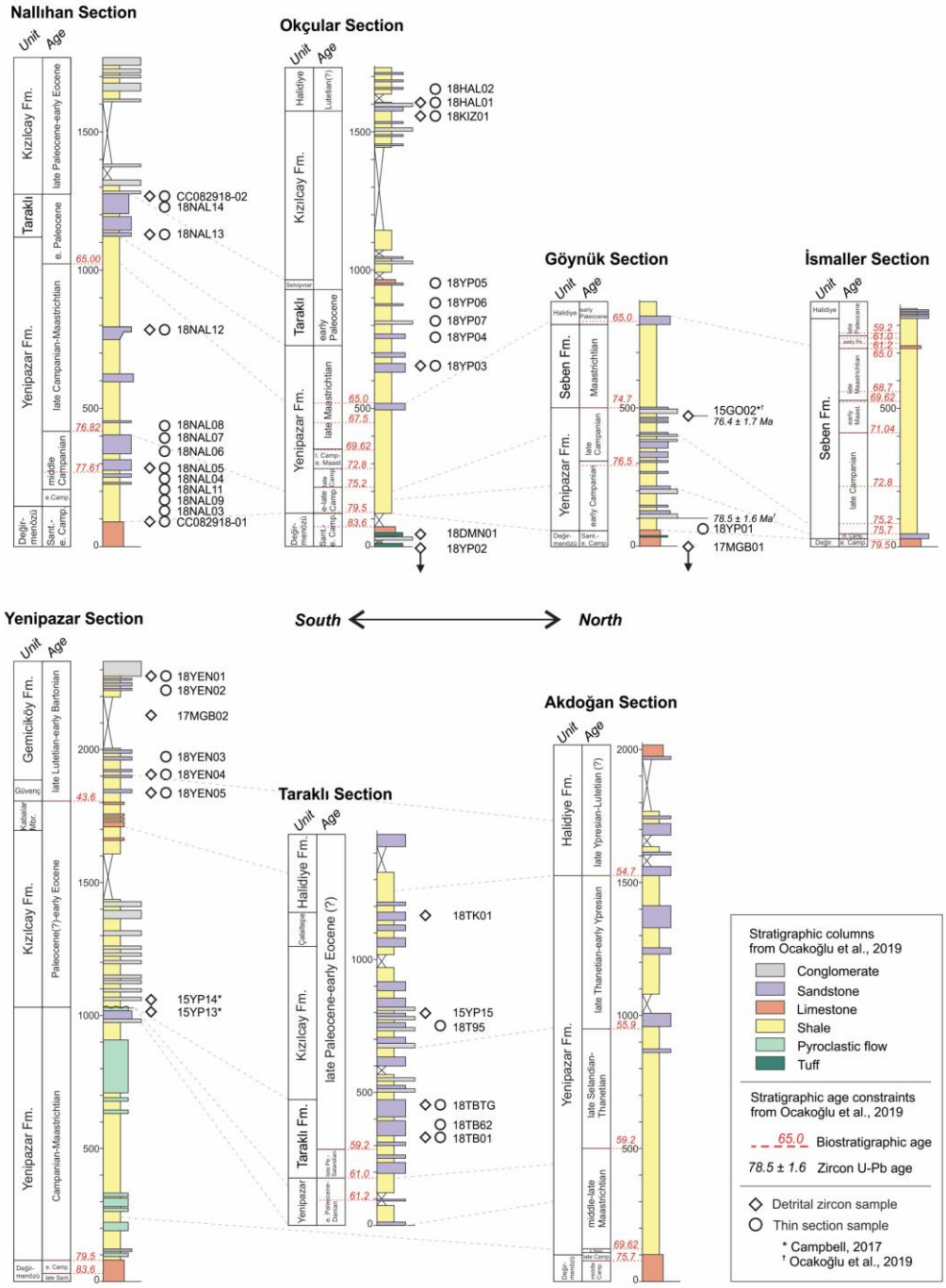

Figure 3.3. Simplified Upper Cretaceous through Eocene stratigraphic columns, biostratigraphic ages, and sample locations in the Central Sakarya Basin. Stratigraphic columns and age constraints are from Ocakoğlu et al. (2018). See Figure 3.2 for stratigraphic column locations.

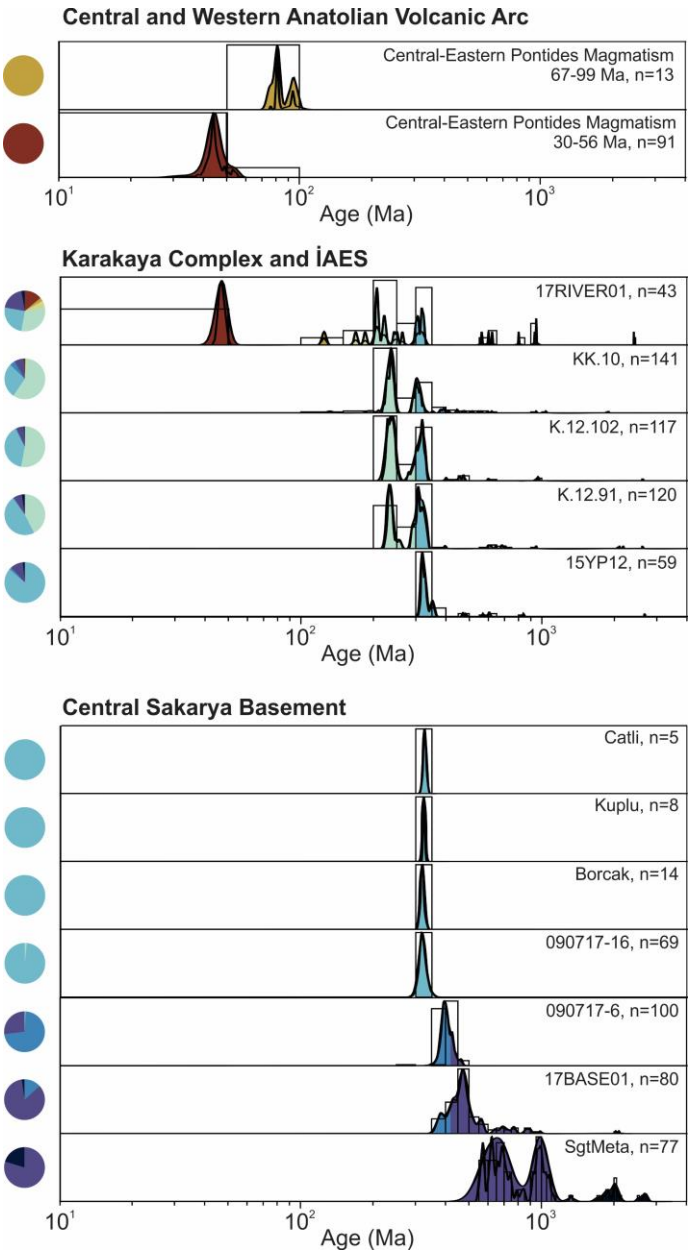

Figure 3.4. Detrital zircon age spectra characterizing potential sediment sources displayed as histograms (50 Myr bins), probability density functions (black lines) and optimized fixed bandwidth kernel density estimates (gray lines and shading). The Karakaya Complex samples are from Triassic sedimentary rocks and one modern river sample draining the İzmir-Ankara-Erzincan suture zone. The Central Sakarya Basement compilation includes bedrock and metasedimentary samples. Figure 3.5 contains the legend for DZ colors. Data sources: Campbell (2017); Mueller et al. (2019); P. Ustaömer et al. (2012); T. Ustaömer et al. (2016); this study.

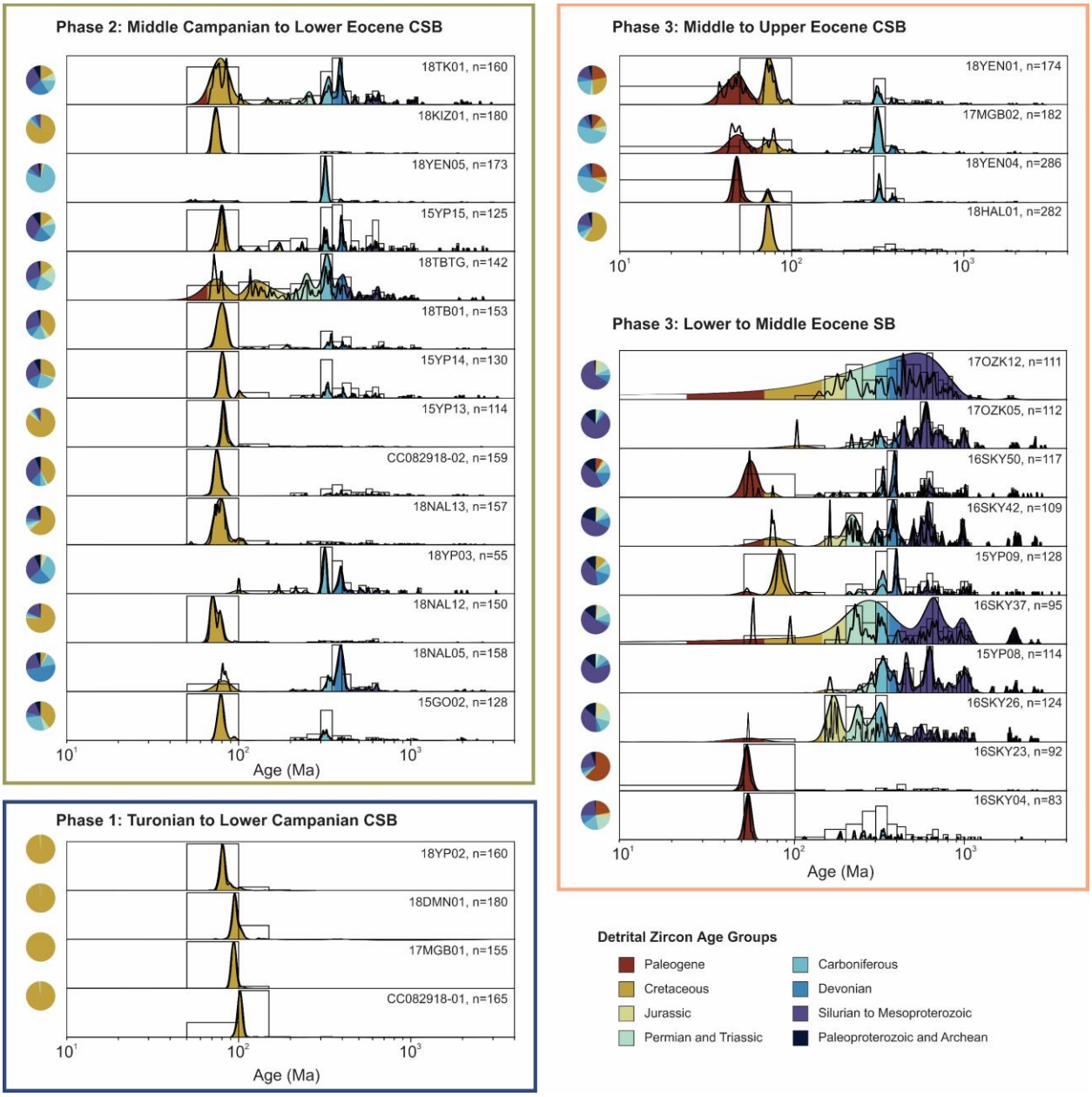

Figure 3.5. Detrital zircon age spectra from Central Sakarya Basin and Sarıcakaya Basin grouped by Phase (see main text); Phase 3 is split into CSB and SB groups. Data are displayed as histograms (50 Myr bins), probability density functions (black lines) and optimized fixed bandwidth kernel density estimates (colored lines and shading). Data sources: Campbell (2017); Mueller et al. (2019); Ocakoğlu et al. (2018); this study.

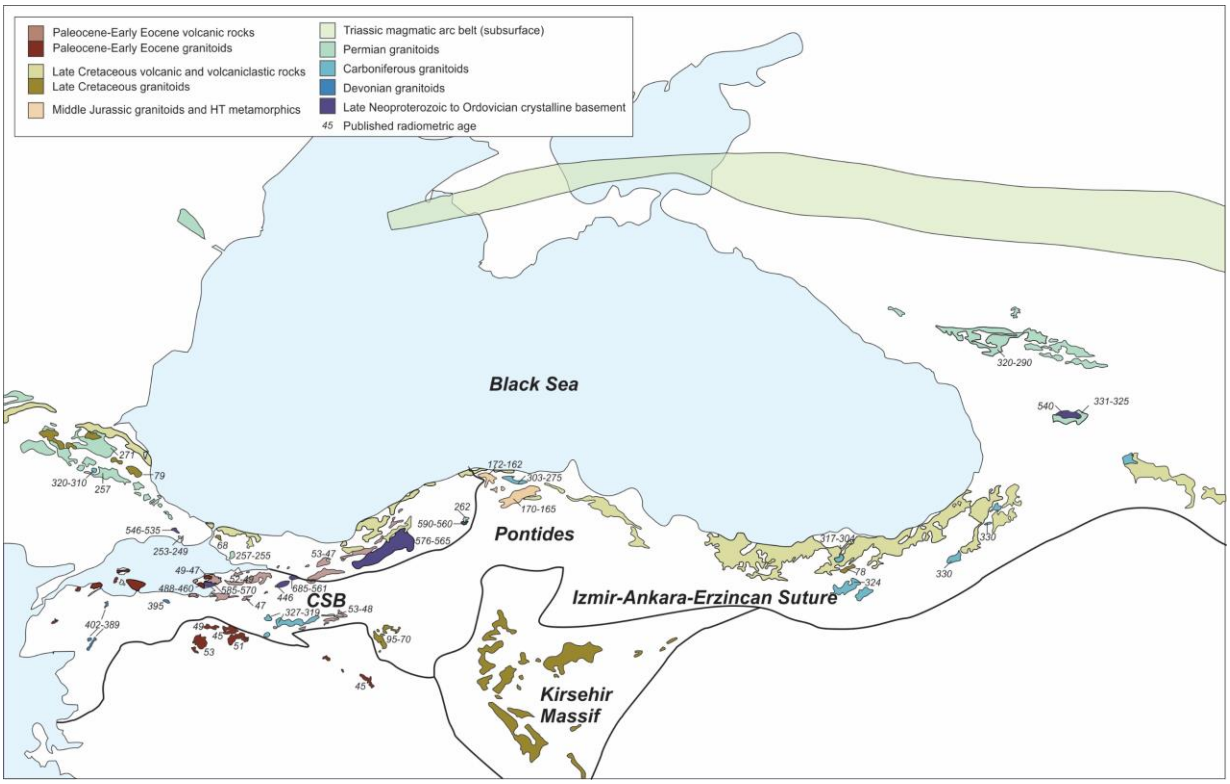

Figure 3.6. Bedrock map of northern Anatolia. Outcrops and isotopic ages of late Neoproterozoic through Eocene magmatic and metamorphic rocks adapted from Akdoğan et al. (2017), Ersoy, Akal, et al. (2017), and Okay & Nikishin (2015) and references therein.

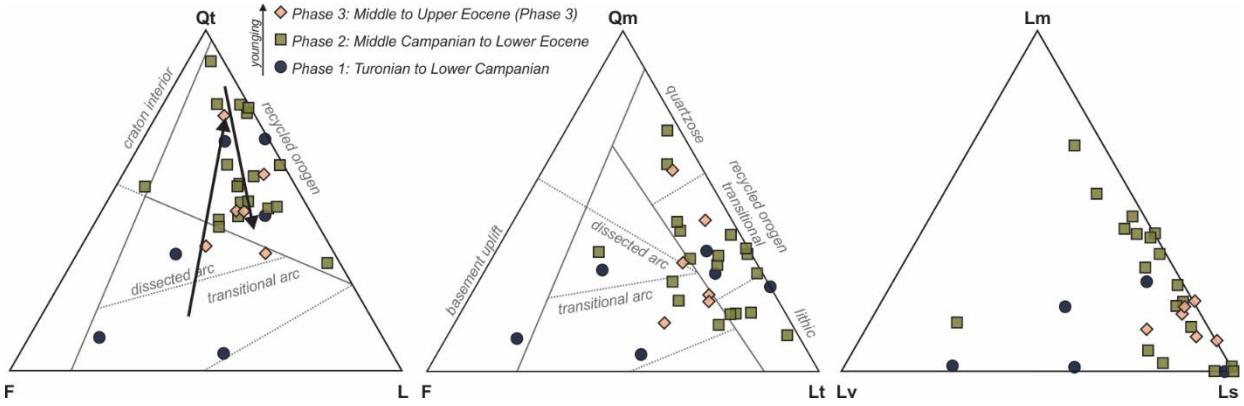

Figure 3.7. Ternary diagrams of CSB sandstone modal compositions. Samples are grouped by the sedimentary basin phases discussed in the text. Poles: Qt: total quartz; Qm: monocrystalline quartz; F: feldspar; L: lithics; Lm: metamorphic lithics; Ls: sedimentary lithics; Lv: volcanic lithics; Lt: total lithics (L + polycrystalline quartz).

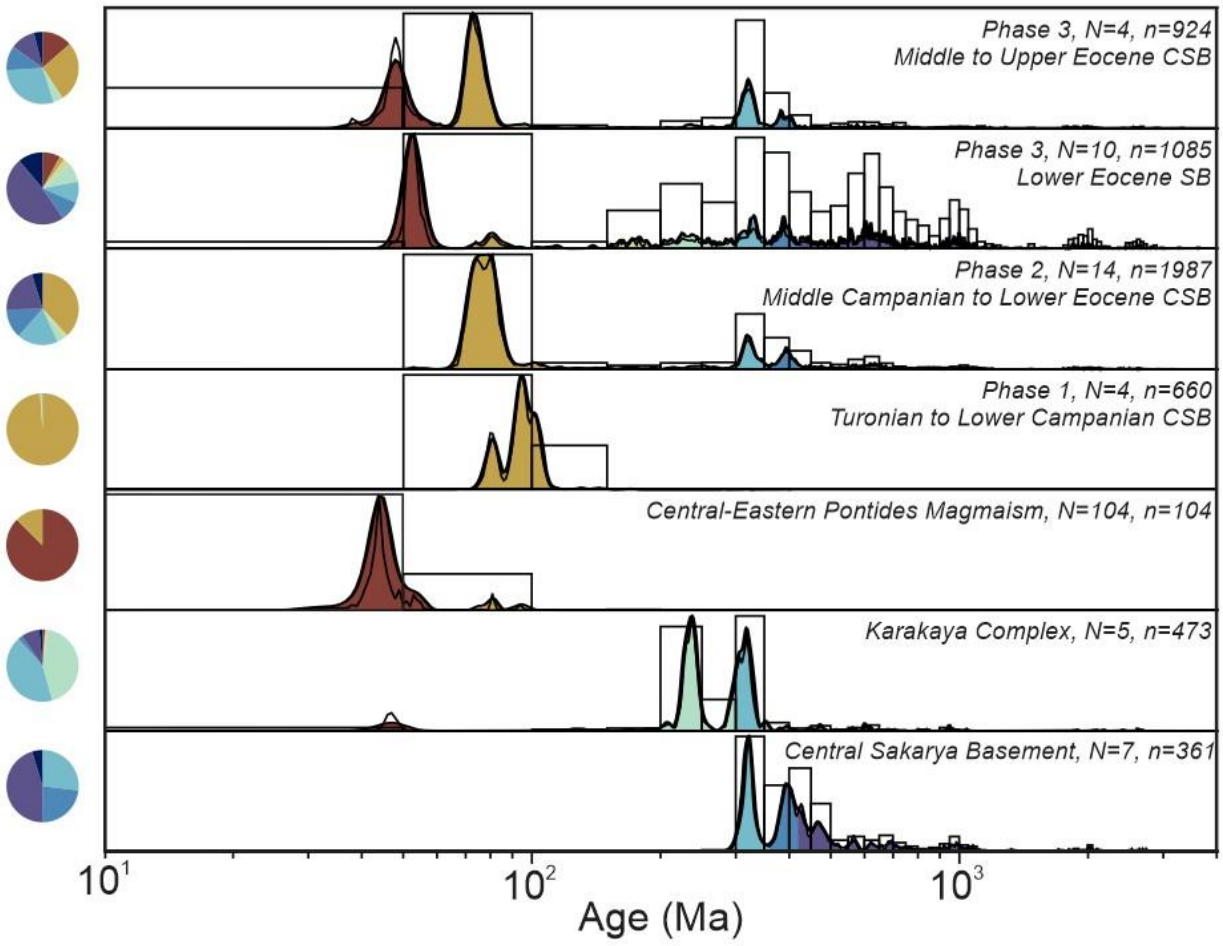

Figure 3.8. Detrital zircon spectra of sample groups. Histograms (50 Myr bins), probability density functions (black lines) and optimized fixed bandwidth kernel density estimates (black lines and colored shading) of all bedrock, modern and detrital zircon ages 10-3000 Ma, grouped by basement terrane, basin, and stratigraphic age. See main text for discussion. Figure 3.5 contains the legend for DZ colors.

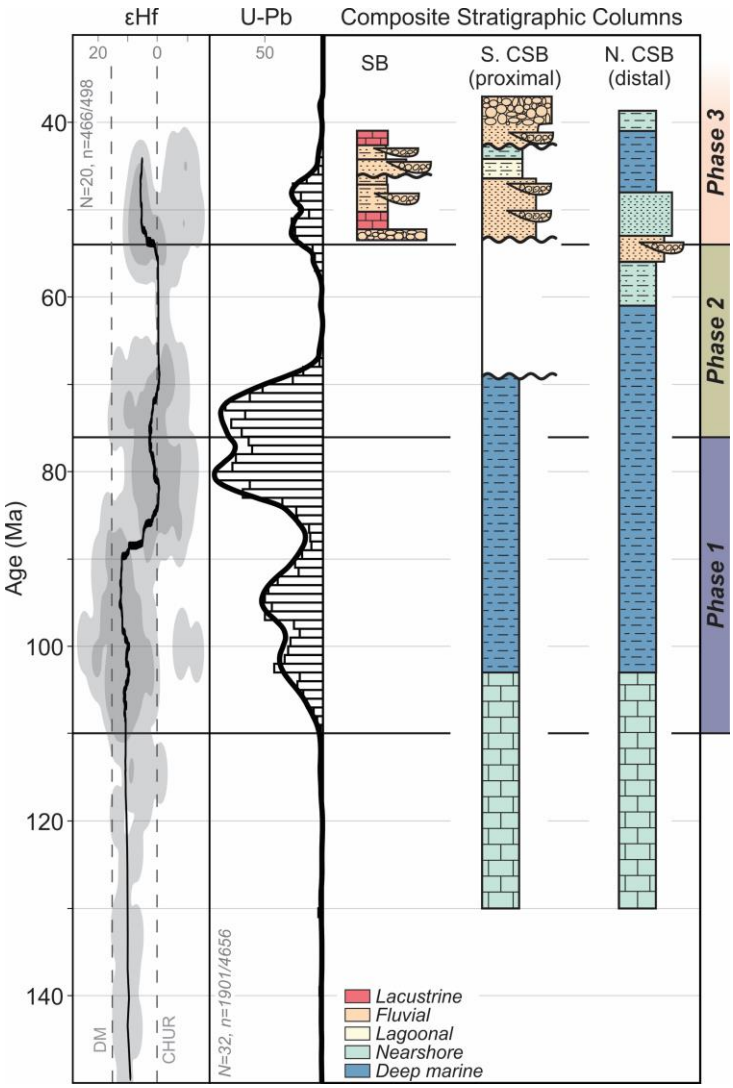

Figure 3.9. Detrital zircon U-Pb and εHf alongside stratigraphic columns. SB and CSB εHf data are plotted as a 40-pt running median, and gray and dark gray envelopes represent the 95% (2-sigma) and 99.7% (3-sigma) confidence intervals, respectively, of bivariate optimized-bandwidth kernel density estimates (data from Campbell et al., in review). All detrital zircon ages from 150 to 30 Ma from a compilation of all SB and CSB samples are displayed as a histogram (1 Myr bin) and probability density function. The CSB and SB composite stratigraphic columns are after Ocakoğlu et al. (2018) and Mueller et al. (2019), respectively (see Figure 3.3). The histogram (1 Myr bin) and probability density function depict all 150 to 30 Ma SB and CSB DZ ages. Shading highlights the three sedimentary basin phases discussed in the text. The CSB and SB composite stratigraphic columns are after Ocakoğlu et al. (2018) and Mueller et al. (2019), respectively. DM: depleted mantle; CHUR: chondritic uniform reservoir.

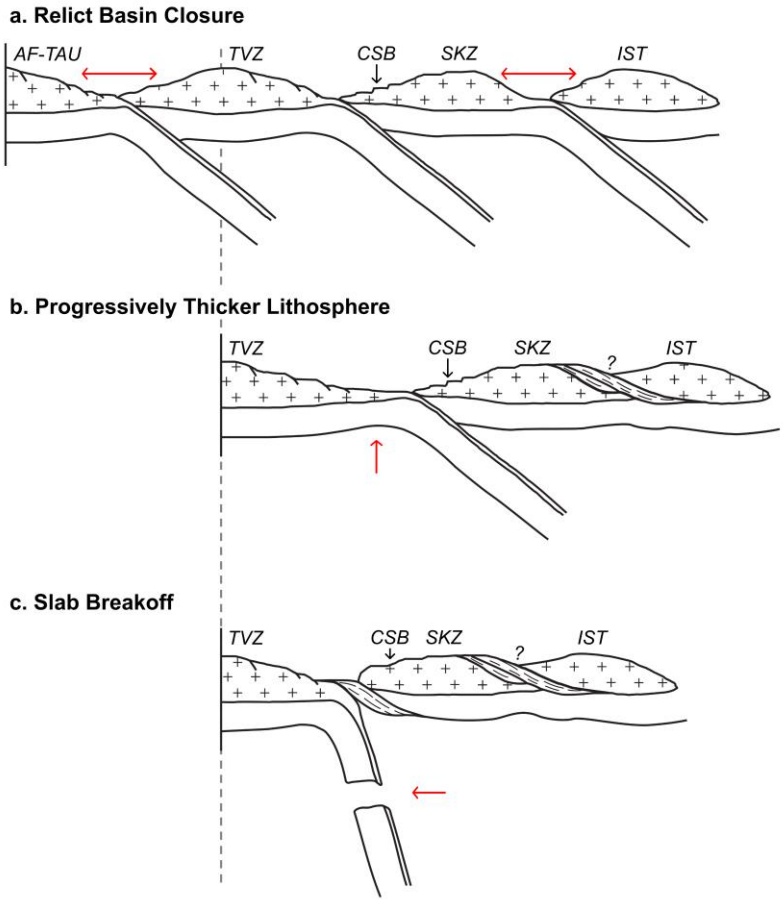

Figure 3.10. Schematic diagram of multi-phase collision scenarios (Göncüoğlu et al., 2014; inspired by Darin et al., 2018; Di Rosa et al., 2019). (a) Relict basin closure between the Sakarya (SKZ) and Istanbul (IST) Zones in the north and/or the Tavşanlı Zone (TVZ) and Afyon Zone or Tauride terrane (AF-TAU) in the south (see Figure 3.1). (b) Subduction and underthrusting of progressively thicker Tavşanlı Zone lithosphere. (c) Tavşanlı Zone slab breakoff.

Table 3.1. New and published samples, units, ages, groups, sample types, and sources. See Figure 3.2 for sample locations.DZ: detrital zircon; TS: thin section. (Data sources: 1: Ustaömer et al., 2012, 2: Ustaömer 2016; 3: Campbell, 2017; 4: Ocakoğlu et al., 2018; 5: Schleiffarth et al., 2018 and references therein; 6: Mueller et al., 2019; 7: this study).

Sample	Unit	Age	Group	Sample Type	Data Source
Central Sakarya Basin					
Yenipazar Section					
15YP13	Yenipazar Fm	Maastrichtian	Middle Campanian-lower Eocene	DZ	3
15YP14	Kızılçay Fm	Paleocene	Middle Campanian-lower Eocene	DZ	3
18YEN05	Kızılçay Fm	Paleocene-lower Eocene	Middle Campanian-lower Eocene	DZ, TS	7
18YEN04	Güvenç Fm	Lutetian	Middle-upper Eocene	DZ, TS	7
18YEN03	Güvenç Fm	Lutetian-Bartonian	Middle-upper Eocene	TS	7
17MGB02	Gemiciköy Fm	Upper Lutetian-Lower Bartonian	Middle-upper Eocene	DZ	7
18YEN02	Gemiciköy Fm	Bartonian-Priabonian	Middle-upper Eocene	TS	7
18YEN01	Gemiciköy Fm	Bartonian-Priabonian	Middle-upper Eocene	DZ, TS	7
Taraklı Section					
18TB01	Taraklı Fm	Paleocene-lower Eocene	Middle Campanian-lower Eocene	DZ, TS	7
18TB62	Taraklı Fm	Paleocene-lower Eocene	Middle Campanian-lower Eocene	TS	7
18TBTG	Taraklı Fm	Paleocene-lower Eocene	Middle Campanian-lower Eocene	DZ, TS	7
18T95	Kızılçay Fm	Paleocene-lower Eocene	Middle Campanian-lower Eocene	TS	7
15YP15	Kızılçay Fm	Paleocene-lower Eocene	Middle Campanian-lower Eocene	DZ	7
18TK01	Çataltepe Fm	Paleocene-lower Eocene	Middle Campanian-lower Eocene	DZ	7
Nallıhan Section					
CC082918-01	Yenipazar Fm	Cenomanian-Turonian	Turonian-lower Campanian	DZ, TS	7
18NAL03	Yenipazar Fm	Lower Campanian	Turonian-lower Campanian	TS	7
18NAL09	Yenipazar Fm	Lower Campanian	Turonian-lower Campanian	TS	7
18NAL11	Yenipazar Fm	Lower Campanian	Turonian-lower Campanian	TS	7

18NAL04	Yenipazar Fm	Lower Campanian	Turonian-lower Campanian	TS	7
18NAL05	Yenipazar Fm	Middle Campanian	Middle Campanian-lower Eocene	DZ, TS	7
18NAL06	Yenipazar Fm	Middle Campanian	Middle Campanian-lower Eocene	TS	7
18NAL07	Yenipazar Fm	Middle Campanian	Middle Campanian-lower Eocene	TS	7
18NAL08	Yenipazar Fm	Middle Campanian	Middle Campanian-lower Eocene	TS	7
18NAL12	Yenipazar Fm	Upper Campanian-Maastrichtian	Middle Campanian-lower Eocene	DZ, TS	7
18NAL13	Taraklı Fm	Upper Campanian-Maastrichtian	Middle Campanian-lower Eocene	DZ, TS	7
18NAL14	Taraklı Fm	Upper Campanian-Maastrichtian	Middle Campanian-lower Eocene	TS	7
CC082918-02	Taraklı Fm	Upper Campanian-Maastrichtian	Middle Campanian-lower Eocene	DZ, TS	7
Okçular Section					
18YP02	Değirmenözü Fm	Santonian-Campanian	Turonian-lower Campanian	DZ	7
18DMN01	Değirmenözü Fm	Santonian	Turonian-lower Campanian	DZ	7
18YP03	Yenipazar Fm	Lower Paleocene	Middle Campanian-lower Eocene	DZ, TS	7
18YP04	Taraklı Fm	Lower-middle Paleocene	Middle Campanian-lower Eocene	TS	7
18YP07	Taraklı Fm	Lower-middle Paleocene	Middle Campanian-lower Eocene	TS	7
18YP06	Taraklı Fm	Lower-middle Paleocene	Middle Campanian-lower Eocene	TS	7
18YP05	Taraklı Fm	Lower-middle Paleocene	Middle Campanian-lower Eocene	TS	7
18KIZ01	Kızılçay Fm	Paleocene-lower Eocene	Middle Campanian-lower Eocene	DZ, TS	7
18HAL01	Halidiye Fm	Lutetian	Middle-upper Eocene	DZ, TS	7
18HAL02	Halidiye Fm	Lutetian	Middle-upper Eocene	TS	7
Göynük Section					
17MGB01	Değirmenözü Fm	Middle Cretaceous	Turonian-lower Campanian	DZ	7
18YP01	Değirmenözü Fm	Lower Campanian	Turonian-lower Campanian	TS	7
15GO02	Yenipazar Fm	Middle-upper Campanian	Middle Campanian-lower Eocene	DZ	3, 4
Saricakaya Basin					
Mayıslar Section					
16SKY04	Kızılçay Gp	Ypresian	Lower-middle Eocene	DZ	6

Iğdir Section					
16SKY23	Kızılçay Gp	Ypresian	Lower-middle Eocene	DZ	6
16SKY26	Kızılçay Gp	Ypresian-Lutetian	Lower-middle Eocene	DZ	6
Kapıkaya Section					
15YP08	Kızılçay Gp	Ypresian-Lutetian	Lower-middle Eocene	DZ	3
16SKY37	Kızılçay Gp	Ypresian-Lutetian	Lower-middle Eocene	DZ	6
15YP09	Kızılçay Gp	Ypresian-Lutetian	Lower-middle Eocene	DZ	3
16SKY42	Kızılçay Gp	Ypresian-Lutetian	Lower-middle Eocene	DZ	6
16SKY50	Kızılçay Gp	Ypresian-Lutetian	Lower-middle Eocene	DZ	6
Ozanköy Section					
17OZK05	Kızılçay Gp	Ypresian-Lutetian	Lower-middle Eocene	DZ	6
17OZK12	Kızılçay Gp	Ypresian-Lutetian	Lower-middle Eocene	DZ	6
Provenance Sources					
Catli	Söğüt magmatics	Carboniferous	Central Sakarya Basement	Bedrock	1
Kuplu	Söğüt magmatics	Carboniferous	Central Sakarya Basement	Bedrock	1
Borcak	Söğüt magmatics	Carboniferous	Central Sakarya Basement	Bedrock	1
17BASE01	Söğüt metamorphics	Devonian	Central Sakarya Basement	Metased DZ	6
SgtMeta	Central Sakarya Basement	Neoproterozoic	Central Sakarya Basement	Bedrock	1
090717-6	Paragneiss	Carboniferous	Central Sakarya Basement	Bedrock	7
090717-16	Orthogneiss	Carboniferous	Central Sakarya Basement	Bedrock	7
17RIVER01	Modern river draining accretionary prism	Quaternary	İzmir-Ankara-Erzincan Suture	Modern river sand	6
KK.10	Kendirli Fm	Upper Triassic	Karakaya Complex	Bedrock	2
K.12.102	Cambazkaya Fm	Norian	Karakaya Complex	Bedrock	2
K.12.91	Cambazkaya Fm	Norian	Karakaya Complex	Bedrock	2
15YP12	Greenschist unit	Carboniferous	Karakaya Complex	Bedrock	3
Central-Eastern Pontides Magmatism	Igneous units compilation	100-30 Ma	Central-Eastern Pontides	Bedrock	5

Chapter 4. Resolving the chronology of Intra-Pontide suturing using multi-proxy sedimentary provenance analysis

The content of this chapter is in preparation:

Megan A. Mueller, Clay F. Campbell, Faruk Ocakoğlu, Andreas Möller, Cailey B. Condit, Michael H. Taylor, K. Christopher Beard, Grégoire Métais, Pauline M. C. Coster, Kyle Lowery, Samuel Shekut, Abel Guihou, Alexis Licht. in prep. Resolving the chronology of Intra-Pontide suturing using multi-proxy sedimentary provenance analysis.

Abstract

This study presents sedimentary provenance results from northwest Anatolia in order to evaluate the chronology of Intra-Pontide suturing. Detrital rutile results yielded highly discordant ages and we discuss a path forward to utilizing detrital rutile as a provenance proxy in accretionary collisional settings. Detrital zircon and sandstone petrography results from across the Intra-Pontide suture demonstrate Paleocene exhumation and sediment recycling of the accretionary prism associated with the onset of collision. Accretionary prism uplift, exhumation and contractional deformation at the Intra-Pontide suture coincided with the onset of basement-involved contractional deformation along the İzmir-Ankara-Erzincan suture. This means that collisional deformation from the İzmir-Ankara-Erzincan suture was taken up at the Intra-Pontide suture zone until Paleocene times. Relict basin closure, therefore, plays an important role in controlling the tempo and style of collisional deformation. This study highlights how close-proximity subduction systems and continental collisions exert a first-order control on collisional geodynamics.

4.1 Introduction

Tectonic reconstructions of the opening and closing of the Neotethys Ocean during the Mesozoic through Cenozoic convergence of Afro-Arabia with Eurasia foundationally underlies our present understanding of subduction zone geodynamics and accretionary collisional tectonics (Royden and Burchfiel, 1989; Royden, 1993; Davies and von Blanckenburg, 1995; Jolivet and Faccenna, 2000). The chronology of subduction, accretion, and collision of these continental domains is heavily debated (Pourteau et al., 2016; Hu et al., 2016; Kapp and DeCelles, 2019; van Hinsbergen et al., 2020). Even though the relative plate motions of Eurasia and Afro-Arabia are well-established, the trajectories of eastern Mediterranean continental terranes are poorly resolved by paleomagnetism, with uncertainties of ± 3-5° latitude (± 300-500 km; Meijers et al., 2015). The location of tectonic units through time is only further complicated by the non-cylindrical nature of the orogens (Gürer and van Hinsbergen, 2018). Plus, the opposing forces of subduction and backarc extension (Royden and Burchfiel, 1989; Stampfli and Borel, 2002), the timing and extent of which are debated, affect the location of continental margins through time. Numerical models of double subduction zones, which are proposed for various branches of the Neotethys Ocean (Speciale et al., 2012; Shin et al., 2013; Plunder et al., 2013a; Jagoutz et al., 2015; Pourteau et al., 2016; van Hinsbergen et al., 2016; Gürer et al., 2018), demonstrate that feedback between the downgoing slabs control subduction speed and trench retreat and advance (Jagoutz et al., 2015; Faccenna et al., 2017; Holt et al., 2018). In addition, in western Anatolia, backarc extension was possibly initiated by the pre-collisional subduction of the lower plate passive margin (i.e., Tavşanlı Zone; Figure 4.1; Campbell et al., in review), demonstrating complex feedbacks between double subduction systems in collisional events. Furthermore, the transfer of collisional stress through the

lithosphere to adjacent subduction systems could control the tempo and style of collisional deformation (Cowgill et al., 2016; see also Chapter 3: Mueller et al., in review).

Therefore, Anatolia is the ideal location to investigate the mechanisms controlling double subduction systems and protracted continental collisions. In northwest Anatolia, the main Neotethyan suture, the İzmir-Ankara-Erzincan suture (İAES), is located ~30-100 km south of the Intra-Pontide suture (Figure 4.1). Each suture zone marks the location of one branch of the Neotethys Ocean; their Mesozoic-Cenozoic closures were facilitated by one or two synchronous or episodic subduction zones in each oceanic basin (Moix et al., 2008; Speciale et al., 2012; Shin et al., 2013; Pourteau et al., 2016). However, the number and polarity of subduction zones and the timing of collisions is highly debated, ranging from the Triassic to Eocene (e.g., Şengör and Yilmaz, 1981; Moix et al., 2008; Pourteau et al., 2016; Akbayram et al., 2016). Sedimentary deposits across the suture zones record near continuous Jurassic through Eocene deposition (Altiner et al., 1991; Tüysüz, 1999; Yiğitbaş et al., 1999; Okay et al., 2001; Ocakoğlu et al., 2018), and therefore preserve the history of suturing in both locations. Sedimentary facies and provenance reconstructions from the forearc-foreland Central Sakarya Basin north of the İAES (Figure 4.2) demonstrate that collision along the İAES began at ca. 76 Ma (Açıkalın et al., 2016; Ocakoğlu et al., 2018; Chapter 3: Mueller et al., in review), yet major contractional deformation and foreland partitioning was delayed by ~20 Myr (Mueller et al., 2019). Geodynamic explanations for protracted İAES suturing include slab breakoff (Harris et al., 1994; Altunkaynak and Dilek, 2006; Kasapoğlu et al., 2016; Ersoy et al., 2017a), and subduction of thinned passive margin lithosphere and relict basin closure at the Intra-Pontide suture (Chapter 3: Mueller et al., in review).

We present new detrital zircon U-Pb, detrital rutile U-Pb and sandstone petrography results from Late Cretaceous-Eocene sedimentary units from the Intra-Pontide suture zone and the

western Central Sakarya Basin on the Sakarya Zone (Figure 4.2). The provenance results are compared to those from the main Central Sakarya basin, located on the Sakarya Zone south of the IPS. There was not shared provenance across the IPS during the Late Cretaceous to Eocene. The evolution of sedimentary provenance in the IPS demonstrates that collision between the Istanbul and Sakarya Zones occurred sometime in the Paleocene-early Eocene.

4.2 Geologic Background

4.2.1 Chronology of the Intra-Pontide Suture

Resolving the timing of the Intra-Pontide suturing is critical for geodynamic and tectonic reconstructions of the İAES. The ~750-km long Intra-Pontide suture (IPS) demarcates the Istanbul Zone (IST) from the Sakarya Zone (SKZ; Figure 4.1) and marks the former location of the Intra-Pontide Ocean, which opened sometime in the Early Triassic to Jurassic (Robertson and Ustaömer, 2004; Akbayram et al., 2013; Marroni et al., 2020). The closure of the Intra-Pontide ocean began by the Early Cretaceous and was facilitated by one, two, or three north- or south-dipping subduction zones (Akbayram et al., 2013; Marroni et al., 2020). The timing of suturing is difficult to determine, in part because of the along-strike variability in lithologic units and extensive late Cenozoic deformation of the Intra-Pontide suture zone by the dextral North Anatolian Fault (ca. 50 to 100 km offset, Şengör et al., 2005). Based on the age of the first transgressive sediments across the suture zone and the timing of metamorphism, a range of collision ages are suggested: Triassic (Bozkurt et al., 2013), Early Cretaceous (Okay et al., 2013; Akbayram et al., 2013; Frassi et al., 2017; Marroni et al., 2020), pre-Santonian (Özcan et al., 2012), Late Cretaceous (Robertson and Ustaömer, 2004; Keskin and Tüysüz, 2018), Paleocene-early Eocene (Şengör and Yilmaz, 1981; Okay et al., 1994; Catanzariti et al., 2013; Göncüoğlu et al., 2014; Akbayram et al., 2016).

It is generally agreed that Triassic metamorphism records an earlier Sakarya-Istanbul collision event (Bozkurt et al., 2013), which was followed by Late Triassic rifting between Sakarya-Istanbul (e.g., Marroni et al., 2020). Subduction initiation is recorded by Late Jurassic-Early Cretaceous metamorphism (155-135 Ma: Akbayram et al., 2013; Marroni et al., 2020) and is coeveal with supra-subduction zone ophiolite formation (Marroni et al., 2020 and references therein). Early Cretaceous metamorphism (135-119 Ma) and the regional transgression of Santonian-Campanian and younger sedimentary units covering the suture zone are interpreted as an Early Cretaceous age for IST-SKZ collision (Akbayram et al., 2013; Marroni et al., 2020). The Late Cretaceous blueschist-eclogite facies metamorphic rocks identified in the eastern and western segments of the IPS are instead considered representative of IST-SKZ collision (Marroni et al., 2020) and their absence in the central segment could be due to late Cenozoic displacement along the North Anatolian Fault (Akbayram et al., 2016). In contrast, Akbayram et al. (2016) rely on Late Paleocene unconformities in the Istanbul and Sakarya Zones (Özcan et al., 2012) to argue that the first transgressive molasse units are Ypresian in age.

4.2.2 Istanbul Zone

The Istanbul Zone (IST) is a ~750 km long, 55-km wide continental fragment located along the southwest coast of the Black Sea (Figure 4.1). The IST is separated from the Central Pontides to the east and Sakarya Zone to the south by the Intra-Pontide Suture (IPS), which contains ophiolitic and accretionary prism units (Akbayram et al., 2016; Marroni et al., 2020). The IST basement units are correlated with Avalonian terranes (Okay et al., 1994, 2008, 2011; Ustaömer et al., 2011), and paleogeographic reconstructions place the IST between the Moesian Platform and Crimea until Aptian-Albian times (Okay et al., 1994). The IST metamorphic basement (i.e., Pamukova Complex, Bolu Massif) comprises Neoproterozoic gneisses and amphibolites intruded

by late Neoproterozoic-Ordovician granites (Chen et al., 2002; Ustaömer et al., 2005; Okay et al., 2008; Akbayram et al., 2013). The IST basement is unconformably overlain by a Paleozoic sedimentary sequence intruded by Permian granitoids (Akbayram et al., 2013; Akdoğan et al., 2020), which is in turn unconformably overlain by Triassic deep marine limestone and flysch (Akbayram et al., 2013). The Paleozoic-Triassic sequence is unconformably overlain by the Kocaeli Basin strata (Akbayram et al., 2013). Late Cretaceous volcanic and plutonic rocks are widespread along the southern Black Sea coast (Okay and Nikishin, 2015; Keskin and Tüysüz, 2018; Aydin et al., 2020).

The units within the Intra-Pontide suture, located on the Armutlu Peninsula within the North Anatolian Fault zone, are poorly exposed, and their names, structural relationships, lateral continuity, and tectonic setting are inconsistent across the literature (see Akbayram et al., 2013). The units that crop out in the central segment of the suture zone are summarized, from top to bottom. The Campanian-Eocene sedimentary units unconformably overlie all older units (Akbayram et al., 2013) and potentially belong to the Kocaeli Basin. The Istanbul Zone basement (Pamukova Complex) is exposed and imbricated with the Late Jurassic-Early Cretaceous Gemlik Mélange (Akbayram et al., 2013). The Istanbul Zone basement tectonically overlies an Early Cretaceous accretionary prism of greenschist facies metabasites, serpentinites, metachert and phyllite (Sapanca Complex; Akbayram et al., 2013). The protoliths are undated but the phyllite has a Rb-Sr muscovite age of 110.8 ± 3.4 Ma (Akbayram et al., 2013). Tectonically underlying the Sapanca Complex are the Triassic arkosic metasandstones and marbles of the Maşukiye Group, metamorphosed to greenschist facies in the Early Cretaceous (Akbayram et al., 2013). This unit is the Triassic IST continental margin succession, variably interpreted as rift basin fill in the Intra-Pontide ocean basin, the equivalent of the Karakaya Complex in the Sakarya Zone, or the lateral

equivalent of the Rhodope-Strandja Zone passive margin (Robertson and Ustaömer, 2004; Akbayram et al., 2013).

South of the Istanbul Zone, the Sakarya Zone is the western segment of the Pontides (Figure 4.1 and Figure 4.2). The Sakarya Zone basement is composed of early Paleozoic metamorphosed continental units intruded by Carboniferous granitoids called the Central Sakarya Basement (Göncüoğlu et al., 2000; P. Ustaömer et al., 2012; T. Ustaömer et al., 2016) and the Permian-Triassic subduction-accretion complex, the Karakaya Complex (Okay and Göncüoglu, 2004). The basement units are unconformably overlain by non-metamorphosed Jurassic through Eocene sedimentary units belonging to the Central Sakarya Basin (CSB; Aksay et al., 2002). The Central Sakarya Basin includes the Eocene broken foreland Sarıcakaya Basin (Mueller et al., 2019) which is bound to the south by the İzmir-Ankara-Erzincan suture zone.

4.2.3 Upper Cretaceous through Eocene Stratigraphy

4.2.3.1 Kocaeli Peninsula

In the eastern IST, the Kocaeli Basin consists of a near-continuous series of Jurassic through Eocene strata (Akbayram et al., 2016), whereas in the western IST, the Kocaeli Basin consists of Late Cretaceous-Eocene strata (Özcan et al., 2012). Upper Cretaceous through Eocene deposition was nearly continuous in the Kocaeli Peninsula (Figure 4.3; Özcan et al., 2012). Near the Black Sea coast, the Santonian-Campanian volcanic and volcaniclastic Yemişliçay Group unconformably overlies Triassic and older sedimentary units (Özcan et al., 2012). The Yemişliçay Group was deposited in a northern magmatic arc basin; a ridge separated the northern volcaniclastic units from the southern siliciclastic turbidites and calcarenites in the Armutlu Peninsula (cf. Section 4.2.2.3; Özcan et al., 2012). The Yemişliçay Group and the southern sub-basin units are conformably overlain by the Campanian-Thanetian Akveren Formation, which

grades into the Thanetian-Ilerdian marl and shale Atbaşı Formation. Across the Istanbul Zone, there is a lower Eocene unconformity (Özcan et al., 2012). Deposition resumes with the Ypresian Çaycuma Formation flysch series, which is unconformably overlain by the early Lutetian shallow marine limestone Yunuslubayır Formation (Özcan et al., 2012).

4.2.3.2 Intra-Pontide Suture

Akbayram et al. (2016) identified seven Late Cretaceous-Eocene sedimentary units within the Intra-Pontide suture zone near Geyve and Pamukova (Figure 4.2) and presented a refined stratigraphy with new paleontologic ages (Figure 4.3): the Upper Cretaceous Gemlik Mélange comprising blocks of ophiolite, metasediments and limestone in a graywacke-phyllite matrix, the Cenomanian–Santonian Vezirhan Formation containing pelagic limestone and shale, and the Maastrichtian neritic Taşlıtepe Limestone unit. The following four units are possibly conformable in some locations: the Campanian-Maastrichtian Osmanyie Formation comprised of clastic rocks, debris flow deposits and limestone blocks, the Paleocene debris flows of the Kaşıkçılar Formation, the carbonate debris of the Kadirler Formation which is upper Paleocene to lower Eocene but Maastrichtian in age in places, and the lower Eocene the Bakacak Formation containing debris flows and flysch matrix (Akbayram et al., 2016). The tectonic setting of the IPS units is unclear, but Akbayram et al. (2016) states that the Osmaniye Fm was deposited in a “tectonically active basin, possibly a foredeep” and the Kadirler Fm is a mélange formed during subduction of the Intra-Pontide Ocean.

4.2.3.3 Armutlu Peninsula

The Armutlu Peninsula stratigraphy (Figure 4.3) includes the Campanian basal deep marine clastic, debris flow and proximal siliciclastic flysch sequence of the Osmaniye Formation,

which is in tectonic contact with the Istanbul Zone metamorphic basement (Özcan et al., 2012). The Osmaniye Formation was deposited in a forearc sub-basin separated from the northern Yemişliçay Group by a forearc ridge (Özcan et al., 2012). The Campanian-Paleocene pelagic limestone Akveren Formation in the north passes laterally into the clayey limestones, marls and calciturbidites of the Üreğil Formation (Özcan et al., 2012). The Paleocene strata are unconformably overlain by the Ypresian-Lutetian shallow marine clastic Çaycuma Formation which, in some places, is capped by andesitic volcaniclastics. The Armutlu Peninsula was originally considered part of the Sakarya Zone (Yiğitbaş et al., 1999), yet correlation of sedimentary, plutonic metamorphic units along the IPS place the Armutlu Peninsula in the Istanbul Zone (Okay et al., 2008; Akbayram et al., 2016).

In the south, the Yemişliçay Group is absent and the Akveren Formation unconformably overlies Triassic and older units (Özcan et al., 2012). The Akveren Formation contains pelagic limestones and coarse-grained turbidites and is disconformably overlain by the Ypresian-Lutetian shallow marine Çaycuma Formation (Özcan et al., 2012).

4.2.3.4 Sakarya Zone

The main sedimentary basin of the Sakarya Zone is the Central Sakarya Basin (CSB). The Jurassic through Lower Cretaceous CSB series includes platform carbonates, calciturbidites and interbedded volcaniclastics (Altiner et al., 1991; Genç and Tüysüz, 2010). Overall, the Upper Cretaceous flysch deposits are unconformably overlain by Paleocene-Eocene molasse deposits (e.g., Okay et al., 2001; Açıkalın et al., 2016; Ocakoğlu et al., 2018). The Upper Cretaceous-Eocene deposits record closure of the southern Neotethys Ocean and progressive collision along the İzmir-Ankara-Erzincan suture zone (Figure 4.1; Okay et al., 2001; Ocakoğlu et al., 2007, 2018; Açıkalın et al., 2016; Chapter 3). The southern CSB transitions from a forearc to foreland basin

fed by north-flowing drainage systems (Ocakoğlu et al., 2018; Chapter 3). In the northern CSB, slide blocks in the Maastrichtian-Paleocene flysch were derived from the Intra-Pontide suture (Di Rosa et al., 2019). Basement-involved deformation was active by the Eocene, during which the Tuzaklı-Gümele Thrust partitioned the CSB and formed the broken foreland Sarıcakaya Basin (SB).

Upper Cretaceous through Eocene sedimentary units crop out north of Bursa in the Sakarya Zone (Figure 4.2). Upper Cretaceous rocks unconformably overlie Jurassic limestones or the Permian-Triassic Karakaya Complex; the Turonian-Santonian Vezirhan Formation of the Gölpazarı Group consists of basal conglomerate and sandstone units and overlying pelagic limestone which passes into the Gölpazarı Group flysch (Özcan et al., 2012). The Lower Eocene series, first defined by (Genç, 1986), includes the Ypresian terrigenous conglomerates of the Kuşkayası Formation, Ypresian (middle Cuisian) shallow marine clastics and limestones of the Fındıcak Formation, Ypresian-Lutetian andesitic lava flows of the Sarıkaya Formation, Lutetian fluvial clastics of the Dürdane Formation, and Lutetian volcaniclastic, sandstone and shallow marine limestones of the Müslümsölöz Formation (Özcan et al., 2012).

In a regional correlation of Bursa region of the Sakarya Zone, Armutlu Peninsula, and Kocaeli Peninsula (Figure 4.2), Özcan et al. (2012) suggest that the Santonian-Campanian and younger units are laterally continuous across this entire region. Transgressive sedimentary sequences across the IPS support at pre-Santonian collision between the Sakarya and Istanbul Zones (Özcan et al., 2012; Akbayram et al., 2016; Marroni et al., 2020). This implies that the strata in the Bursa region are part of the Central Sakarya Basin and, by extension, that the Kocaeli and Central Sakarya Basins were connected from the Upper Cretaceous through Eocene. We tentatively consider the Bursa region stratigraphy as the western CSB.

4.3 Analytical Methods

This study presents new sedimentary provenance data from across the Istanbul Zone. Samples were collected from Late Cretaceous-Eocene sedimentary units in the western CSB (Bursa region), Armutlu Peninsula, Intra-Pontide suture zone near Geyve, and the Kocaeli Peninsula (Figure 4.2).

4.3.1 Detrital Zircon Geochronology

The 12 new detrital zircon samples (Table 4.1) were collected from the Bursa region of the Central Sakarya Basin, the Armutlu Peninsula, and the Intra-Pontide Suture Zone. Samples were also collected from the Kocaeli Peninsula but are not included in the results and discussion at this time (Figure 4.3). The samples were processed following standard procedures for detrital heavy mineral separation, including mechanical crushing and density and magnetic separation. The grain size of analyzed grains was not measured directly but ranged from silt- to sand-sized in most samples. Zircons were mounted with reference materials in 25-mm epoxy cups and imaged with a TFS Apreo-S with Lovac Scanning Electron Microscope (SEM). The samples were analyzed in two labs at two different times. Samples from the Intra-Pontide suture (i.e., '17IST' samples) were first analyzed at the University of Washington TraceLab using an iCAP RQ quadrupole ICP-MS coupled to a Photon Machines AnalyteG2 excimer laser ablation system. Analyses were performed using a 25-μm beam diameter and were normalized against the Plešovice zircon (337 Ma; Sláma et al., 2008) and a suite of secondary reference materials (Table A.1). In addition, the 'CC' samples and additional zircons from the '17IST' samples were analyzed at CEREGE using an Element XR ICP-MS coupled to an ESI NWR213 laser ablation system using a 20-μm beam diameter and were calibrated against the same suite of reference materials. The data were reduced in *iolite* (Paton et

al., 2011) and an in-house MATLAB algorithm for updating age uncertainties according to current practices in U-Pb geochronology (see Shekut and Licht, 2020). Detrital zircon U-Pb ages are presented with 2-sgima measurement error and uncorrected for common lead; typical measurement uncertainties are 1%-4% and the systematic uncertainties are 1%-3%. All detrital zircon methods and data are included in the supporting information, including U-Pb ages corrected for common lead with the Andersen Routine of the VizualAge Data Reduction scheme (Chew et al., 2014).

Detrital zircon results are presented as histograms, pie charts, kernel density estimates and probability density functions (detritalPy: Sharman et al., 2018). We group the new Istanbul Zone samples by stratigraphic age and compare the results to published detrital zircon age spectra from the Istanbul Zone, Central Sakarya Basin, Sarıcakaya Basin, Karakaya Complex, and Central Sakarya Basement. Sample information is given in Table 4.1 and data are included in the supplemental data files.

Maximum depositional ages of the new detrital zircon samples were calculated using *detritalPy* (Sharman et al., 2018). Three maximum depositional ages are presented: the youngest single grain, the youngest cluster of 2 or more ages with overlapping 1-sigma uncertainties, and the youngest cluster of 3 or more ages with overlapping 2-sigma uncertainties (Table 4.2).

4.3.2 Sandstone Petrography

Modal sandstone compositions were determined using the Gazzi-Dickinson point counting method (Dickinson, 1985). Petrographic thin sections were prepared by National Petrographic Service, Inc. and by Alpine Vantage Geological Consulting, LLC. Between 384 and 437 points per slide were counted then plotted on ternary diagrams using *Triplot* (Graham and Midgley, 2000b). Ternary diagrams are interpreted using typical provenance source fields (Dickinson and

Suczek, 1979; Dickinson et al., 1983; Dickinson, 1985). Modal data are included in the supplemental data files.

4.3.3 Detrital Rutile Geochronology

4.3.3.1 Detrital Rutile as a Provenance Proxy for Accreted Terranes

Rutile is a durable and abundant heavy mineral in sedimentary rocks and preserves information about the last metamorphic cycle (Zack et al., 2004a). Detrital rutile as a provenance proxy is becoming more popular (Zack et al., 2004a; Meinhold, 2010; Okay et al., 2011; Triebold et al., 2012; Gaschnig, 2019; Odlum et al., 2019; Pereira et al., 2020) and is especially advantageous when tracking sediment flux from moderate- to high-temperature metapelitic and metabasic rocks (Zack and Kooijman, 2017). Rutile U-Pb, with a closure temperature of 490–640 °C (Kooijman et al., 2010), records cooling through greenschist facies conditions following higher grade metamorphism (Zack et al., 2004b; Kooijman et al., 2010; Zack and Kooijman, 2017). Therefore, detrital rutile is a promising sedimentary provenance proxy in forearc-foreland basin settings, like northwestern Anatolia, in which accreted terranes and exhumed accretionary prism units are thought to be a significant sediment source.

The lithologies of potential sediment sources must be considered when choosing which rutile grains to analyze. Rutile varies in U concentration depending on the metamorphic protolith: rutile from eclogites have, on average, 75% less U than those from metapelites (i.e., 5 ppm vs. 21 ppm; Meinhold, 2010). Some detrital rutile methods propose to first analyze trace elements in order to selectively filter out rutile grains with low U concentrations (ca. < 4-5 ppm; Zack et al., 2004; Okay et al., 2011; Rösel et al., 2019). Although filtering out low U rutile produces a higher proportion of concordant analyses and reduces U-Pb analytical times, it introduces bias into the provenance results: not analyzing low U rutile may introduce bias by not fully capturing sediment

flux from mafic sources. For example, when using a filter of [U] > 4 ppm, Rösel et al. (2014) determined that 94% of analyzed rutile were metapelitic in origin. This method may make sense for some studies based on the lithologies of potential sediment sources (e.g., Rösel et al., 2014). However, metamafic suture zone units, presumably with low U rutile, are expected to be a major contributor of detritus to northwestern Anatolian basins. Therefore, analyzing detrital rutile of all U concentrations offers the opportunity to reconstruct sedimentary provenance in forearc and accretionary tectonic settings.

4.3.3.2 Rutile Separation and EDS Imaging

In order to extract detrital rutile, all heavy mineral fractions from post-water table separation steps were recombined and reprocessed. Samples were first separated in heavy liquids (i.e., methylene iodide). The Frantz magnetic separator was set to 20° side slope and 20° forward slope such that rutile grains were separated into the 0.3 to 0.7 amp. fraction (Rosenblum and Brownfield, 2000). Rutile grains were handpicked with a Leica M205C binocular microscope using transmitted and polarized light. For samples with a small quantity of heavy mineral grains, rutile was picked from all 0.3 to >1.5 amp. magnetic fractions. Rutile grains were red-brown-yellow color in reflected light, red to opaque in plane polarized light, and displayed a resinous to vitreous luster; grains were well rounded to euhedral with many displaying twinning characteristic of rutile's tetragonal crystal system and striations parallel to the long axis. Grains were placed on Kapton tape and mounted in epoxy in 25-mm diameter cups. The mounts were polished to expose the internal structure of the grains.

Rutile mounts were carbon coated and imaged with a TFS Apreo-S with Lovac SEM with an energy-dispersive detector (EDS) to distinguish rutile grains from other spurious heavy minerals. The carbon coat was removed first with isopropanol and in an ultrasonic. The epoxy

mounts were polished again with 1 um and 0.25 um grit in felt. Samples were soaked in 2M nitric acid (HNO_3) in the ultrasonic, then in ultra-pure water in the ultrasonic.

4.3.3.3 Rutile U-Pb Analytical Protocol, Validation, and Data Reduction

Detrital rutile U-Pb geochronology and trace element analysis was conducted at the Isotope Geochemistry Lab at the University of Kansas using a Thermo Element2 magnetic sector field ICP-MS coupled to a Photon Machines AnalyteG2 excimer laser ablation system. We used a modified protocol from Rösel et al. (2019). Because metamafic rocks, which have low U concentrations, were suspected to be an important sedimentary source, we designed a protocol to maximize U sensitivity. We spent a significant amount of time tuning acquisition parameters and in the end opted for a beam diameter of laser beam diameter of 50 μm, running the secondary electron multiplier in 'both mode' to handle both the high U counts in the standards and low U counts in the unknowns, and using a long washout time of 15 seconds time to get a steady, low ^{238}U background. Rutile unknowns were calibrated against a suite of reference materials: R10 (Luvizotto et al., 2009), Wodgina (Ewing, 2011), 9826J (Kylander-Clark, 2008), LJ04-08 (Apen et al., 2020), and Kragerø (Kellett et al., 2018). The protocols reproduced the published ages of the reference materials (Figure A.1).

The data were reduced in *iolite 4* (Paton et al., 2011), calibrated against the R10 standard. Individual analyses with >15% discordance in $^{207}Pb/^{206}Pb$ ratios (Lippert, 2014) or abnormal patterns in raw signal intensity were excluded from analyses and interpretations but are included in the supplementary data files.

4.3.3.4 Discordance and Best Age Calculation

We encountered several complications in collecting, reducing, and interpreting the data, mostly revolving around low U and high common Pb concentrations. The incorporation of common (non-radiogenic) Pb and low initial U concentration which only decays to a small amount of radiogenic Pb, makes common Pb corrections important (Cherniak, 2000; Meinhold, 2010). Common Pb corrections use either measured ^{208}Pb (Zack et al., 2011) or isochrons on concordia diagrams (Tera and Wasserburg, 1972; Meinhold, 2010). Most of the analyzed detrital rutile are discordant and many have high concentrations of common Pb. An initial attempt at a ^{208}Pb correction increased the average discordance by 50% (following Odlum et al., 2019; M. Odlum, pers. comm., 2021). Therefore, we use the Tera-Wasserburg method to evaluate discordia arrays; results were plotted using IsoplotR (Vermeesch, 2018) with a $^{238}U/^{235}U$ value of 137.88 (Steiger and Jäger, 1977) and unanchored discordia linear regressions calculate the age of rutile populations.

4.4 Sedimentary Provenance Results

4.4.1 Detrital Zircon Results

4.4.1.1 Maximum Depositional Age

We present new detrital zircon ages (N=12, n=3114) from Late Cretaceous through Eocene strata and modern river sands in the Istanbul Zone (Figure 4.4; Table 4.1). The maximum depositional ages (MDAs) provide age constraint for 5 of the 10 pre-Quaternary samples (Table 4.2). For 5 samples (17IST01, 17IST05, 17IST03, CC083118-02, CC090118-02), the youngest zircons are ~40-150 Myr older than published biostratigraphic ages so do not offer additional age constraints (Özcan et al., 2012; Akbayram et al., 2016). For 3 of the samples (CC083118-07,

CC083118-06, CC090118-01), the three calculated MDA ages agree within 1-2 Myr and are aligned with published biostratigraphic ages (Özcan et al., 2012). Sample 17IST04 was collected from the lower Eocene Bakacak Formation (Figure 4.3) and has one zircon at 39.9 ± 1.4 Ma (1s) and the next youngest zircon is 109.7 ± 1.4 Ma (1s), and the youngest cluster with overlapping 1-sigma error gives an MDA of 145.1 ± 1.7 Ma (1s). Even though the MDA from the youngest single grain can be spurious (Dickinson and Gehrels, 2009), we accept a Ypresian age for sample 17IST04. Similarly, sample 17IST02 was collected from the Kadirler Fm and has a youngest single grain MDA of 52.7 ± 0.8 Ma (1s) and the youngest cluster with overlapping 1-sigma error gives an MDA of 65.5 ± 0.8 Ma (1s). Sample 17IST02 is important for provenance and geodynamic interpretations (cf. Section 4.5), therefore we prefer to conservatively consider this sample upper Paleocene-lower Eocene.

4.4.1.2 Istanbul Zone

The three Upper Cretaceous samples from the Armutlu Peninsula and IPS have a prominent age peak around 300-315 Ma, a broad 450-650 Ma peak, and a small proportion of zircons older than 650 Ma (Figure 4.4). The upper Paleocene-lower Eocene sample has a wide range of zircon ages, including a prominent 80 Ma peak, minor peaks around 50 Ma, 160 Ma, 235 Ma and 300 Ma, and a broad distribution of 400-800 Ma zircons. The two Lower Eocene samples have a prominent 315 Ma peak and smaller 150-175 Ma, 225-250 Ma, and 380 Ma peaks, and a range of Proterozoic age zircons, including 425-650 Ma grains. Additionally, these samples have very few Eocene grains (n=1/615), no Late Cretaceous grains, few Early Cretaceous grains (n=3/615). The Quaternary sample that was collected from a river draining Upper Cretaceous-Eocene strata in the Kocaeli Peninsula contains prominent peaks around 80 Ma, 300 Ma, 450 Ma, and 525-575 Ma; there is one Eocene zircon (54 Ma), and minor populations around 150 Ma and >800 Ma.

4.4.1.3 Western Central Sakarya Basin

Samples from the Bursa region of the Sakarya Zone are possibly the western Central Sakarya Basin (Figure 4.2; cf. Section 4.2.3.4). Upper Cretaceous through Eocene samples are characterized by zircon age peaks at 250 Ma and 325 Ma with minor populations around 425-475 Ma and 525-700 Ma (Figure 4.4). The Upper Cretaceous samples contain Late Cretaceous zircons and a minor proportion of ca. 900 Ma and 1800 Ma zircons. Two samples, CC090118-01 (Santonian) and CC083118-06 (Ypresian) have a minor Jurassic age peak. The Eocene samples have a large proportion of early Eocene age zircons. Additionally, the modern river sample and Santonian sample contain a small proportion of Devonian age zircons.

4.4.1.4 Age Signature of Potential Sediment Sources

The new detrital zircon samples are grouped into broad age bins by geographic region (Figure 4.5). The sample groups are used to compare with compilations of detrital and bedrock zircon U-Pb ages from northwest Anatolia (cf. Chapter 3; Table 4.1; Figure 4.5). In short, Carboniferous-Ordovician sedimentary rocks from the Istanbul Zone are characterized by a ~350 Ma peak and a broad 450-675 Ma peak (Ustaömer et al., 2011; Okay et al., 2011; Okay and Topuz, 2017). Ustaömer et al. (2016) demonstrate that Triassic sandstones from the Kocaeli Peninsula have abundant Carboniferous (297-339 Ma) and Neoproterozoic (554-655 Ma) populations and no Triassic-aged zircons. Outcrops of the Istanbul Zone basement (i.e., Bolu Massif) contain Triassic intrusions. The main Central Sakarya Basement is characterized by 300 Ma, 400 Ma and 475 Ma populations with minor >500 Ma ages (Ustaömer et al., 2012; Mueller et al., 2019; Chapter 3). The Karakaya Complex has a characteristic doublet around 235 and 325 Ma (e.g., Ustaömer et al., 2016). In the main Central Sakarya Basin, Turonian-Lower Campanian (>76 Ma) samples are characterized by a Late Cretaceous peak (110-76 Ma) and the absence of >150 Ma zircons; both

the middle Campanian-Maastrichtian and Paleocene-Eocene groups have 325 Ma and 400 Ma peaks as well as Late Cretaceous and Eocene peaks (depending on sample age). The Sarıcakaya Basin samples are similar to the middle Campanian through Eocene CSB samples, except the SB samples have a slightly larger proportion of the populations centered around ca. 175 Ma, 235 Ma, 425 Ma, 600 Ma, 1000 Ma, 2000 Ma, and 2650 Ma.

One significant complication is that the potential sediment sources in the Istanbul and Sakarya Zone have similar age peaks (Figure 4.5). The sediment sources can be parsed with careful consideration. The Central Sakarya Basement and Karakaya Complex on the Sakarya Zone have the same Triassic, Carboniferous and Proterozoic age peaks that are present in the Paleozoic strata and basement units in the Istanbul Zone. The main distinctions are the presence of Devonian ages in the Central Sakarya Basement, the Neoproterozoic peak (ca. 600 Ma) and minor Mesoproterozoic ages (ca. 1200-1600 Ma) in the Istanbul Zone Proterozoic sedimentary rocks. The Ordovician intrusions in the Istanbul Zone are not captured in the included published ages but are present in the Istanbul Zone basement (Chen et al., 2002; Ustaömer et al., 2005; Okay et al., 2008; Akbayram et al., 2013).

4.4.2 Sandstone Petrography Results

The five new Istanbul Zone samples plot within the recycled orogen field and are dominated by sedimentary lithics (Figure 4.6). There does not appear to be a temporal trend in sandstone composition. The sandstone petrography results demonstrate sediment recycling during the Late Cretaceous through Eocene.

4.4.3 Preliminary Detrital Rutile Results

Preliminary results from 4 Ypresian samples from the Sarıcakaya Basin are depicted on a Tera-Wasserburg diagram (Figure 4.7a). When plotted together, one age population around 187 Ma, defined by 176 rutile ages, becomes apparent, in addition to a small number of Paleozoic rutile grains. Figure 4.7b depicts one Ypresian sample from the Central Sakarya Basin (18YEN05) and two Ypresian samples from the western Central Sakarya Basin (CC083118-06 and CC083118-07). These preliminary results suggest dissimilar sediment sources in the SB, CSB and western CSB in Ypresian times. Both the CSB and western CSB samples appear to have a more diverse population of Paleozoic-Proterozoic and late Mesozoic ages. The dissimilarity of the western CSB samples to the SB and CSB could be due to lateral changes in sediment source terranes across the CSB or because the western CSB deposits do not belong to the CSB.

The preliminary results highlight two important findings regarding the utility of detrital rutile as a sedimentary provenance proxy. First, detrital rutile grains from northwest Anatolia have low U concentrations, and a 4-5 ppm U concentration filter would remove most analyses. Even though rutile grains with low U and high Pb are discordant, calculating ages using discordia offers a promising avenue forward. This introduces a second important finding: increasing the samples size highlights the need for an objective method to select sub-group populations. Figure 4.7c displays results from sample 16SKY37, including the discordia linear regression for all Mesozoic-aged rutile grains and two sub-group populations. The sub-groups were chosen by visually inspecting the Tera-Wasserburg diagram.

The path forward is to use the trace element composition of detrital rutile to differentiate sediment sources. Trace element data was collected to better differentiate age populations (^{49}Ti, ^{51}V, ^{53}Cr, ^{56}Fe, ^{66}Zn, ^{69}Ga, ^{89}Y, ^{90}Zr, ^{93}Nb, ^{95}Mo, ^{118}Sn, ^{121}Sb, ^{177}Hf, ^{181}Ta, and ^{182}W). In addition

to using trace element compositions to distinguish age populations, the data can also be used to gather information about the source rock. The Cr/Nb ratio is demonstrated to be an effective proxy to distinguish mafic from pelitic sources (Zack et al., 2004b; Meinhold, 2010; Triebold et al., 2011, 2012) and Zr concentrations can be used to calculate Zr-in-rutile thermometry estimates which can further elucidate the thermal history of sediment sources (e.g., Zack et al., 2004b; Tomkins et al., 2007; Meinhold et al., 2008; Triebold et al., 2012).

4.5 Sedimentary Provenance Interpretation

4.5.1 Late Cretaceous Sedimentary Provenance

The detrital zircon age spectra from the Late Cretaceous Istanbul Zone (both the IPS and Armutlu Peninsula), western CSB, and (main) CSB differ in several important ways (Figure 4.5). First, the Turonian-Santonian CSB samples are dominated by Late Cretaceous aged zircons whereas the Turonian-Santonian western CSB samples have a wide range of zircon ages, including a doublet around 235 and 325 Ma. Therefore, the western CSB and main CSB were either not part of the same basin or had significantly different sediment sources along-strike. The western CSB samples have age spectra similar to the Karakaya Complex and Central Sakarya Basement which is likely from uplift and recycling within the Sakarya Zone (cf. Chapter 3). Second, in the Campanian-Maastrichtian, the CSB remains dominated by Late Cretaceous zircons with minor Carboniferous and Devonian peaks with minor Proterozoic ages, and the IST samples have a different age spectrum, consisting of Carboniferous and Neoproterozoic peaks. The appearance of Carboniferous, Devonian and Proterozoic grains in the CSB in the middle Campanian was previously interpreted as uplift, exhumation and sediment recycling near the İAES due to incipient collision along the İAES (Chapter 3). The absence of Late Cretaceous zircons confirms that the

IST forearc basin was isolated from the magmatic arc by a broad ridge (Özcan et al., 2012). The sediment recycling signature of the sandstone petrography results and the prominent Neoproterozoic age peak in the Late Cretaceous IST samples suggests that Paleozoic strata were unroofed and recycled in the Late Cretaceous. The sandstone compositions do not indicate that sediment was derived directly from the IST basement. Carboniferous igneous and metamorphic rocks are absent in the IST, therefore their presence in Paleozoic strata is interpreted as evidence for the Carboniferous-Triassic juxtaposition of the Sakarya and Istanbul Zones (Akdoğan et al., 2020). The included IST Paleozoic strata are older than 325 Ma, and therefore do not capture the middle Carboniferous event. In any case, the presence of the Carboniferous age peak in the Late Cretaceous IST samples is likely derived from reworked Carboniferous-Triassic sedimentary units. The Paleozoic samples contain a ca. 350 Ma peak that is absent in the Late Cretaceous IST samples, which could be a result of sampling bias. The dissimilarity of the Late Cretaceous IST and CSB detrital zircon spectra indicates that the Sakarya and Istanbul Zones drainage networks were not connected in the Late Cretaceous.

4.5.2 Paleocene-Eocene Sedimentary Provenance

The dissimilarity of Paleocene-Eocene detrital zircon ages for the IST, western CSB and CSB indicate that there were not similar sediment sources at that time (Figure 4.5). The zircon age spectra from the CSB and western CSB display no major provenance shifts from the middle Campanian through Eocene. The CSB and western CSB differ in their proportions of Late Cretaceous and Eocene aged zircons. Additionally, the CSB has Carboniferous and Devonian age peaks characteristic of the Central Sakarya Basement whereas the western CSB appears more similar to the Karakaya Complex; neither have the Proterozoic ages characteristic of the Istanbul Zone. The preliminary detrital rutile results also display different age populations for the main and

western CSB (Figure 4.7). This does not preclude that the western CSB was disconnected from the CSB as east-west differences in uplift and exhumation patterns could have differentially exposed older Sakarya Zone units.

Unlike the CSB samples, the IST samples display a major provenance shift from the Maastrichtian to Paleocene-Eocene. The Paleocene-Eocene samples still plot in the recycled orogenic field (Figure 4.6), yet Cretaceous, Jurassic, Triassic and Ordovician aged zircons appear (Figure 4.5). The IST samples differ from the Sakarya Zone samples in the proportion of Eocene, Triassic, Devonian, and Ordovician and older zircon populations. The larger proportion of Ordovician and Meosproterozoic zircons in the IST samples suggests that an IST sediment source is more likely than a Sakarya Zone source. Given that the Istanbul and Sakarya Zones were connected until Late Triassic rifting (e.g., Marroni et al., 2020), it is not surprising that similar zircon ages appear in sedimentary units across the suture zone. Unlike other Tethyan collision for which the appearance of upper plate detritus on the lower plate is a marker of collision (e.g., Wang et al., 2011), this method is not an unequivocal marker of intercontinental collision along the IPS.

Even still, the major provenance shift in the IPS samples records uplifts and exhumation along the IPS. The Paleocene-Eocene IST samples are most similar to the SB. However, the provenance results from the intervening CSB do not indicate that the IST, CSB and SB were connected in one sedimentary basin system. Therefore, the similarly of the IST and SB samples, especially with respect to Triassic-Carboniferous age zircons, likely reflects the input of sediment from accretionary prism units. Jurassic age plutons are present in the Intra-Pontide suture and were metamorphosed to greenschist facies in the Early Cretaceous (Marroni et al., 2020). Furthermore, the Triassic IST units present in the IPS are considered the conjugate margin of the Karakaya

Complex which crops out in the İzmir-Ankara-Erzincan suture. The similarity in IST and SB samples likely reflects the uplift and erosion of the suture zone.

4.6 Collision at the Intra-Pontide Suture

4.6.1 Timing of IPS Closure

The Intra-Pontide Ocean formed during Late Triassic rifting between the Istanbul and Sakarya Zones (e.g., Göncüoğlu et al., 2014). Intra-oceanic subduction began in the Late Jurassic-Early Cretaceous (155-135 Ma: Akbayram et al., 2013; Göncüoğlu et al., 2014; Marroni et al., 2020), coeveal with supra-subduction zone ophiolite formation (Marroni et al., 2020 and references therein). Early Cretaceous metamorphism (135-119 Ma) during the accumulation of subduction-accretion complexes (e.g., Okay et al., 2006; Marroni et al., 2020) was closely followed by Albian underplating and basal accretion along the subduction interface (Aygül et al., 2016). Increased sediment flux to the trench forced Turonian exhumation of HP/LT metamorphic rocks in the forearc (Aygül et al., 2016) and coincided with Black Sea basin extension (Görür, 1988; Okay et al., 2013; Okay and Nikishin, 2015). We tentatively suggest that this forearc extensional regime set the stage for Late Cretaceous forearc basin partitioning as inferred from an unconformity related to a forearc ridge (Özcan et al., 2012) and dissimilar detrital zircon results across the forearc (Figure 4.4). In the Campanian-Maastrichtian, the limestone, shale and debris flow deposits containing ophiolitic and limestone clasts were deposited in the Istanbul Zone forearc basin, which was disconnected from the magmatic arc along the Black Sea coast (Özcan et al., 2012). Recycling of Paleozoic strata could have taken place along the ridge that separated the forearc basin from the volcanic arc (Özcan et al., 2012; this study). The regional transgression

of late Campanian-Paleocene IST sedimentary units connected the two forearc sub-basins (Özcan et al., 2012), but did not reach the Sakarya Zone (Özcan et al., 2012; this study).

In Paleocene-Eocene times, the appearance of Jurassic and Triassic aged zircons suggests the exhumation and erosion of accretionary prism units and the appearance of Ordovician aged zircons suggests IST basement exposure. The provenance data presented here do not indicate sediment flux from the IST into the CSB in the Paleogene. However, olistostromes of IPS accretionary prism material are found in Paleocene CSB deposits (Di Rosa et al., 2019). There was a late Paleocene-early Eocene unconformity across the Istanbul Zone (Özcan et al., 2012) and early Eocene units record exhumation, uplift and erosion of the accretionary prism and basement units (this study). During the middle to late Eocene, Lutetian and older sedimentary units were folded and thrusted in the IPS region and Istanbul Zone basement rocks were thrust over lower Eocene sedimentary units; at the same time, Paleozoic sedimentary units were back-thrusted over Late Cretaceous arc rocks in the Kocaeli Peninsula in a north-south shortening regime (Akbayram et al., 2016). Sediment recycling, accretionary prism uplift, a regional unconformity, and thin- and thick-skinned deformation indicate that collision occurred in the Paleocene.

4.6.2 Geodynamic Mechanisms of Collision in Western Anatolia

Resolving western Anatolian geodynamics is particularly difficult due to synchronous subduction and collision at the İzmir-Ankara-Erzincan suture and Intra-Pontide suture and late Cenozoic deformation along the North Anatolian Fault. A refined chronology of İAES suturing indicates that collision at 76 Ma was marked by accretionary prism uplift and exhumation and the recycling of pre-collisional forearc strata, yet significant upper plate deformation was delayed by ca. 20 Myr (Chapter 3: Mueller et al., in review). One mechanism to explain this delay is relict basin closure (Cowgill et al., 2016; Chapter 3: Mueller et al., in review). Collisional stress

transferred through the lithosphere and taken up by the closure of relict basins would delay collisional deformation in the upper plate (Cowgill et al., 2016). The chronology of suturing presented for the IPS in this study is compatible with relict basin closure. Unlike the İAES, accretionary prism uplift, sediment recycling, and thin- and thick-skinned deformation occur nearly simultaneously at the IPS. Without another upper plate relict basin to mitigate the stress of IPS closure, collision processes occurred all together instead of over a 20 Myr period. This means that nearby subduction zone systems and relict basins play an important role in controlling the tempo and style of continental collisions.

4.7 Conclusion

Anatolia is a complex mosaic of terranes whose chronology of accretion and collision are debated. In western Anatolia in particular, there are up to 5 separate continental fragments that accreted and collided throughout the Mesozoic-Cenozoic (e.g., Şengör and Yilmaz, 1981; Moix et al., 2008; Pourteau et al., 2016). Therefore, Anatolia is an ideal location to resolve how subduction and collision dynamics evolve in systems with coeval and geographically close collisions. It is hypothesized that collisional deformation from the main Neotethyan suture, the İzmir-Ankara-Erzincan suture, was mitigated by concurrent relict basin closure along the Intra-Pontide suture zone. Due to the cycles of collision and rifting in the eastern Mediterranean continental domains, sediment recycling and the persistence of age populations prohibits definitive provenance reconstructions. Preliminary detrital rutile results indicate that this proxy is viable for tracing sediment flux in accretionary orogenies and future work is needed to differentiate sediment sources of similar age. Provenance results from the Intra-Pontide suture zone indicate accretionary prism uplift and exhumation was underway by the Eocene, supporting a Paleocene closure. Therefore,

collisional deformation from incipient collision at the İzmir-Ankara-Erzincan at 76 Ma was in part taken up by Intra-Pontide subduction. Paleocene closure at the Intra-Pontide suture resulted in accretionary prism uplift, exhumation and contractional deformation at the Intra-Pontide suture and coincided with the onset of basement-involved contractional deformation along the İzmir-Ankara-Erzincan suture. Close-proximity subduction systems and continental collisions exert a first-order control on the tempo and location of collision processes and therefore pose an exciting frontier for continued investigation.

Acknowledgements

We thank Çelik Ocakoğlu, Jan Westerweel, Scott Braswell, Pierre Deschamps, and Alison Duvall for field and lab assistance. We thank Andrew Kylander-Clark, Francisco Apen, Peter Downes and Margo Odlum for rutile reference materials and rutile methods discussions. This work was supported by NSF EAR-1543684 and the University of Washington Department of Earth and Space Sciences.

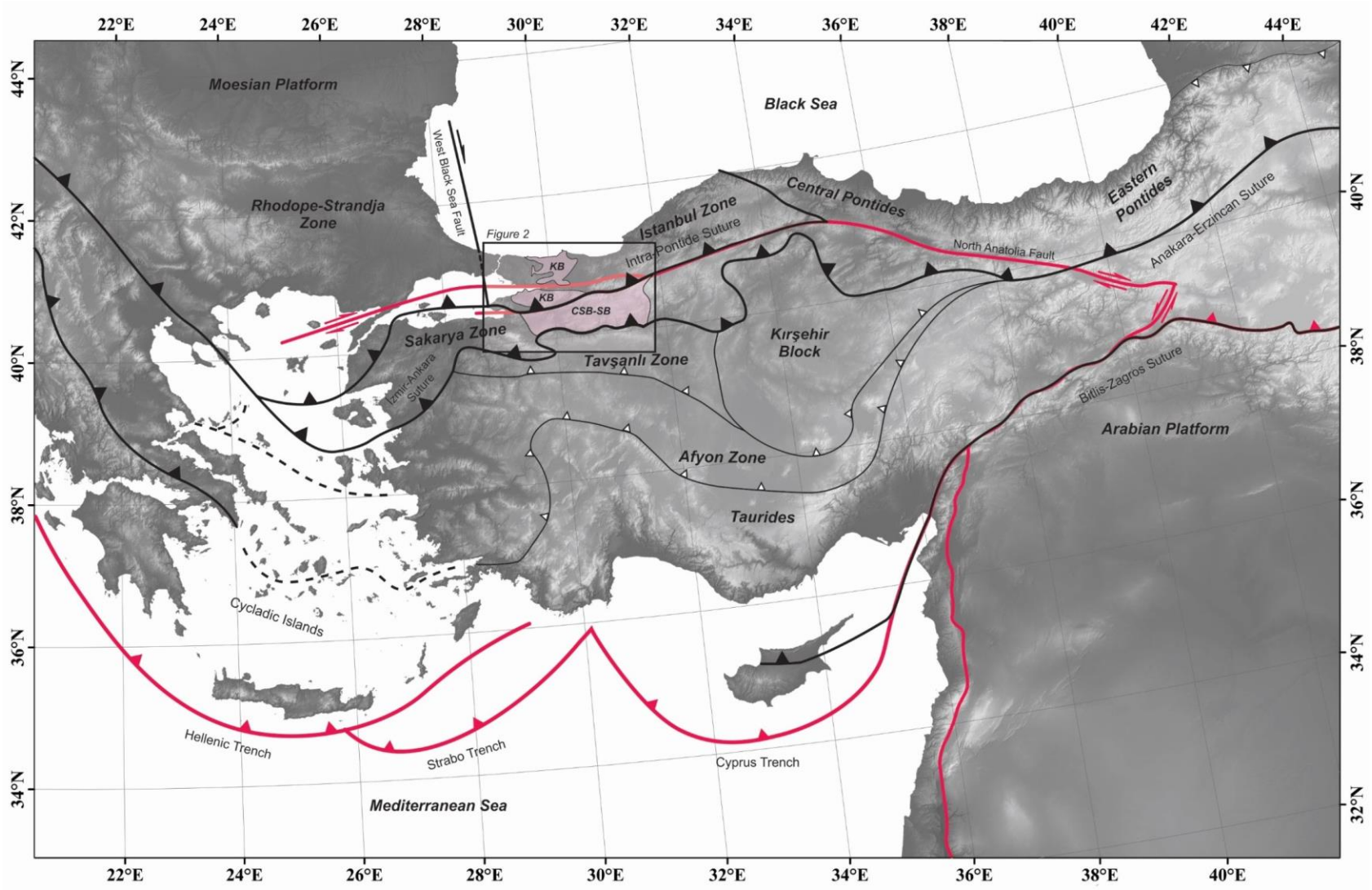

Figure 4.1. Simplified terrane map of Anatolia, modified from Campbell, 2017. The Kocaeli Basin (KB) and Central Sakarya-Sarıcakaya basin system (CSB-SB) are highlighted in pink. Active Quaternary faults are in dark pink.

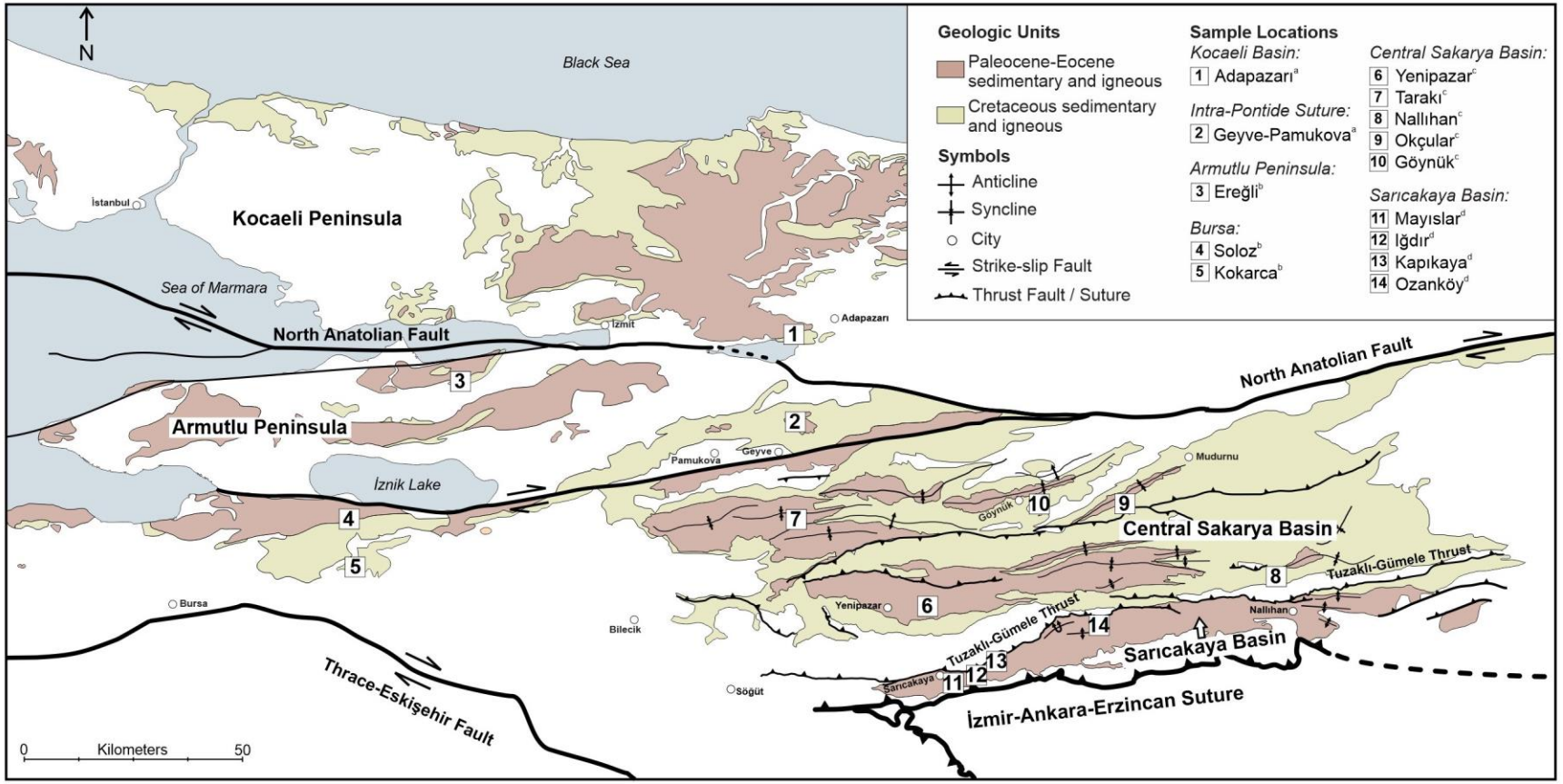

Figure 4.2. Simplified geologic map of northwest Anatolia depicting outcrops of Cretaceous-Eocene sedimentary and igneous units (after Aksay et al., 2002; Duru and Aksay, 2002; Gedik and Aksay, 2002; Timur and Aksay, 2002; Özcan et al., 2012). The southern strand of the North Anatolian Fault occupies the Intra-Pontide suture. Samples were collected from published stratigraphic sections ([a]Akbayram et al., 2016; [b]Özcan et al., 2012; [c]Ocakoğlu et al., 2018; [d]Mueller et al., 2019). See Figure 4.1 for location.

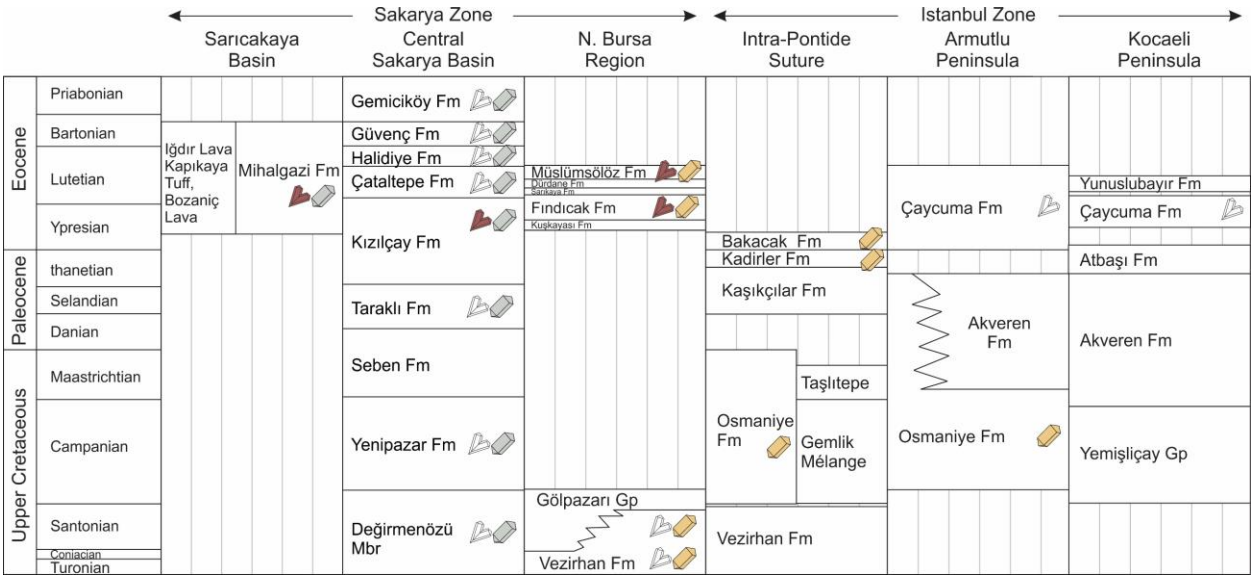

Figure 4.3. Stratigraphic correlation chart for northwest Anatolia. New detrital rutile (red: included in this study; see main text) and new (yellow) and published (gray) detrital zircon samples are depicted schematically. The new modern river samples are not shown. (Stratigraphy after Özcan et al., 2012; Yildiz et al., 2015; Akbayram et al., 2016; Ocakoğlu et al., 2018; Mueller et al., 2019).

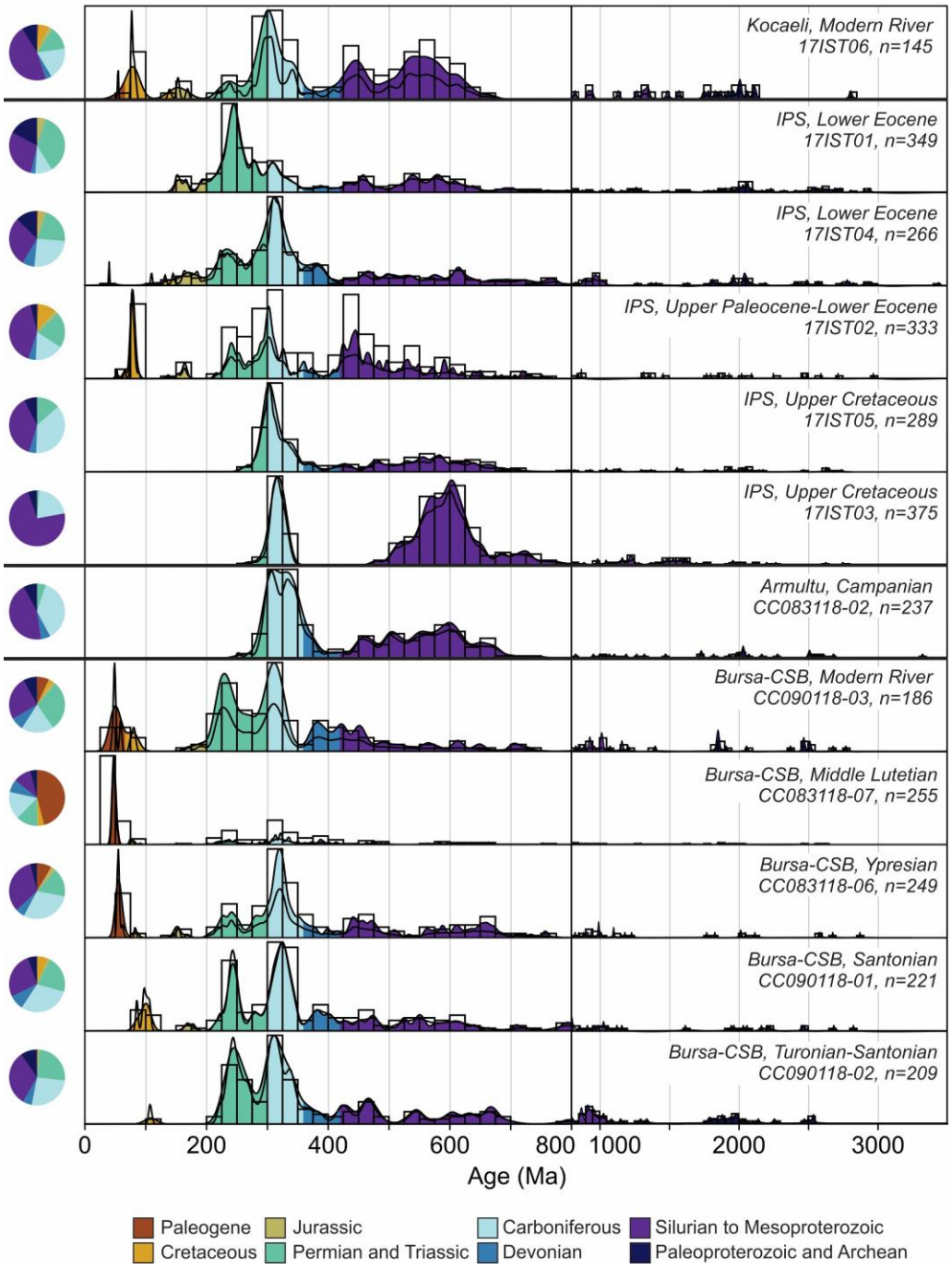

Figure 4.4. New detrital zircon results plotted as histograms (<800 Ma, 25 Myr bins; >800 Ma, 50 Myr bins), pie charts, probability density functions (black lines) and optimized fixed bandwidth kernel density estimates (colored shading). The samples are grouped by geographic location and ordered by age. Data were plotted with *detritalPy* (Sharman et al., 2018).

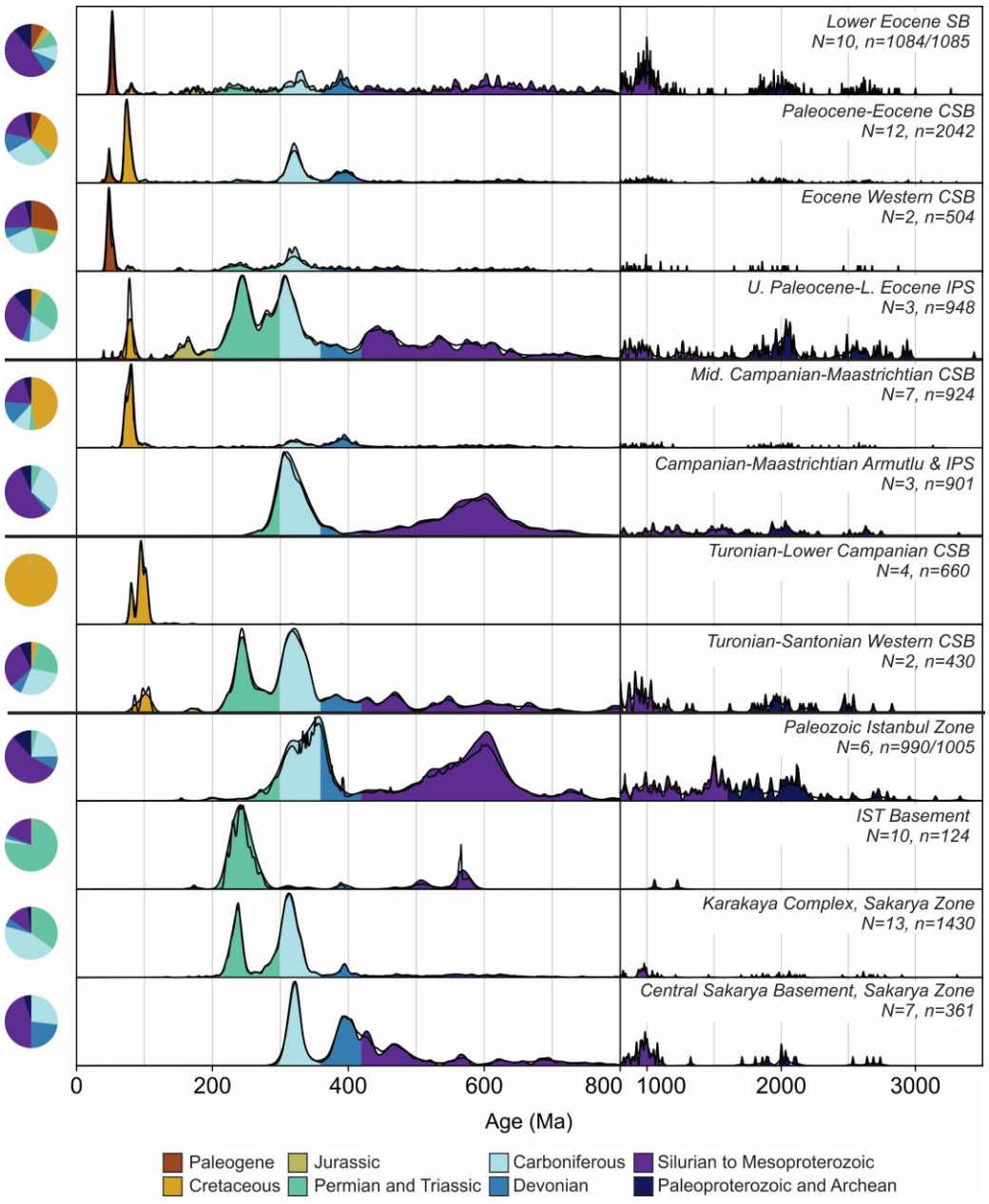

Figure 4.5. Comparison of zircon ages across northwest Anatolia. Individual samples are grouped together by age, and age groups are ordered from oldest (bottom) to youngest (top). All zircon ages 0-3500 Ma are displayed as pie charts, probability density functions (black lines) and optimized fixed bandwidth kernel density estimates (colored shading). Note the y-axis scale jump at 800 Ma. Data were plotted with detritalPy (Sharman et al., 2018). References for published samples are given in Table 4.1.

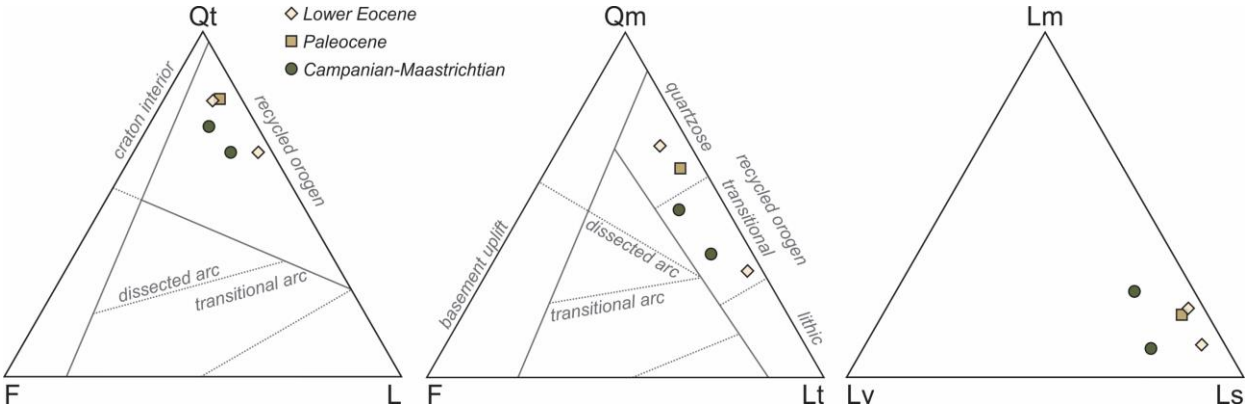

Figure 4.6. Ternary diagrams of IST sandstone modal compositions. Samples are colored by age. Poles: Qt: total quartz; Qm: monocrystalline quartz; F: feldspar; L: lithics; Lm: metamorphic lithics; Ls: sedimentary lithics; Lv: volcanic lithics; Lt: total lithics (L + polycrystalline quartz).

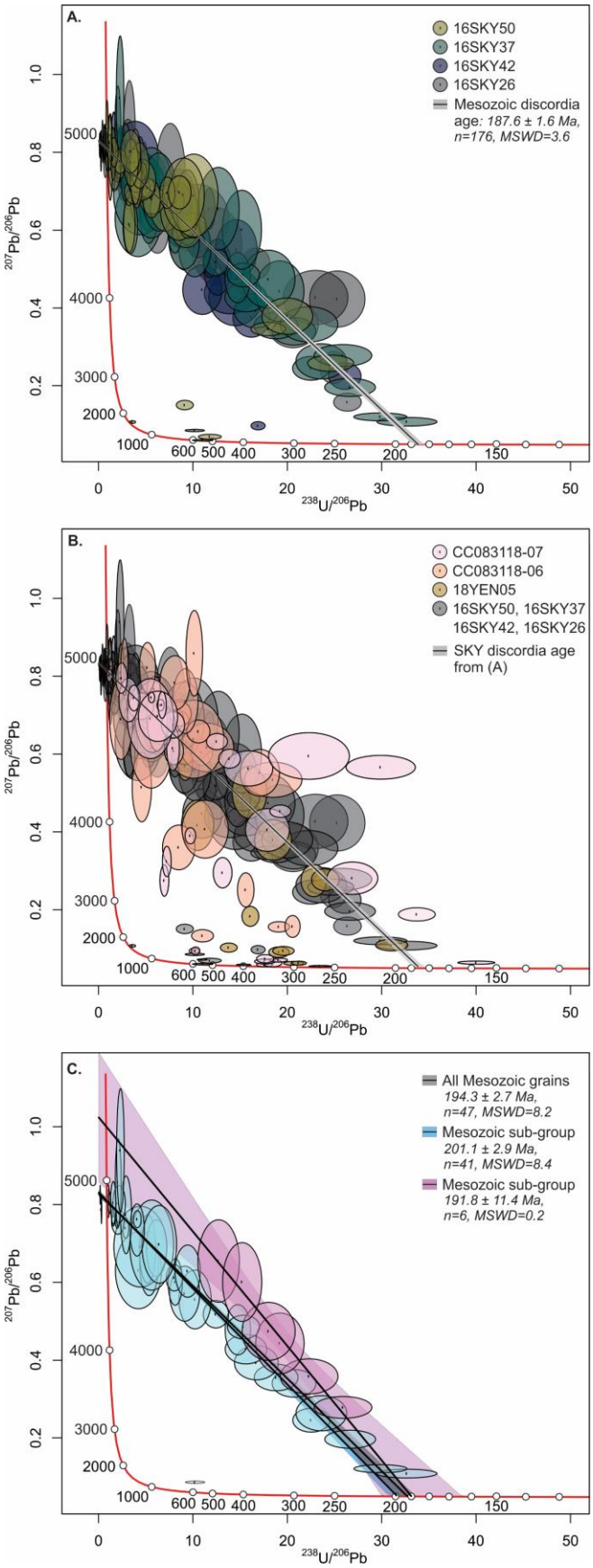

Figure 4.7. Detrital rutile results from Ypresian samples shown on Tera-Wasserburg diagrams. (A) A linear regression of discordant grains shows a cluster of Early Jurassic aged rutile grains in Ypresian samples from the Sarıcakaya Basin. (B) Ypresian samples from the Central Sakarya Basin (18YEN05) and the western Central Sakarya Basin (CC083118-06, CC083118-07) appear to have more diverse rutile populations than the Sarıcakaya Basin. (C) For detrital samples with potentially several age populations, choosing sub-groups of samples makes calculating ages from discordia arrays subjective.

Table 4.1. List of new and published zircon U-Pb samples ordered approximately from oldest (top) to youngest within groupings. Source column refers to data sources (1: P. Ustaömer et al., 2005, 2: P. Ustaömer 2011, 3: P. Ustaömer 2012, 4: T. Ustaömer 2016; 5: Okay et al., 2011; 6: Bozkurt et al., 2013; 7: Campbell, 2017; 8: Okay and Topuz, 2017; 9: Ocakoğlu et al., 2018; 10: Mueller et al., 2019, 11: Chapter 3: Mueller et al., in review). Data from this study are in the supplementary data files.

Sample Name	Unit	Sample Type	Category	Age	Data Source
New Samples					
17IST03	Osmaniye Fm	DZ	Intra-Pontide Suture	Camp.-Maast.	10
17IST05	Volcaniclastic SS	DZ	Intra-Pontide Suture	Camp.-Maast.	10
17IST02	Kadirler Fm	DZ	Intra-Pontide Suture	Paleocene	10
17IST01	Bakacak Fm	DZ	Intra-Pontide Suture	Lower Eocene	10
17IST04	Bakacak Fm	DZ	Intra-Pontide Suture	Lower Eocene	10
17IST06	Modern river sand	DZ	Intra-Pontide Suture	Quaternary	10
CC083118-02	Osmaniye Fm	DZ	Armutlu Peninsula	Campanian	10
CC090118-03	Modern river sand	DZ	Western CSB	Quaternary	10
CC083118-07	Müslümsölöz Fm	DZ	Western CSB	Middle Lutetian	10
CC083118-06	Fındıcak Fm	DZ	Western CSB	Ypresian	10
CC090118-02	Vezirhan Fm	DZ	Western CSB	Santonian	10
CC090118-01	Vezirhan Fm	DZ	Western CSB	Turonian	10
Published Basin Samples					
17MGB01	Değirmenözü Fm	DZ	Turonian to lower Campanian (main CSB)	Upper Aptian	9
18DMN01	Değirmenözü Fm	DZ	Turonian to lower Campanian (main CSB)	Santonian	9
CC082918-01	Yenipazar Fm	DZ	Turonian to lower Campanian (main CSB)	Turonian	9
18YP02	Değirmenözü Fm	DZ	Turonian to lower Campanian (main CSB)	Santonian-Campanian	9
CC082918-02	Taraklı Fm	DZ	Middle Campanian to Maastrichtian (main CSB)	Upper Camp.-Maastrichtian	9
18NAL13	Taraklı Fm	DZ	Middle Campanian to Maastrichtian (main CSB)	Upper Camp.-Maastrichtian	9
15GO02	Yenipazar Fm	DZ	Middle Campanian to Maastrichtian (main CSB)	Campanian	5,7
18NAL05	Yenipazar Fm	DZ	Middle Campanian to Maastrichtian (main CSB)	Middle Campanian	9
18NAL12	Yenipazar Fm	DZ	Middle Campanian to Maastrichtian (main CSB)	Upper Camp.-Maast.	9

15YP13	Yenipazar Fm	DZ	Middle Campanian to Maastrichtian (main CSB)	Maastrichtian	5
18TK01	Çataltepe Fm	DZ	Paleocene-Eocene (main CSB)	Paleocene-lower Eocene	9
18KIZ01	Kızılçay Fm	DZ	Paleocene-Eocene (main CSB)	Paleocene-lower Eocene	9
15YP15	Kızılçay Fm	DZ	Paleocene-Eocene (main CSB)	Paleocene-lower Eocene	9
15YP14	Kızılçay Fm	DZ	Paleocene-Eocene (main CSB)	Paleocene	5
18YEN05	Kızılçay Fm	DZ	Paleocene-Eocene (main CSB)	Paleocene-lower Eocene	9
18TB01	Taraklı Fm	DZ	Paleocene-Eocene (main CSB)	Paleocene-lower Eocene	9
18TBTG	Taraklı Fm	DZ	Paleocene-Eocene (main CSB)	Paleocene-lower Eocene	9
18YP03	Yenipazar Fm	DZ	Paleocene-Eocene (main CSB)	Lower Paleocene	9
17MGB02	Gemiciköy Fm	DZ	Paleocene-Eocene (main CSB)	Up. Lutetian-Low. Bartonian	9
18YEN01	Gemiciköy Fm	DZ	Paleocene-Eocene (main CSB)	Upper Bartonian-Priabonian	9
18YEN04	Güvenç Fm	DZ	Paleocene-Eocene (main CSB)	Lutetian	9
18HAL01	Halidiye Fm	DZ	Paleocene-Eocene (main CSB)	Lutetian	9
16SB26	Mihalgazi Fm	DZ	Lower Eocene (SB)	Ypresian-Lutetian	8
16SB23	Mihalgazi Fm	DZ	Lower Eocene (SB)	Ypresian	8
15YP08	Mihalgazi Fm	DZ	Lower Eocene (SB)	Ypresian-Lutetian	5
15YP09	Mihalgazi Fm	DZ	Lower Eocene (SB)	Ypresian-Lutetian	5
16SB37	Mihalgazi Fm	DZ	Lower Eocene (SB)	Ypresian-Lutetian	8
16SB42	Mihalgazi Fm	DZ	Lower Eocene (SB)	Ypresian-Lutetian	8
16SB50	Mihalgazi Fm	DZ	Lower Eocene (SB)	Ypresian-Lutetian	8
16SB04	Mihalgazi Fm	DZ	Lower Eocene (SB)	Ypresian	8
17OZK05	Mihalgazi Fm	DZ	Lower Eocene (SB)	Ypresian-Lutetian	8
17OZK12	Mihalgazi Fm	DZ	Lower Eocene (SB)	Ypresian-Lutetian	8
Published Pre-Mesozoic Samples					
17BASE01	Gneiss	Bedrock	Central Sakarya Basement	--	8
SgtMeta	Söğüt metamorphics	Metased. DZ	Central Sakarya Basement	--	2
090717-6	Paragneiss	Bedrock	Central Sakarya Basement	--	9
090717-16	Orthogneiss	Bedrock	Central Sakarya Basement	--	9
Catli	Söğüt magmatics	Bedrock	Central Sakarya Basement	Carboniferous	2
Kuplu	Söğüt magmatics	Bedrock	Central Sakarya Basement	Carboniferous	2
Borcak	Söğüt magmatics	Bedrock	Central Sakarya Basement	Carboniferous	2
K.12.102	Cambazkaya Fm	DZ	Karakaya Complex	Carnian–Norian	3
K.12.91	Cambazkaya Fm	DZ	Karakaya Complex	Carnian–Norian	3
KK.10	Kendirli Fm	DZ	Karakaya Complex	Carnian–Norian	3

15YP12	Greenschist	Metased. DZ	Karakaya Complex	--	5
K.12.42	Ortaoba Unit	DZ	Karakaya Complex	Carnian	3
K.12.43	Ortaoba Unit	DZ	Karakaya Complex	Carnian	3
K.12.45	Ortaoba Unit	DZ	Karakaya Complex	Carnian	3
K.12.63	Hodul Unit	DZ	Karakaya Complex	Norian	3
K.12.64	Hodul Unit	DZ	Karakaya Complex	Norian	3
K.12.65	Hodul Unit	DZ	Karakaya Complex	Norian	3
K.12.71	Hodul Unit	DZ	Karakaya Complex	Norian	3
K.13.44	Çal Unit	DZ	Karakaya Complex	Artinskian-Kungurian	3
K.13.91	Nilufer Unit	Metased. DZ	Karakaya Complex	Norian	3
Sample3	Trakya Fm	DZ	Istanbul Zone	Carboniferous	4
Sample8	Trakya Fm	DZ	Istanbul Zone	Carboniferous	4
Sample1B	Trakya Fm	DZ	Istanbul Zone	Carboniferous	4
Sample18	Trakya Fm	DZ	Istanbul Zone	Carboniferous	4
Sample3550	Alacaağzı Fm	DZ	Istanbul Zone	Late Carboniferous	6
Ustaomer2011	Quartzite	Metased. DZ	Istanbul Zone	Lower Ordovician	1
K.12.9	Bolu Massif	Bedrock	Istanbul Zone	Triassic	3
BY-1	Bolu Massif	Bedrock	Istanbul Zone	Triassic	6
Bozkurt30	Bolu Massif	Bedrock	Istanbul Zone	Triassic	6
EBII	Bolu Massif	Bedrock	Istanbul Zone	Triassic	6
D1	Bolu Massif	Bedrock	Istanbul Zone	Triassic	6
Y1A	Bolu Massif	Bedrock	Istanbul Zone	Triassic	6
R1	Bolu Massif	Bedrock	Istanbul Zone	Triassic	6
99-3B	Kapıkaya Pluton	Bedrock	Istanbul Zone	Triassic	1
99-5	Tüllükiriş Pluton	Bedrock	Istanbul Zone	Triassic	1
99-13	Sünnice Meta-granitoid	Bedrock	Istanbul Zone	Triassic	1

Table 4.2. Maximum depositional ages of the new detrital zircon samples calculated using *detritalPy* (Sharman et al., 2018). Depositional ages are calculated in three ways: the youngest single grain (YSG), the youngest cluster of 2 or more ages with overlapping 1-sigma uncertainties (YC1S), and the youngest cluster of 3 or more ages with overlapping 2-sigma uncertainties (YC2S). The two modern river sand samples are excluded.

Sample	N	YSG	1s err.	YC1S	1s err.	YC1S MSWD	YC1S cluster size	YC2S	1s err.	YC2S MSWD	YC2S cluster size
17IST01	349	150.0	2.7	151.0	1.4	0.2	4	153.4	1.1	1.5	7
17IST04	266	39.9	0.7	145.1	1.7	0.0	2	167.0	1.3	3.0	4
17IST02	333	52.7	0.8	65.5	0.8	1.4	2	77.1	0.3	1.0	17
17IST05	289	256.0	4.8	261.1	2.5	0.8	3	264.9	1.7	2.0	4
17IST03	375	266.0	5.6	271.5	3.9	1.9	2	300.5	1.3	1.6	8
CC083118-02	237	252.6	3.7	290.4	2.5	0.4	5	298.9	1.1	1.0	23
CC083118-07	255	42.5	0.8	43.2	0.3	0.6	7	44.3	0.2	1.2	21
CC083118-06	249	52.3	0.8	53.0	0.4	0.6	6	53.8	0.3	1.5	11
CC090118-01	221	84.5	1.6	85.5	1.0	0.3	3	85.5	1.0	0.3	3
CC090118-02	209	106.5	2.2	107.4	1.6	0.4	2	229.7	1.5	1.7	9

Chapter 5. The State of Tethyan Collisions

Since the recognition and wide acceptance of plate tectonics, decades of work have steadily advanced our understanding of convergent margin processes, including the interrelated links between tectonics, landscape evolution, global climate, and species evolution (Burbank et al., 1988; Royden and Burchfiel, 1989; Raymo and Ruddiman, 1992; von Blanckenburg and Davies, 1995; Beaumont et al., 1996; Yin and Harrison, 2000; Zeitler et al., 2001; Zachos et al., 2001; Rowley et al., 2001; Willett and Brandon, 2002; Clark et al., 2004; Ruhl and Hodges, 2005; Clift et al., 2008; Carrapa, 2009; Lippert et al., 2014; Ballato and Strecker, 2014; Goddéris et al., 2014; Licht et al., 2014; Caves et al., 2015; Beard, 2016). In the last two decades in particular, significant advances in geo-, petro- and thermochronologic methods and their widespread application have created a high-resolution temporal framework of convergent margin processes. The structural, metamorphic, magmatic, and sedimentary records of intercontinental collisions across the Alpine-Himalayan belt, for example, differ by 15-40 Myr. Consequently, new questions have arisen, including how to unite the structural, metamorphic, magmatic, and sedimentary evolution of individual subduction zones and their subsequent collisions into a temporally, spatially, and geologically credible reconstruction. A series of multi-stage collision models have been proposed as solutions to the protracted nature of Tethyan collisions.

The work set forth in this dissertation, in concert with contemporaneous work, situates the Anatolian segment of the Alpine-Himalayan orogenic belt in the broader discussion on the timescales, drivers and effects of intercontinental collisions. In fact, near-continuous deposition in western Anatolian sedimentary basins preserve an unbroken record of subduction through collision that is unparalleled across the Tethyan realm. The work included here includes stratigraphic,

sedimentologic, geochronologic and provenance constraints on the chronology of two suturing events in western Anatolia: collision along the İzmir-Ankara-Erzincan suture zone and collision along the Intra-Pontide suture zone.

Forearc and suture zone sedimentary strata from both suturing events reveal a similar basin response to initial intercontinental collision. Initial intercontinental collisions at the İAES and IPS are recorded as uplift, exhumation and sediment flux from the accretionary prism and sediment recycling (e.g., Açıkalın et al., 2016; Chapter 3 and Chapter 4). For the next 15 Myr along the İAES, as collision progressed, sedimentary basins record prograding deltas, transverse drainages, proximal angular unconformities, and increased sedimentation rates, (Ocakoğlu et al., 2018). The sedimentary basin changes were coeval with Barrovian metamorphism and subsequent exhumation (Seaton et al., 2009; Whitney et al., 2011) and a magmatic lull observed across the entire Pontides (Kasapoğlu et al., 2016; Schleiffarth et al., 2018; Mueller et al., 2019; Chapter 3). During this phase, the along-strike segment in the Central Pontides experienced oroclinal bending (Kaymakci et al., 2003; Meijers et al., 2010), lower plate deformation and rotation (Lefebvre et al., 2013), and foreland-propagating thrust belts, depocenters, and syntectonic unconformities (Kaymakci et al., 2009). Similar changes across the western and central Pontides support a synchronous İAES collision along-strike (van Hinsbergen et al., 2016; Gürer et al., 2016; Gürer and van Hinsbergen, 2018; Mueller et al., 2019: Chapter 2).

In the western Pontides, the İAES exhibits a distinct second phase of collision 20 Myr after initial collision. The main forearc-foreland basin was partitioned by a ~150-km long basement-involved thrust fault (Mueller et al. 2019: Chapter 2), and flexural loading from the fault formed a broken foreland sub-basin (Mueller et al. 2019: Chapter 2). Both thin-and thick-skinned deformation occurred within the forearc-foreland basin (Şahin et al., 2019; Mueller et al., 2019:

Chapter 2). Around the same time, deposition resumed in the proximal region of the main foreland basin and transitioned from flysch to molasse facies (Ocakoğlu et al., 2018), and magmatism resumed across the Pontides (Harris et al., 1994; Okay and Satir, 2006; Altunkaynak, 2007; Dilek and Altunkaynak, 2009; Yildiz et al., 2015; Kasapoğlu et al., 2016; Ersoy et al., 2017b, 2017a; Schleiffarth et al., 2018; Mueller et al., 2019). Lutetian marine deposition across the Pontides and Anatolides (e.g., Racey, 2001; MTA, 2002; Ocakoğlu et al., 2012; Lygina et al., 2016; Licht et al., 2017; Özcan et al., 2019) implies that, for at least 30 Myr following collision, continental landmasses remained near sea level and there was not significant topographic development. Future work is needed to resolve the timing and mechanisms controlling topographic development in collisions between small, accreted continental domains like Anatolia.

Reconstructing the evolution of continental collisions using the nearly uninterrupted depositional record of western Anatolian sedimentary basins can unify other proxies for collision into a consistent temporal framework. This dissertation has two main implications in terms of Tethyan geodynamics and biogeography. First, three, non-exclusive mechanisms proposed for collisions across the Tethyan realm can explain the protracted nature of Anatolian collisions: slab breakoff, relict basin closure, and subduction of progressively thicker lithosphere (cf. Chapter 3). Suturing at the Intra-Pontide suture during the second phase of İAES collision indicates that relict basin closure may be an important mechanism in transferring collisional stress through the lithosphere and delaying upper plate deformation (cf. Chapter 4). Second, the onset of terrestrial deposition on the Pontides occurred around 15 Myr after initial continental collision (Okay et al., 2001; Ocakoğlu et al., 2018), coinciding with the colonization of the Pontides by Laurasian and Gondwanan mammalian fauna (Kappelman et al., 1996; Sen, 2013; Métais et al., 2017; Jones et al., 2018; Beard et al., 2020). Even in the late stages of collision, the persistence of marine barriers

kept the Pontides isolated such that endemism remained (Maas et al., 2001; Licht et al., 2017; Métais et al., 2018). Therefore, topography in continental collision between small, accreted terranes takes millions of years to develop such that dispersals are perhaps related to other geodynamic or climatic mechanisms (e.g., Licht et al., 2014, 2017; Göğüş et al., 2017). Future work on the topographic and climatic evolution of western Anatolia is poised to advance our understanding of links between tectonics, geodynamics and biogeography.

Bibliography

Açıkalın, S. et al., 2015, Geochemical and palaeontological characterization of a new K-Pg Boundary locality from the Northern branch of the Neo-Tethys: Mudurnu – Göynük Basin, NW Turkey: Cretaceous Research, v. 52, p. 251–267, doi:10.1016/j.cretres.2014.07.011.

Açıkalın, S., Ocakoğlu, F., Yılmaz, İ.Ö., Vonhof, H., Hakyemez, A., and Smit, J., 2016, Stable isotopes and geochemistry of a Campanian–Maastrichtian pelagic succession, Mudurnu–Göynük Basin, NW Turkey: Implications for palaeoceanography, palaeoclimate and sea-level fluctuations: Palaeogeography, Palaeoclimatology, Palaeoecology, v. 441, p. 453–466, doi:10.1016/j.palaeo.2015.10.005.

Advokaat, E.L., van Hinsbergen, D.J.J., Kaymakcı, N., Vissers, R.L.M., and Hendriks, B.W.H., 2014, Late Cretaceous extension and Palaeogene rotation-related contraction in Central Anatolia recorded in the Ayhan-Büyükkışla basin: International Geology Review, v. 56, p. 1813–1836, doi:10.1080/00206814.2014.954279.

Agard, P., Plunder, A., Angiboust, S., Bonnet, G., and Ruh, J., 2018, The subduction plate interface: rock record and mechanical coupling (from long to short timescales): Lithos, v. 320–321, p. 537–566, doi:10.1016/j.lithos.2018.09.029.

Akbayram, K., Okay, A.I., and Satır, M., 2013, Early Cretaceous closure of the Intra-Pontide Ocean in western Pontides (northwestern Turkey): Journal of Geodynamics, v. 65, p. 38–55, doi:10.1016/j.jog.2012.05.003.

Akbayram, K., Sengor, A.M.C., and Ozcan, E., 2016, The evolution of the intra-Pontide suture; implications of the discovery of late Cretaceous-early Tertiary melanges: Geological Society of America, v. Special Paper 525, doi:10.1130/2016.2525(18).

Akdoğan, R., Hu, X., Okay, A.I., and Topuz, G., 2020, Provenance of the Paleozoic-Mesozoic siliciclastic rocks of the Istanbul Zone: Constraints on the location of the Rheic suture in Turkey: 22nd EGU General Assembly, p. 5706, doi:https://ui.adsabs.harvard.edu/#abs/2020EGUGA..22.5706A/abstract.

Akdoğan, R., Okay, A.I., and Dunkl, I., 2019, Striking Variation in the Provenance of the Lower and Upper Cretaceous Turbidites in the Central Pontides (Northern Turkey) Related to the Opening of the Black Sea: Tectonics, v. 38, p. 1050–1069, doi:https://doi.org/10.1029/2018TC005119.

Akdoğan, R., Okay, A.I., Sunal, G., Tari, G., Meinhold, G., and Kylander-Clark, A.R.C., 2017, Provenance of a large Lower Cretaceous turbidite submarine fan complex on the active Laurasian margin: Central Pontides, northern Turkey: Journal of Asian Earth Sciences, v. 134, p. 309–329, doi:10.1016/j.jseaes.2016.11.028.

Aksay, A., Pehlivan, Ş., Gedik, I., Bılginer, E., Duru, M., Akbaş, B., and Altun, I., 2002, Geologic map of Turkey (Zonguldak, Scale 1:500,000): Maden Tetkik ve Arma Genel Müdürlüğü.

Altiner, D., Kocyigit, A., Farinacci, A., Nicosia, U., and Conti, M.A., 1991, Jurrasic-Lower Cretaceous stratigraphy and paleogeographic evolution of the southern part of North-Western Anatolia (Turkey): Geologica Romana, v. 27, p. 13–80.

Altunkaynak, Ş., 2007, Collision-Driven Slab Breakoff Magmatism in Northwestern Anatolia, Turkey: The Journal of Geology, v. 115, p. 63–82, doi:10.1086/509268.

Altunkaynak, Ş., and Dilek, Y., 2006, Timing and nature of postcollisional volcanism in western Anatolia and geodynamic implications, *in* Special Paper 409: Postcollisional Tectonics and

Magmatism in the Mediterranean Region and Asia, Geological Society of America, v. 409, p. 321–351, doi:10.1130/2006.2409(17).

Altunkaynak, Ş., Sunal, G., Aldanmaz, E., Genç, C.Ş., Dilek, Y., Furnes, H., Foland, K.A., Yang, J., and Yıldız, M., 2012, Eocene Granitic Magmatism in NW Anatolia (Turkey) revisited: New implications from comparative zircon SHRIMP U–Pb and 40Ar–39Ar geochronology and isotope geochemistry on magma genesis and emplacement: Lithos, v. 155, p. 289–309, doi:10.1016/j.lithos.2012.09.008.

Alvarez, W., 2010, Protracted continental collisions argue for continental plates driven by basal traction: Earth and Planetary Science Letters, v. 296, p. 434–442, doi:10.1016/j.epsl.2010.05.030.

Apen, F.E., Rudnick, R.L., Cottle, J.M., Kylander-Clark, A.R.C., Blondes, M.S., Piccoli, P.M., and Seward, G., 2020, Four-dimensional thermal evolution of the East African Orogen: accessory phase petrochronology of crustal profiles through the Tanzanian Craton and Mozambique Belt, northeastern Tanzania: Contributions to Mineralogy and Petrology, v. 175, p. 97, doi:10.1007/s00410-020-01737-6.

Avdeev, B., and Niemi, N.A., 2011, Rapid Pliocene exhumation of the central Greater Caucasus constrained by low-temperature thermochronometry: Tectonics, v. 30, doi:10.1029/2010TC002808.

Aydin, F., Oğuz Saka, S., Şen, C., Dokuz, A., Aiglsperger, T., Uysal, İ., Kandemir, R., Karslı, O., Sarı, B., and Başer, R., 2020, Temporal, geochemical and geodynamic evolution of the Late Cretaceous subduction zone volcanism in the eastern Sakarya Zone, NE Turkey: Implications for mantle-crust interaction in an arc setting: Journal of Asian Earth Sciences, v. 192, p. 104217, doi:10.1016/j.jseaes.2019.104217.

Aygül, M., Okay, A.I., Oberhänsli, R., and Sudo, M., 2016, Pre-collisional accretionary growth of the southern Laurasian active margin, Central Pontides, Turkey: Tectonophysics, v. 671, p. 218–234, doi:10.1016/j.tecto.2016.01.010.

Ballato, P., Parra, M., Schildgen, T.F., Dunkl, I., Yıldırım, C., Özsayın, E., Sobel, E.R., Echtler, H., and Strecker, M.R., 2018, Multiple Exhumation Phases in the Central Pontides (N Turkey): New Temporal Constraints on Major Geodynamic Changes Associated With the Closure of the Neo-Tethys Ocean: Tectonics, v. 37, p. 1831–1857, doi:10.1029/2017TC004808.

Ballato, P., and Strecker, M.R., 2014, Assessing tectonic and climatic causal mechanisms in foreland-basin stratal architecture: insights from the Alborz Mountains, northern Iran: Tectonic And Climatic Forcing In A Foreland Basin Stratigraphy: Earth Surface Processes and Landforms, v. 39, p. 110–125, doi:10.1002/esp.3480.

Ballato, P., Uba, C.E., Landgraf, A., Strecker, M.R., Sudo, M., Stockli, D.F., Friedrich, A., and Tabatabaei, S.H., 2011, Arabia-Eurasia continental collision: Insights from late Tertiary foreland-basin evolution in the Alborz Mountains, northern Iran: GSA Bulletin, v. 123, p. 106–131, doi:10.1130/B30091.1.

Bang, M., 2020, “Native Science and Student Wellness” with Dr. Megan Bang: Two Feathers NAFS, https://www.youtube.com/watch?v=5qgTxP0SFag (accessed August 2021).

Barrier, E., and Vrielynck, B., 2008, Palaeotectonic Maps of the Middle East: Paris, Commission for the Geological Map of the World.

Baş, H., 1986, Tertiary geology of the Domaniç-Tavsanli-Kütahya-Gediz Region: Jeoloji Mühendisliği, v. 27, p. 11–18.

Beard, K.C., 2016, Out of Asia: Anthropoid Origins and the Colonization of Africa: Annual Review of Anthropology, v. 45, p. 199–213, doi:10.1146/annurev-anthro-102215-100019.

Beard, K.C., Métais, G., Ocakoğlu, F., and Licht, A., 2020, An omomyid primate from the Pontide microcontinent of north-central Anatolia: Implications for sweepstakes dispersal of terrestrial mammals during the Eocene: Geobios, doi:10.1016/j.geobios.2020.06.008.

Beaumont, C., Ellis, S., Hamilton, J., and Fullsack, P., 1996, Mechanical model for subduction-collision tectonics of Alpine-type compressional orogens: Geology, v. 24, p. 675–678, doi:10.1130/0091-7613(1996)024<0675:MMFSCT>2.3.CO;2.

Black, L.P. et al., 2004, Improved 206Pb/238U microprobe geochronology by the monitoring of a trace-element-related matrix effect; SHRIMP, ID–TIMS, ELA–ICP–MS and oxygen isotope documentation for a series of zircon standards: Chemical Geology, v. 205, p. 115–140, doi:10.1016/j.chemgeo.2004.01.003.

von Blanckenburg, F., and Davies, J.H., 1995, Slab breakoff: A model for syncollisional magmatism and tectonics in the Alps: Tectonics, v. 14, p. 120–131, doi:10.1029/94TC02051.

Botev, Z.I., Grotowski, J.F., and Kroese, D.P., 2010, Kernel density estimation via diffusion: The Annals of Statistics, v. 38, p. 2916–2957, doi:10.1214/10-AOS799.

Bozkurt, E., Winchester, J.A., and Satır, M., 2013, The Çele mafic complex: Evidence for Triassic collision between the Sakarya and İstanbul Zones, NW Turkey: Tectonophysics, v. 595–596, p. 198–214, doi:10.1016/j.tecto.2012.11.005.

Burbank, D.W., Beck, R.A., Raynolds, R.G.H., Hobbs, R., and Tahirkheli, R.A.K., 1988, Thrusting and gravel progradation in foreland basins: A test of post-thrusting gravel dispersal: Geology, v. 16, p. 1143, doi:10.1130/0091-7613(1988)016<1143:TAGPIF>2.3.CO;2.

Campbell, C.F., 2017, Tectonic Evolution of the Izmir-Ankara Suture Zone in Northwest Turkey using Zircon U-Pb Geochronology and Zircon Lu-Hf Isotopic Tracers [M.S.]: University of Kansas, 99 p., http://search.proquest.com/pqdtglobal/docview/2019635859/abstract/4D50BF261D204844PQ/1 (accessed July 2019).

Campbell, C.F., Mueller, M.A., Taylor, M.H., Ocakoğlu, F., Möller, A., Métais, G., Coster, P.M.C., Beard, K.C., and Licht, A., in review, Closing the Neotethys in Western Anatolia, Part 1: Evidence for Protracted Extension as Continental Lithosphere Subducted in Late Cretaceous Times: Geochemistry, Geophysics, Geosystems,.

Carrapa, B., 2009, Tracing exhumation and orogenic wedge dynamics in the European Alps with detrital thermochronology: Geology, v. 37, p. 1127–1130, doi:10.1130/G30065A.1.

Catanzariti, R., Ellero, A., Göncüoglu, M.C., Marroni, M., Ottria, G., and Pandolfi, L., 2013, The Taraklı Flysch in the Boyali area (Sakarya Terrane, northern Turkey): Implications for the tectonic history of the IntraPontide suture zone: Comptes Rendus Geoscience, v. 345, p. 454–461, doi:10.1016/j.crte.2013.11.001.

Caves, J.K., Sjostrom, D.J., Mix, H.T., Winnick, M.J., and Chamberlain, C.P., 2014, Aridification of Central Asia and uplift of the Altai and Hangay Mountains, Mongolia: Stable isotope evidence: American Journal of Science, v. 314, p. 1171–1201, doi:10.2475/08.2014.01.

Caves, J.K., Winnick, M.J., Graham, S.A., Sjostrom, D.J., Mulch, A., and Chamberlain, C.P., 2015, Role of the westerlies in Central Asia climate over the Cenozoic: Earth and Planetary Science Letters, v. 428, p. 33–43, doi:10.1016/j.epsl.2015.07.023.

Chaimanee, Y. et al., 2012, Late Middle Eocene primate from Myanmar and the initial anthropoid colonization of Africa: Proceedings of the National Academy of Sciences, v. 109, p. 10293–10297, doi:10.1073/pnas.1200644109.

Chapman, J.B., Ducea, M.N., Kapp, P., Gehrels, G.E., and DeCelles, P.G., 2017, Spatial and temporal radiogenic isotopic trends of magmatism in Cordilleran orogens: Gondwana Research, v. 48, p. 189–204, doi:10.1016/j.gr.2017.04.019.

Chen, F., Siebel, W., Satir, M., Terzioğlu, M., and Saka, K., 2002, Geochronology of the Karadere basement (NW Turkey) and implications for the geological evolution of the Istanbul zone: International Journal of Earth Sciences, v. 91, p. 469–481, doi:10.1007/s00531-001-0239-6.

Cherniak, D.J., 2000, Pb diffusion in rutile: Contributions to Mineralogy and Petrology, v. 139, p. 198–207, doi:10.1007/PL00007671.

Chew, D.M., Petrus, J.A., and Kamber, B.S., 2014, U-Pb LA-ICPMS dating using accessory mineral standards with variable common Pb: Chemical Geology, v. 363, p. 185–199.

Çimen, O., Göncüoğlu, M.C., Simonetti, A., and Sayit, K., 2017, Whole rock geochemistry, Zircon U–Pb and Hf isotope systematics of the Çangaldağ Pluton: Evidences for Middle Jurassic Continental Arc Magmatism in the Central Pontides, Turkey: Lithos, v. 290–291, p. 136–155, doi:10.1016/j.lithos.2017.06.020.

Clark, M.K., and Royden, L.H., 2000, Topographic ooze: Building the eastern margin of Tibet by lower crustal flow: Geology, v. 28, p. 703–706.

Clark, M.K., Schoenbohm, L.M., Royden, L.H., Whipple, K.X., Burchfiel, B.C., Zhang, X., Tang, W., Wang, E., and Chen, L., 2004, Surface uplift, tectonics, and erosion of eastern Tibet from large-scale drainage patterns: Tectonics, v. 23, doi:10.1029/2002TC001402.

Clift, P.D., Hodges, K.V., Heslop, D., Hannigan, R., Van Long, H., and Calves, G., 2008, Correlation of Himalayan exhumation rates and Asian monsoon intensity: Nature Geoscience, v. 1, p. 875–880, doi:10.1038/ngeo351.

Coulthard, G.S., 2014, Introduction: Subjects of Empire, *in* Red Skin, White Masks: Rejecting the Colonial Politics of Recognition, Minneapolis, University of Minnesota Press, p. 1–24, https://muse.jhu.edu/book/35470.

Cowgill, E., Forte, A.M., Niemi, N., Avdeev, B., Tye, A., Trexler, C., Javakhishvili, Z., Elashvili, M., and Godoladze, T., 2016, Relict basin closure and crustal shortening budgets during continental collision: An example from Caucasus sediment provenance: Tectonics, v. 35, p. 2918–2947, doi:10.1002/2016TC004295.

Cowie, P.A., and Scholz, C.H., 1992, Displacement-length scaling relationship for faults: data synthesis and discussion: Journal of Structural Geology, v. 14, p. 1149–1156, doi:10.1016/0191-8141(92)90066-6.

Darin, M.H., Umhoefer, P.J., and Thomson, S.N., 2018, Rapid Late Eocene Exhumation of the Sivas Basin (Central Anatolia) Driven by Initial Arabia-Eurasia Collision: Tectonics, doi:10.1029/2017TC004954.

Davies, J.H., and von Blanckenburg, F., 1995, Slab breakoff: A model of lithosphere detachment and its test in the magmatism and deformation of collisional orogens: Earth and Planetary Science Letters, v. 129, p. 85–102, doi:10.1016/0012-821X(94)00237-S.

DeCelles, P.G., Kapp, P., Quade, J., and Gehrels, G.E., 2011, Oligocene–Miocene Kailas basin, southwestern Tibet: Record of postcollisional upper-plate extension in the Indus-Yarlung suture zone: GSA Bulletin, v. 123, p. 1337–1362, doi:10.1130/B30258.1.

Di Rosa, M., Farina, F., Marroni, M., Pandolfi, L., Göncüoğlu, M.C., Ellero, A., and Ottria, G., 2019, U-Pb zircon geochronology of intrusive rocks from an exotic block in the Late Cretaceous – Paleocene Taraklı Flysch (northern Turkey): Constraints on the tectonics of the Intrapontide suture zone: Journal of Asian Earth Sciences, v. 171, p. 277–288, doi:10.1016/j.jseaes.2018.11.017.

Dickinson, W.R., 1985, Interpreting provenance relations from detrital modes of sandstones, *in* Zuffa, G.G. ed., Provenance of Arenites, Dordrecht, Reidel, NATO Advanced Studies Institute Series 148, p. 333–361.

Dickinson, W.R., Beard, L.S., Brakenridge, G.R., Erjavec, J.L., Ferguson, R.C., Inman, K.F., Knepp, R.A., Lindberg, F.A., and Ryberg, P.T., 1983, Provenance of North American Phanerozoic sandstones in relation to tectonic setting: Geological Society of America Bulletin, v. 94, p. 222, doi:10.1130/0016-7606(1983)94<222:PONAPS>2.0.CO;2.

Dickinson, W.R., and Gehrels, G.E., 2009, U-Pb ages of detrital zircons in Jurassic eolian and associated sandstones of the Colorado Plateau: Evidence for transcontinental dispersal and intraregional recycling of sediment: Geological Society of America Bulletin, v. 121, p. 408–433, doi:10.1130/B26406.1.

Dickinson, W.R., Klute, M.A., Hayes, M.J., Janecke, S.U., Lundin, E.R., McKITTRICK, M.A., and Olivares, M.D., 1988, Paleogeographic and paleotectonic setting of Laramide sedimentary basins in the central Rocky Mountain region: GSA Bulletin, v. 100, p. 1023–1039, doi:10.1130/0016-7606(1988)100<1023:PAPSOL>2.3.CO;2.

Dickinson, W.R., and Suczek, C.A., 1979, Plate Tectonics and Sandstone Compositions: AAPG Bulletin, v. 63, p. 2164–2182.

Dilek, Y., and Altunkaynak, Ş., 2009, Geochemical and temporal evolution of Cenozoic magmatism in western Turkey: mantle response to collision, slab break-off, and lithospheric tearing in an orogenic belt: Geological Society, London, Special Publications, v. 311, p. 213–233, doi:10.1144/SP311.8.

Dilek, Y., Thy, P., Hacker, B., and Grundvig, S., 1999, Structure and petrology of Tauride ophiolites and mafic dike intrusions (Turkey): Implications for the Neotethyan ocean: Geological Society of America Bulletin, p. 25.

Ding, L., Kapp, P., and Wan, X., 2005, Paleocene–Eocene record of ophiolite obduction and initial India-Asia collision, south central Tibet: Tectonics, v. 24, doi:10.1029/2004TC001729.

Ding, L., Qasim, M., Jadoon, I.A.K., Khan, M.A., Xu, Q., Cai, F., Wang, H., Baral, U., and Yue, Y., 2016, The India–Asia collision in north Pakistan: Insight from the U–Pb detrital zircon provenance of Cenozoic foreland basin: Earth and Planetary Science Letters, v. 455, p. 49–61, doi:10.1016/j.epsl.2016.09.003.

Duru, M., and Aksay, A., 2002, Geological map of the Adapazari quadrangle (Sheet H 24, Scale 1:100,000): Maden Tetkik ve Arma Genel Müdürlüğü 1:100,000 scale geological maps of Turkey.

Eddy, M.P., Bowring, S.A., Miller, R.B., and Tepper, J.H., 2016, Rapid assembly and crystallization of a fossil large-volume silicic magma chamber: Geology, v. 44, p. 331–334, doi:10.1130/G37631.1.

Ersoy, E.Y., Akal, C., Genç, Ş.C., Candan, O., Palmer, M.R., Prelević, D., Uysal, İ., and Mertz-Kraus, R., 2017a, U-Pb zircon geochronology of the Paleogene – Neogene volcanism in the NW Anatolia: Its implications for the Late Mesozoic-Cenozoic geodynamic evolution of the Aegean: Tectonophysics, v. 717, p. 284–301, doi:10.1016/j.tecto.2017.08.016.

Ersoy, E.Y., Palmer, M.R., Genç, Ş.C., Prelević, D., Akal, C., and Uysal, İ., 2017b, Chemo-probe into the mantle origin of the NW Anatolia Eocene to Miocene volcanic rocks: Implications for the role of, crustal accretion, subduction, slab roll-back and slab break-off processes in genesis of post-collisional magmatism: Lithos, v. 288–289, p. 55–71, doi:10.1016/j.lithos.2017.07.006.

Ewing, T.A., 2011, Hf isotope analysis and U-Pb geochronology of rutile : technique development and application to a lower crustal section (Ivrea-Verbano Zone, Italy):, doi:10.25911/5d74e68841e8d.

Faccenna, C., Holt, A.F., Becker, T.W., Lallemand, S., and Royden, L.H., 2017, Dynamics of the Ryukyu/Izu-Bonin-Marianas double subduction system: Tectonophysics, v. 746, p. 229–238, doi:10.1016/j.tecto.2017.08.011.

Flemings, P.B., and Jordan, T.E., 1990, Stratigraphic modeling of foreland basins: Interpreting thrust deformation and lithosphere rheology: Geology, v. 18, p. 430–434, doi:10.1130/0091-7613(1990)018<0430:SMOFBI>2.3.CO;2.

Floyd, P.A., Göncüoğlu, M.C., Winchester, J.A., and Yaliniz, M.K., 2000, Geochemical Character and Tectonic Environment of Neotethyan Ophiolitic Fragments and Metabasites in the Central Anatolian Crystalline Complex, Turkey: Geological Society, London, Special Publications, v. 173, p. 183–202, doi:10.1144/GSL.SP.2000.173.01.09.

Frassi, C., Marroni, M., Pandolfi, L., Göncüoğlu, M.C., Ellero, A., Ottria, G., Sayit, K., Mcdonald, C.S., Balestrieri, M.L., And Malasoma, A., 2017, Burial and exhumation history of the Daday Unit (Central Pontides, Turkey): implications for the closure of the Intra-Pontide oceanic basin: Geological Magazine, v. 155, p. 356–376, doi:10.1017/S0016756817000176.

Garzanti, E., 2018, Petrographic classification of sand and sandstone: Earth-Science Reviews, doi:10.1016/j.earscirev.2018.12.014.

Garzanti, E., Radeff, G., and Malusà, M.G., 2018, Slab breakoff: A critical appraisal of a geological theory as applied in space and time: Earth-Science Reviews, v. 177, p. 303–319, doi:10.1016/j.earscirev.2017.11.012.

Gaschnig, R.M., 2019, Benefits of a Multiproxy Approach to Detrital Mineral Provenance Analysis: An Example from the Merrimack River, New England, USA: Geochemistry, Geophysics, Geosystems, v. 20, p. 1557–1573, doi:10.1029/2018GC008005.

Gedik, I., and Aksay, A., 2002, Geological map of the Adapazari quadrangle (Sheet H 25, Scale 1:100,000): Maden Tetkik ve Arma Genel Müdürlüğü 1:100,000 scale geological maps of Turkey.

Gehrels, G., 2014, Detrital Zircon U-Pb Geochronology Applied to Tectonics: Annual Review of Earth and Planetary Sciences, v. 42, p. 127–149, doi:10.1146/annurev-earth-050212-124012.

Gehrels, G., 2012, Detrital Zircon U-Pb Geochronology: Current Methods and New Opportunities, *in* Busby, C. and Azor, A. eds., Tectonics of Sedimentary Basins, Chichester, UK, John Wiley & Sons, Ltd, p. 45–62, doi:10.1002/9781444347166.ch2.

Genç, Ş., 1986, 1986. Uludağ-İznik Gölü Arasının Jeolojisi [Geology of the Area Between Uludağ and İznik Lake].: Maden Tetkik ve Arama (MTA), v. Report no. 7853, p. [in Turkish, unpublished].

Genç, Ş.C., and Tüysüz, O., 2010, Tectonic setting of the Jurassic bimodal magmatism in the Sakarya Zone (Central and Western Pontides), Northern Turkey: A geochemical and isotopic approach: Lithos, v. 118, p. 95–111, doi:10.1016/j.lithos.2010.03.017.

Goddéris, Y., Donnadieu, Y., Le Hir, G., Lefebvre, V., and Nardin, E., 2014, The role of palaeogeography in the Phanerozoic history of atmospheric CO2 and climate: Earth-Science Reviews, v. 128, p. 122–138, doi:10.1016/j.earscirev.2013.11.004.

Göğüş, O.H., Pysklywec, R.N., Şengör, A.M.C., and Gün, E., 2017, Drip tectonics and the enigmatic uplift of the Central Anatolian Plateau: Nature Communications, v. 8, doi:10.1038/s41467-017-01611-3.

Göncüoğlu, M.C., 2010, Introduction to the Geology of Turkey: Geodynamic evolution of the pre-Alpine and Alpine terranes: General Directorate of Mineral Research and Exploration, http://www.academia.edu/download/31280681/MTA_Monogr_Ing_Geology_of_Turkey.pdf (accessed June 2017).

Göncüoğlu, M.C., Marroni, M., Pandolfi, L., Ellero, A., Ottria, G., Catanzariti, R., Tekin, U.K., and Sayit, K., 2014, The Arkot Dağ Mélange in Araç area, central Turkey: Evidence of its origin within the geodynamic evolution of the Intra-Pontide suture zone: Journal of Asian Earth Sciences, v. 85, p. 117–139, doi:10.1016/j.jseaes.2014.01.013.

Göncüoğlu, M.C., Turhan, N., Şentürk, K., Özcan, A., Uysal, Ş., and Yaliniz, M.K., 2000, A Geotraverse Across Northwestern Turkey: Tectonic Units of the Central Sakarya Region and their Tectonic Evolution: Geological Society, London, Special Publications, v. 173, p. 139–161, doi:10.1144/GSL.SP.2000.173.01.06.

Görür, N., 1988, Timing of opening of the Black Sea basin: Tectonophysics, v. 147, p. 247–262, doi:10.1016/0040-1951(88)90189-8.

Görür, N., Oktay, F.Y., Seymen, I., and Şengör, A.M.C., 1984, Palaeotectonic evolution of the Tuzgölü basin complex, Central Turkey: sedimentary record of a Neo-Tethyan closure: Geological Society, London, Special Publications, v. 17, p. 467–482, doi:10.1144/GSL.SP.1984.017.01.34.

Görür, N., Tüysüz, O., and Celal Şengör, A.M., 1998, Tectonic Evolution of the Central Anatolian Basins: International Geology Review, v. 40, p. 831–850, doi:10.1080/00206819809465241.

Graham, D.J., and Midgley, N.G., 2000a, Graphical representation of particle shape using triangular diagrams: an Excel spreadsheet method: , p. 5.

Graham, D.J., and Midgley, N.G., 2000b, Graphical representation of particle shape using triangular diagrams: an Excel spreadsheet method: Earth Surface Processes and Landforms, v. 25, p. 1473–1477, doi:10.1002/1096-9837(200012)25:13<1473::AID-ESP158>3.0.CO;2-C.

Guillong, M., Hametner, K., Reusser, E., Wilson, S.A., and Günther, D., 2005, Preliminary Characterisation of New Glass Reference Materials (GSA-1G, GSC-1G, GSD-1G and GSE-1G) by Laser Ablation-Inductively Coupled Plasma-Mass Spectrometry Using 193 nm, 213 nm and 266 nm Wavelengths: Geostandards and Geoanalytical Research, v. 29, p. 315–331, doi:10.1111/j.1751-908X.2005.tb00903.x.

Gürer, D., and van Hinsbergen, D.J.J., 2018, Diachronous demise of the Neotethys Ocean as a driver for non-cylindrical orogenesis in Anatolia: Tectonophysics, doi:10.1016/j.tecto.2018.06.005.

Gürer, D., van Hinsbergen, D.J.J., Matenco, L., Corfu, F., and Cascella, A., 2016, Kinematics of a former oceanic plate of the Neotethys revealed by deformation in the Ulukışla basin (Turkey): Kinematic Evolution Of Central Anatolia: Tectonics, v. 35, p. 2385–2416, doi:10.1002/2016TC004206.

Gürer, D., Plunder, A., Kirst, F., Corfu, F., Schmid, S.M., and van Hinsbergen, D.J.J., 2018, A long-lived Late Cretaceous–early Eocene extensional province in Anatolia? Structural evidence from the Ivriz Detachment, southern central Turkey: Earth and Planetary Science Letters, v. 481, p. 111–124, doi:10.1016/j.epsl.2017.10.008.

Harris, N.B.W., Kelley, S., and Okay, A.I., 1994, Post-collisional magmatism and tectonics in northwest Anatolia: Contributions to Mineralogy and Petrology, v. 117, p. 241–252.

Heller, P.L., and Paola, C., 1992, The large-scale dynamics of grain-size variation in alluvial basins, 2: Applications to syntectonic conglomerate: Basin Research, v. 4, p. 91–102.

van Hinsbergen, D.J.J. et al., 2015, Dynamics of intraoceanic subduction initiation: 2. Suprasubduction zone ophiolite formation and metamorphic sole exhumation in context of absolute plate motions: SSZ Ophiolites And Metamorphic Soles: Geochemistry, Geophysics, Geosystems, v. 16, p. 1771–1785, doi:10.1002/2015GC005745.

van Hinsbergen, D.J.J. van et al., 2016, Tectonic evolution and paleogeography of the Kırşehir Block and the Central Anatolian Ophiolites, Turkey: Tectonics, v. 35, p. 983–1014, doi:10.1002/2015TC004018.

van Hinsbergen, D.J.J., Kapp, P., Dupont-Nivet, G., Lippert, P.C., DeCelles, P.G., and Torsvik, T.H., 2011, Restoration of Cenozoic deformation in Asia and the size of Greater India: Tectonics, v. 30, doi:https://doi.org/10.1029/2011TC002908.

van Hinsbergen, D.J.J., Kaymakci, N., Spakman, W., and Torsvik, T.H., 2010, Reconciling the geological history of western Turkey with plate circuits and mantle tomography: Earth and Planetary Science Letters, v. 297, p. 674–686, doi:10.1016/j.epsl.2010.07.024.

van Hinsbergen, D.J.J., Lippert, P.C., Dupont-Nivet, G., McQuarrie, N., Doubrovine, P.V., Spakman, W., and Torsvik, T.H., 2012, Greater India Basin hypothesis and a two-stage Cenozoic collision between India and Asia: Proceedings of the National Academy of Sciences, v. 109, p. 7659–7664, doi:10.1073/pnas.1117262109.

van Hinsbergen, D.J.J., Torsvik, T.H., Schmid, S.M., Maţenco, L.C., Maffione, M., Vissers, R.L.M., Gürer, D., and Spakman, W., 2020, Orogenic architecture of the Mediterranean region and kinematic reconstruction of its tectonic evolution since the Triassic: Gondwana Research, v. 81, p. 79–229, doi:10.1016/j.gr.2019.07.009.

Hippolyte, J.-C., Espurt, N., Kaymakci, N., Sangu, E., and Müller, C., 2016, Cross-sectional anatomy and geodynamic evolution of the Central Pontide orogenic belt (northern Turkey): International Journal of Earth Sciences, v. 105, p. 81–106, doi:10.1007/s00531-015-1170-6.

Hippolyte, J.-C., Müller, C., Kaymakci, N., and Sangu, E., 2010, Dating of the Black Sea Basin: new nannoplankton ages from its inverted margin in the Central Pontides (Turkey): Geological Society, London, Special Publications, v. 340, p. 113–136, doi:10.1144/SP340.7.

Holt, A.F., and Condit, C.B., 2021, Slab Temperature Evolution Over the Lifetime of a Subduction Zone: Geochemistry, Geophysics, Geosystems, v. 22, p. e2020GC009476, doi:10.1029/2020GC009476.

Holt, A.F., Royden, L.H., Becker, T.W., and Faccenna, C., 2018, Slab interactions in 3-D subduction settings: The Philippine Sea Plate region: Earth and Planetary Science Letters, v. 489, p. 72–83, doi:10.1016/j.epsl.2018.02.024.

Horstwood, M.S.A. et al., 2016, Community-Derived Standards for LA-ICP-MS U-(Th-)Pb Geochronology – Uncertainty Propagation, Age Interpretation and Data Reporting:

Geostandards and Geoanalytical Research, v. 40, p. 311–332, doi:10.1111/j.1751-908X.2016.00379.x.

Hu, X., Garzanti, E., Wang, J., Huang, W., An, W., and Webb, A., 2016, The timing of India-Asia collision onset – Facts, theories, controversies: Earth-Science Reviews, v. 160, p. 264–299, doi:10.1016/j.earscirev.2016.07.014.

Huntington, K.W., Klepeis, K.A., and with 66 community contributors, 2018, Challenges and opportunities for research in tectonics: Understanding deformation and the processes that link Earth systems, from geologic time to human time. A community vision document submitted to the U.S. National Science Foundation.: University of Washington, p. 84.

Jackson, S.E., Pearson, N.J., Griffin, W.L., and Belousova, E.A., 2004, The application of laser ablation-inductively coupled plasma-mass spectrometry to in situ U–Pb zircon geochronology: Chemical Geology, v. 211, p. 47–69, doi:10.1016/j.chemgeo.2004.06.017.

Jaeger, J.-J. et al., 2010, Late middle Eocene epoch of Libya yields earliest known radiation of African anthropoids: Nature, v. 467, p. 1095–1098, doi:10.1038/nature09425.

Jagoutz, O., Macdonald, F.A., and Royden, L., 2016, Low-latitude arc–continent collision as a driver for global cooling: Proceedings of the National Academy of Sciences, v. 113, p. 4935–4940, doi:10.1073/pnas.1523667113.

Jagoutz, O., Royden, L., Holt, A.F., and Becker, T.W., 2015, Anomalously fast convergence of India and Eurasia caused by double subduction: Nature Geoscience, v. 8, p. 475–478, doi:10.1038/ngeo2418.

Janbu, N.E., Nemec, W., Kirman, E., and zaksoy, V., 2007, Facies Anatomy of a Sand-Rich Channelized Turbiditic System: The Eocene Kusuri Formation in the Sinop Basin, North-Central Turkey, *in* Nichols, G., Williams, E., and Paola, C. eds., Sedimentary Processes, Environments and Basins, Oxford, UK, Blackwell Publishing Ltd., p. 457–517, doi:10.1002/9781444304411.ch19.

Jochum, K.P., Willbold, M., Raczek, I., Stoll, B., and Herwig, K., 2005, Chemical Characterisation of the USGS Reference Glasses GSA-1G, GSC-1G, GSD-1G, GSE-1G, BCR-2G, BHVO-2G and BIR-1G Using EPMA, ID-TIMS, ID-ICP-MS and LA-ICP-MS: Geostandards and Geoanalytical Research, v. 29, p. 285–302, doi:10.1111/j.1751-908X.2005.tb00901.x.

Jolivet, L., and Faccenna, C., 2000, Mediterranean extension and the Africa-Eurasia collision: Tectonics, v. 19, p. 1095–1106, doi:10.1029/2000TC900018.

Jones, M.F., Coster, P.M.C., Licht, A., Métais, G., Ocakoğlu, F., Taylor, M.H., and Beard, K.C., 2018, A stem bat (Chiroptera: Palaeochiropterygidae) from the late middle Eocene of northern Anatolia: implications for the dispersal and palaeobiology of early bats: Palaeobiodiversity and Palaeoenvironments, doi:10.1007/s12549-018-0338-z.

Jones, C.H., Farmer, G.L., Sageman, B., and Zhong, S., 2011, Hydrodynamic mechanism for the Laramide orogeny: Geosphere, v. 7, p. 183–201, doi:10.1130/GES00575.1.

Jones, C.H., Sonder, L.J., and Unruh, J.R., 1998, Lithospheric gravitational potential energy and past orogenesis: Implications for conditions of initial Basin and Range and Laramide deformation: , p. 4.

Kapp, P., and DeCelles, P.G., 2019, Mesozoic–Cenozoic geological evolution of the Himalayan-Tibetan orogen and working tectonic hypotheses: American Journal of Science, v. 319, p. 159–254, doi:10.2475/03.2019.01.

Kappelman, J., Maas, M.C., Sen, S., Alpagut, B., Fortelius, M., and Lunkka, J.-P., 1996, A new early Tertiary mammalian fauna from Turkey and its paleobiogeographic significance:

Journal of Vertebrate Paleontology, v. 16, p. 592–595, doi:10.1080/02724634.1996.10011345.

Kasapoğlu, B., Ersoy, Y.E., Uysal, İ., Palmer, M.R., Zack, T., Koralay, E.O., and Karlsson, A., 2016, The petrology of Paleogene volcanism in the Central Sakarya, Nallıhan Region: Implications for the initiation and evolution of post-collisional, slab break-off-related magmatic activity: Lithos, v. 246–247, p. 81–98, doi:10.1016/j.lithos.2015.12.024.

Kaymakci, N., Özçelik, Y., White, S.H., and Van Dijk, P.M., 2009, Tectono-stratigraphy of the Çankırı Basin: Late Cretaceous to early Miocene evolution of the Neotethyan Suture Zone in Turkey: Geological Society, London, Special Publications, v. 311, p. 67–106, doi:10.1144/SP311.3.

Kaymakci, N., White, S.H., and Vandijk, P.M., 2003, Kinematic and structural development of the Çankiri Basin (Central Anatolia, Turkey): a paleostress inversion study: Tectonophysics, v. 364, p. 85–113, doi:10.1016/S0040-1951(03)00043-X.

Kellett, D.A., Weller, O.M., Zagorevski, A., and Regis, D., 2018, A petrochronological approach for the detrital record: Tracking mm-sized eclogite clasts in the northern Canadian Cordillera: Earth and Planetary Science Letters, v. 494, p. 23–31, doi:10.1016/j.epsl.2018.04.036.

Kerrick, D.M., and Caldeira, K., 1998, Metamorphic CO2 degassing from orogenic belts: Chemical Geology, v. 145, p. 213–232, doi:10.1016/S0009-2541(97)00144-7.

Keskin, M., and Tüysüz, O., 2018, Stratigraphy, petrogenesis and geodynamic setting of Late Cretaceous volcanism on the SW margin of the Black Sea, Turkey: Geological Society, London, Special Publications, v. 464, p. 95–130, doi:10.1144/SP464.5.

Kibici, Y., İlbeyli, N., Yıldız, A., and Bağcı, M., 2010, Geochemical constraints on the genesis of the Sarıcakaya intrusive rocks, Turkey: Late Paleozoic crustal melting in the central Sakarya Zone: Chemie der Erde - Geochemistry, v. 70, p. 243–256, doi:10.1016/j.chemer.2009.12.001.

Kimmerer, R.W., 2020, Braiding sweetgrass: indigenous wisdom, scientific knowledge, and the teachings of plants: Minneapolis, Minnesota, Milkweed Editions.

Kooijman, E., Mezger, K., and Berndt, J., 2010, Constraints on the U–Pb systematics of metamorphic rutile from in situ LA-ICP-MS analysis: Earth and Planetary Science Letters, v. 293, p. 321–330, doi:10.1016/j.epsl.2010.02.047.

Koshnaw, R.I., Stockli, D.F., and Schlunegger, F., 2019, Timing of the Arabia-Eurasia continental collision—Evidence from detrital zircon U-Pb geochronology of the Red Bed Series strata of the northwest Zagros hinterland, Kurdistan region of Iraq: Geology, v. 47, p. 47–50, doi:10.1130/G45499.1.

Kotowski, A.J., and Behr, W.M., 2019, Length scales and types of heterogeneities along the deep subduction interface: Insights from exhumed rocks on Syros Island, Greece: Geosphere, v. 15, p. 1038–1065, doi:10.1130/GES02037.1.

Kylander-Clark, A.R.C., 2008, Slow subduction and exhumation of a thick ultrahigh -pressure terrane: Western Gneiss Region, Norway [Ph.D.]: University of California, Santa Barbara, 121 p., http://www.proquest.com/docview/304664652/abstract/5E92F297A66A4294PQ/1 (accessed July 2021).

Leary, R., Orme, D.A., Laskowski, A.K., DeCelles, P.G., Kapp, P., Carrapa, B., and Dettinger, M., 2016, Along-strike diachroneity in deposition of the Kailas Formation in central southern Tibet: Implications for Indian slab dynamics: Geosphere, v. 12, p. 1198–1223, doi:10.1130/GES01325.1.

Lefebvre, C., Meijers, M.J.M., Kaymakci, N., Peynircioğlu, A., Langereis, C.G., and van Hinsbergen, D.J.J., 2013, Reconstructing the geometry of central Anatolia during the late Cretaceous: Large-scale Cenozoic rotations and deformation between the Pontides and Taurides: Earth and Planetary Science Letters, v. 366, p. 83–98, doi:10.1016/j.epsl.2013.01.003.

Leren, B.L.S., Janbu, N.E., Nemec, W., Kirman, E., and Ilgar, A., 2007, Late Cretaceous to Early Eocene Sedimentation in the Sinop–Boyabat Basin, North-Central Turkey: A Deep-Water Turbiditic System Evolving into Littoral Carbonate Platform, *in* Nichols, G., Williams, E., and Paola, C. eds., Sedimentary Processes, Environments and Basins, Oxford, UK, Blackwell Publishing Ltd., p. 401–456, doi:10.1002/9781444304411.ch18.

Licht, A. et al., 2014, Asian monsoons in a late Eocene greenhouse world: Nature, v. 513, p. 501–506, doi:10.1038/nature13704.

Licht, A. et al., 2018, Paleogene evolution of the Burmese forearc basin and implications for the history of India-Asia convergence: GSA Bulletin, v. 5–6, p. 730–748, doi:10.1130/B35002.1.

Licht, A., Coster, P., Ocakoğlu, F., Campbell, C., Métais, G., Mulch, A., Taylor, M., Kappelman, J., and Beard, K.C., 2017, Tectono-stratigraphy of the Orhaniye Basin, Turkey: Implications for collision chronology and Paleogene biogeography of central Anatolia: Journal of Asian Earth Sciences, v. 143, p. 45–58, doi:10.1016/j.jseaes.2017.03.033.

Lippert, P.G., 2014, Detrital U-Pb geochronology provenance analyses: case studies in the Greater Green River Basin, Wyoming, and the Book Cliffs, Utah [Thesis]: University of Kansas, https://kuscholarworks.ku.edu/handle/1808/14549 (accessed July 2021).

Lippert, P.C., van Hinsbergen, D.J.J., and Dupont-Nivet, G., 2014, Early Cretaceous to present latitude of the central proto-Tibetan Plateau: A paleomagnetic synthesis with implications for Cenozoic tectonics, paleogeography, and climate of Asia, *in* Toward an Improved Understanding of Uplift Mechanisms and the Elevation History of the Tibetan Plateau, Geological Society of America, doi:10.1130/2014.2507(01).

Ludwig, K.R., 2012, User's Manual for Isoplot 3.00: A Geochronologic Toolkit for Microsoft Excel: Berkeley Geochronological Center Special Publication No. 5, p. 1–75.

Luvizotto, G.L. et al., 2009, Rutile crystals as potential trace element and isotope mineral standards for microanalysis: Chemical Geology, v. 261, p. 346–369, doi:10.1016/j.chemgeo.2008.04.012.

Lygina, E.A., Fokin, P.A., Kopaevich, L.F., Nikishin, A.M., and Yakovishina, E.V., 2016, Nummulitic facies of the Crimean-Caucasian Region: Turkish Journal of Earth Sciences, v. 25, p. 163–178, doi:10.3906/yer-1404-20.

Maas, M.C., Thewissen, J.G.M., Sen, S., Kazanci, N., and Kappelman, J., 2001, Enigmatic new ungulates from the Early Middle Eocene of central Anatolia, Turkey: Journal of Vertebrate Paleontology, v. 21, p. 578–590, doi:10.1671/0272-4634(2001)021[0578:ENUFTE]2.0.CO;2.

Maffione, M., Hinsbergen, D.J.J. van, Koornneef, L.M.T., Guilmette, C., Hodges, K., Borneman, N., Huang, W., Ding, L., and Kapp, P., 2015, Forearc hyperextension dismembered the south Tibetan ophiolites: Geology, v. 43, p. 475–478, doi:10.1130/G36472.1.

Marrett, R., and Allmendinger, R.W., 1991, Estimates of strain due to brittle faulting: sampling of fault populations: Journal of Structural Geology, v. 13, p. 735–738, doi:10.1016/0191-8141(91)90034-G.

Marroni, M., Göncüoğlu, M.C., Frassi, C., Sayit, K., Pandolfi, L., Ellero, A., and Ottria, G., 2020, The Intra-Pontide ophiolites in Northern Turkey revisited: From birth to death of a Neotethyan oceanic domain: Geoscience Frontiers, v. 11, p. 129–149, doi:10.1016/j.gsf.2019.05.010.

Martin, C.R., Jagoutz, O., Upadhyay, R., Royden, L.H., Eddy, M.P., Bailey, E., Nichols, C.I.O., and Weiss, B.P., 2020, Paleocene latitude of the Kohistan–Ladakh arc indicates multistage India–Eurasia collision: Proceedings of the National Academy of Sciences, doi:10.1073/pnas.2009039117.

McLean, N.M., Bowring, J.F., and Gehrels, G., 2016, Algorithms and software for U-Pb geochronology by LA-ICPMS: Geochemistry, Geophysics, Geosystems, v. 17, p. 2480–2496, doi:https://doi.org/10.1002/2015GC006097.

McQuarrie, N., and van Hinsbergen, D.J.J., 2013, Retrodeforming the Arabia-Eurasia collision zone: Age of collision versus magnitude of continental subduction: Geology, v. 41, p. 315–318, doi:10.1130/G33591.1.

McQuarrie, N., Stock, J.M., Verdel, C., and Wernicke, B.P., 2003, Cenozoic evolution of Neotethys and implications for the causes of plate motions: Geophysical Research Letters, v. 30, doi:10.1029/2003GL017992.

Meijers, M.J.M. et al., 2015, A paleolatitude reconstruction of the South Armenian Block (Lesser Caucasus) for the Late Cretaceous: Constraints on the Tethyan realm: Tectonophysics, v. 644–645, p. 197–219, doi:10.1016/j.tecto.2015.01.012.

Meijers, M.J.M., Brocard, G.Y., Cosca, M.A., Lüdecke, T., Teyssier, C., Whitney, D.L., and Mulch, A., 2018, Rapid late Miocene surface uplift of the Central Anatolian Plateau margin: Earth and Planetary Science Letters, v. 497, p. 29–41, doi:10.1016/j.epsl.2018.05.040.

Meijers, M.J.M., Kaymakci, N., Hinsbergen, D.J.J. van, Langereis, C.G., Stephenson, R.A., and Hippolyte, J.-C., 2010, Late Cretaceous to Paleocene oroclinal bending in the central Pontides (Turkey): Tectonics, v. 29, doi:10.1029/2009TC002620.

Meinhold, G., 2010, Rutile and its applications in earth sciences: Earth-Science Reviews, v. 102, p. 1–28, doi:10.1016/j.earscirev.2010.06.001.

Meinhold, G., Anders, B., Kostopoulos, D., and Reischmann, T., 2008, Rutile chemistry and thermometry as provenance indicator: An example from Chios Island, Greece: Sedimentary Geology, v. 203, p. 98–111, doi:10.1016/j.sedgeo.2007.11.004.

Menant, A., Jolivet, L., and Vrielynck, B., 2016, Kinematic reconstructions and magmatic evolution illuminating crustal and mantle dynamics of the eastern Mediterranean region since the late Cretaceous: Tectonophysics, v. 675, p. 103–140, doi:10.1016/j.tecto.2016.03.007.

Métais, G., Beard, K., Erdal, O., and Erturaç, K., 2017, Tarsal morphology of the pleuraspidotheriid mammal Hilalia from the middle Eocene of Turkey: Acta Palaeontologica Polonica, v. 62, doi:10.4202/app.00314.2016.

Métais, G., Coster, P.M., Kappelman, J.R., Licht, A., Ocakoglu, F., Taylor, M.H., and Beard, K.C., 2018, Eocene metatherians from Anatolia illuminate the assembly of an island fauna during Deep Time: PLoS ONE, v. 13, p. e0206181.

Moix, P., Beccaletto, L., Kozur, H.W., Hochard, C., Rosselet, F., and Stampfli, G.M., 2008, A new classification of the Turkish terranes and sutures and its implication for the paleotectonic history of the region: Tectonophysics, v. 451, p. 7–39, doi:10.1016/j.tecto.2007.11.044.

MTA, 2002, Geological map of Turkey, scale 1:500,000: Mineral Research and Exploration Institute of Turkey,.

Mueller, M.A. et al., 2019, Collision Chronology Along the İzmir-Ankara-Erzincan Suture Zone: Insights From the Sarıcakaya Basin, Western Anatolia: Tectonics, v. 38, p. 3652–3674, doi:10.1029/2019TC005683.

Mueller, M.A., Licht, A., Campbell, C., Ocakoğlu, F., Akşit, G., Métais, G., Coster, P.M.C., Beard, K.C., and Taylor, M.H., in review, Closing the Neotethys in western Anatolia, Part 2: Protracted intercontinental collision from evolving plate coupling: Geochemistry, Geophysics, Geosystems,.

Nairn, S.P., Robertson, A.H.F., Ünlügenç, U.C., Tasli, K., and İnan, N., 2013, Tectonostratigraphic evolution of the Upper Cretaceous–Cenozoic central Anatolian basins: an integrated study of diachronous ocean basin closure and continental collision: Geological Society, London, Special Publications, v. 372, p. 343–384, doi:10.1144/SP372.9.

Najman, Y. et al., 2010, Timing of India-Asia collision: Geological, biostratigraphic, and palaeomagnetic constraints: Journal of Geophysical Research: Solid Earth, v. 115, doi:10.1029/2010JB007673.

NASEM, 2020, A Vision for NSF Earth Sciences 2020-2030: Earth in Time.: The National Academies Press.

Nichols, G., 2009, Sedimentology and stratigraphy: Chichester, UK ; Hoboken, NJ, Wiley-Blackwell, 419 p.

Niu, Y., 2017, Slab breakoff: a causal mechanism or pure convenience? Science Bulletin, v. 62, p. 456–461, doi:10.1016/j.scib.2017.03.015.

Noda, A., 2016, Forearc basins: Types, geometries, and relationships to subduction zone dynamics: Geological Society of America Bulletin, v. 128, p. 879–895, doi:10.1130/B31345.1.

Ocakoğlu, F. et al., 2018, Chronology of subduction and collision along the İzmir-Ankara suture in Western Anatolia: records from the Central Sakarya Basin: International Geology Review, p. 1–26, doi:10.1080/00206814.2018.1507009.

Ocakoğlu, F. et al., 2007, Orta Sakarya Bölgesi Geç Kretase-Paleojen Çökellerinin Sekans Stratigrafisi: The Scientific and Technological Research Council of Turkey (TUBİTAK, Project no: 104Y153), Final Report, p. 476.

Ocakoğlu, F., Açıkalın, S., Yılmaz, I.ö., Şafak, ü., and Gökçeoğlu, C., 2012, Evidence of orbital forcing in lake-level fluctuations in the Middle Eocene oil shale-bearing lacustrine successions in the Mudurnu-Göynük Basin, NW Anatolia (Turkey): Journal of Asian Earth Sciences, v. 56, p. 54–71, doi:10.1016/j.jseaes.2012.04.021.

Odlum, M.L., Stockli, D.F., Capaldi, T.N., Thomson, K.D., Clark, J., Puigdefàbregas, C., and Fildani, A., 2019, Tectonic and sediment provenance evolution of the South Eastern Pyrenean foreland basins during rift margin inversion and orogenic uplift: Tectonophysics, v. 765, p. 226–248, doi:10.1016/j.tecto.2019.05.008.

Okay, A., 2002, Jadeite-chloritoid-glaucophane-lawsonite blueschists in north-west Turkey: unusually high P/T ratios in continental crust: Jadeite-Chloritoid-Lawsonite Blueschists: Journal of Metamorphic Geology, v. 20, p. 757–768, doi:10.1046/j.1525-1314.2002.00402.x.

Okay, A., 2011, Tavsanli Zone: The Northern Subducted Margin Of The Anatolide-Tauride Block: Mineral Res. Expl. Bull., v. 142, p. 191–221.

Okay, A.İ., 2000, Was the Late Triassic orogeny in Turkey caused by the collision of an oceanic plateau? Geological Society, London, Special Publications, v. 173, p. 25–41, doi:10.1144/GSL.SP.2000.173.01.02.

Okay, A.I., Bozkurt, E., Satır, M., Yiğitbaş, E., Crowley, Q.G., and Shang, C.K., 2008, Defining the southern margin of Avalonia in the Pontides: Geochronological data from the Late Proterozoic and Ordovician granitoids from NW Turkey: Tectonophysics, v. 461, p. 252–264, doi:10.1016/j.tecto.2008.02.004.

Okay, A.I., and Göncüoglu, M.C., 2004, The Karakaya Complex: A Review of Data and Concepts: Turkish Journal of Earth Sciences, v. 13, p. 77–95.

Okay, A., Harris, N.B.W., and Kelley, S.P., 1998, Exhumation of blueschists along a Tethyan suture in northwest Turkey: Tectonophysics, v. 285, p. 275–299, doi:10.1016/S0040-1951(97)00275-8.

Okay, A.I., Monod, O., and Monié, P., 2002, Triassic blueschists and eclogites from northwest Turkey: vestiges of the Paleo-Tethyan subduction: Lithos, v. 64, p. 155–178, doi:10.1016/S0024-4937(02)00200-1.

Okay, A.I., and Nikishin, A.M., 2015, Tectonic evolution of the southern margin of Laurasia in the Black Sea region: International Geology Review, v. 57, p. 1051–1076, doi:10.1080/00206814.2015.1010609.

Okay, A., and Satir, M., 2006, Geochronology of Eocene plutonism and metamorphism in northwest: Geodinamica Acta, v. 19, p. 251–266, doi:10.3166/ga.19.251-266.

Okay, A., Satir, M., maluski, H., SIYAKO, M., Monie, P., Metzger, R., and Akyüz, S., 1996, Paleo- and Neo-Tethyan events in northwestern Turkey: Geologic and geochronologic constraints (A. Yin & T. M. Harrison, Eds.): Cambridge University Press, p. 420–441.

Okay, A.I., Şengör, A.M.C., and Görür, N., 1994, Kinematic history of the opening of the Black Sea and its effect on the surrounding regions: Geology, v. 22, p. 267–270, doi:10.1130/0091-7613(1994)022<0267:KHOTOO>2.3.CO;2.

Okay, A.I., Sunal, G., Sherlock, S., Altiner, D., Tüysüz, O., Kylander-Clark, A.R.C., and Aygül, M., 2013, Early Cretaceous sedimentation and orogeny on the active margin of Eurasia: Southern Central Pontides, Turkey: Tectonics, v. 32, p. 1247–1271, doi:10.1002/tect.20077.

Okay, A.I., Tansel, I., and TüYsüZ, O., 2001, Obduction, subduction and collision as reflected in the Upper Cretaceous–Lower Eocene sedimentary record of western Turkey: Geological Magazine, v. 138, doi:10.1017/S0016756801005088.

Okay, A.I., and Topuz, G., 2017, Variscan orogeny in the Black Sea region: International Journal of Earth Sciences, v. 106, p. 569–592, doi:10.1007/s00531-016-1395-z.

Okay, A.I., Tüysüz, O., Satır, M., Özkan-Altiner, S., Altiner, D., Sherlock, S., and Eren, R.H., 2006, Cretaceous and Triassic subduction-accretion, high-pressure–low-temperature metamorphism, and continental growth in the Central Pontides, Turkey: GSA Bulletin, v. 118, p. 1247–1269, doi:10.1130/B25938.1.

Okay, A.I., and Whitney, D.L., 2010, Blueschists, Eclogites, Ophiolites and Suture Zones in Northwest Turkey: A Review and a Field Excursion Guide: Ofioliti, v. 35, p. 131–172.

Okay, N., Zack, T., Okay, A.I., and Barth, M., 2011, Sinistral transport along the Trans-European Suture Zone: detrital zircon–rutile geochronology and sandstone petrography from the Carboniferous flysch of the Pontides: Geological Magazine, v. 148, p. 380–403, doi:10.1017/S0016756810000804.

Okay, A.I., Zattin, M., and Cavazza, W., 2010, Apatite fission-track data for the Miocene Arabia-Eurasia collision: Geology, v. 38, p. 35–38, doi:10.1130/G30234.1.

Özcan, Z., Okay, A.I., Özcan, E., Hakyemez, A., and Özkan-Altiner, S., 2012, Late Cretaceous–Eocene Geological Evolution of the Pontides Based on New Stratigraphic and Palaeontologic Data Between the Black Sea Coast and Bursa (NW Turkey): Turkish Journal of Earth Sciences, v. 21, p. 933–960, doi:10.3906/yer-1102-8.

Özcan, E., Özcan, Z., Okay, A.I., Akbayram, K., and Hakyemez, A., 2019, The Ypresian to Lutetian marine record in NW Turkey: a revised biostratigraphy and chronostratigraphy and implications for Eocene paleogeography: Turkish Journal of Earth Sciences, v. 28, p. 27.

Özdamar, Ş., Sunal, G., Demiroğlu, M., Yaltirak, C., Billor, M.Z., Georgiev, S., Hames, W., Dunkl, I., and Aydin, H.C., 2018, Metamorphism, magmatism, and exhumation history of the Tavşanlı Zone, NW Turkey: new petrological constraints: TURKISH JOURNAL OF EARTH SCIENCES, v. 27, p. 269–293, doi:10.3906/yer-1712-14.

Özgen-Erdem, N., Akyazı, M., and Karabaşoğlu, A., 2007, Biostratigraphic interpretation and systematics of Alveolina assemblages from the Ilerdian–Cuisian limestones of Southern Eskişehir, Central Turkey: Journal of Asian Earth Sciences, v. 29, p. 911–927, doi:10.1016/j.jseaes.2006.05.010.

Paces, J.B., and Miller, J.D., 1993, Precise U-Pb ages of Duluth Complex and related mafic intrusions, northeastern Minnesota: Geochronological insights to physical, petrogenetic, paleomagnetic, and tectonomagmatic processes associated with the 1.1 Ga Midcontinent Rift System: Journal of Geophysical Research: Solid Earth, v. 98, p. 13997–14013, doi:10.1029/93JB01159.

Paola, C., Heller, P.L., and Angevine, C.L., 1992, The large-scale dynamics of grain-size variation in alluvial basins, 1: Theory: Basin Research, v. 4, p. 73–90.

Parker, S.D., and Pearson, D.M., 2021, Pre-Thrusting Stratigraphic Control on the Transition From a Thin-Skinned to Thick-Skinned Structural Style: An Example From the Double-Decker Idaho-Montana Fold-Thrust Belt: Tectonics, v. 40, p. e2020TC006429, doi:https://doi.org/10.1029/2020TC006429.

Paterson, S.R., and Ducea, M.N., 2015, Arc Magmatic Tempos: Gathering the Evidence: Elements, v. 11, p. 91–98, doi:10.2113/gselements.11.2.91.

Paton, C., Hellstrom, J., Paul, B., Woodhead, J., and Hergt, J., 2011, Iolite: Freeware for the visualisation and processing of mass spectrometric data: Journal of Analytical Atomic Spectrometry, v. 26, p. 2508, doi:10.1039/c1ja10172b.

Pereira, I., Storey, C.D., Strachan, R.A., Bento dos Santos, T., and Darling, J.R., 2020, Detrital rutile ages can deduce the tectonic setting of sedimentary basins: Earth and Planetary Science Letters, v. 537, p. 116193, doi:10.1016/j.epsl.2020.116193.

Plunder, A., Agard, P., Chopin, C., and Okay, A.I., 2013a, Geodynamics of the Tavşanlı zone, western Turkey: Insights into subduction/obduction processes: Tectonophysics, v. 608, p. 884–903, doi:10.1016/j.tecto.2013.07.028.

Plunder, A., Agard, P., Chopin, C., and Okay, A., 2013b, Tectono-metamorphic evolution of the Tavşanli zone, Western Anatolia: implications for mechanical coupling during subduction/obduction processes, *in* v. 15, p. EGU2013-8404, http://adsabs.harvard.edu/abs/2013EGUGA..15.8404P (accessed June 2018).

Plunder, A., Agard, P., Chopin, C., Pourteau, A., and Okay, A.I., 2015, Accretion, underplating and exhumation along a subduction interface: From subduction initiation to continental

subduction (Tavşanlı zone, W. Turkey): Lithos, v. 226, p. 233–254, doi:10.1016/j.lithos.2015.01.007.

Plunder, A., Plunder, A., Thieulot, C., and Hinsbergen, D.J.J. van, 2018, The effect of obliquity on temperature in subduction zones: insights from 3-D numerical modeling: Solid Earth, v. 9, p. 759–776.

Portner, D.E., Delph, J.R., Biryol, C.B., Beck, S.L., Zandt, G., Özacar, A.A., Sandvol, E., and Türkelli, N., 2018, Subduction termination through progressive slab deformation across Eastern Mediterranean subduction zones from updated P-wave tomography beneath Anatolia: Geosphere, v. 14, p. 907–925, doi:10.1130/GES01617.1.

Pourteau, A., Candan, O., and Oberhänsli, R., 2010, High-pressure metasediments in central Turkey: Constraints on the Neotethyan closure history: Tectonics, v. 29, doi:10.1029/2009TC002650.

Pourteau, A., Oberhänsli, R., Candan, O., Barrier, E., and Vrielynck, B., 2016, Neotethyan closure history of western Anatolia: a geodynamic discussion: International Journal of Earth Sciences, v. 105, p. 203–224, doi:10.1007/s00531-015-1226-7.

Pourteau, A., Scherer, E.E., Schorn, S., Bast, R., Schmidt, A., and Ebert, L., 2019, Thermal evolution of an ancient subduction interface revealed by Lu–Hf garnet geochronology, Halilbağı Complex (Anatolia): Geoscience Frontiers, v. 10, p. 127–148, doi:10.1016/j.gsf.2018.03.004.

Pourteau, A., Sudo, M., Candan, O., Lanari, P., Vidal, O., and Oberhänsli, R., 2013, Neotethys closure history of Anatolia: insights from ^{40}Ar-^{39}Ar geochronology and *P*-*T* estimation in high-pressure metasedimentary rocks: Journal of Metamorphic Geology, v. 31, p. 585–606, doi:10.1111/jmg.12034.

Prothero, D.R., and Schwab, F., 1996, Sedimentary geology: An introduction to sedimentary rocks and stratigraphy: New York, W. H. Freeman, 593 p.

de Queiroz, A., 2014, The Monkey's Voyage: How Improbable Journeys Shaped the History of Life: Basic Books, 370 p.

Racey, A., 2001, A review of Eocene nummulite accumulations: Structure, formation and reservoir potential: Journal of Petroleum Geology, v. 24, p. 79–100, doi:10.1111/j.1747-5457.2001.tb00662.x.

Raymo, M.E., and Ruddiman, W.F., 1992, Tectonic forcing of late Cenozoic climate: Nature, v. 359, p. 117–122, doi:10.1038/359117a0.

Retallack, G.J., 1988, Field recognition of paleosols: Special Paper of the Geological Society of America, v. 216, p. 1–20, doi:10.1130/SPE216-p1.

Robertson, A.H.F., Parlak, O., and Ustaömer, T., 2009, Melange genesis and ophiolite emplacement related to subduction of the northern margin of the Tauride–Anatolide continent, central and western Turkey: Geological Society, London, Special Publications, v. 311, p. 9–66, doi:10.1144/SP311.2.

Robertson, A.H.F., and Ustaömer, T., 2004, Tectonic evolution of the Intra-Pontide suture zone in the Armutlu Peninsula, NW Turkey: Tectonophysics, v. 381, p. 175–209, doi:10.1016/j.tecto.2002.06.002.

Rösel, D., Zack, T., and Boger, S.D., 2014, LA-ICP-MS U–Pb dating of detrital rutile and zircon from the Reynolds Range: A window into the Palaeoproterozoic tectonosedimentary evolution of the North Australian Craton: Precambrian Research, v. 255, p. 381–400, doi:10.1016/j.precamres.2014.10.006.

Rösel, D., Zack, T., and Möller, A., 2019, Interpretation and significance of combined trace element and U–Pb isotopic data of detrital rutile: a case study from late Ordovician sedimentary rocks of Saxo-Thuringia, Germany: International Journal of Earth Sciences, v. 108, p. 1–25, doi:10.1007/s00531-018-1643-5.

Rosenblum, S., and Brownfield, I.K., 2000, Magnetic susceptibilities of minerals: U.S. Geological Survey Open-File Report USGS Numbered Series 99–529, doi:10.3133/ofr99529.

Rowley, D.B., Pierrehumbert, R.T., and Currie, B.S., 2001, A new approach to stable isotope-based paleoaltimetry: implications for paleoaltimetry and paleohypsometry of the High Himalaya since the Late Miocene: Earth and Planetary Science Letters, v. 188, p. 253–268, doi:10.1016/S0012-821X(01)00324-7.

Royden, L.H., 1993, Evolution of retreating subduction boundaries formed during continental collision: Tectonics, v. 12, p. 629–638, doi:10.1029/92TC02641.

Royden, L., and Burchfiel, B.C., 1989, Are systematic variations in thrust belt style related to plate boundary processes? (The western Alps versus the Carpathians): Tectonics, v. 8, p. 51–61, doi:10.1029/TC008i001p00051.

Ruhl, K.W., and Hodges, K.V., 2005, The use of detrital mineral cooling ages to evaluate steady state assumptions in active orogens: An example from the central Nepalese Himalaya: Tectonics, v. 24, doi:10.1029/2004TC001712.

Şahin, M., Yaltırak, C., and Karacık, Z., 2019, A case study of compression to escape tectonic transition: Tectonic evolution of the Nallıhan Wedge and comparison with the Tercan Wedge (Eastern Mediterranean, Turkey): Journal of Asian Earth Sciences, v. 174, p. 311–331, doi:10.1016/j.jseaes.2018.12.016.

Sarıfakıoğlu, E., Dilek, Y., and Sevin, M., 2017, New synthesis of the Izmir-Ankara-Erzincan suture zone and the Ankara mélange in northern Anatolia based on new geochemical and geochronological constraints, *in* Sorkhabi, R. ed., Tectonic Evolution, Collision, and Seismicity of Southwest Asia: In Honor of Manuel Berberian's Forty-Five Years of Research Contributions, Geological Society of America Special Paper, v. 525, p. 1–63, https://doi.org/10.1130/2017.2525(19).

Schildgen, T.F., Cosentino, D., Bookhagen, B., Niedermann, S., Yıldırım, C., Echtler, H., Wittmann, H., and Strecker, M.R., 2012, Multi-phased uplift of the southern margin of the Central Anatolian plateau, Turkey: A record of tectonic and upper mantle processes: Earth and Planetary Science Letters, v. 317–318, p. 85–95, doi:10.1016/j.epsl.2011.12.003.

Schleiffarth, W.K., Darin, M.H., Reid, M.R., and Umhoefer, P.J., 2018, Dynamics of episodic Late Cretaceous–Cenozoic magmatism across Central to Eastern Anatolia: New insights from an extensive geochronology compilation: Geosphere, v. 14, p. 1990–2008, doi:10.1130/GES01647.1.

Seaton, N.C.A., Whitney, D.L., Teyssier, C., Toraman, E., and Heizler, M.T., 2009, Recrystallization of high-pressure marble (Sivrihisar, Turkey): Tectonophysics, v. 479, p. 241–253, doi:10.1016/j.tecto.2009.08.015.

Sen, S., 2013, Dispersal of African mammals in Eurasia during the Cenozoic: Ways and whys: Geobios, v. 46, p. 159–172, doi:10.1016/j.geobios.2012.10.012.

Şengör, A.M.C., 1979, Mid-Mesozoic closure of Permo–Triassic Tethys and its implications: Nature, v. 279, p. 590–593, doi:10.1038/279590a0.

Şengör, A.M.C., Tüysüz, O., İmren, C., Sakınç, M., Eyidoğan, H., Görür, N., Le Pichon, X., and Rangin, C., 2005, The North Anatolia Fault: A New Look: Annual Review of Earth and Planetary Sciences, v. 33, p. 37–112, doi:10.1146/annurev.earth.32.101802.120415.

Şengör, A.M.C., and Yilmaz, Y., 1981, Tethyan evolution of turkey: a plate tectonic approach: Tectonophysics, v. 75, p. 181–241.

Şengüler, İ., and Izladi, E., 2013, Neogene stratigraphy of the Eskişehir Graben and the investigation of coal deposition by seismic reflection method: Bulletin of MTA, v. 146, p. 105–116.

Sharman, G.R., Sharman, J.P., and Sylvester, Z., 2018, detritalPy: A Python-based toolset for visualizing and analysing detrital geo-thermochronologic data: The Depositional Record, v. 4, p. 202–215, doi:10.1002/dep2.45.

Shekut, S., and Licht, A., 2020, Late Middle Miocene Emergence of the Olympic Peninsula Shown by Sedimentary Provenance: Lithosphere, v. 2020, p. 1–20, doi:10.2113/2020/7040598.

Sherlock, S., Kelley, S., Inger, S., Harris, N., and Okay, A., 1999, 40Ar-39Ar and Rb-Sr geochronology of high-pressure metamorphism and exhumation history of the Tavsanli Zone, NW Turkey: Contributions to Mineralogy and Petrology, v. 137, p. 46–58, doi:10.1007/PL00013777.

Shield, A.E., Paris, D., Paris, R., and Sab Pedro, T. (Eds.), 2020, Education in movement spaces: Standing Rock to Chicago Freedom Square: New York, Routledge, v. 67, 174 p., https://doi.org/10.1007/s11159-021-09894-x (accessed August 2021).

Shin, T.A., Catlos, E.J., Jacob, L., and Black, K., 2013, Relationships between very high pressure subduction complex assemblages and intrusive granitoids in the Tavşanlı Zone, Sivrihisar Massif, central Anatolia: Tectonophysics, v. 595–596, p. 183–197, doi:10.1016/j.tecto.2012.07.012.

Simpson, L.B., 2014, Land as pedagogy: Nishnaabeg intelligence and rebellious transformation: Decolonization: Indigeneity, Education & Society, v. 3, p. 25.

Sinclair, H.D., 1997, Flysch to molasse transition in peripheral foreland basins: The role of the passive margin versus slab breakoff: Geology, v. 25, p. 1123–1126.

Sláma, J. et al., 2008, Plešovice zircon — A new natural reference material for U–Pb and Hf isotopic microanalysis: Chemical Geology, v. 249, p. 1–35, doi:10.1016/j.chemgeo.2007.11.005.

Soret, M., Larson, K.P., Cottle, J., and Ali, A., 2021, How Himalayan collision stems from subduction: Geology, doi:10.1130/G48803.1.

Speciale, P.A., Catlos, E.J., Yıldız, G.O., Shin, T.A., and Black, K.N., 2012, Zircon ages from the Beypazarı granitoid pluton (north central Turkey): tectonic implications: Geodinamica Acta, v. 25, p. 162–182, doi:10.1080/09853111.2013.858955.

Stampfli, G.M., and Borel, G.D., 2002, A plate tectonic model for the Paleozoic and Mesozoic constrained by dynamic plate boundaries and restored synthetic oceanic isochrons: Earth and Planetary Science Letters, v. 196, p. 17–33, doi:10.1016/S0012-821X(01)00588-X.

Steiger, R.H., and Jäger, E., 1977, Subcommission on geochronology: Convention on the use of decay constants in geo- and cosmochronology: Earth and Planetary Science Letters, v. 36, p. 359–362, doi:10.1016/0012-821X(77)90060-7.

Sundell, K., Saylor, J.E., and Pecha, M., 2019, Provenance and recycling of detrital zircons from Cenozoic Altiplano strata and the crustal evolution of western South America from combined U-Pb and Lu-Hf isotopic analysis, *in* Andean Tectonics, Elsevier, p. 363–397, doi:10.1016/B978-0-12-816009-1.00014-9.

Tera, F., and Wasserburg, G.J., 1972, U-Th-Pb systematics in three Apollo 14 basalts and the problem of initial Pb in lunar rocks: Earth and Planetary Science Letters, v. 14, p. 281–304, doi:10.1016/0012-821X(72)90128-8.

Timur, E., and Aksay, A., 2002, Geological map of the Adapazari quadrangle (Sheet H 26, Scale 1:100,000): Maden Tetkik ve Arma Genel Müdürlüğü 1:100,000 scale geological maps of Turkey.

Tomkins, H.S., Powell, R., and Ellis, D.J., 2007, The pressure dependence of the zirconium-in-rutile thermometer: Journal of Metamorphic Geology, v. 25, p. 703–713, doi:https://doi.org/10.1111/j.1525-1314.2007.00724.x.

Triebold, S., von Eynatten, H., and Zack, T., 2012, A recipe for the use of rutile in sedimentary provenance analysis: Sedimentary Geology, v. 282, p. 268–275, doi:10.1016/j.sedgeo.2012.09.008.

Triebold, S., Luvizotto, G.L., Tolosana-Delgado, R., Zack, T., and von Eynatten, H., 2011, Discrimination of TiO2 polymorphs in sedimentary and metamorphic rocks: Contributions to Mineralogy and Petrology, v. 161, p. 581–596, doi:10.1007/s00410-010-0551-x.

Tuck, E., and Yang, K.W., 2012, Decolonization is not a metaphor: Decolonization: Indigeneity, Education & Society, v. 1, p. 40.

Turhan, N., 2002, Geologic map of Turkey (Ankara, Scale 1:500,000): Maden Tetkik ve Arma Genel Müdürlüğü.

Tüysüz, O., 1999, Geology of the Cretaceous sedimentary basins of the Western Pontides: Geological Journal, v. 34, p. 75–93.

Tye, A.R., Niemi, N.A., Safarov, R.T., Kadirov, F.A., and Babayev, G.R., 2020, Sedimentary response to a collision orogeny recorded in detrital zircon provenance of Greater Caucasus foreland basin sediments: Basin Research, v. n/a, doi:10.1111/bre.12499.

Uğuz, M.F., 2013, A New Age Finding in the Central Sakarya Region (NW Turkey): Bulletin of MTA, v. 146, p. 1–25.

Ustaömer, P.A., Mundil, R., and Renne, P.R., 2005, U/Pb and Pb/Pb zircon ages for arc-related intrusions of the Bolu Massif (W Pontides, NW Turkey): evidence for Late Precambrian (Cadomian) age: Terra Nova, v. 17, p. 215–223, doi:10.1111/j.1365-3121.2005.00594.x.

Ustaömer, P.A., Ustaömer, T., Collins, A.S., and Reischpeitsch, J., 2009, Lutetian arc-type magmatism along the southern Eurasian margin: New U-Pb LA-ICPMS and whole-rock geochemical data from Marmara Island, NW Turkey: Mineralogy and Petrology, v. 96, p. 177–196, doi:10.1007/s00710-009-0051-8.

Ustaömer, P., Ustaömer, T., Gerdes, A., and Zulauf, G., 2011, Detrital zircon ages from a Lower Ordovician quartzite of the Istanbul exotic terrane (NW Turkey): evidence for Amazonian affinity: International Journal of Earth Sciences : Geologische Rundschau; Berlin, v. 100, p. 23–41, doi:http://dx.doi.org/10.1007/s00531-009-0498-1.

Ustaömer, P., Ustaömer, T., and Robertson, Alastair.H.F., 2012, Ion Probe U-Pb Dating of the Central Sakarya Basement: A peri-Gondwana Terrane Intruded by Late Lower Carboniferous Subduction/Collision-related Granitic Rocks: Turkish Journal of Earth Sciences, v. 21, p. 905–932, doi:10.3906/yer-1103-1.

Ustaömer, T., Ustaömer, P., Robertson, A.H.F., and Gerdes, A., 2016, Implications of U–Pb and Lu–Hf isotopic analysis of detrital zircons for the depositional age, provenance and tectonic setting of the Permian–Triassic Palaeotethyan Karakaya Complex, NW Turkey: International Journal of Earth Sciences, v. 105, p. 7–38, doi:10.1007/s00531-015-1225-8.

Vermeesch, P., 2018, IsoplotR: A free and open toolbox for geochronology: Geoscience Frontiers, v. 9, p. 1479–1493, doi:10.1016/j.gsf.2018.04.001.

Vermeesch, P., 2013, Multi-sample comparison of detrital age distributions: Chemical Geology, v. 341, p. 140–146, doi:10.1016/j.chemgeo.2013.01.010.

Walsh, J.J., and Watterson, J., 1988, Analysis of the relationship between displacements and dimensions of faults: Journal of Structural Geology, v. 10, p. 239–247, doi:10.1016/0191-8141(88)90057-0.

Wang, J., Hu, X., Jansa, L., and Huang, Z., 2011, Provenance of the Upper Cretaceous–Eocene Deep-Water Sandstones in Sangdanlin, Southern Tibet: Constraints on the Timing of Initial India-Asia Collision: The Journal of Geology, v. 119, p. 293–309, doi:10.1086/659145.

Whitney, D.L., and Davis, P.B., 2006, Why is lawsonite eclogite so rare? Metamorphism and preservation of lawsonite eclogite, Sivrihisar, Turkey: Geology, v. 34, p. 473–476, doi:10.1130/G22259.1.

Whitney, D.L., Teyssier, C., Toraman, E., Seaton, N.C.A., and Fayon, A.K., 2011, Metamorphic and tectonic evolution of a structurally continuous blueschist-to-Barrovian terrane, Sivrihisar Massif, Turkey: Journal of Metamorphic Geology, v. 29, p. 193–212, doi:https://doi.org/10.1111/j.1525-1314.2010.00915.x.

Whittaker, R.J., Fernández-Palacios, J.M., Matthews, T.J., Borregaard, M.K., and Triantis, K.A., 2017, Island biogeography: Taking the long view of nature's laboratories: Science, v. 357, p. eaam8326, doi:10.1126/science.aam8326.

Whyte, K.P., 2018, Food Sovereignty, Justice, and Indigenous Peoples (A. Barnhill, M. Budolfson, & T. Doggett, Eds.): Oxford University Press, v. 1, doi:10.1093/oxfordhb/9780199372263.013.34.

Wildcat, D.R., 2001, Understanding the crisis in American Education, *in* Deloria, V. and Wildcat, D.R. eds., Power and place: Indian education in America, Golden, Colo, Fulcrum Pub.

Willett, S.D., and Brandon, M.T., 2002, On steady states in mountain belts: Geology, v. 30, p. 175, doi:10.1130/0091-7613(2002)030<0175:OSSIMB>2.0.CO;2.

Wotzlaw, J.-F., Schaltegger, U., Frick, D.A., Dungan, M.A., Gerdes, A., and Günther, D., 2013, Tracking the evolution of large-volume silicic magma reservoirs from assembly to supereruption: Geology, v. 41, p. 867–870, doi:10.1130/G34366.1.

Yaliniz, M.K., Göncüoğlu, M.C., and Ozkan-Altiner, S., 2000, Formation and emplacement ages of the SSZ-type Neotethyan ophiolites in Central Anatolia, Turkey: palaeotectonic implications: Geological Journal, v. 35, p. 53–68, doi:10.1002/1099-1034(200004/06)35:2<53::AID-GJ837>3.0.CO;2-6.

Yiğitbaş, E., Elmas, A., and Yïlmaz, Y., 1999, Pre-Cenozoic tectono-stratigraphic components of the Western Pontides and their geological evolution: Geological Journal, v. 34, p. 55–74, doi:10.1002/(SICI)1099-1034(199901/06)34:1/2<55::AID-GJ814>3.0.CO;2-0.

Yildiz, A., Kibici, Y., Bağci, M., Dumlupunar, İ., Kocabaş, C., and Aritan, A.E., 2015, Petrogenesis of the post-collisional Eocene volcanic rocks from the Central Sakarya Zone (Northwestern Anatolia, Turkey): Implications for source characteristics, magma evolution, and tectonic setting: Arabian Journal of Geosciences, v. 8, p. 11239–11260, doi:10.1007/s12517-015-1991-4.

Yilmaz, I.O., Altiner, D., Tekin, U.K., Tuysuz, O., Ocakoglu, F., and Acikalin, S., 2010, Cenomanian – Turonian Oceanic Anoxic Event (OAE2) in the Sakarya Zone, northwestern Turkey: Sedimentological, cyclostratigraphic, and geochemical records: Cretaceous Research, v. 31, p. 207–226, doi:10.1016/j.cretres.2009.10.005.

Yin, A., and Harrison, T.M., 2000, Geologic Evolution of the Himalayan-Tibetan Orogen: Annual Review of Earth and Planetary Sciences, v. 28, p. 211–280, doi:10.1146/annurev.earth.28.1.211.

Zachos, J., Pagani, M., Sloan, L., Thomas, E., and Billups, K., 2001, Trends, Rhythms, and Aberrations in Global Climate 65 Ma to Present: Science, v. 292, p. 686–693, doi:10.1126/science.1059412.

Zack, T., von Eynatten, H., and Kronz, A., 2004a, Rutile geochemistry and its potential use in quantitative provenance studies: Sedimentary Geology, v. 171, p. 37–58, doi:10.1016/j.sedgeo.2004.05.009.

Zack, T., and Kooijman, E., 2017, Petrochronology and Geochronology of Rutile (M. J. Kohn, M. Engi, & P. Lanari, Eds.): Reviews in Mineralogy and Geochemistry, v. 83, p. 443–467.

Zack, T., Moraes, R., and Kronz, A., 2004b, Temperature dependence of Zr in rutile: empirical calibration of a rutile thermometer: Contributions to Mineralogy and Petrology, v. 148, p. 471–488, doi:10.1007/s00410-004-0617-8.

Zack, T., Stockli, D.F., Luvizotto, G.L., Barth, M.G., Belousova, E., Wolfe, M.R., and Hinton, R.W., 2011, In situ U–Pb rutile dating by LA-ICP-MS: 208Pb correction and prospects for geological applications: Contributions to Mineralogy and Petrology, v. 162, p. 515–530, doi:10.1007/s00410-011-0609-4.

Zeitler, P.K., Meltzer, A.S., Koons, P.O., Craw, D., and Hallet, B., 2001, Erosion, Himalayan Geodynamics, and the Geomorphology of Metamorphism: GSA TODAY, p. 6.

Zhang, Z., Ramstein, G., Schuster, M., Li, C., Contoux, C., and Yan, Q., 2014, Aridification of the Sahara desert caused by Tethys Sea shrinkage during the Late Miocene: Nature, v. 513, p. 401–404, doi:10.1038/nature13705.

Appendix A.
Geochronologic and Geochemical Methods

Zircon U-Pb Dating Methods at the University of Washington

Our methods follow the zircon U-Pb geochronology protocol at the University of Washington, first reported in Licht et al. (2018) and updated in Shekut and Licht (2020). All samples in Chapter 2 and all samples except three in Chapter 3 were analyzed at the University of Washington. Metadata are given in Table A.1.

Zircon Extraction

At the University of Washington, traditional methods are used to extract zircon crystals from samples of 1 to 5 kg. Crushing and grinding is followed by separation with a Holman-Wilfley gravity shaking table, heavy liquids (methylene iodide), and Frantz magnetic separator. Aliquots of 100-1000 zircons (less for samples with poor zircon yields), including all grain sizes, are mounted in 1”-diameter epoxy cups with fragments of zircon standards. The mounts are polished to expose the internal structure of the zircon grains, then imaged with a backscattered electron detector with a JEOL 733 Superprobe microprobe backscattered electron detector (BSE) or TFS Apreo-S with Lovac Scanning Electron Microscope (SEM) to distinguish zircon from other heavy minerals. Finally, the epoxy mounts are polished again in preparation for isotopic analysis.

Zircon Standards

We use a suite of international and in-house standards for calibration. The Plešovice (PLS) international standard zircon is used as the primary standard, and has an ID-TIMS U–Pb age of 337.13±0.37 Ma (2s) (Sláma et al., 2008). The secondary standards are FC-1, with an ID-TIMS age of 1099.5 ± 0.33 Ma (2σ) (Paces and Miller, 1993), R33, with an ID-TIMS age of 419.26±0.39 Ma (2s) (Black et al., 2004), and Green Horn Batholith (GHB), the internal standard at the

University of Washington. The GHB standard has an average CA-ID-TIMS age of 48.20±0.02 Ma (2s) (Eddy et al., 2016) and comes from the hypersolvus granite of the Golden Horn Batholith in the North Cascades Mountains, WA.

LA-ICP-MS

Zircon U-Pb geochronology analyses at the University of Washington are conducted via laser ablation-inductively coupled plasma-mass spectrometry (LA-ICP-MS) with an iCAP RQ Quadrupole ICP-MS coupled to an Analyte G2 excimer laser. The ICP-MS is tuned daily using the QTegra auto-tuning plug-in with custom in-house tuning parameters and NIST SRM 612 reference material glass to yield Th/U ratios close to unity (typically between 0.95 and 1.05) and low oxide production rates (ThO+/Th+ typically < 0.15%) while keeping 238U sensitivity high.

For each detrital sample, ~100-300 zircon grains (> 25-μm diameter) are selected for ablation; for each volcaniclastic sample, ~10-100 zircon grains are selected. Small-*n* zircon analyses are limited by the number of zircons in the sample. All zircons—standards and unknowns—are pre-ablated with an Analyte G2 excimer laser operating at a 193-nm wavelength and 10-Hz pulse repetition rate before the analytical session: 2 ablation shots with a laser spot diameter at 50 microns and fluence of 1.47 J/cm2. The zircons are ablated with an Analyte G2 excimer laser operating at a 193-nm wavelength, 25-μm spot diameter, 10-Hz pulse repetition rate, and 4.12 J/cm^2 energy fluence. The ablated material is carried in helium gas and mixed with nitrogen gas into the plasma source of an iCAP RQ Quadrupole ICP-MS. Each 40-s analysis consists of (1) a background baseline established by a 10-s integration on peaks with the laser off, (2) 38 s of acquisition with the laser firing, and (3) a 17-s delay to purge the previous sample and prepare for the next analysis. Analyzed masses include ^{238}U, ^{235}U, ^{232}Th, ^{207}Pb, ^{206}Pb, and ^{204}Pb, for a total, combined dwell time of ~0.4 s.

Data Reduction and Presentation

Data reduction is performed with the Geochron Data Reduction Scheme in *Iolite* to get U-Pb ages uncorrected for common lead (^{204}Pb) (Paton et al., 2011), and with the Andersen Routine of the *Vizualage* Data Reduction scheme (Chew et al., 2014) to correct U-Pb ages common lead. To ensure that grains with a complex history (e.g., inheritance, Pb loss, overgrowths, or detectable amount of ^{204}Pb) do not compromise data quality, the time-resolved pattern of ^{206}Pb/^{238}U is scrutinized during data reduction, and analyses with abnormal patterns (e.g., different fractionation from standards or jumps in value) are rejected (e.g. Gehrels, 2012, 2014).

The U-Pb results are presented in three ways: (1) measured isotopic ratios corrected for downhole fractionation and instrument bias with *Iolite,* (2) U-Pb ages uncorrected for common lead, and (3) U-Pb ages corrected for common lead using the Andersen Routine. The measurement errors for each analysis result in ~1-3% (2s) uncertainty for the ^{206}Pb/^{238}U age. Similarly, the measurement error results in ~1-3% (2s) uncertainty for ^{206}Pb/^{207}Pb ages that are >1 Ga, but the low intensity ^{207}Pb signal produces significantly larger uncertainties in the <1.0 Ga ages. The crossover precision from the ^{206}Pb/^{238}U to ^{206}Pb/^{207}Pb ages occurs at ~1.2 to 1.4 Ga. For this reason, the best age for every analysis is determined from the ^{206}Pb/^{238}U age for analyses with a ^{206}Pb /^{238}U age < 1.2 Ga for Chapter 2 and <1.4 Ga for Chapter 3 and from the ^{206}Pb/^{207}Pb age for analyses with ^{206}Pb /^{238}U age above the crossover age.

Shekut and Licht (2020) presented two years of analyses of igneous ages and found additional systematic uncertainty during the sessions: ~2.67% for 206Pb/238U ratio, and ~1.17% for 206Pb/207Pb ratio (2s). This is a conservative estimate.

Discordant data are present in the supplementary data tables but omitted from the results and interpretation. Ages are marked as “discordant” if: (1) the 206Pb/238U age is >1300 Ma and

with >20% discordance (<80% concordance) or with >5% reverse discordance (<105% concordance) following the ratio of 206Pb/238U and 206Pb/207Pb ages; or (2) the 206Pb/238U age is between 300 and 1300 Ma and with >20% discordance (<80% concordance) or with >5% reverse discordance (<105% concordance) following the ratio of 207Pb/235U and 206Pb/238U ages. Ages are noted as "high age uncertainty" zircons and excluded when the "Best Age" 2s error is >20%.

Protocol Calibration and Accuracy

The University of Washington protocol is regularly tested with our in-house GHB standard and a suite of international standards. The accuracy of measurements is detailed in (Licht et al., 2018), but, in short, the ages uncorrected for common lead for all standards are offset by < 1.5% from the TIMS U-Pb age. Ages corrected for common lead display a larger offset (~1.5% to 3-5% for Proterozoic grains), so we prefer ages uncorrected for common lead.

The uncertainty resulting from the calibration correction is generally 1-2% (2-sigma) for both $^{206}Pb/^{207}Pb$ and $^{206}Pb/^{238}U$ ages. Uncertainties from this calibration correction are not included in the age uncertainties provided in the supporting information and should be combined (quadratically) with the uncertainty of the age of the standard to yield an external uncertainty for each sample. Therefore, we provide a minimum uncertainty for each set of analyses. However, we do report the volcaniclastic zircon U-Pb age uncertainty including the 1.3% modeling error in Table 2.2.

Zircon U-Pb Geochronology Methods at the University of Kansas IGL

Three samples presented in Chapter 3—15YP15, 090717-6 and 090717-16—were analyzed at the University of Kansas Isotope Geochemistry Laboratory (IGL) following the U-Pb analytical protocol outlined in Campbell (2017). Metadata are given in Table A.2.

Detrital Rutile U-Pb Geochronology Methods

Rutile Extraction

Conventional heavy mineral separation methods were used to extract rutile crystals from samples of 1 to 5 kg. Crushing and grinding was followed by water table separation with a Holman-Wilfley or Gemeni table then heavy liquids (methylene iodide). The Frantz magnetic separator was set to 20° side slope and 20° forward slope such that rutile grains were separated into the 0.3 to 0.7 amp. fraction (Rosenblum and Brownfield, 2000). Rutile grains were handpicked with a Leica M205C binocular microscope using transmitted and polarized light. Rutile grains were identified by red-brown-yellow color in reflected light, red to opaque in PPL, resinous to vitreous luster; grains were well rounded to euhedral, many displaying twinning characteristic of rutile's tetragonal crystal system and striations parallel to the long axis. Grains were placed on Kapton tape and mounted in epoxy in 25-mm diameter cups. The mounts were polished to expose the internal structure of the grains.

Rutile mounts were carbon coated (10 nm) and imaged with a TFS Apreo-S with Lovac Scanning Electron Microscope (SEM) using an energy-dispersive (EDS) detector to distinguish rutile grains from other spurious heavy minerals. The carbon coat was removed with isopropanol and in an ultrasonic, then by polishing the mounts with 1-μm and 0.25-μm grit in felt. Samples were soaked in 2M nitric acid (HNO_3) in the ultrasonic, then in ultra-pure water in the ultrasonic.

Rutile Standards and Protocol Accuracy

The accuracy of the protocol was evaluated using a suite of international standards. The concordia age for the reference materials over 3 analytical sessions reproduces the published ages (Figure A.1): 1090 Ma (n=155) for R10 is within 0.1% of the TIMS age (1091.6 Ma; Luvizotto et al., 2009); 2824 Ma (n=47) for Wodgina is within 0.8% of the TIMS age (2845.8 Ma; Ewing, 2011); 1087 Ma (n=18) for Kragerø is within 1.7% of the TIMS age (1085.7 Ma; Kellett et al., 2018); 380 Ma (n=50) for 9826J is within 0.5% of the TIMS age (382 Ma; Kylander-Clark, 2008); 498 Ma for LJ04-08 (n=32) is within 4% of the LA-ICP-MS age (498 Ma; Apen et al., 2020).

Many of the Wodgina analyses display an atypical downhole fractionation pattern (Figure A.2). The Pb signal increased throughout the analysis. This is a problem because it means that the downhole fractionation correction, based on the calibration standard R10, does not work for the atypical grains. This could explain the large discordance in many Wodgina analyses (Figure A.1). This finding suggests that the use of Wodgina as a LA-ICP-MS reference material needs more investigation.

LA-ICP-MS

Detrital rutile U-Pb geochronology analyses at the University of Kansas Isotope Geochemistry Lab (IGL) are conducted via laser ablation-inductively coupled plasma-mass spectrometry (LA-ICP-MS) with a Thermo Element2 magnetic sector field ICP-MS coupled to a Photon Machines AnalyteG2 excimer laser ablation system. We used a modified protocol from Rösel et al. (2019). an iCAP RQ Quadrupole ICP-MS coupled to an Analyte G2 excimer laser. The ICP-MS is tuned daily manually using NIST SRM 612 reference material glass to yield Th/U ratios close to 0.8 and low oxide production rates while keeping ^{238}U sensitivity high. We spent a

significant amount of time adjusting the analytical parameters and present the final methods in Table A.3.

Data Reduction and Presentation

Data reduction is performed with the U-Pb Geochronology Data Reduction Scheme in *Iolite 4* to get U-Pb ages uncorrected for common lead (Paton et al., 2011). To ensure that grains with a complex history (e.g., inheritance, Pb loss, or overgrowths) or inclusions do not compromise data quality, the time-resolved pattern of ^{206}Pb, ^{232}Th, and ^{238}U counts per second are scrutinized during data reduction. Analyses with abnormal patterns (e.g., different fractionation from standards or jumps in value) are not rejected in *Iolite*, but instead the analyses are rejected by the >15% discordance cutoff for $^{207}Pb/^{206}Pb$ ratios. The U-Pb results are presented in two ways: (1) measured isotopic ratios corrected for downhole fractionation and instrument bias with *Iolite 4*, and (2) U-Pb ages and 2-sigma propagated errors uncorrected for common lead. See the main text for a discussion on the treatment of discordant data.

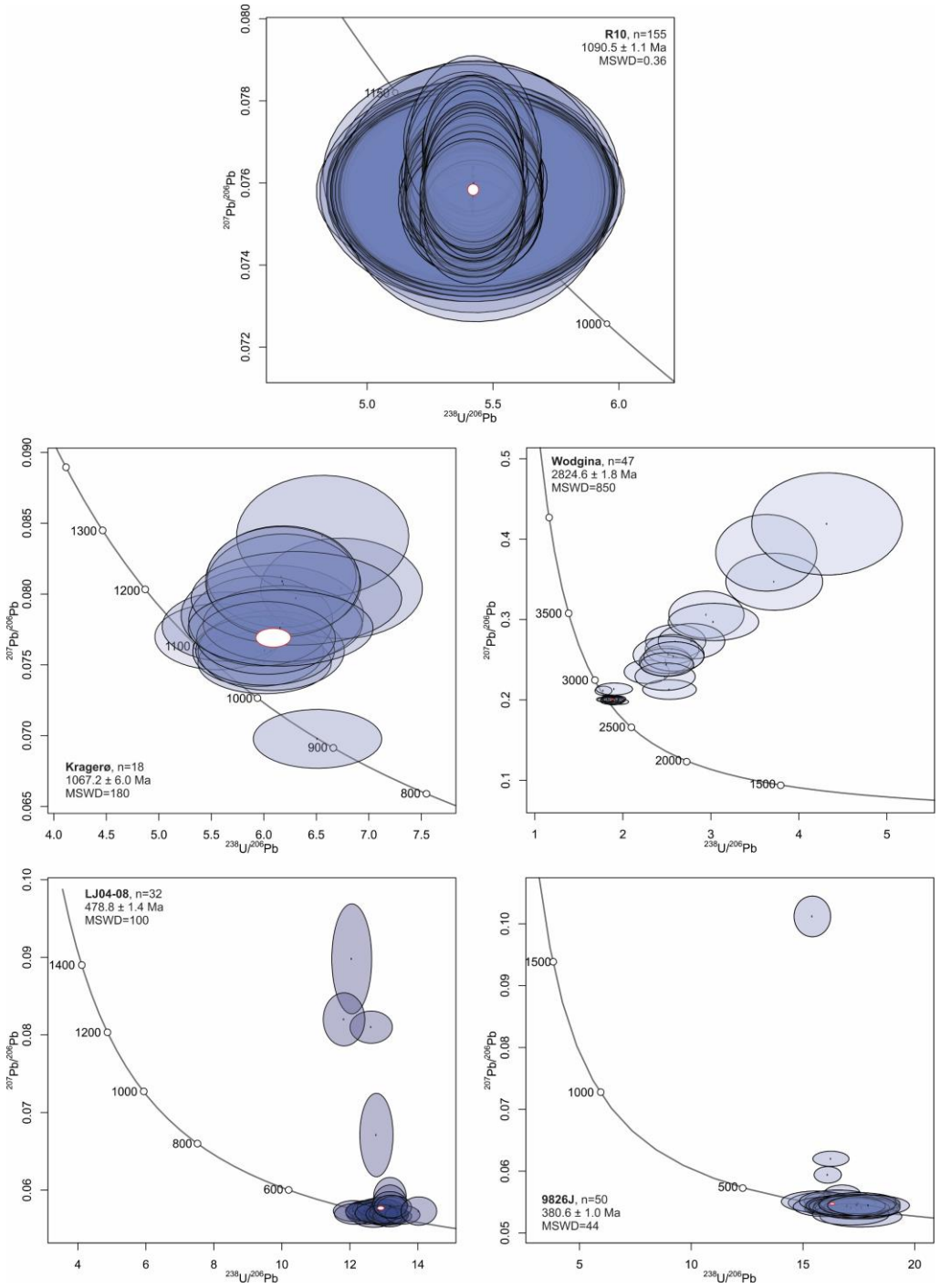

Figure A.1. Concordia ages of rutile reference materials displayed on Tera-Wasserburg plots created with *IsoplotR* (Vermeesch, 2018) with 2-sigma uncertainty ellipses. Reference materials were analyzed in three LA-ICP-MS sessions. There is no discordance or outlier filter.

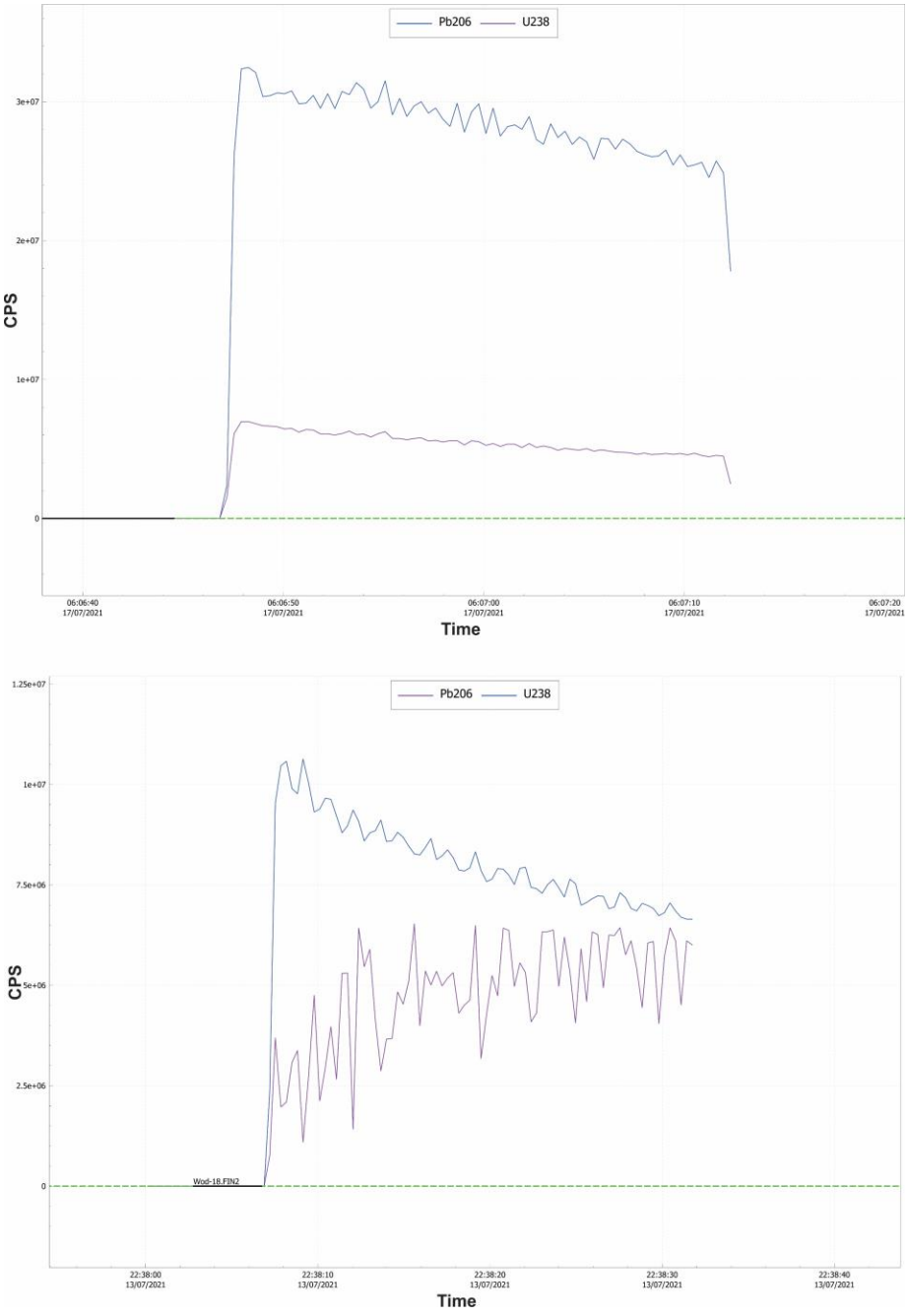

Figure A.2. Wodgina downhole fractionation. Representative examples of downhole fractionation pattern in Wodgina. The typical U-Pb LA-ICP-MS downhole fractionation pattern where the signal decreases throughout the ablation duration (top). Some Wodgina analyses showed an inverse relationship between Pb and U, where Pb increased throughout the analysis (bottom).

Table A.1. University of Washington TraceLab zircon U-Pb metadata, following reporting recommendations (Horstwood et al., 2016).

Laboratory and Sample Preparation	
Laboratory name	TraceLab, University of Washington, Seattle
Sample type/mineral	Zircons
Sample preparation	Conventional mineral separation, 1-inch epoxy mount, 5 μm polish to finish
Imaging	TFS Apreo-S with Lovac Scanning Electron Microscope and Directional-backscatter (DBS)
Laser Ablation System	
Make, Model & type	Analyte-G2 Excimer
Ablation cell	HelEx 2-volume sample cell
Laser wavelength (nm)	193 nm
Pulse width (ns)	< 5 ns
Fluence (J/cm^2)	4.12 J/cm^2
Repetition rate (Hz)	10 Hz
Ablation duration (s)	38 seconds
Ablation pit depth / ablation rate	18 μm pit depth, measured using a SEM and a profilometer, equivalent to 0.05 μm/pulse
Spot diameter (μm) nominal/actual	25 μm / 29 μm
Sampling mode / pattern	Static spot ablation
Carrier gas	100% He in the cell, N_2 added downstream
Cell carrier gas flow (L/min)	0.5 L/min for He (Mass Flow Controller 1), 0.2 L/min for He (Mass Flow Controller 2), and 10 mL/min for N_2 (Mass Flow Controller 3)
ICP-MS Instrument	
Make, Model & type	iCAP RQ, Q-ICP-MS
Sample introduction	Ablation aerosol
RF power (W)	1150 W
Make-up gas flow (L/min)	Cool flow 14 L/min, Auxiliary gas flow 0.8 L/min
Detection system	Dual mode secondary electron multiplier (SEM)
Masses measured	90Zr, 204 Pb, 206-208 Pb, 232Th, 235U, 238U
Integration time per peak/dwell times (ms); quadrupole settling time between mass jumps	90Zr: 0.01s; 204Pb: 0.01s; 206Pb: 0.015s; 207Pb: 0.012s; 208Pb: 0.1s; 232Th: 0.1s; 235U: 0.01s; 238U: 0.12s
Total integration time per output datapoint	0.62s
'Sensitivity' as useful yield (%, element)	0.2% U
ICP-MS dead time (ns)	40 ns
Data Processing	
Gas blank	27 second on-peak zero subtracted
Calibration strategy	Plešovice (PLS) used as primary reference material, GHB and FC-1 used as secondary reference materials and validation
Reference material information	Plešovice (Sláma et al., 2008) GHB (Eddy et al., 2016) FC-1 (Paces and Miller, 1993)
Data processing package used / Correction for LIEF	*Iolite* (*U_Pb_Geochron4* and *VizualAge* DRS) (Paton et al., 2011; Chew et al., 2014)
Mass discrimination	NIST612 used for initial mass bias correction during autotuning, then 207Pb/206Pb and 206Pb/238U normalized to reference material
Common-Pb correction, composition and uncertainty	No common-Pb correction applied (see discussion in Shekut and Licht (2020) supplementary materials)
Uncertainty level & propagation	Ages are quotes as 2s absolute, propagation is by quadratic addition
Quality control / Validation	GHB and FC-1 used as secondary reference materials. See also Shekut and Licht (2020) (Table 2 in their Supplemental File 1) for validation of international reference materials

Table A.2. University of Kansas IGL zircon U-Pb metadata from Campbell (2017).

Laboratory and Sample Preparation	
Laboratory name	KU Geology Isotope Geochemistry Laboratories
Sample type/mineral	Zircon
Sample preparation	Standard mineral separation & epoxy grain mount
Laser Ablation System	
Make, Model & type	ArF excimer 193 nm, Photon Machines Analyte G2, ATLEX 300
Ablation cell	Helex 2, two-volume cell
Laser wavelength (nm)	193
Pulse width (ns)	5 ns
Fluence (J/cm^2)	2 J/cm^2
Repetition rate (Hz)	10 Hz
Ablation duration (s)	26 seconds
Spot diameter (μm) nominal/actual	20 μm / 20 μm
Sampling mode / pattern	Single spot ablation
Carrier gas	He, 1.01 (cell); Ar, 1.1
ICP-MS Instrument	
Make, Model & type	Thermo Element2 magnetic sector field ICP-MS
Sample introduction	Ablation aerosol
RF power (W)	1100 W
Make-up gas flow (L/min)	Ar, 1.1/min
Detection system	Single detector, counting & analog
Masses measured	206Pb, 207Pb, 208Pb, 232Th, 238U
Integration time per peak (ms)	1-5 (long)
Total integration time per reading (secs)	23 (long)
Total method time (secs)	42 (long)
Sensitivity/Efficiency	~0.1% U, GJ-1
UO+/U+(%)	< 0.01
$^{238}U+/^{232}Th+$	> 0.6
Data Processing	
Gas blank	21 (long)
Calibration strategy	Sample/ standard bracketing. GJ-1 used as primary calibration standard. Plešovice and Fish Canyon Tuff used as secondary reference materials.
Reference material information	GJ-1 (Jackson et al., 2004) Plešovice (Sláma et al., 2008) Fish Canyon Tuff (Wotzlaw et al., 2013)
Data processing package used	ET_Redux-3.6.14 (McLean et al., 2016), IGOR PRO, Iolite 2.5
Mass discrimination	Y-Intercept, Downhole
Common-Pb correction, composition and uncertainty	No common-Pb correction applied to the data
Uncertainty level & propagation	Age uncertainties at ±2σ absolute, propagation is by quadratic addition following McLean et al., 2016 and Paton et al., 2010
Quality control / Validation	Plešovice and Fish Canyon Tuff used as secondary reference materials

Table A.3. University of Kansas IGL detrital rutile U-Pb metadata.

Laboratory and Sample Preparation	
Laboratory name	The University of Kansas, Dept. of Geology, Isotope Geochemistry Lab
Sample type/mineral	Rutile
Sample preparation	1-in epoxy rounds
Imaging	EDS in SEM
Laser Ablation System	
Make, model & type	ATL ArF excimer laser (193 nm), Photon Machines AnalyteG2
Ablation cell & volume	HeLex 9-sample cell
Laser wavelength	193 nm
Pulse width (ns)	5 ns
Fluence	3.0 J/cm2 (77% at 5mJ output)
Repetition rate	10 Hz
Spot size (um)	Trace elements: 25 µm; U-Pb: 50 µm
Sampling mode / pattern	Single spots
Carrier gas	He, 1.1 l/min, Ar, 1.07 l/min
Ablation duration	25s
Cell carrier gas flow	He, 1.1 l/min
ICP-MS Instrument	
Make, Model & type	Thermo Element2 magnetic sector field ICP-MS (single collector)
Sample introduction	Aerosol with sample + He was mixed with Ar using a T-connector 15 cm upstream from torch
RF power	1200–1250 W
Make-up gas flow	Ar, 1.07 l/min
Sampling depth	ca. 20 µm
Detection system	single detector (SEM), counting & analog modes
Elements/ isotopes analyzed	Trace elements: 49Ti, 51V, 53Cr, 56Fe, 66Zn, 69Ga, 90Zr, 93Nb, 95Mo, 118Sn, 121Sb, 177Hf, 181Ta, 182W. U-Pb: 206Pb, 207Pb, 208Pb, 232Th, 238U
Integration time per channel (Sample Time)	Trace elements: 49Ti=3 ms, 90Zr=20 ms, and 10 ms for all other isotopes; U-Pb: 206=8 ms, 207=10 ms, 208=2 ms, 232=2 ms, 238=4 ms
Total integration time (Segment Duration)	Trace elements: 49Ti=9 ms, 90Zr=20 ms, and 10 ms for all other isotopes; U-Pb: 206Pb=32 ms, 207Pb=40 ms, 208Pb=8 ms, 232Th=8 ms, 238U=20 ms
Total method time	Trace elements: 40s (120 runs, 1 pass); U-Pb: 31s (100 runs, 3 passes)
ICP Dead time	6 ns
UO+/U+	≤0.25%
232Th+/238U+	>0.75

…continued on next page

Data Processing	
Gas blank	Trace elements: 7-15 s, U-Pb: 7-15 s
Calibration strategy	Trace elements: standard-sampling bracketing + internal standardization assuming 99% TiO2; U-Pb: standard-sampling bracketing
Reference material info	Trace elements: GSD-1G (Guillong et al., 2005; Jochum et al., 2005); U-Pb: R10 (Luvizotto et al., 2009)
Internal std for trace elements	49Ti
Data processing package used / Correction for LIEF	Iolite 4 (Paton et al., 2011): Trace elements: Trace Elements data reduction scheme; U-Pb: U-Pb Geochronology data reduction scheme; exponential LIEF correction for U-Pb ratios.
Common-Pb correction, composition and uncertainty	Not performed
Uncertainty level & propagation	Trace elements: 2se internal uncertainty; U:Pb: 2se propogated uncertainty from U-Pb Geochronology data reduction scheme. Concordia diagrams were plotted using IsoplotR (Vermeesch, 2018) with 2s uncertainty ellipses
Reproducibility	Trace elements: 5–7%. U-Pb ratios: 2–4%
Quality control / Validation	Trace elements: R10 (Luvizotto et al., 2009) and GSC-1G (Guillong et al., 2005; Jochum et al., 2005); U-Pb: Wodgina (Ewing, 2011), Kragerø (Kellett et al., 2018), 9826J (Kylander-Clark, 2008), LJ04-08 (Apen et al., 2020)

Appendix B. Supplementary Materials for Chapter 2

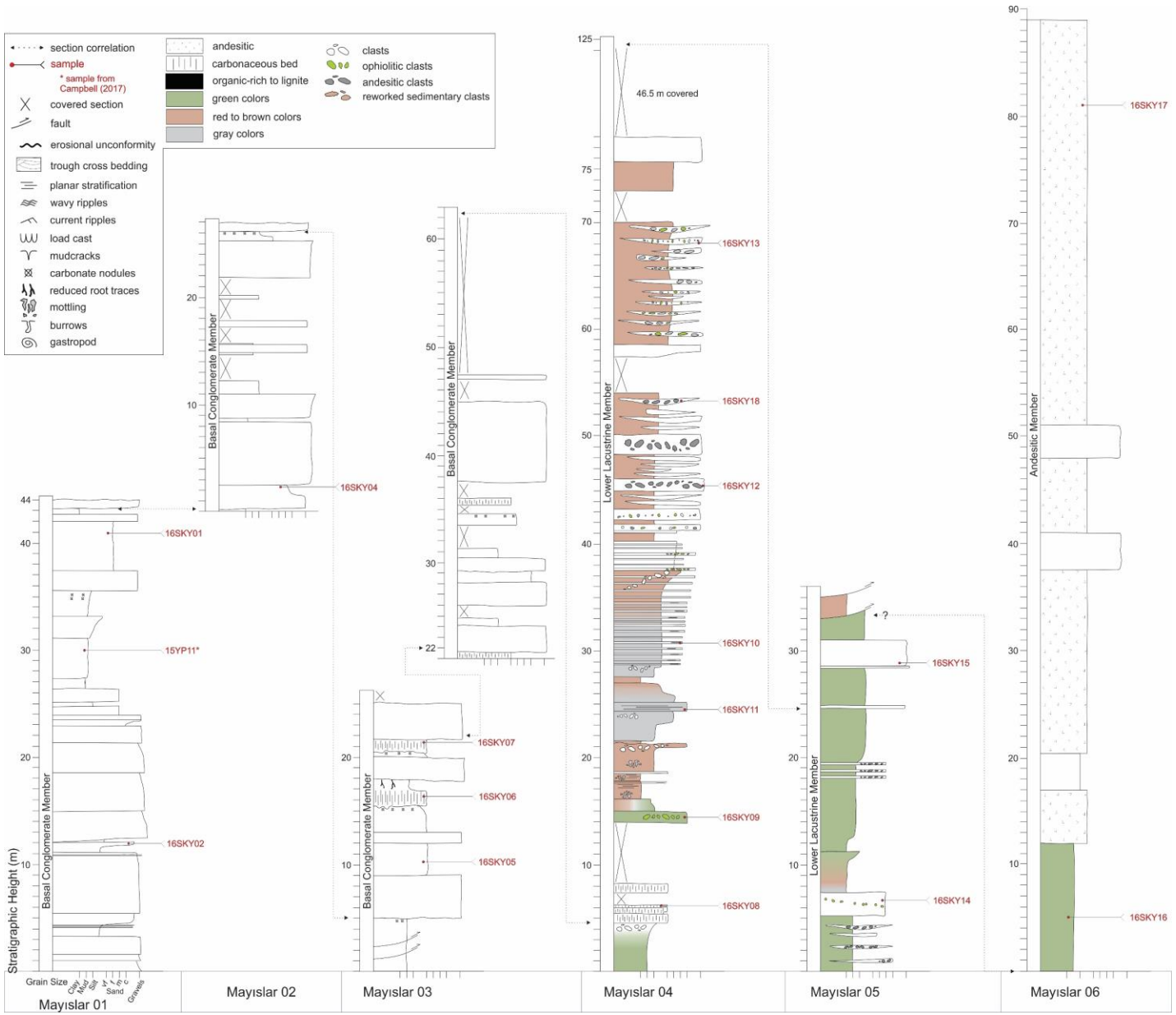

Figure B.1. Measured sections in the Mayıslar area of the Sarıcakaya Basin. Measured section locations are given in Table B.2 and displayed on Figure 2.2.

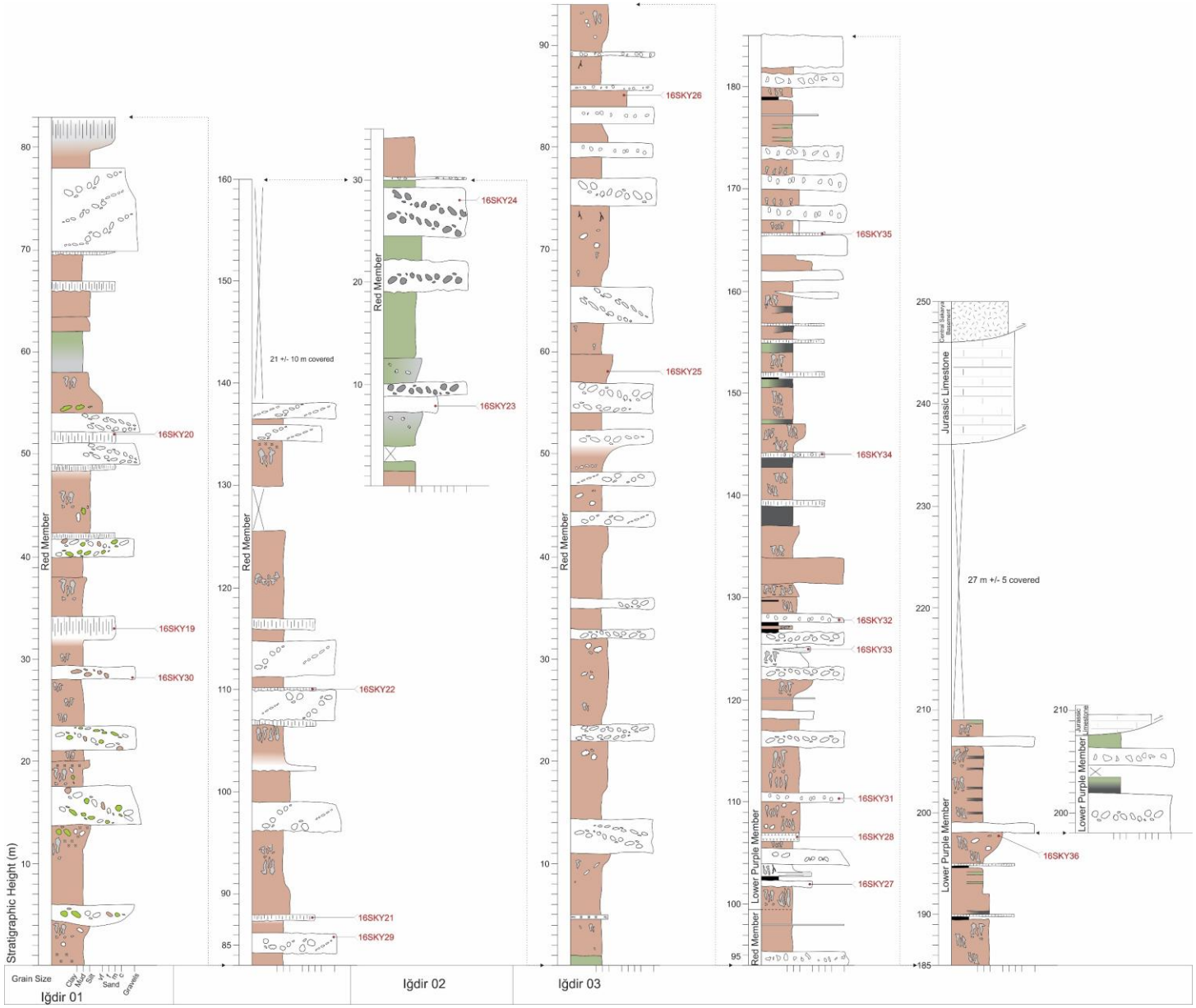

Figure B.2. Measured sections in the Iğdir area of the Sarıcakaya Basin. Measured at 10 to 50-cm resolution. Legend in Figure B.1. Measured section locations are given in Table B.2 and displayed on Figure 2.2.

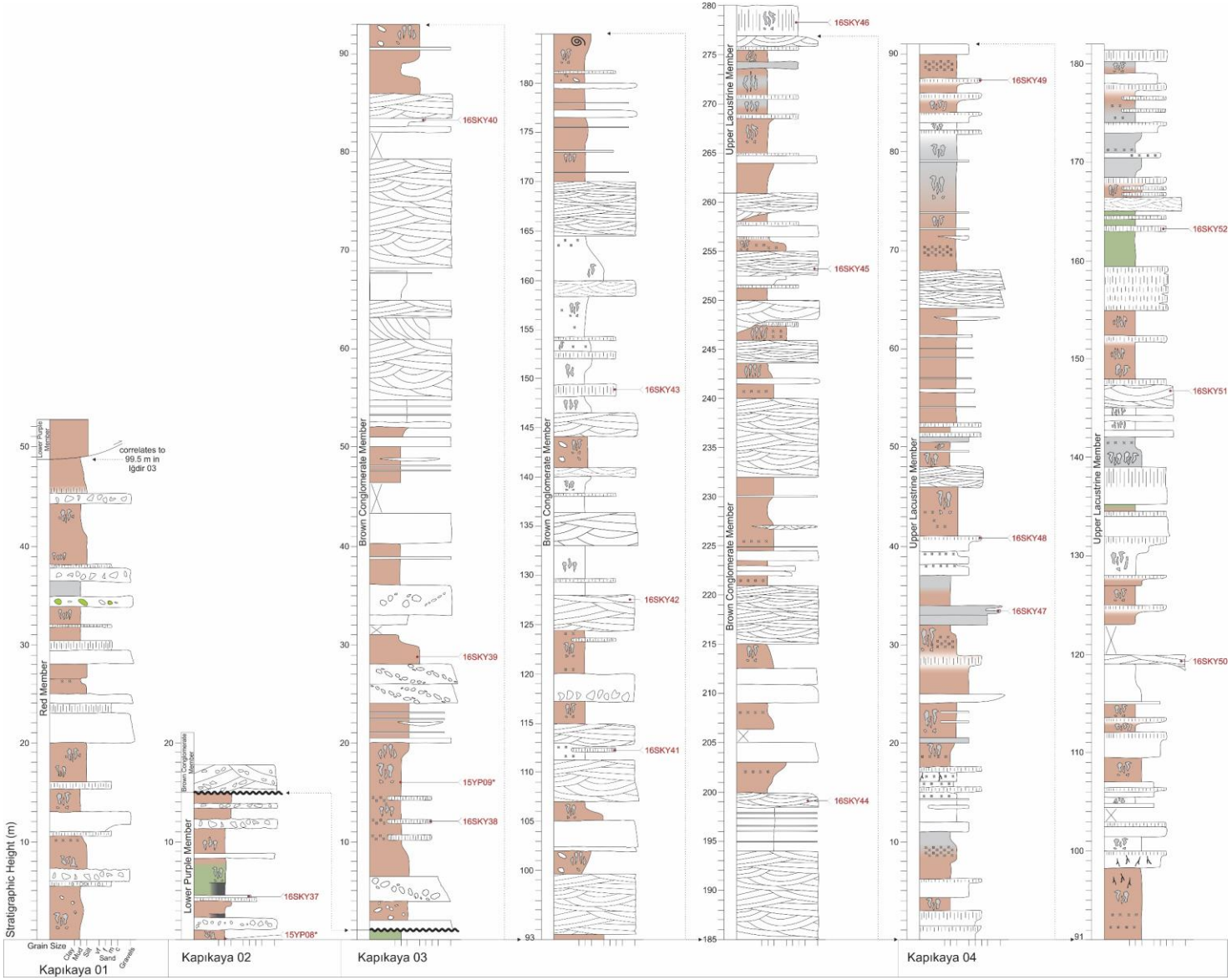

Figure B.3. Measured sections in the Kapıkaya area of the Sarıcakaya Basin. Measured at 10 to 50-cm resolution. Legend in Figure B.1. Measured section locations are given in Table B.2 and displayed on Figure 2.2.

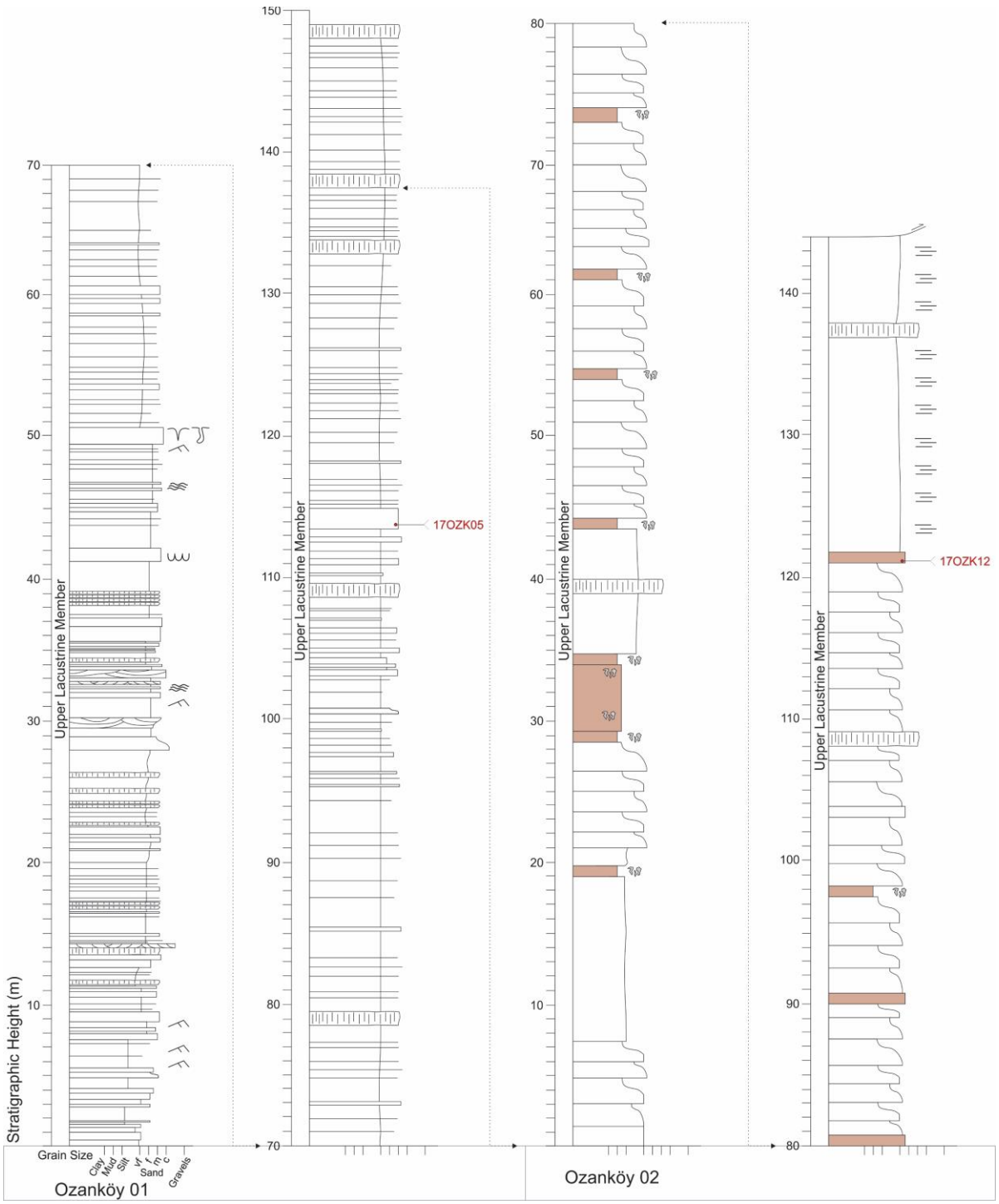

Figure B.4. Measured sections in the Ozanköy area of the Sarıcakaya Basin. Measured at 1.5-m resolution, except 0 to 50 m of Ozanköy Section 01 which was measured at 0.5-m resolution. Legend in Figure B.1. Measured section locations are given in Table B.2 and displayed on Figure 2.2.

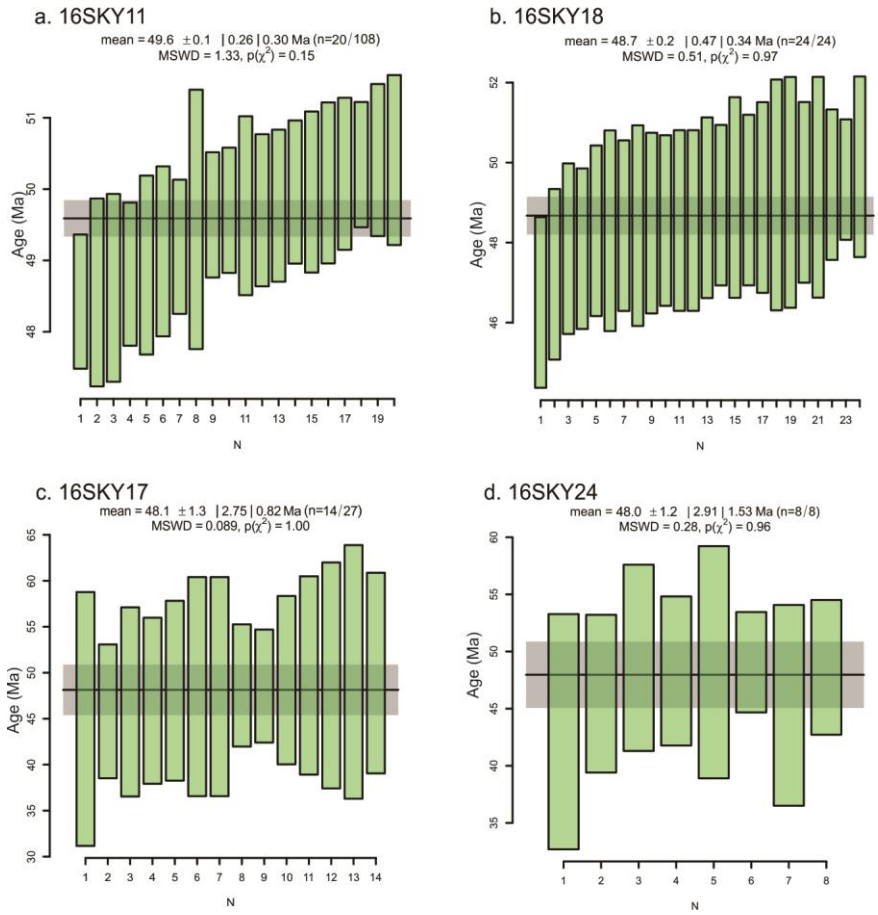

Figure B.5. Weighted mean age of new volcaniclastic samples calculated using *IsoplotR* (Vermeesch, 2018). Black line and gray bar depict the weighted mean age and the 2-sigma error not including the modelling error. N are the zircon ages ordered from youngest to oldest. Raw data are in in the appendix files.

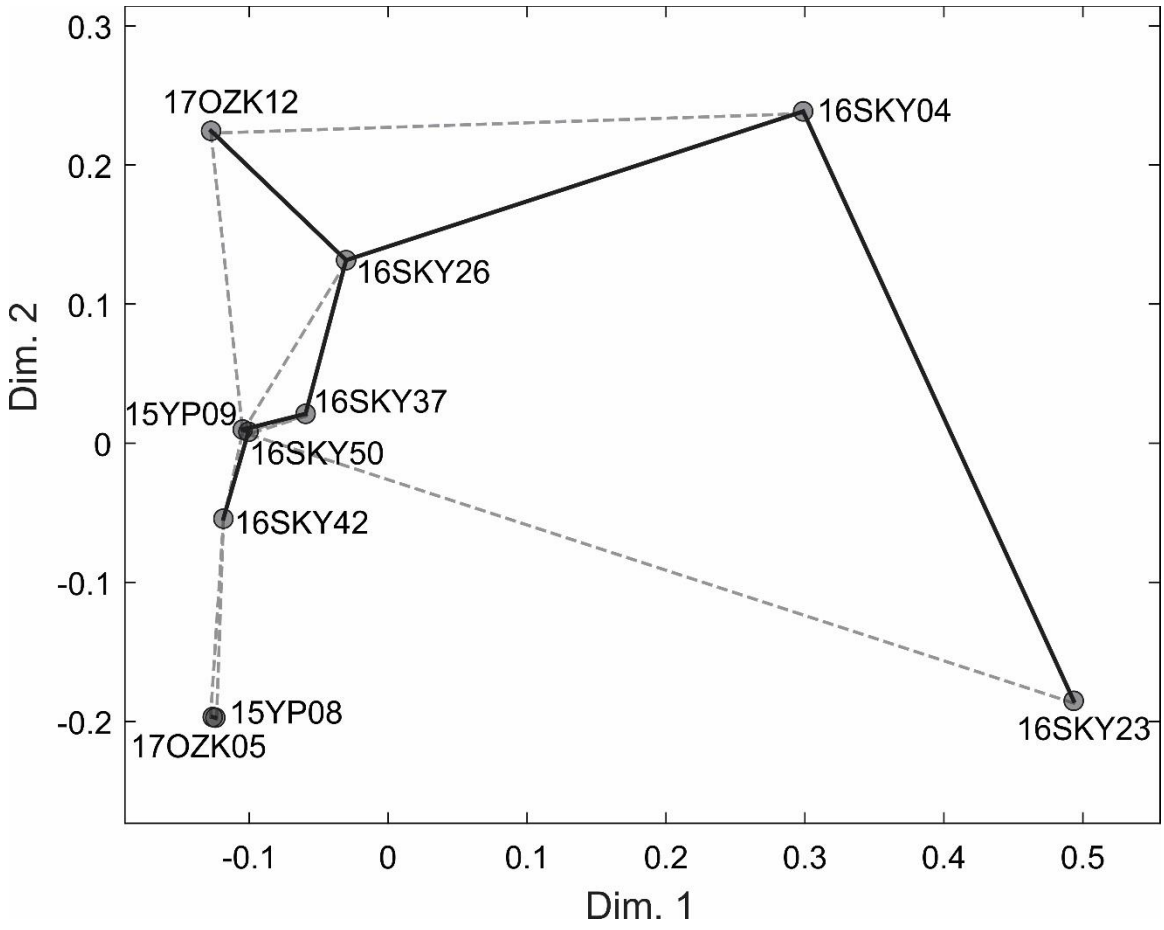

Figure B.6. Multidimensional scaling map showing the dissimilarities between individual Sarıcakaya Basin samples from this study and Campbell (2017). Solid lines connect closest neighbors (least dissimilar) and dashed lines connect second closest neighbors. Axes are in dimensionless "KeS units" ($-1 < KS < 1$) of dissimilarity between samples. Final "stress" value is 0.018, indicating a goodness-of-fit between "excellent" and "perfect" (Vermeesch, 2013).

Table B.1. Detrital and volcaniclastic zircon samples, IGSN, location and description.

Sample Name	**IGSN**	**Latitude**	**Longitude**	**Description**
16SKY04	IEMUE0017	40°01'48.9"N	30°39'08.3"E	Sandstone, Mayıslar 02, 2 m
16SKY11	IEMUE001A	40°01'59.7"N	30°39'04.4"E	Volcaniclastic, Mayıslar 04, 24.5 m
16SKY18	IEMUE001G	40°01'59.7"N	30°39'04.4"E	Volcaniclastic, Mayıslar 04, 54 m
16SKY17	IEMUE001F	40°02'13.4"N	30°39'01.6"E	Volcaniclastic, Mayıslar 06, 81 m
16SKY23	IEMUE001H	40°03'28.1"N	30°41'12.6"E	Sandstone, Iğdir 02, 8.5 m
16SKY24	IEMUE001I	40°03'28.1"N	30°41'12.6"E	Volcaniclastic, Iğdir 02, 28 m
16SKY26	IEMUE001K	40°03'30.9"N	30°41'17.1"E	Sandstone, Iğdir 03, 85 m
16SKY37	IEMUE001Q	40°04'22.4"N	30°44'30.5"E	Sandstone, Kapıkaya 02, 4.5 m
16SKY42	IEMUE001T	40°04'28.2"N	30°44'38.2"E	Conglomerate, Kapıkaya 03, 127 m
16SKY50	IEMUE001W	40°04'43.1"N	30°44'41.0"E	Conglomerate, Kapıkaya 04, 127 m
17OZK05	IEMUE001Z	40°08'20.1"N	30°55'52.0"E	Sandstone, Ozanköy 01, 113 m
17OZK12	IEMUE0020	40°08'30.5"N	30°55'9.8"E	Sandstone, Ozanköy 02, 121 m
16ESK01	IEMUE0014	39°42'15.7"N	30°55'33.8"E	Modern river draining accretionary prism and Karakaya Complex schist
17RIVER01	IEMUE0021	40°00'07.9"N	30°34'18.3"E	Modern river draining the accretionary prism into Sarıcakaya Basin
17BASE01	IEMUE001Y	40°02'31.7"N	30°28'18.2"E	Gneiss from Söğüt Metamorphics

Table B.2. GPS location of measured stratigraphic sections depicted in Figure 2.2, Figure 2.4, Figure B.1, Figure B.2, Figure B.3, and Figure B.4.

Measured Section	**Latitude**	**Longitude**
Mayıslar 01 Base	40°01'45.9"N	30°39'11.5"E
Mayıslar 02 Base	40°01'48.9"N	30°39'08.3"E
Mayıslar 03 Base	40°01'53.1"N	30°39'07.7"E
Mayıslar 04 Base	40°01'59.7"N	30°39'04.4"E
Mayıslar 05 Base	40°02'07.4"N	30°38'56.5"E
Mayıslar 05 Top	40°02'08.8"N	30°39'01.2"E
Mayıslar 06 Base	40°02'08.8"N	30°39'01.2"E
Mayıslar 06 Top	40°02'13.4"N	30°39'01.6"E
Iğdir 01 Base	40°03'22.6"N	30°41'20.4"E
Iğdir 02 Base	40°03'28.1"N	30°41'12.6"E
Iğdir 03 Base	40°03'30.9"N	30°41'17.1"E
Kapıkaya 01 Base	40°04'14.4"N	30°44'22.0"E
Kapıkaya 02 Base	40°04'22.4"N	30°44'30.5"E
Kapıkaya 03 Base	40°04'28.2"N	30°44'38.2"E
Kapıkaya 03 Top	40°04'38.8"N	30°44'32.6"E
Kapıkaya 04 Base	40°04'43.1"N	30°44'41.0"E
Ozanköy 01 Base	40°08'20.1"N	30°55'52.0"E
Ozanköy 02 Base	40°08'30.5"N	30°55'59.8"E

Table B.3. Description of published detrital zircon samples. Raw data included in the appendix files.

Sample Name	Source	Location	Description
15YP09	Campbell (2017)	N40°04'09.6" E30°44'37.5"	Volcaniclastic sandstone in Paleogene series of Saricakaya, 15 m above the major unconformity
15YP08	Campbell (2017)	N40°04'09.6" E30°44'37.5"	Volcaniclastic sandstone in Paleogene series of Saricakaya, 15 m below the major unconformity
15YP12	Campbell (2017)	N40°01'18.9" E30°39'22.9"	Greenschist, basement of Pontides, below Pg section and next to suture
15YP14	Campbell (2017)	N40°10'01.7" E30°31'18.5"	Paleogene sandstone, Yenipazar section, 10m above the disconformity with Maastrichian flysch
15YP13	Campbell (2017)	N40°10'01.7" E30°31'18.5"	Volcaniclastic sandstone in Maastrichian(?) flysch, Yenipazar section, 5m below the disconformity
15YP04	Campbell (2017)	N40°06'06.0" E30°37'02.3"	Lower Jurassic sandstone, base of the Tethyan series, South of Yenipazar
15YP11	Campbell (2017)	N40°01'18.9" E30°39'22.9"	Volcaniclastic sandstone in Paleogene series of Saricakaya, ~30 m above the base of the Pg section
15GO02	Campbell (2017); Ocakoğlu et al. (2018)	40°24'21.6"N 30°47'00.5"E	Upper Cretaceous Yenipazar Fm conglomerate
SgtMeta	Ustaömer et al. (2012)	40°07'24.2"N 30°00'09.0"E	Central Sakarya Basement sillimanite-garnet schist
KK.10	Ustaömer et al. (2016)	40°08'49.4"N 29°50'05.9"E	Upper Triassic Kendirli Fm (Karakaya Complex) sandstone

Appendix C.
Supplementary Materials for Chapter 3

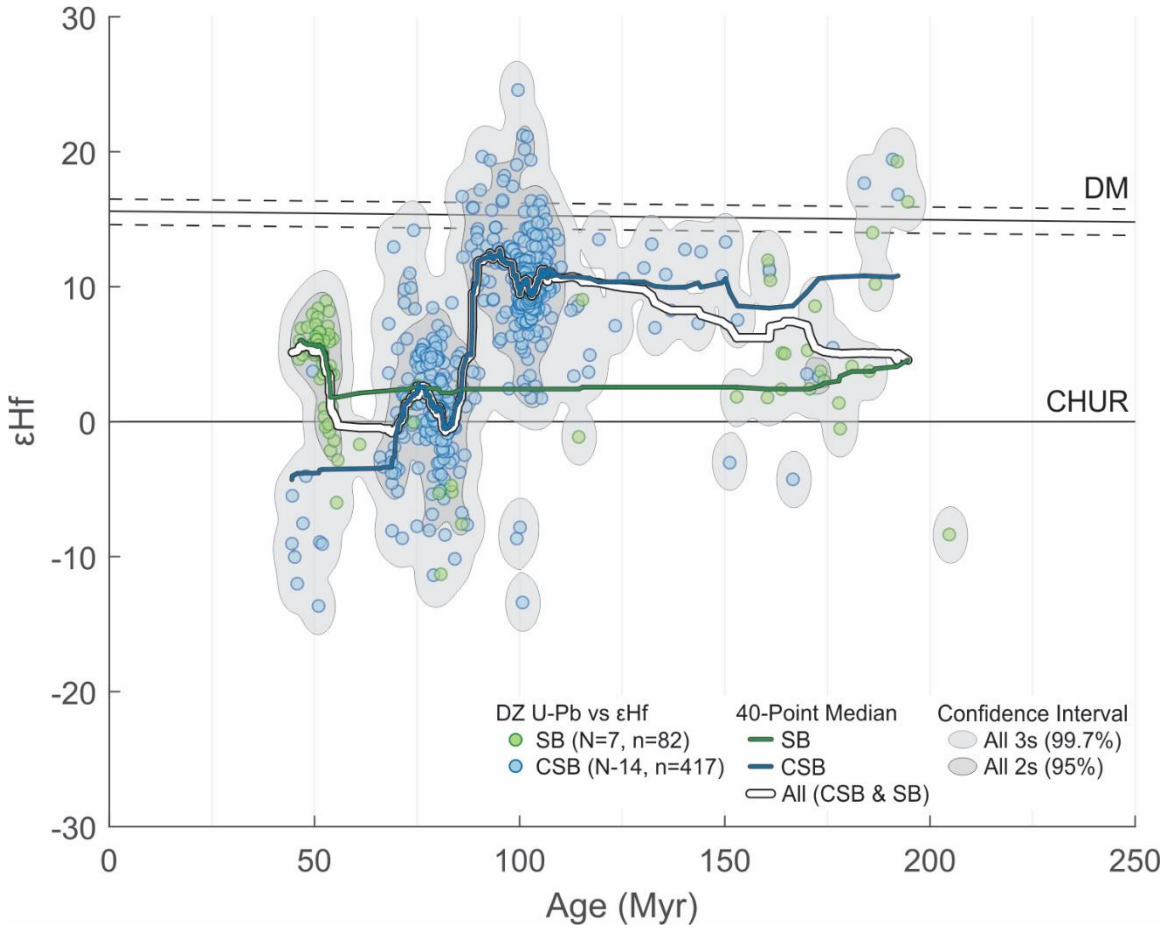

Figure C.1. Volcaniclastic and detrital zircon U-Pb and εHf isotopic data for samples from the Central Sakarya and Sarıcakaya basins. The data are from (Campbell et al., in review) and visualized using *HafniumPlotter* (Sundell et al., 2019). All results are plotted as individual data points (circles) and a 40-point running medians (lines). Gray envelopes represent the 95% (2-sigma) and 99.7% (3-sigma) confidence intervals for bivariate kernel density estimates. DM: depleted mantle; CHUR: chondritic uniform reservoir.